Production of Charmonia in Cu+Cu and p+p Collisions at $\sqrt{s_{NN}} = 200$ GeV

ODA, Susumu

Center for Nuclear Study
Graduate School of Science
The University of Tokyo

A Dissertation Submitted in Partial Fulfillment of
the Requirements for the Degree of Doctor of Science

February 15, 2008

Abstract

Quantum chromodynamics (QCD) is the gauge theory to describe the strong interaction among quarks and gluons. Theoretical calculations based on QCD predict that quarks deconfine and nuclear matter transits to the quark gluon plasma (QGP) under the condition of the energy density of > 1 GeV/fm^3 and temperature of $>$ 150–200 MeV. In the QGP phase, interactions occur with not the freedom of hadrons but the freedom of partons (quarks and gluons). Since the charmonium yield in QGP is expected to be suppressed due to the color Debye screening, the suppression of the charmonium yield has been considered as the most promising signature of QGP formation.

Such high temperature and high density state is expected to have been realized in the early universe. On earth, high-energy heavy-ion collisions are a unique tool to realize such an extreme state.

The productions of J/ψ in ^{63}Cu+^{63}Cu collisions and χ_c in $p+p$ collisions at the center of mass energy per nucleon pair ($\sqrt{s_{NN}}$) of 200 GeV have been studied at the PHENIX experiment at Relativistic Heavy Ion Collider at Brookhaven National Laboratory. The observed J/ψ yield in Cu+Cu collisions is suppressed by a factor of 2 compared with that in the superposition of nucleon-nucleon collisions. However, the charmonium yield is modified by not only QGP but also cold nuclear matter (CNM) in initial and final stages of collisions. A phenomenological model of CNM well describes the observed J/ψ yield suppression in Cu+Cu collisions. Although the charmonium production mechanism is not well understood theoretically, the obtained upper bound of the fraction of J/ψ produced in the decay of χ_c does not exclude the theoretical production model which is used in the CNM model. Furthermore, the assumed fraction of J/ψ from χ_c decay in the CNM model is consistent with the obtained upper bound.

The J/ψ data in heavier nucleus-nucleus collisions, ^{197}Au+^{197}Au collisions, at the same energy by PHENIX shows a much suppression compared with the same CNM model. It is concluded that the J/ψ suppression in Au+Au collisions is caused by other contributions than CNM.

Contents

List of Figures

List of Tables

Chapter 1

Introduction

1.1 QCD and QGP

Quantum Chromodynamics (QCD) is a local $SU(3)$ gauge theory and is recognized as the theory of strong interaction among quarks and gluons. The two important features of QCD are color confinement and asymptotic freedom. Quarks and gluons have the degree of color, and they are confined in color-singlet hadrons in low energy. The strong coupling constant, α_s, can be expressed in terms of the momentum transfer, Q^2, the number of quark flavors, N_f, and the typical QCD scale, $\Lambda_{\rm QCD} \simeq 0.2$ GeV as follows:

$$\alpha_s(Q^2) \simeq \frac{12\pi}{(33-2N_f)\ln\left(\frac{Q^2}{\Lambda_{\rm QCD}}\right)}. \tag{1.1}$$

Thus, with increase of momentum transfer in high-energy collisions, α_s decreases [1, 2]. The environment of extremely high temperature and/or density can also decrease α_s. The color confinement may be broken by the asymptotic freedom with increase of the temperature and/or density of a many body system consisted of hadrons which could result in a phase transition from the confined nuclear matter (ordered phase) to the deconfined state (disordered phase). The deconfined state is called quark gluon plasma (QGP).

The lattice QCD calculations predict that the phase transition to the QGP state occurs at a critical temperature, T_c, of 150–200 MeV. Figure 1.1 shows the calculated results of the entropy density s/T^3 as a function of temperature T. The entropy density increases in stepwise at T_c ∼200 MeV due to the increase of the degree of freedom by deconfinement.

A schematic phase diagram of hadronic matter including QGP is shown in Fig. 1.2. The horizontal axis is the baryon density normalized to the density of the normal nuclear matter (∼0.15 GeV/fm^3) and the vertical axis is the temperature. QGP is considered to have existed in high temperature circumstances of the early universe, a few micro second after the Big Bang.

High-energy heavy-ion collisions provides a possibility to create QGP on earth. Fixed target experiments with high-energy heavy-ion collisions began at Bevalac at Lawrence Berkeley with $\sim 2A$ GeV beams in the middle of 1970's. In 1986, Experiments with higher energy started at Alternating Gradient Synchrotron (AGS) in

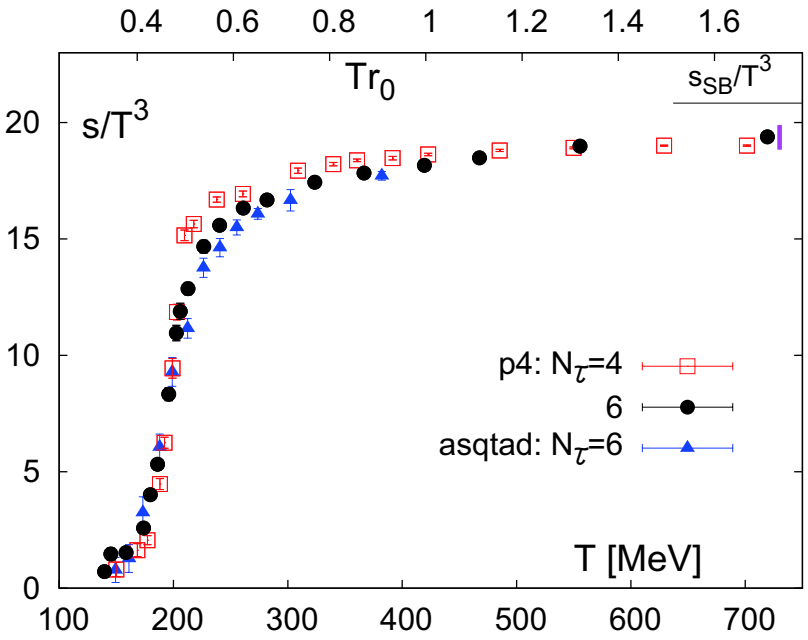

Figure 1.1: The entropy density ($s = \varepsilon + p$) in units of T^3 as a function of T calculated with lattice QCD [3].

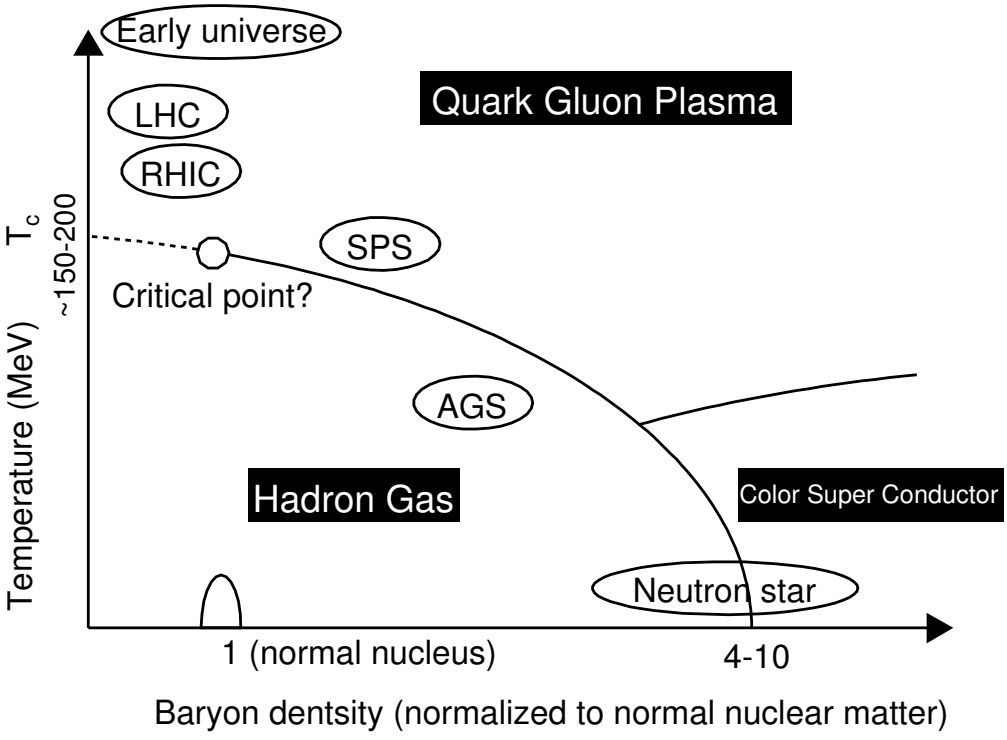

Figure 1.2: A schematic phase diagram of QCD matter.

Brookhaven National Laboratory (BNL) with $\sim$14A GeV beams and at Super Proton Synchrotron (SPS) in European Organization for Nuclear Research (CERN) with $\sim$160A GeV beams.

The Relativistic Heavy Ion Collider (RHIC) at the BNL is the first colliding-type accelerator which can collide heavy nuclei up to gold (^{197}Au) at the center of mass energy per nucleon pair of $\sqrt{s_{NN}} = 200$ GeV and started its operation in 2000. The energy density achieved by the collisions at RHIC is expected to be well above the critical temperature.

1.2 Quarkonia as Probes of QGP

The PHENIX experiment is one of four experiments at RHIC and has been constructed to measure various observables to find signatures of QGP formation. The investigation of J/ψ suppression proposed by Matsui and Satz [4] has long been considered as one of the most promising signatures of QGP formation and is one of the primary subjects of the PHENIX experiment. In QGP, Debye screening limits reach of the color field of a quark within the Debye length λ_D. As temperature increases, λ_D decreases. If λ_D becomes smaller than the radius of a quarkonium (J/ψ, ψ', χ_c, Υ), the quarkonium becomes unbound. J/ψ has a large production cross section and di-lepton (e^+e^-, $\mu^+\mu^-$) decay channels. Leptons have the advantage that they are experimentally easily identified. Therefore, among quarkonia, J/ψ has been used as a tool of QGP search in high-energy heavy-ion collisions.

In high-energy heavy-ion collisions, the J/ψ yield is also reduced by cold nuclear matter (CNM) effects. The CNM effects include absorption of J/ψ into nuclei and the modification of parton distribution function in nuclei.

The NA50 experiment at the SPS measured the J/ψ yield in ^{208}Pb+Pb collisions at $\sqrt{s_{NN}} = 17.3$ GeV (158A GeV/c beams) in 2000 [5]. It was assumed that the initial yield of J/ψ scales with the yield of Drell-Yan di-leptons. The absorption cross section was determined by $p + A$ collisions (A =Be, Al, Cu, Ag, W and Pb). The ratio of the measured yield to the expected yield of J/ψ extrapolated from the results in $p + A$ collisions is suppressed up to $\sim$0.6 in Pb+Pb collisions. The NA50 experiment concluded that their data can be naturally understood with a deconfinement scenario as resulting from the melting of the excited χ_c states above a certain energy density, followed by the suppression of directly produced J/ψ mesons.

The PHENIX experiment measured the J/ψ yields in ^{197}Au+^{197}Au collisions at $\sqrt{s_{NN}} = 200$ GeV in the RHIC Run-4 in 2004 [6] and in p+p collisions at $\sqrt{s} = 200$ GeV in the RHIC Run-5 in 2005 [7]. The yield of J/ψ is strongly suppressed by a factor of > 3 relative to binary collision scaling of the $p + p$ reaction yield. However, the magnitude of the J/ψ suppression is smaller than predictions of phenomenological models which describe the SPS data. At RHIC, d+Au collisions are performed to estimate the CNM effects and the J/ψ yield in d+Au collisions was measured in the RHIC Run-3 in 2002–2003 [8].

To disentangle the competing effects, systematic study of the J/ψ production in high-energy heavy-ion collisions across the entire range of the collision system size is needed. The collision system size is determined by the impact parameter. However, the

statistics of peripheral Au+Au collisions with large impact parameters in Run-4 were limited and the determination of collision geometry in peripheral Au+Au collisions from experimental observables has large ambiguity.

Collisions of lighter nuclei, copper (Cu), have advantages of higher beam intensity and of better collision geometry determination of the small system. Data of the J/ψ production in Cu+Cu collisions can provide complementary information about the CNM effects to that in d+Au collisions and where the J/ψ suppression starts.

Information of χ_c feed down into J/ψ is needed since it is poorly known that about 30% of J/ψ is produced from the decay of χ_c by the experiments at lower and higher energy than RHIC energy with large errors and the χ_c mesons have not been measured around RHIC energy. Dissociation of χ_c can occur at lower temperature than that of J/ψ due to smaller bounding energy (larger mass). Since the production mechanism of quarkonia is not well understood theoretically, measurement of χ_c at RHIC should also become an important input data for quarkonium production models. The ratio of the color singlet contribution to the color octet contribution is important for the CNM effects.

1.3 Organization of This Thesis

Production of J/ψ in ^{63}Cu+^{63}Cu collisions at $\sqrt{s_{NN}} = 200$ GeV in the RHIC Run-5 in 2005 and production of χ_c in $p+p$ collisions at $\sqrt{s} = 200$ GeV in the RHIC Run-5 and Run-6 in 2006 have been studied at the PHENIX experiment at RHIC. These are the objectives of this thesis. These charmonia were detected using the decay of $J/\psi \to e^+e^-$ at midrapidity.

The organization of this thesis is as follows. Chapter 2 introduces the theoretical and experimental background for the charmonium production in high-energy heavy-ion collisions. In chapter 3, the RHIC accelerator complex and the PHENIX detectors are described. In chapter 4, the conditions of beam and trigger in the Cu+Cu run in 2005 and in the $p+p$ runs in 2005 and 2006 are summarized. In chapter 5, the analysis of the $J/\psi \to e^+e^-$ measurement is explained and the results are shown. In chapter 6, the analysis of the $\chi_c \to J/\psi\gamma \to e^+e^-\gamma$ measurement is explained and the result is shown. Interpretations of the results are discussed in chapter 7. Chapter 8 concludes this thesis.

1.4 Major Contributions

The author studied the production of J/ψ in Cu+Cu collisions and χ_c in $p+p$ collisions as a collaborator of the PHENIX experiment. The author carried out the measurements and analysis of J/ψ and χ_c with electron pairs at the PHENIX experiment for the determination of J/ψ and χ_c yields. The result of J/ψ production in Cu+Cu collisions was submitted to Physical Review Letter as the paper entitled "J/ψ Production in $\sqrt{s_{NN}} = 200$ GeV Cu+Cu Collisions" [9]. The author carried out the data taking of the PHENIX experiment and was involved in the operation and calibration of Ring Imaging Cherenkov detector which is a primary device to identify electrons.

Chapter 2

Physics Background

In this chapter, the expected properties of the QGP, and the experimental approach to study the deconfined phase will be described first. Then, the current knowledge and existing results of charmonia, which are related to the motivation of this thesis, will be described [10, 11, 12].

2.1 Thermodynamics of QGP

The "Quark Gluon Plasma" (QGP) is a state where quarks and gluons are deconfined. For quarks being confined inside a hadron, a useful phenomenological description is provided by the MIT bag model [13]. In the MIT bag model, quarks are treated as massless and non-interacting particles ("Stefan-Boltzmann" limit) inside a bag of finite dimensions, and are infinitely massive outside the bag. Confinement in the model is the result of the balance of the bag pressure B, directed inward, and the stress arising from the kinetic energy of the quarks. The bag pressure B is a phenomenological quantity introduced to take into account the nonperturbative effects of QCD. In the MIT bag model, the energy of a system of N confined quarks in a bag of radius R is represented as follows:

$$E = \frac{2.04N}{R} + \frac{4\pi}{3}R^3B. \tag{2.1}$$

The equilibrium radius of the system is located at the radius R determined by $dE/dR = 0$, which leads to a bag pressure constant B related to the radius by

$$B^{\frac{1}{4}} = \left(\frac{2.04N}{4\pi}\right)^{\frac{1}{4}}\frac{1}{R}. \tag{2.2}$$

If we take the confinement radius of 0.8 fm for a 3 quark system in a baryon, we obtain an estimate of the bag pressure constant

$$B^{\frac{1}{4}} = 206 \text{ MeV}. \tag{2.3}$$

In case of a system with zero net baryon density, the dominant excitation in the hadronic phase is the massless pion (Nambu-Goldstone boson), while that in the QGP is the massless quark and gluon. As a first approximation, one may assume a free pion gas (free quark gluon gas) in the low (high) temperature, T, limit.

The equations of state, pressure (EoS), energy density and entropy density, of the massless pion gas are given as follows:

$$P_{\rm H} = d_\pi \frac{\pi^2}{90} T^4, \tag{2.4}$$

$$\varepsilon_{\rm H} = 3 d_\pi \frac{\pi^2}{90} T^4, \tag{2.5}$$

$$s_{\rm H} = 4 d_\pi \frac{\pi^2}{90} T^3, \tag{2.6}$$

where d_π is the number of massless Nambu-Gold bosons in N_f flavors:

$$d_\pi = N_f^2 - 1. \tag{2.7}$$

The EoS in the deconfined QGP phase are:

$$P_{\rm QGP} = d_{\rm QGP} \frac{\pi^2}{90} T^4 - B, \tag{2.8}$$

$$\varepsilon_{\rm QGP} = 3 d_{\rm QGP} \frac{\pi^2}{90} T^4 + B, \tag{2.9}$$

$$s_{\rm QGP} = 4 d_{\rm QGP} \frac{\pi^2}{90} T^3, \tag{2.10}$$

where $d_{\rm QGP}$ is an effective degree of freedom of the quarks and gluons in the QGP phase:

$$d_{\rm QGP} = d_g + \frac{7}{8} d_q, \tag{2.11}$$

$$d_q = 2_{\rm spin} \times 2_{q\bar{q}} \times N_c \times N_f, \tag{2.12}$$

$$d_g = 2_{\rm spin} \times (N_c^2 - 1), \tag{2.13}$$

where 7/8 is due to the difference between the Fermi-Dirac statistics and the Bose-Einstein statistics. In Table 2.1, d_π and $d_{\rm QGP}$ for $N_c = 3$ and $N_f = 0, 1, 2, 3, 4$ are summarized. The degree of freedom increases by an order of magnitude from the hadronic phase to the QGP phase due to the liberation of color degrees of freedom.

N_f	0	1	2	3	4
d_π	0	0	3	8	15
d_q	0	12	24	36	48
d_g	16	16	16	16	16
$d_{\rm QGP}$	16	26.5	37	47.5	58

Table 2.1: Degrees of freedom of the pion (Nambu-Goldstone boson), d_π, the quark, d_q, the gluon, d_g, and effective degrees of freedom in the QGP phase for $N_c = 3$ and with massless N_f flavors.

Since the Helmholtz free energy ($F = E - TS = -P$) has its minimum at equilibrium, the phase which has a higher pressure P is realized in this system. The pressures

of the two phases are shown as a function of T in Fig. 2.1. The critical point is obtained from the phase equilibrium condition,

$$P_{\rm H}(T_c) \;=\; P_{\rm QGP}(T_c), \tag{2.14}$$

which leads to

$$T_c^4 \;=\; \frac{90}{\pi^2}\frac{B}{d_{\rm QGP}-d_\pi}. \tag{2.15}$$

Using Eq. (2.3) with $N_c = 3$, we obtain

$$T_c \;=\; 148\ {\rm MeV}(N_f=2),\ 143\ {\rm MeV}(N_f=3), \tag{2.16}$$

and these values may be compared with the result from the first-principle lattice QCD simulations (Fig. 1.1). The Stefan-Boltzmann limit of the entropy density, $s_{\rm SB} = 4d_{\rm QGP}\pi^2/90 \simeq 20.8$ ($N_f = 3$), is also shown in Fig. 1.1. The entropy density does not reach the limit even at temperature three times higher than the critical temperature and this result indicates that interaction between quarks and gluons are still not negligible at the temperature.

The critical energy density required to realize the QGP is estimated to be

$$\varepsilon_c \sim \varepsilon_{\rm QGP}(T_c) \sim 4B \sim 1\ {\rm GeV/fm}^3. \tag{2.17}$$

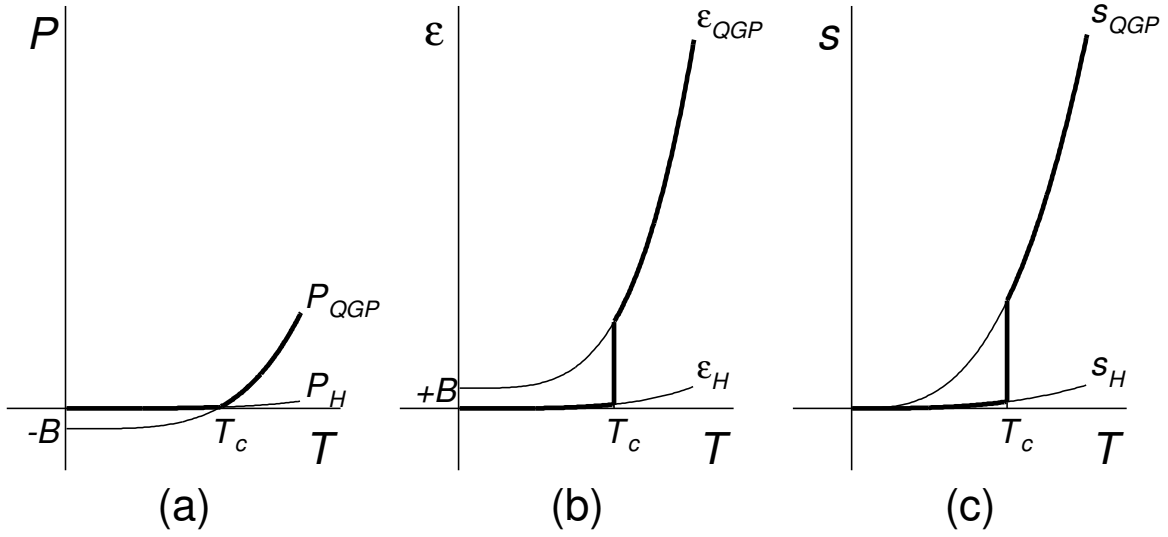

Figure 2.1: The equations of state on the bag model at finite temperature T with zero chemical potential: (a) the pressure, (b) the energy density, (c) the entropy density.

2.2 High-Energy Heavy-Ion Collisions

High-energy heavy-ion collisions have been used to realize a high temperature and high density state which is required for the QGP formation.

2.2.1 Collision Geometry

The geometric aspects of high-energy heavy-ion collisions play an important role in collision dynamics. Since the de Broglie wavelength of the nucleons in high-energy heavy nucleus-nucleus collision is much smaller than the size of the nucleus, the collision is described by the impact parameter, b, of the colliding nuclei. Figure 2.2 illustrates a central collision and a peripheral collision of nuclei with radii of R. As illustrated in Fig. 2.3, the nucleons in high-energy heavy-ion collisions are classified into two groups, the participants and the spectators. The impact parameter b determines the sizes of participants and spectators. Since the spectators keep those longitudinal momenta and emerge at nearly zero degrees in the collision, it is easy to experimentally separate the spectators and the participants. Information about the impact parameter b is obtained by measuring the sizes of the spectators and/or the participants.

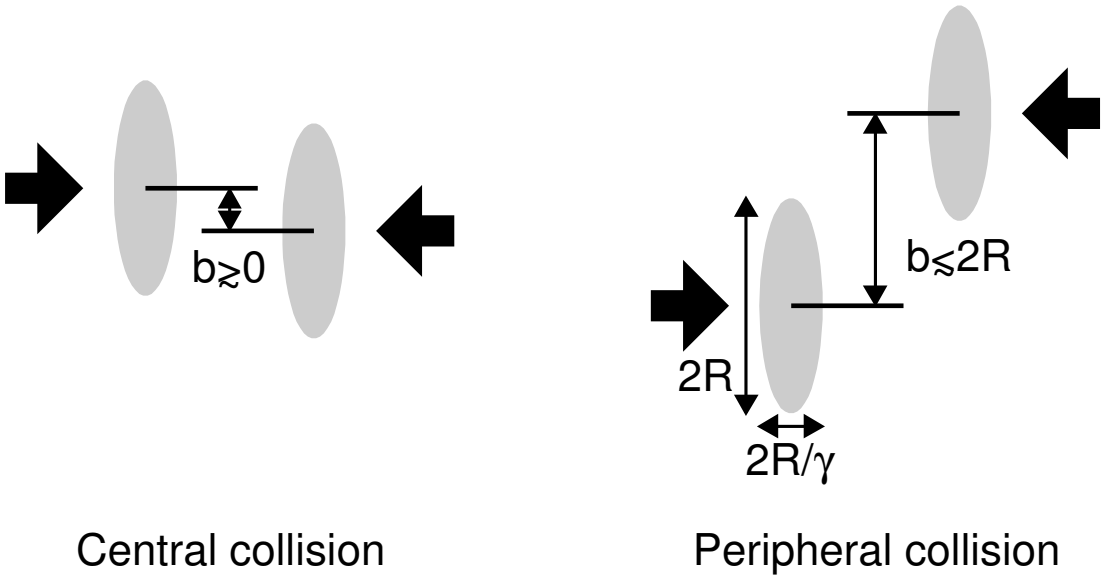

Figure 2.2: A cartoon of central (left) and peripheral (right) collisions.

The relation among impact parameter (b), the number of binary nucleon-nucleon collisions (N_{coll}) and the number of participants (N_{part}) can be evaluated using the Glauber model [14]. The Glauber model describes the heavy-ion collisions based on the participant-spectator model, the nuclear density distribution and the interaction between constituent nucleons. The total inelastic cross section of collisions of a nucleus A and a nucleus B is provided from the nucleon-nucleon inelastic cross section, σ_{NN}. The nucleons in each colliding nucleus are assumed to be distributed according to the Woods-Saxon distribution,

$$\rho(r) \;=\; \frac{\rho_0}{1+\exp\left(\frac{r-R}{d}\right)}, \tag{2.18}$$

where ρ_0 stands for the normal nuclear density, R is the radius and d is the diffuseness parameter.

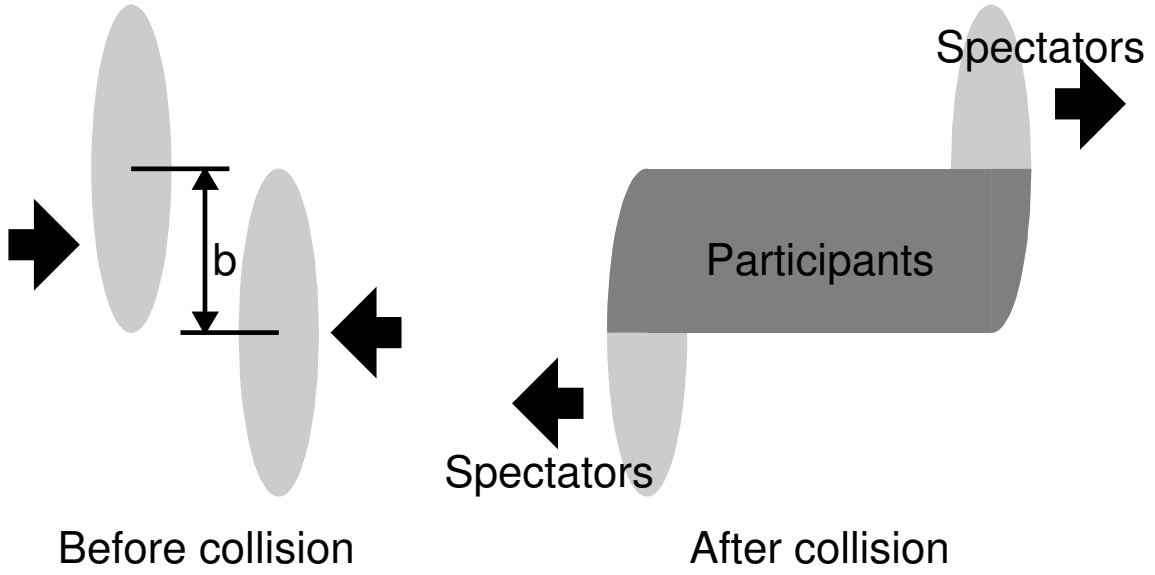

Figure 2.3: A cartoon of before and after a collision of nuclei.

The probability of occurrence of a nucleon-nucleon collision between the nuclei A and B along the z-axis at an impact parameter $\mathbf{b}$ is expressed in the integral formula,

$$T_{AB}(\mathbf{b})\sigma_{NN} \;=\; \int d\mathbf{b}_A dz_A \rho_{\rm A}(\mathbf{b}_A, z_A) d\mathbf{b}_B dz_B \rho_B(\mathbf{b}_B, z_B) t(\mathbf{b} - \mathbf{b}_A - \mathbf{b}_B)\sigma_{NN}, \quad (2.19)$$

where $t(\mathbf{b})$ is the probability for having a nucleon-nucleon collision within the transverse element $d\mathbf{b}$ when A and B collide with an impact parameter $\mathbf{b}$. The number of nucleon-nucleon collisions in an $A+B$ collision can be up to $A \times B$ (63×63=3969 in a Cu+Cu collision). The probability having n nucleon-nucleon collisions can be written using binomial relation,

$$p(n, \mathbf{b}) \;=\; {}_{AB}C_n \left[T_{AB}(\mathbf{b})\sigma_{NN}\right]^n \left[1 - T_{AB}(\mathbf{b})\sigma_{NN}\right]^{AB-n}. \quad (2.20)$$

The total probability for having at least one nucleon-nucleon collision in the collision of nuclei A and B at an impact parameter $\mathbf{b}$ is

$$\frac{d\sigma_{AB}}{d\mathbf{b}} \;=\; \sum_{n=1}^{AB} p(n, \mathbf{b}) \;=\; 1 - p(0, \mathbf{b}) \;=\; 1 - \left[1 - T_{AB}(\mathbf{b})\sigma_{NN}\right]^{AB}. \quad (2.21)$$

Therefore, the total inelastic cross section σ_{AB} is described as follows:

$$\sigma_{AB} \;=\; \int d\mathbf{b} \left(1 - \left[1 - T_{AB}(\mathbf{b})\sigma_{NN}\right]^{AB}\right). \quad (2.22)$$

The average number of inelastic nucleon-nucleon collisions N_{coll} at the impact parameter $\mathbf{b}$ is expressed as follows:

$$N_{coll}(\mathbf{b}) \;=\; \langle n(\mathbf{b}) \rangle \;=\; \sum_{n=1}^{AB} n p(n, \mathbf{b}) \;=\; AB T_{AB}(\mathbf{b})\sigma_{NN}. \quad (2.23)$$

2.2.2 Space-Time Evolution

A high-energy heavy-ion collision is a complicated process, because various phases are expected to exist from the initial collision through the final cold hadronic phase. Bjorken proposed a scenario to describe the space-time evolution of the heavy-ion collisions [15].

Figure 2.4 shows the space time picture of evolution of the matter created in high-energy heavy-ion collisions at RHIC with the longitudinal coordinate z and the time coordinate t. It is assumed that the space-time evolution is dependent on only the proper time $\tau = \sqrt{t^2 - z^2}$, in the high-energy limit.

At the proper time $\tau = 0$, a huge amount of energy is released in a tiny volume and free partons, mainly gluons, are produced by a collision between the two nuclei. The system is initially not in thermal equilibrium, and the dynamics may be described by a cascade of colliding partons. The subsequent multiple parton scattering brings the matter to local equilibrium.

If the deposited energy is large enough and exceeds the critical energy density, the QGP might be formed at the proper time $\tau = \tau_0$. After the QGP is formed, the system would evolve like fluid, expand and cool down according to hydrodynamics.

At $\tau = \tau_C$, the system will reach the critical temperature T_c between the QGP and ordinary hadrons. If the transition is first order, the system passes through the mixed phase consisting of the quarks, gluons and hadrons.

At $\tau = \tau_H$, the system finishes hadronization and produced hadrons keep interacting with each other until the temperature drops to the freeze-out temperature.

At $\tau = \tau_F$, hadrons cease to interact and move away, which is called as kinetic freeze-out.

2.2.3 Initial Energy Density

The achieved energy density at the formation time, τ_0, can be estimated from the physics observables, particle multiplicity and transverse energy, from Bjorken's scenario [15]. In a high-energy heavy-ion collision, nuclei look like pancakes due to the Lorentz contraction ($\gamma \sim 106$ at $\sqrt{s_{NN}} = 200$ GeV) in the center of mass system of the collision. Once a high-energy heavy-ion collision occurs, the two colliding pancakes pass through each other, and many inelastic nucleon-nucleon collisions occur in a very short time. Then a large amount of energy is deposited in a small region of space. For an overlap region with the longitudinal thickness Δz and the transverse area S at $z = 0$ and at $t = \tau_0$, the particle density is

$$\frac{\Delta N}{S\Delta z} = \frac{1}{S}\frac{dN}{dy}\left.\frac{dy}{dz}\right|_{y=0}, \tag{2.24}$$

$$= \frac{1}{S}\frac{dN}{dy}\left.\frac{1}{\tau_0 \cosh y}\right|_{y=0}, \tag{2.25}$$

where y is the rapidity as defined in Appendix A. The energy of a particle with a rapidity y is $m_T \cosh y$ where m_T is the transverse mass of a particle (Appendix A). Then, the energy density, ε_0, is estimated as follows:

$$\varepsilon_0 = m_T \cosh y \frac{\Delta N}{\Delta z S}, \tag{2.26}$$

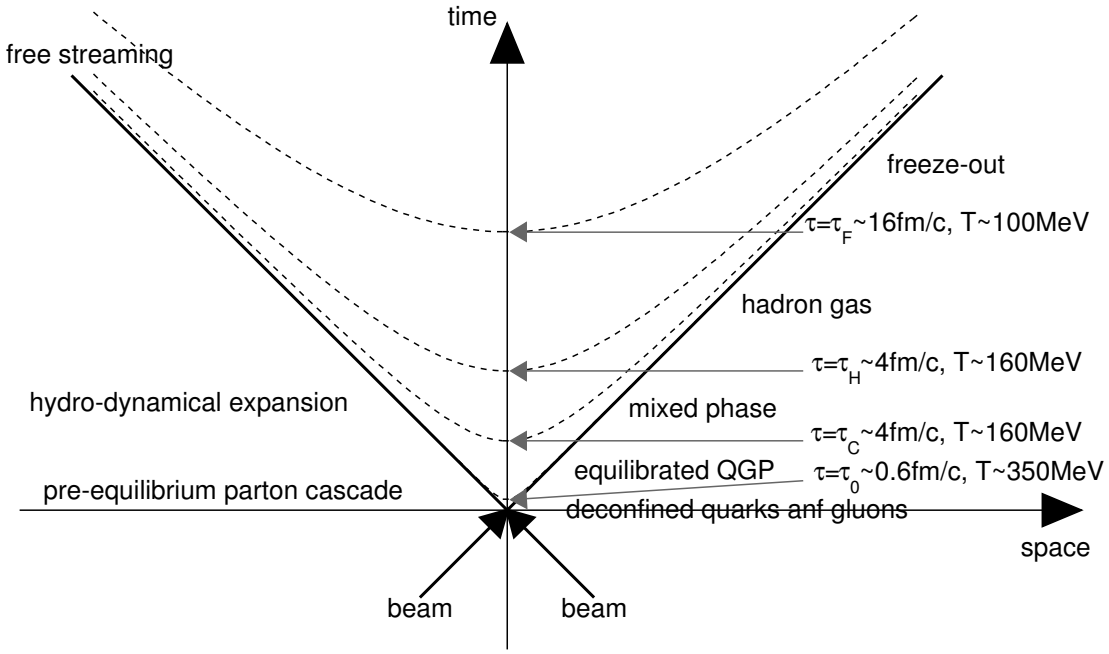

Figure 2.4: A space-time picture of a nucleus-nucleus collision. The times and temperatures for different phases are taken from Ref. [16] based on a hydrodynamic model. Mixed phase would exist only if the transition is first order.

$$= \frac{m_T}{S\tau_0}\frac{dN}{dy}\bigg|_{y=0}, \tag{2.27}$$

$$= \frac{1}{S\tau_0}\frac{dE_T}{dy}\bigg|_{y=0}, \tag{2.28}$$

where E_T is the transverse energy in the collision.

If $\tau_0 = 1$ fm/c is used in central collisions, the Bjorken energy density is estimated to be $\sim$3.2 GeV/fm^3 in Pb+Pb collisions at SPS ($\sqrt{s_{NN}} = 17.3$ GeV) [17] and $\sim$5.4 GeV/fm^3 in Au+Au collisions at RHIC ($\sqrt{s_{NN}} = 200$ GeV) [18]. Figure 2.5 shows $\varepsilon_0\tau_0$ deduced from the PHENIX data in Au+Au collisions at three energies, $\sqrt{s_{NN}} = 19.6$, 130 and 200 GeV. These energy densities exceed the critical energy density of $\varepsilon_c \sim 1$ GeV/fm^3 for the phase transition (Eq. (2.17)).

2.3 Charmonium System

Quarkonia are bound states of heavy quark-antiquark pairs. Quarkonia composed of charm quarks and anti-charm quarks ($c\bar{c}$) are called charmonia and quarkonia composed of bottom quarks and anti-bottom quarks ($b\bar{b}$) are called bottomonia. Figure 2.6 shows the level scheme of the charmonium family with quantum numbers in the vacuum. Properties of J/ψ and three states of χ_c are listed in Table 2.2. The branching ratio (BR) of J/ψ in the e^+e^- ($\mu^+\mu^-$) mode is $BR = 5.94 \pm 0.06\%$ ($5.93 \pm 0.06\%$).

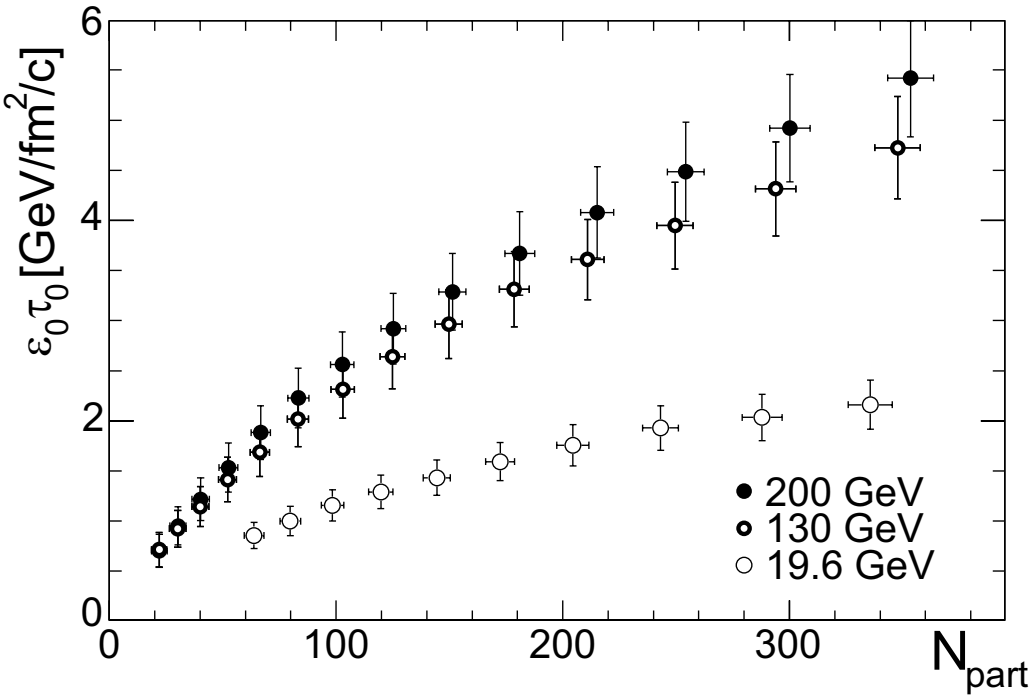

Figure 2.5: $\varepsilon_0\tau_0$ deduced from the PHENIX data in Au+Au collisions at three RHIC energies [18].

Particle	Mass (MeV/c^2)	Mass width (MeV/c^2)	Mass difference from J/ψ (MeV/c^2)	$BR(\chi_{cJ} \to J/\psi\gamma)$
$J/\psi(1S)$	3096.916 ± 0.011	0.0934 ± 0.0021	–	–
$\chi_{c0}(1P)$	3414.76 ± 0.35	10.4 ± 0.7	318	1.30 ± 0.11%
$\chi_{c1}(1P)$	3510.66 ± 0.07	0.89 ± 0.05	414	35.6 ± 1.9%
$\chi_{c2}(1P)$	3556.20 ± 0.09	2.06 ± 0.12	459	20.2 ± 1.0%

Table 2.2: Mass, mass width and radiative decay branching ratio (BR) of J/ψ and three χ_c states from PDG2006 [19].

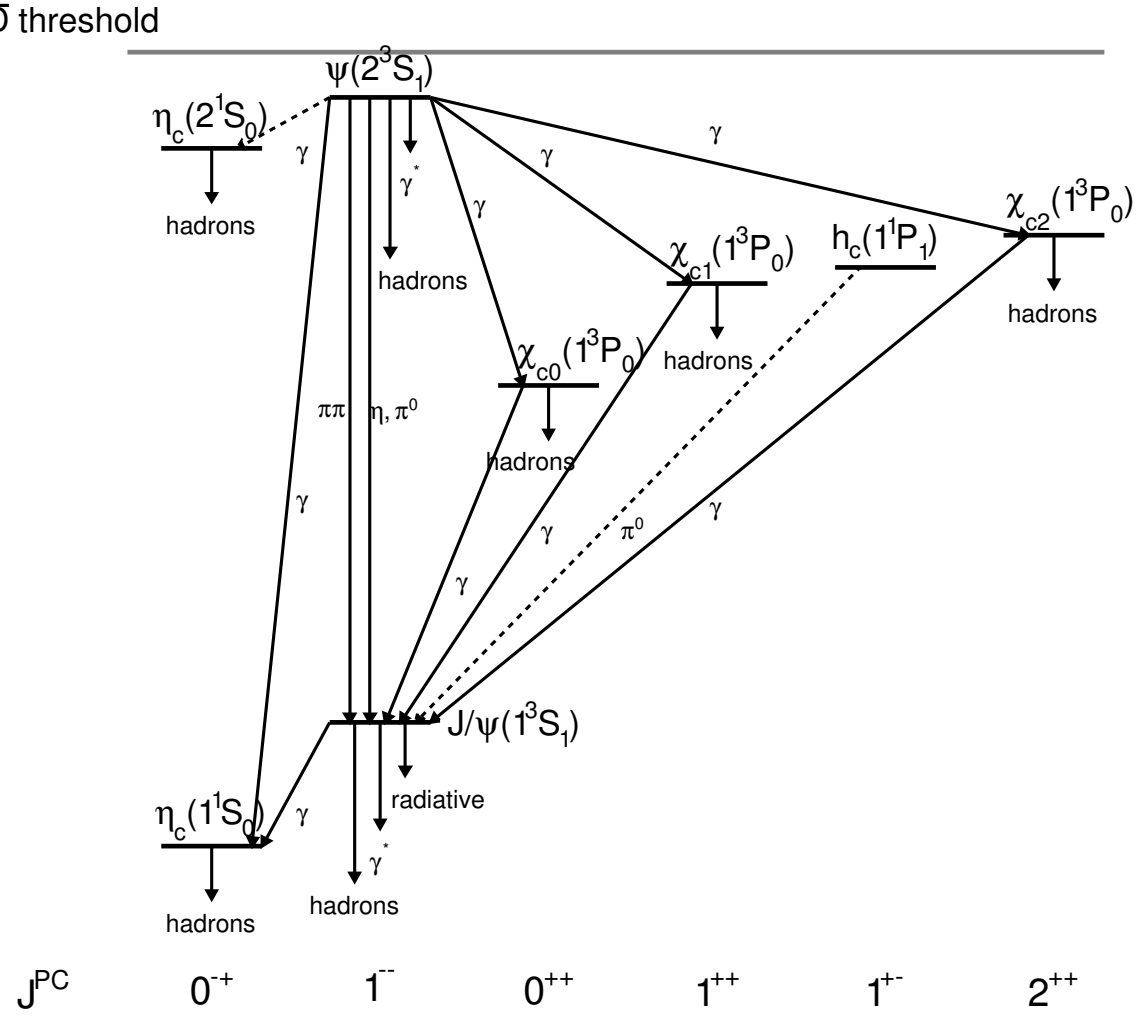

Figure 2.6: The current state of knowledge of the charmonium system and transitions, as interpreted by the charmonium model. Uncertain transitions are indicated by dashed lines. The notation γ^* refers to decay processes involving intermediate virtual photons, including decays to e^+e^- and $\mu^+\mu^-$ [19].

J/ψ was discovered in p+Be$\rightarrow$ e^+e^-X reaction at the AGS at BNL [64] and in e^+e^- annihilation at SPEAR at Stanford Linear Accelerator Center (SLAC) [21] in November, 1974. ψ' was also discovered in e^+e^- annihilation at SPEAR in the same month [22]. The first observation of χ_c was in the channel of $\psi' \rightarrow \chi_c\gamma \rightarrow J/\psi\gamma\gamma$ at DORIS at Deutsches Elektronen-Synchrotron (DESY) in July, 1975 [23].

At temperature $T = 0$, the level scheme of the quarkonium bound states can be reasonably described with the nonrelativistic potential,

$$V(r, T = 0) = -\frac{4}{3}\frac{\alpha_s(r)}{r} + \sigma r, \tag{2.29}$$

where r is the separation between the heavy quark Q and the heavy antiquark $\bar{Q}$. This naive potential does not account for spin-orbit or spin-spin couplings needed to separate the three χ_c states or to separate J/ψ from η_c, respectively.

The $1/r$ term is Coulomb-like and governs the short distance behavior of the potential. It arises from the exchange of a gluon between the Q and $\bar{Q}$. The shorter the distance scale, corresponding to increasing momentum scales, the weaker the coupling.

The linear term corresponds to the confining potential. The strength of the confining term is determined by the string tension, σ.

The quarkonium energy levels depend not only on the potential but also on the a priori unknown masses of heavy quarks, m_c and m_b. The four parameters α_s, σ, m_c and m_b can be roughly determined by fitting the spectra and the obtained values are [24]

$$\alpha_s = 0.353, \tag{2.30}$$
$$\sigma = 0.192 \text{ GeV}^2, \tag{2.31}$$
$$m_c = 1.32 \text{ GeV}/c^2, \tag{2.32}$$
$$m_b = 4.75 \text{ GeV}/c^2. \tag{2.33}$$

The masses and radii of charmonia estimated by the potential model are shown in Table 2.3.

Particle	Mass (GeV/c^2)	Radius (fm)
$J/\psi(1S)$	3.070	0.453
$\chi_c(1P)$	3.500	0.696
$\psi'(2S)$	3.698	0.875
$\Upsilon(1S)$	9.445	0.226
$\Upsilon(2S)$	9.778	0.509
$\chi_b(1P)$	9.829	0.408

Table 2.3: Mass and radius of each quarkonium obtained from a potential model [24].

2.4 Production Mechanism of Charmonia

In this section, production mechanism of charmonia is described.

The production of heavy quark pairs is expected to be a perturbative process since the mass of charm quarks is large compared to the typical QCD scale $\Lambda_{\rm QCD} \sim 0.2$ GeV, which corresponds to $\alpha_s(m_c) \ll 1$. Figure 2.7 shows the examples of heavy quark production diagrams [25], where (a) and (b) are the leading order (LO) processes [26] and (c)–(f) are higher order processes [27]. The dominant process for $c\bar{c}$ production is gluon fusion as shown in Fig. 2.7 (a) and a typical time scale of this process is considered to be $\tau_{pert} \simeq 1/2m_c \simeq 0.06$ fm.

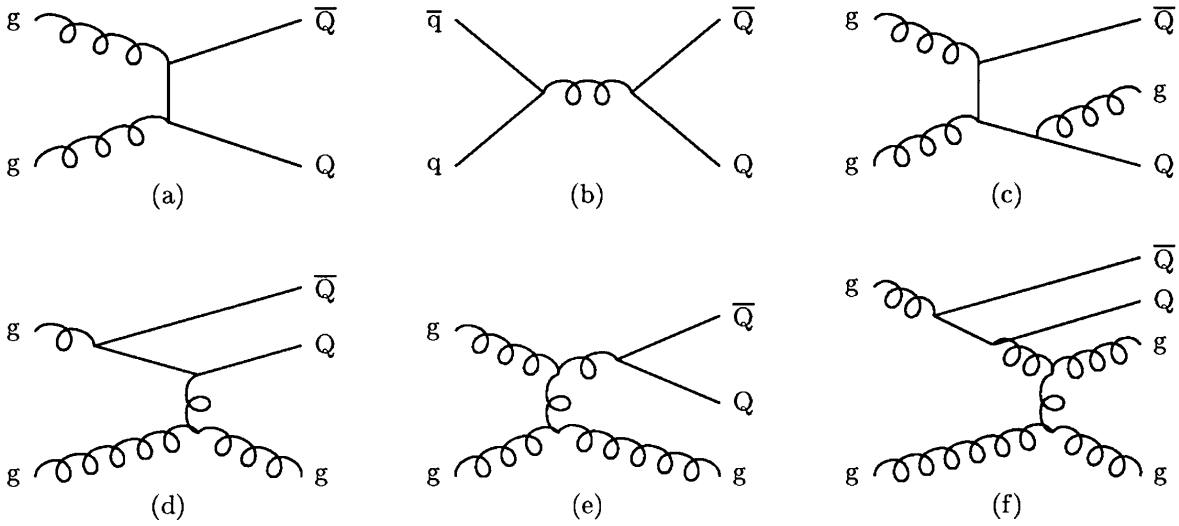

Figure 2.7: Examples of heavy flavor production diagrams [25]. (a) Gluon fusion (leading order). (b) Quark-antiquark annihilation (leading order). (c) Pair creation with gluon emission. (d) Flavor excitation. (e) Gluon splitting. (f) Events classified as gluon splitting but of flavor excitation character.

The tricky part of the charmonium production is to form the bound charmonium state with the right quantum numbers from the $c\bar{c}$ pair. Most $c\bar{c}$ pairs are not produced as color singlets, as required for bound states.

Several models have been employed for quarkonium production including the color singlet model (CSM), nonrelativistic QCD (NRQCD), the color evaporation model (CEM) and the comover enhancement scenario (CES). However, no model succeeded to make unified description of the quarkonium production. Perhaps the most fundamentally approach is the NRQCD and it works best for high p_T charmonium production. However, the CEM predicts better both the total yields and the rapidity distributions.

2.4.1 Color Singlet Model

The color singlet model (CSM) was first proposed shortly after the discovery of J/ψ [28, 29, 30]. The CSM requires that colorless $c\bar{c}$ pair is created to have the same quantum numbers as J/ψ. Figure 2.8 shows an example of the lowest order diagram of J/ψ in the CSM, where the $c\bar{c}$ pair has ${}^{2S+1}L_J = {}^3S_1$ and is in a color singlet state as J/ψ. In this model, hard gluon emission is necessary to conserve the C-parity. This model can describe the J/ψ production cross section in photoproduction ($\gamma + N$) [30] but failed

to explain p_T differential cross section in $p + \bar{p}$ collisions at $\sqrt{s} = 1.8$ TeV at Tevatron at Fermi National Accelerator Laboratory (FNAL) by a factor of ~ 6 for J/ψ and a factor ~ 50 for ψ' (Fig. 2.9) [31].

Since the dominant process of heavy quark production is gluon fusion and a gluon has spin 1, the production of quarkonia whose spins are 1 (J/ψ, χ_{c1} and ψ') is largely suppressed than that of quarkonia whose spins are 0 (η_c and χ_{c0}) and 2 (χ_{c2}) in the CSM.

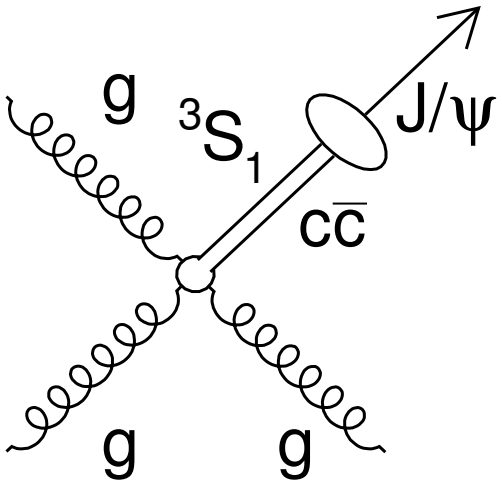

Figure 2.8: An example of the lowest order diagram for direct J/ψ production from gluon fusion with the color singlet model. The $c\bar{c}$ pair is in the color singlet state.

2.4.2 Color Evaporation Model

The color evaporation model (CEM) was first proposed in 1977 [32, 33]. In the CEM, production cross section of charmonium state C is given as a fraction F_C of the cross section for the production of $c\bar{c}$ pairs with the invariant mass below $D\bar{D}$ threshold, $2m_D$. The CEM has the restriction for the $c\bar{c}$ mass to be below $D\bar{D}$ mass, but does not have constraints on the color or other quantum numbers for $c\bar{c}$ pairs. The $c\bar{c}$ pair is assumed to neutralize its color by interaction with collision induced color field, that is "color evaporation". In the CEM, a charmonium is formed through multiple soft-gluon emission as shown in Fig. 2.10. The CEM describes the total J/ψ production cross sections in both hadroproduction and photoproduction at lower energies. The CEM predicts zero polarization of J/ψ, which is not consistent with the results at high p_T region (Fig. 2.11) [34].

At leading order, the production cross section of quarkonium state C in an $A + B$

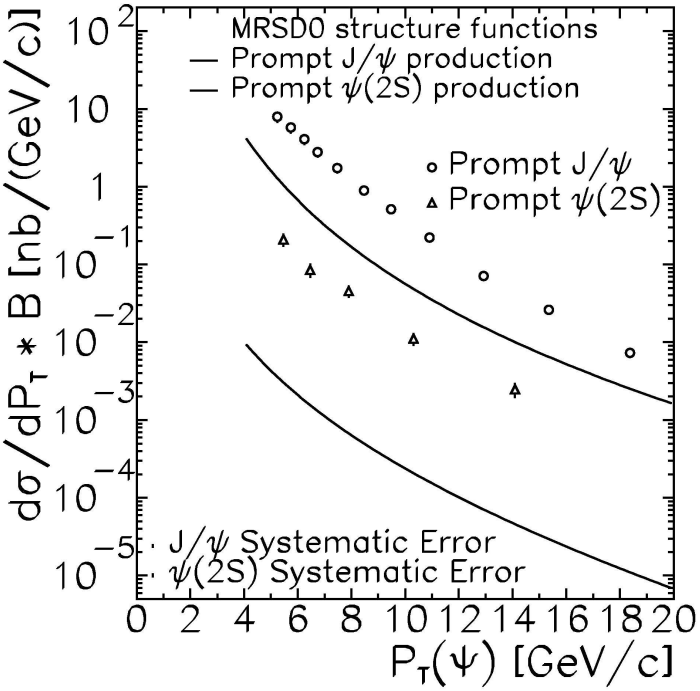

Figure 2.9: The differential cross section times branching ratio $B(\psi \to \mu^+\mu^-)$ for $|\eta(\psi)| < 0.6$ for prompt ψ mesons in $p + \bar{p}$ collisions at $\sqrt{s} = 1.8$ TeV [31]. The lines are the theoretical expectations based of the color singlet model.

collision at the center of mass energy $\sqrt{s}$ is

$$\begin{aligned}\sigma_C^{\rm CEM} &= F_C \sum_{i,j} \int_{4m_Q^2}^{4m_H^2} dm^2 \int dx_1 dx_2 f_{i/A}(x_1,\mu^2) f_{j/B}(x_2,\mu^2) \\ &\quad \times \sigma_{ij}(m^2)\delta(x_1 x_2 s - m^2), \end{aligned} \tag{2.34}$$

where A and B can be any hadron or nucleus, $2m_H$ is the heavy hadron threshold, $ij = q\bar{q}$ or gg, $\sigma_{ij}(m^2)$ is the $ij \to Q\bar{Q}$ subprocess cross section and $f_{i/A}(x,\mu^2)$ is the parton density in the hadron or nucleus.

Depending on the quantum numbers of the initial $Q\bar{Q}$ pair and the final state quarkonium, a different nonperturbative matrix element is needed for the production of the quarkonium state. The average of these nonperturbative matrix elements are combined into the universal factor F_C which depends on m_Q, the scale of α_s and the parton densities, but does not depend on the collision system and collision energy [35].

At leading order, heavy quark hadroproduction is the sum of contributions from $q\bar{q}$ annihilation and gg fusion. If y is the $Q\bar{Q}$ rapidity in the $A + B$ center of mass frame, the cross section for free $Q\bar{Q}$ pairs of invariant mass m is [36]

$$\frac{d^2\sigma}{dydm^2} = \frac{1}{s}\int_0^1 dx_1 \int_0^1 dx_2 \delta(x_1 x_2 - m^2)\delta\left(y - \frac{1}{2}\ln\left(\frac{x_1}{x_2}\right)\right) H_{AB}(x_1,x_2;\mu^2), \tag{2.35}$$

$$= \frac{1}{s} H_{AB}(x_{01},x_{02};\mu^2), \tag{2.36}$$

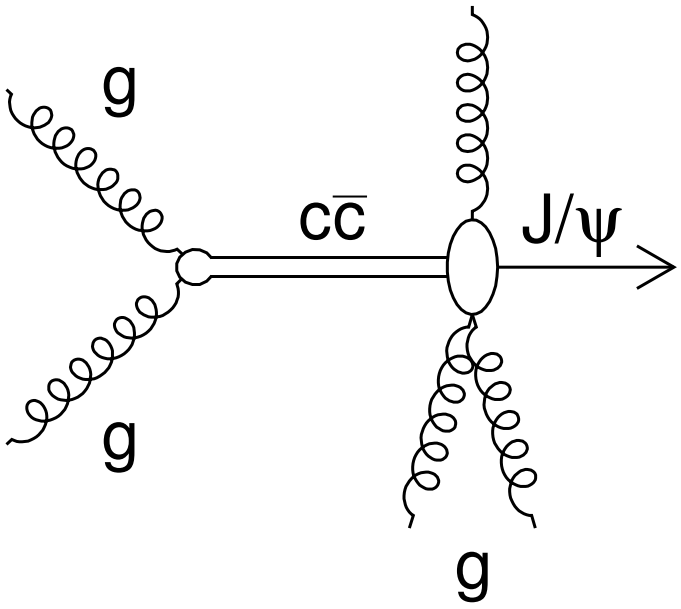

Figure 2.10: An example of the lowest order diagram for direct J/ψ production from gluon fusion with the color evaporation model. Multiple soft gluon emissions destroy the information on quantum numbers of the $c\bar{c}$ pair.

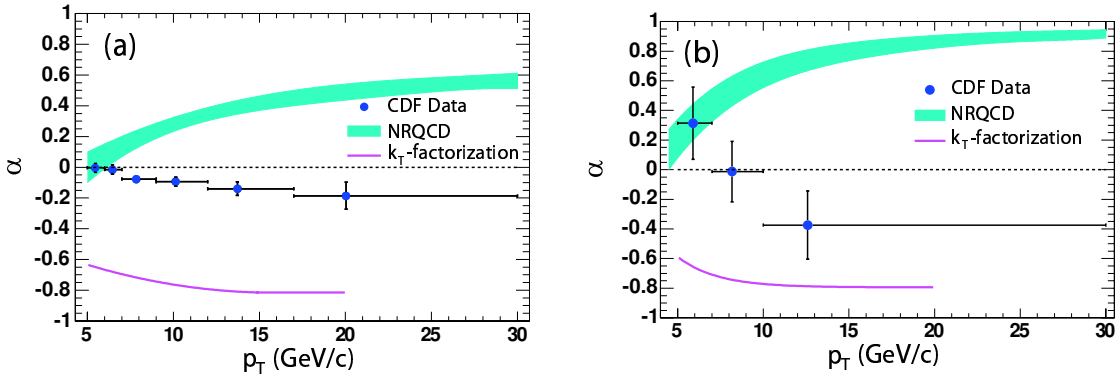

Figure 2.11: Prompt polarizations as functions of p_T: (a)J/ψ and (b)$\psi(2S)$. The band (line) is the prediction from NRQCD (the k_T-factorization model) [34].

where $x_{01,02} = (m/\sqrt{s})\exp(\pm y)$ and

$$H_{AB}(x_1, x_2, \mu^2) = f_g^A(x_1, \mu^2) f_g^B(x_2, \mu^2) \sigma_{gg}(m^2) + \sum_{q=u,d,s} \left(f_q^A(x_1, \mu^2) f_{\bar{q}}^B(x_2, \mu^2) + f_{\bar{q}}^A(x_1, \mu^2) f_q^B(x_2, \mu^2) \right) \sigma_{q\bar{q}}(m^2). \quad (2.37)$$

At $\sqrt{s} = 200$ GeV, x_{01} and x_{02} for J/ψ are $x_{01} = x_{02} = 0.016$ at $y = 0$, and $x_{01} = 0.085$ and $x_{02} = 0.003$ at $y = 1.7$. The leading order partonic cross sections are

$$\sigma_{gg}(m^2) = \frac{\pi\alpha_s^2}{3m^2} \left\{ \left(1 + \frac{4m_Q^2}{m^2} + \frac{m_Q^4}{m^4} \right) \ln\left(\frac{1+\lambda}{1-\lambda} \right) - \frac{1}{4} \left(7 + \frac{31 m_Q^2}{m^2} \right) \lambda \right\}, \quad (2.38)$$

$$\sigma_{q\bar{q}}(m^2) = \frac{8\pi\alpha_s^2}{27m^2} \left(1 + \frac{2m_Q^2}{m^2} \right) \lambda, \quad (2.39)$$

where $\lambda = \sqrt{1 - 4m_Q^2/m^2}$. The strong coupling constant $\alpha(\mu^2)$ is given by Eq. (1.1). The cross section can also be expressed as a function of the fraction of the total longitudinal momentum carried out by the $Q\bar{Q}$ pair, $x_F = x_1 - x_2$,

$$\frac{d^2\sigma}{dm dx_F} = \frac{2m}{\sqrt{x_F^2 s + 4m^2}} H_{AB}(x_{01}, x_{02}; x_{01} x_{02} s), \quad (2.40)$$

where now $x_{01,02} = \frac{1}{2}(\pm x_F + \sqrt{x_F^2 + 4m^2/s})$.

The relation between x_F of J/ψ with rapidity y and $\sqrt{s}$ is shown in Fig. 2.12.

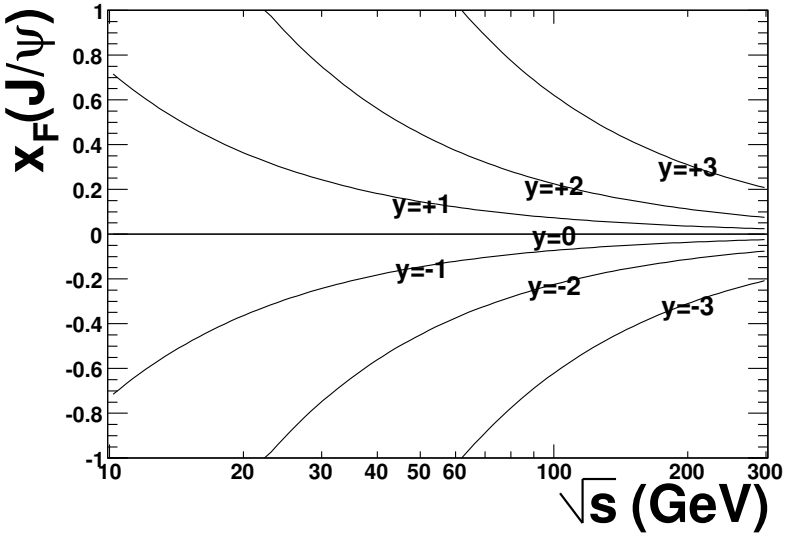

Figure 2.12: x_F of J/ψ with rapidity y as a function of $\sqrt{s}$.

Then, the leading order quarkonium cross section x_F distribution is

$$\frac{d\sigma_C}{dx_F} = 2F_C \int_{2m_Q}^{2m_H} m dm \frac{H_{AB}(x_{01}, x_{02}; x_{01} x_{02} s)}{\sqrt{x_F^2 s + 4m^2}}. \quad (2.41)$$

The leading order calculation in Eq. (2.36) is not sufficient to describe high p_T quarkonium production since the $Q\bar{Q}$ pair p_T is zero at leading order. Therefore, the next-to-leading order needs to be taken into account in the total cross section [35, 37].

2.4.3 NRQCD (Color Octet Model)

The color octet model (COM) has been developed in the 1990's based on the NRQCD. The NRQCD allows the formation of a charmonium from a color octet $c\bar{c}$ pair with emissions of one or a few soft gluons as illustrated in Fig. 2.13. Using appropriate color octet matrix elements, which are additional free parameters needed to be extracted from experimental data, the COM reproduces the p_T distribution in $p + \bar{p}$ collisions at $\sqrt{s} = 1.8$ TeV and total cross sections at lower energy experiments. The COM predicts large transverse polarization of J/ψ, while large longitudinal polarization is experimentally observed (Fig. 2.11) [34].

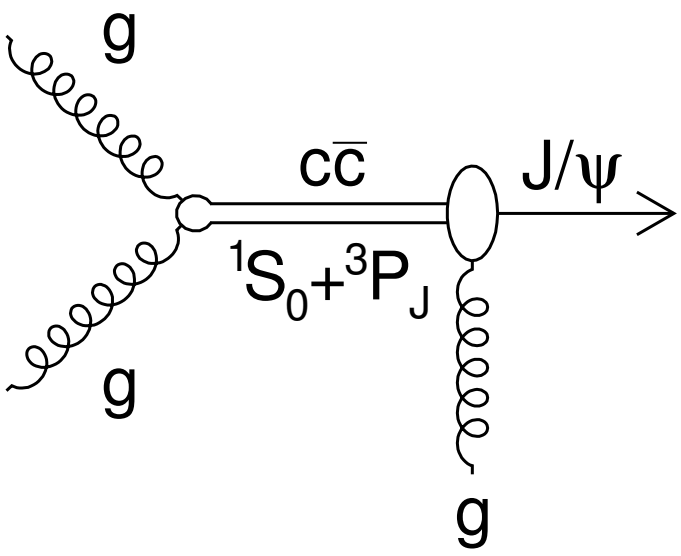

Figure 2.13: An example of the lowest order diagram for direct J/ψ production from gluon fusion with the color octet model. . The $c\bar{c}$ pair is in the color octet state.

In both the quarkonium production and quarkonium decay, large energy-momentum scales compared to $\Lambda_{\rm QCD}$ appear. One might hope that it would be possible to calculate the rates for quarkonium production and decay accurately in perturbation theory. However, there are clearly low momentum, nonperturbative effects associated with the dynamics of the quarkonium bound state that make the direct application of perturbation theory questionable.

To use the perturbative methods, one must factorize the short distance, high momentum, perturbative effects from the long distance, low momentum, nonperturbative effects. The effective field theory nonrelativistic QCD (NRQCD) carries out this separation. The partonic quarkonium production cross section of the quarkonium state C can be written as a sum of the products of NRQCD matrix elements and short distance

coefficients with an expansion in powers of the typical velocity of the heavy quark:

$$\sigma_C \;=\; \sum_n \frac{F_n(\Lambda)}{m_Q^{d_n-4}} \langle 0|\mathcal{O}_n^C(\Lambda)|0\rangle, \tag{2.42}$$

where Λ is the ultra violet cutoff of the effective theory, F_n are short distance, perturbative coefficients, and the $\mathcal{O}_n^C$ are nonperturbative operators with mass dimensions d_n.

The short distance coefficients $F_n(\Lambda)$ are essentially the process dependent partonic cross sections to make a $Q\bar{Q}$ pair. The $Q\bar{Q}$ pair can be produced in a color singlet or in a color octet state. The short distance coefficient are determined by matching the square of the production amplitude in NRQCD to full QCD.

The vacuum matrix element of the operators in Eq. (2.42) is the probability for a $Q\bar{Q}$ pair to form a quarkonium plus anything. The matrix elements contain all of the nonperturbative physics associated with evolution of the $Q\bar{Q}$ pair into a quarkonium state.

The x_F distribution of quarkonium state C in NRQCD is

$$\frac{d\sigma_C}{dx_F} \;=\; \sum_{i,j}\sum_n \int_0^1 dx_1 dx_2 \delta(x_F - x_1 + x_2) f_i^A(x_1,\mu^2) f_j^B(x_2,\mu^2) \frac{F_n^C(\Lambda)}{m_Q^{d_n-1}} \langle \mathcal{O}_n^C \rangle. \tag{2.43}$$

The expansion coefficients $\langle \mathcal{O}_n^C \rangle$ are determined from experimental data.

The color octet contributions calculated for total cross sections measured by the fixed target experiments [38] are quite different from that for the high p_T Tevatron data [39]. The value of matrix element of the color octet contribution for fixed-target data is a factor 4 (7) smaller than that for Tevatron data for J/ψ (ψ') as shown in Fig. 2.14 and Fig. 2.15.

Figure 2.14 shows NRQCD fit results for the J/ψ cross section, ψ' cross section and the ratio of the cross sections in $p+A$ collisions as a function of the center of mass energy $\sqrt{s}$ from the fixed-target energy to the RHIC energy. The total cross section (color octet+color singlet) and the color singlet contributions are separately shown. At the RHIC energy, the singlet contribution to the J/ψ production is about a half.

Figure 2.15 shows NRQCD fit results for the cross sections for J/ψ (top), ψ' (middle) and χ_{cJ} (bottom) in $p+\bar{p}$ collisions at $\sqrt{s} = 1.8$ TeV as a function of p_T. At $p_T = 5$ GeV/c, the singlet contribution to the J/ψ production is less than 5%.

The large difference of color octet contribution of J/ψ and ψ' production in the fixed-target energy and the Tevatron energy is seen in these figures.

2.4.4 Feed-down into J/ψ

There is an important feature for J/ψ production in hadron-hadron collisions. There are four origins of J/ψ in hadron-hadron collisions:

1. Directly produced J/ψ
2. J/ψ produced from decay of three χ_c states
3. J/ψ produced from decay of ψ'
4. J/ψ produced from decay of bottom quark

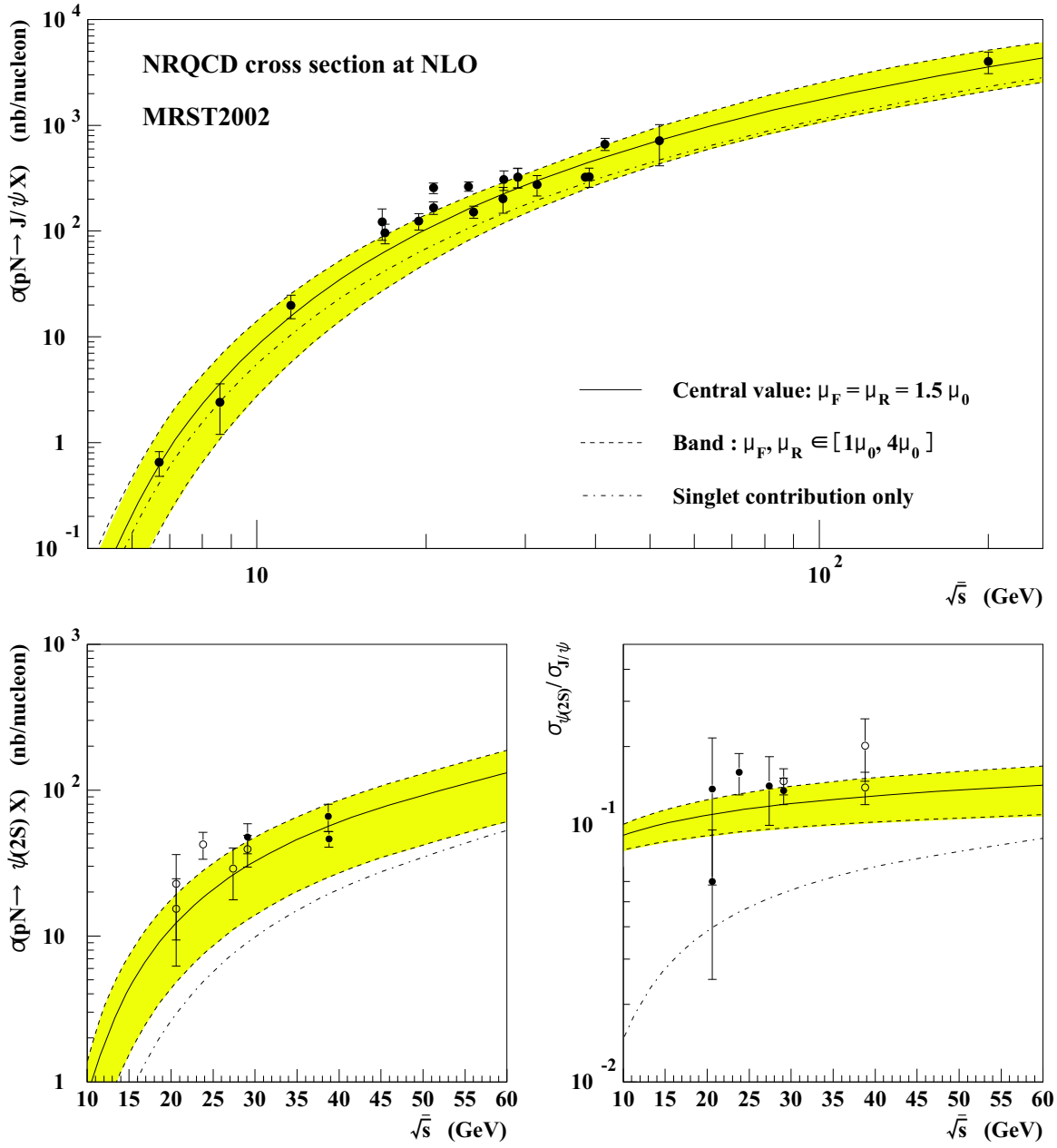

Figure 2.14: J/ψ cross section (top), $\psi(2S)$ cross section (bottom left) and $\sigma_{\psi(2S)}/\sigma_{J/\psi}$ ratio (bottom right) with NRQCD fit results [41].

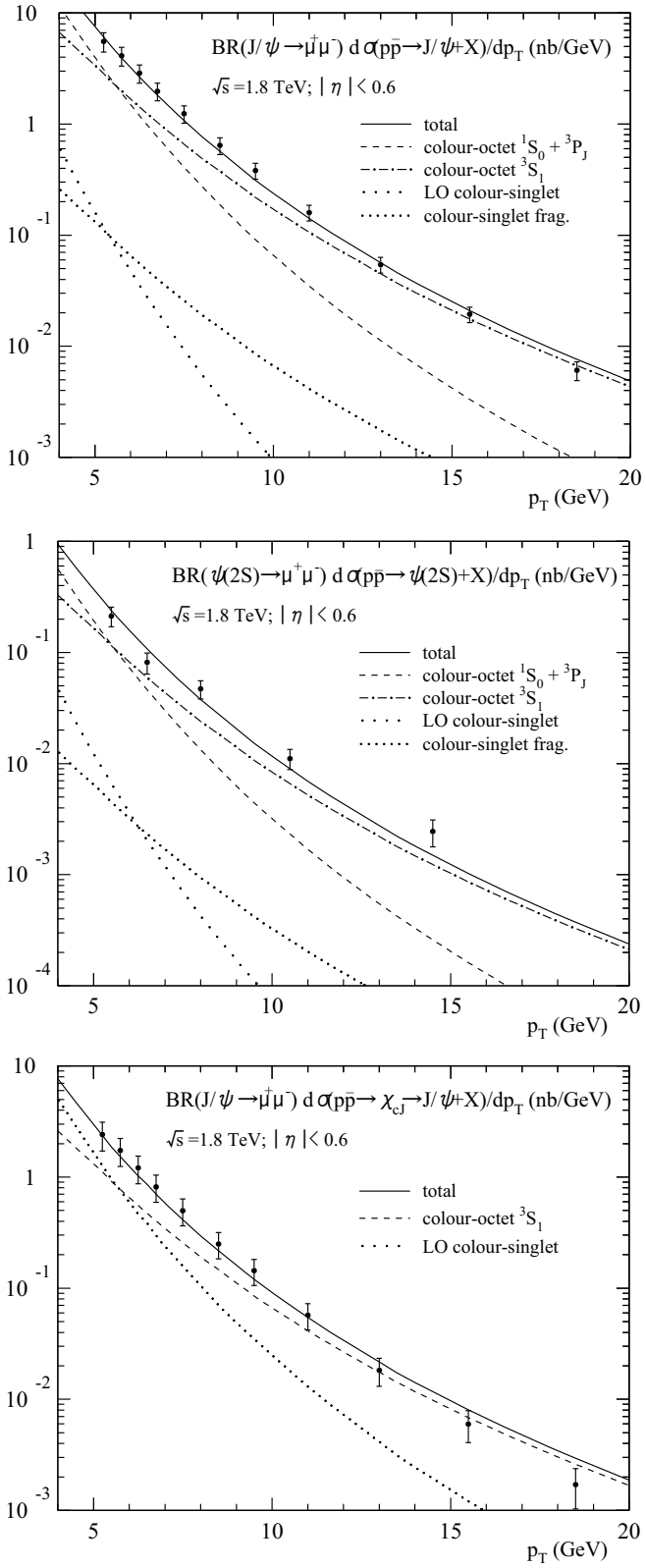

Figure 2.15: Cross sections for J/ψ (top), ψ' (middle) and χ_{cJ} (bottom) in $p + \bar{p}$ collisions at $\sqrt{s} = 1.8$ TeV as a function of p_T. The data points are from the CDF measurements [31, 42]. Color singlet and color octet contributions from the NRQCD calculation [43] are shown separately.

J/ψ Produced from Decay of Three χ_c States

The fraction of J/ψ from the χ_c decays in hadron-hadron collisions is represented by the ratio R_{χ_c} which is defined as follows:

$$R_{\chi_c} = \frac{1}{\sigma_{J/\psi}} \sum_{J=0}^{2} BR\,(\chi_{cJ} \to J/\psi\gamma)\,\sigma_{\chi_{cJ}}, \tag{2.44}$$

where BR and σ are the branching ratio of the $\chi_{cJ} \to J/\psi\gamma$ decay and cross section of the charmonium, respectively. The branching ratios of χ_c mesons are shown in Table 2.2. The branching ratio of χ_{c0} is small (1.30±0.11%) and its contribution is usually neglected.

Figure 2.16 shows the fraction of J/ψ from χ_c decay, R_{χ_c}, obtained in hadron-hadron collisions as a function of the center of mass energy, $\sqrt{s}$. There is no measurement of R_{χ_c} at the RHIC energy of $\sqrt{s}$ =62.4–500 GeV. The average value of R_{χ_c} is about 0.3.

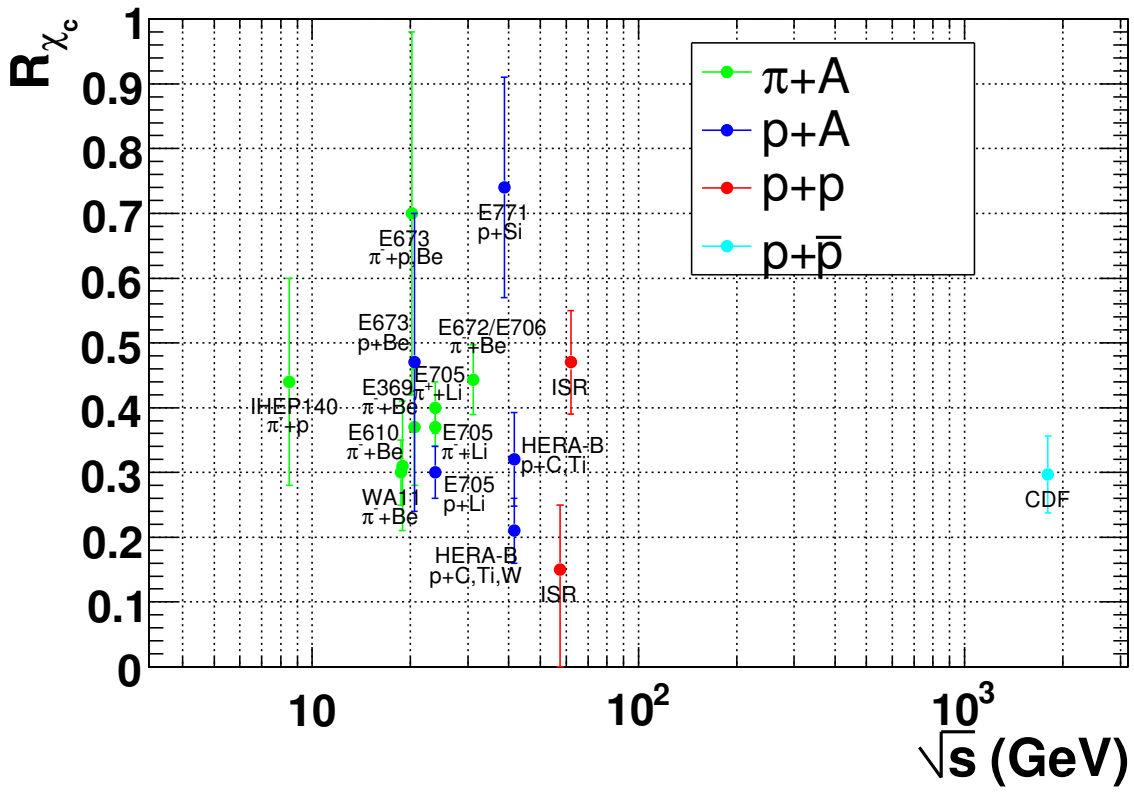

Figure 2.16: R_{χ_c} value by hadroproduction in various experiments [44, 45, 46, 42].

J/ψ Produced from ψ' Decay

The fraction of J/ψ from the ψ' decays is represented by the ratio $R_{\psi'}$ which is defined as follows:

$$R_{\psi'} \;=\; BR\,(\psi' \to J/\psi + X)\,\frac{\sigma_{\psi'}}{\sigma_{J/\psi}}, \tag{2.45}$$

where $BR(\psi' \to J/\psi + X)$ is 0.561±0.009 [19]. The branching ratio of ψ' in the e^+e^- ($\mu^+\mu^-$) mode is $BR(\psi' \to l^+l^-) = (7.35 \pm 0.18) \times 10^{-3}$ ($(7.3 \pm 0.8) \times 10^{-3}$). From the bottom left panel of Fig. 2.14, the ratio of $\sigma_{\psi'}/\sigma_{J/\psi}$ at $\sqrt{s} = 30$ GeV is found to be 0.12 and $R_{\psi'}$ will be 0.067. In $p + \bar{p}$ collisions at $\sqrt{s}$=1.8 TeV, $R_{\psi'}$ is 0.07±0.02 at $p_{T,J/\psi} = 5$ GeV/c and 0.15±0.05 at $p_{T,J/\psi}$=18 GeV/c [42]. If $\sqrt{s}$ dependence of $R_{\psi'}$ is assumed to be weak, $R_{\psi'}$ at $\sqrt{s}$=200 GeV is expected to be less than 0.1.

J/ψ Produced from Bottom Quark Decay

The total cross sections for $c\bar{c}$ and $b\bar{b}$ in $p + p$ collisions at $\sqrt{s} = 200$ GeV from the fixed-order plus next-to-leading-log (FONLL) perturbative QCD (pQCD) calculation is $\sigma_{c\bar{c}}^{\mathrm{FONLL}} = 256^{+400}_{-146}$ μb and $\sigma_{b\bar{b}}^{\mathrm{FONLL}} = 1.87^{+0.99}_{-0.67}$ μb [40]. The experimental data agrees with the FONLL pQCD calculation within experimental and experimental uncertainties as shown in Fig. 2.17 [47].

The admixture of $B^{\pm}$, B^0, B_s^0 and b-baryon has the branching ratio of the inclusive J/ψ mode of $BR(b \to J/\psi + \mathrm{anything}) = 1.16 \pm 0.10\%$ [19].

Therefore, the production cross section of J/ψ produced from the decay of bottom quark is estimated to be $0.043^{+0.023}_{-0.016}$ μb.

As will be described in subsection 2.6.2, the inclusive production cross section of J/ψ at the same energy ($\sqrt{s} = 200$ GeV) is $\sigma_{J/\psi}$=3.00±0.94 μb. Therefore, the fraction of J/ψ produced from bottom quark decay is estimated to be $1.4^{+0.9}_{-0.7}\%$.

Thus, the contributions from the four origins in hadron-hadron collisions will be as follows:

1. Directly produced J/ψ : ~ 0.6
2. J/ψ produced from decay of three χ_c states : ~ 0.3
3. J/ψ produced from decay of ψ' : ~ 0.1
4. J/ψ produced from decay of bottom quark : ~ 0.01

Since there is relatively large uncertainty in the fraction of J/ψ produced from decay of χ_c (R_{χ_c}), one of the main objectives of this thesis is the measurement of R_{χ_c} in $p + p$ collisions at $\sqrt{s} = 200$ GeV. R_{χ_c} in $p + p$ collisions is important to estimate the nuclear absorption of inclusive J/ψ and to understand the suppression of inclusive J/ψ in high-energy heavy-ion collisions, as will be explained in the next chapter. R_{χ_c} is also important to reveal the charmonium production mechanism.

2.5 Charmonium Production in Heavy-Ion Collisions

Medium effects on the charmonium production in high-energy heavy-ion collisions can be categorized into two parts. One part is the effects on the charmonium production after the QGP formation, called as "final state effects". The other part is the effects before the QGP formation, called as "initial state effects" or "cold nuclear matter effects" (CNM effects). Since they contribute to charmonium production even without the QGP formation, they are referred as cold nuclear matter effects.

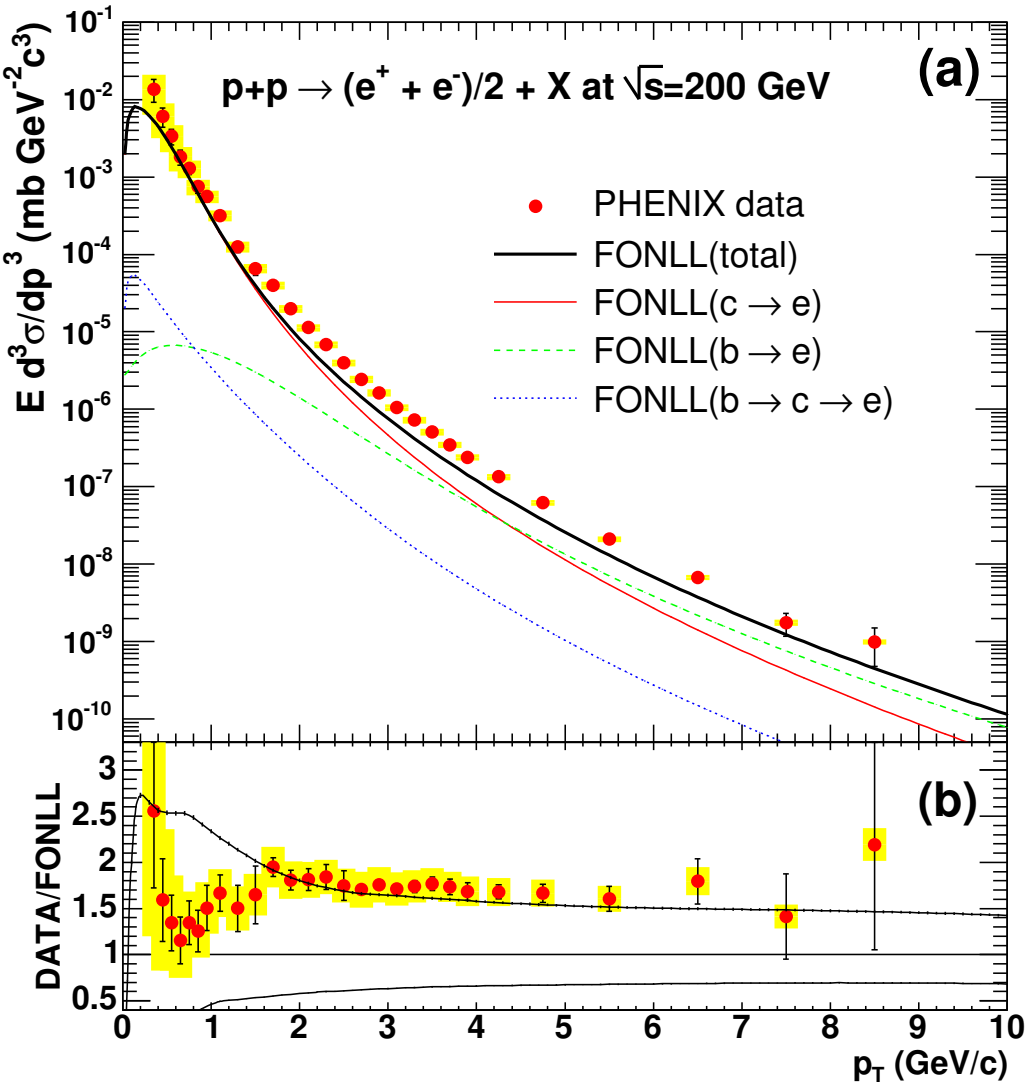

Figure 2.17: (a) Invariant differential cross sections of electrons from heavy-flavor decays. The error bars (bands) represent the statistical (systematic) errors. The curves are the FONLL calculations. (b) Ratio of the data and the FONLL calculation. The upper (lower) curve shows the theoretical upper (lower) limit of the FONLL calculation. In both panels a 10% normalization uncertainty is not shown.

Since the charm quark mass ($m_c \simeq 1.5$ GeV/c^2) and bottom quark mass ($m_b \simeq 5$ GeV/c^2) are heavy, the production of charm quark and antiquark pairs and bottom quark and antiquark pairs takes place only at the beginning of collisions. The time scale of the $c\bar{c}$ ($b\bar{b}$) pair creation is $\tau_{pert} \simeq 1/2m_c \simeq 0.06$ fm/c ($1/2m_b \simeq 0.02$ fm/c). Preresonant color octet $c\bar{c}$ states exist before charmonium formation. The time scale of the color neutralization from a color octet state to a color singlet state is estimated to be $\tau_8 \sim 1/\sqrt{2m_c\Lambda_{\rm QCD}} \simeq 0.25$ fm/c, where $\Lambda_{\rm QCD}$ is the typical QCD scale ($\Lambda_{\rm QCD} \simeq 0.2$ GeV) [48]. The formation time of charmonia from a color singlet $c\bar{c}$ state obtained from potential models is $\tau_{J/\psi} = 0.9$ fm/c, $\tau_{\psi'} = 1.5$ fm/c and $\tau_{\chi_c} = 2.0$ fm/c [49]. Therefore, the color singlet and color octet $c\bar{c}$ states and charmonium are involved in the evolution of collisions. The produced preresonant $c\bar{c}$ state or charmonium sweeps through the remaining fast traveling cold nuclear matter, of length L, as shown in Fig. 2.18. The length L is called the path length. Figure 2.19 shows time scales of charmonium production and charmonium-nucleus interaction in p+Pb collisions at $\sqrt{s_{NN}} = 17.3$ GeV and in d+Au collisions at $\sqrt{s_{NN}} = 200$ GeV.

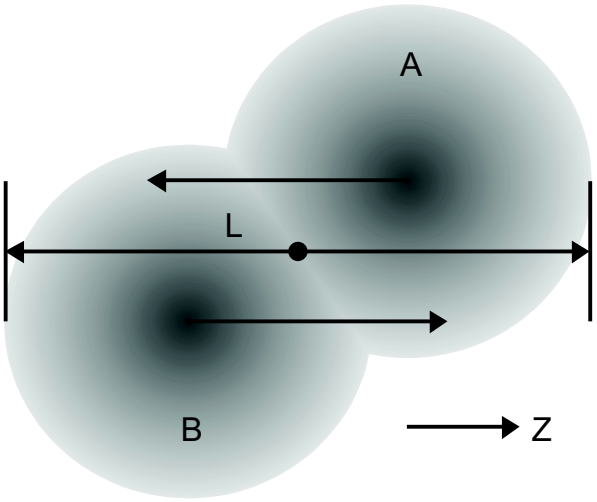

Figure 2.18: Diagram of a nucleus-nucleus collision [70]. Arrows at the center of each nucleus indicate the direction of travel. The dot in the center represents a nucleon-nucleon collision, and the distance L depicts the amount of cold nuclear matter which is created in the nucleon-nucleon collision and will pass through. The shading of the nuclei indicate the non-uniform density which should be accounted for when calculating the path length L.

As the final state effects, the following mechanism are the possible contributions to the modification of charmonium production in high-energy heavy-ion collisions.

- Color screening and dissociation of $c\bar{c}$ pairs and charmonia by thermal partons in the QGP.
- Recombination (coalescence) of charmonia from uncorrelated $c\bar{c}$ pairs in the QGP.
- Interaction of charmonia with secondary comoving hadrons (comovers).

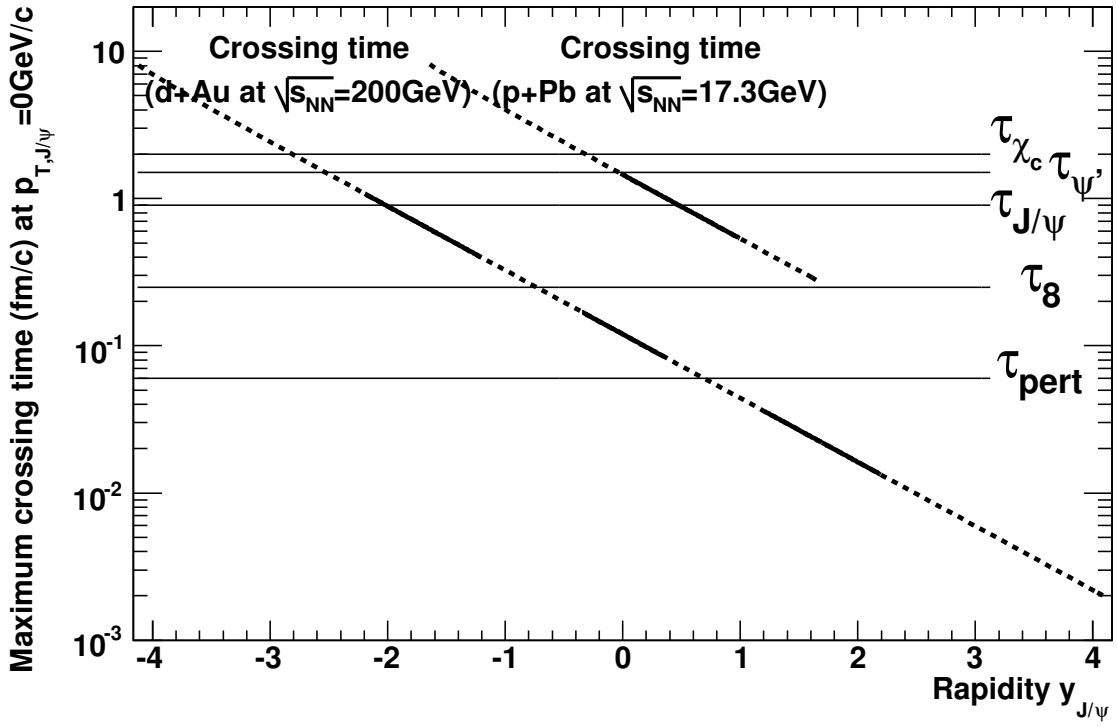

Figure 2.19: Time scales of charmonium production and charmonium-nucleus interaction in p+Pb collisions at $\sqrt{s_{NN}} = 17.3$ GeV and in d+Au collisions at $\sqrt{s_{NN}} = 200$ GeV. The positive rapidity is the p or d going direction. The maximum crossing time of the nucleus for J/ψ with p_T is shown as a function rapidity y of J/ψ. Solid lines represent detector acceptance of the NA50 detector ($0 < y < 1$) at $\sqrt{s_{NN}} = 17.3$ GeV and the PHENIX detector ($|y| < 0.35$ and $1.2 < |y| < 2.2$) at $\sqrt{s_{NN}} = 200$ GeV. τ_{pert} denotes the time scale of $c\bar{c}$ production, $\tau_{pert} \simeq 1/2m_c \simeq 0.06$ fm/c. τ_8 denotes the time scale of the color neutralization from a color octet state to a color singlet state, $\tau_8 \sim 1/\sqrt{2m_c\Lambda_{\rm QCD}} \simeq 0.25$ fm/c. $\tau_{J/\psi} = 0.9$ fm/c, $\tau_{\psi'} = 1.5$ fm/c and $\tau_{\chi_c} = 2.0$ fm/c are the charmonium formation times from color singlet $c\bar{c}$ states.

As the cold nuclear matter effects, there are the following possible contributions to the modification of charmonium production.

- Modification of gluon distribution function in heavy nuclei (gluon shadowing, gluon anti-shadowing, EMC effect, color glass condensate (CGC) [71]).
- Interaction of preresonant $c\bar{c}$ states and charmonia with the target and projectile nuclei (nuclear absorption or nuclear breakup).
- Multiple interactions of partons inside the nuclei (Cronin effect).

2.5.1 Final State Effects

The final state effects on the charmonium production such as color screening, dissociation of charmonia by thermal gluons, recombination of charmonia from uncorrelated $c\bar{c}$ pairs and comover interaction will be explained in this subsection.

Color Screening in QGP

In vacuum, the potential energy of a quarkonium can be described by Eq. (2.29). The potential is modified at finite temperature due to color screening. Color screening can be quantified in the potential through the Debye screening length, $\lambda_D(T)$. The potential at finite temperature becomes

$$V(r,T) = -\frac{\alpha_{eff}}{r}\exp\left[-\frac{r}{\lambda_D(T)}\right] + \sigma\lambda_D(T)\left(1-\exp\left[-\frac{r}{\lambda_D(T)}\right]\right). \quad (2.46)$$

In the QGP, when the screening length of the quark color charge is less than the hadronic radius, the valence quarks of the quarkonium state can no longer "feel" each other and are unable to form a bound state.

Figure 2.20 shows the free energy of the color singlet quark anti-quark, $F_1(r,T)$, from lattice QCD calculation as a function of distance r at different temperature [50]. The solid line is the potential at $T=0$, where the potential is composed of the Coulomb potential and confining potential. The asymptotic value of $F_1(r=\infty,T)$, which corresponds to separation energy of the quark and anti-quark, decreases with increase of temperature.

The Debye screening length is evaluated by the one-loop calculation in perturbative QCD as follows [51]:

$$\lambda_D = \frac{1}{\sqrt{\left(\frac{N_c}{3}+\frac{N_f}{6}\right)g^2T}}, \quad (2.47)$$

where N_c is the degree of freedom of color, N_f is the number of quark flavors, T is the temperature of the medium and $g^2 = 4\pi\alpha_{eff}$. The Debye screening length depends on temperature and becomes smaller with increase of temperature. For the QGP with $N_c=3$, $N_f=3$ and $T=200$ MeV in Eq. (2.47), the screening length with $\alpha_{eff}=0.47$ becomes $\lambda_D = 0.33$ fm. Since the J/ψ radius in Table 2.3 is 0.453 fm, J/ψ cannot be bound in the QGP at $T=200$ MeV ($\sim T_c$).

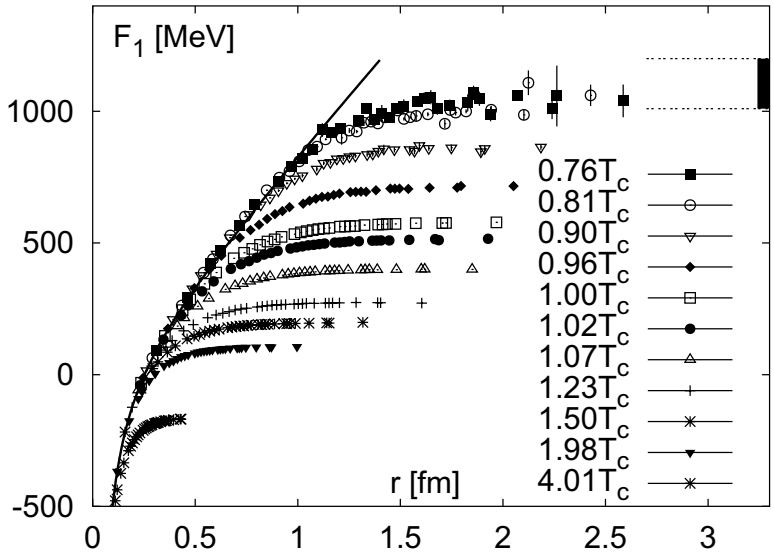

Figure 2.20: The color singlet quark anti-quark free energy, $F_1(r,T)$, at several temperatures close to the phase transition as a function of distance in physical units. Shown results are from lattice studies of 2-flavor QCD. The solid line represents the $T = 0$ heavy quark potential, $V(r)$ [50].

Lattice QCD calculations and potential models have been used to extract the dissociation temperature of each quarkonium [52, 53, 54, 55, 56]. Figure 2.21 shows the spectral functions based on a quenched lattice QCD calculation for J/ψ and η_c. This calculation shows that J/ψ and η_c are stable up to 1.6 T_c.

Table 2.4 is the summary of the dissociation temperature T_d in unit of T_c for each quarkonium from a potential model calculation [53].

In this sequential dissociation scenario, to understand the inclusive J/ψ suppression, the feed-down fractions R_{χ_c} in $p+p$ and heavy-ion collisions are important.

State	$J/\psi(1S)$	$\chi_c(1P)$	$\psi'(2S)$	$\Upsilon(1S)$	$\chi_b(1P)$	$\Upsilon(2S)$	$\chi_b(2P)$	$\Upsilon(3S)$
T_d/T_c	2.10	1.16	1.12	$\geq$4.0	1.76	1.60	1.19	1.17

Table 2.4: Dissociation temperature T_d in unit of T_c for for each quarkonium from a potential model calculation [53].

Recombination of Charmonia

Recent theoretical models predict that the charmonium yield will be enhanced due to the recombination (coalescence) of uncorrelated $c\bar{c}$ pairs at RHIC energy, where $c\bar{c}$ pairs are abundantly created by different nucleon-nucleon collisions [57, 58, 59, 60, 61]. This scenario is derived from the assumption that the number of charmonia from recombination are approximately proportional to N_c^2/N_h, where N_c and N_h are the numbers of produced charm quarks and hadrons. The cross section of the charm production

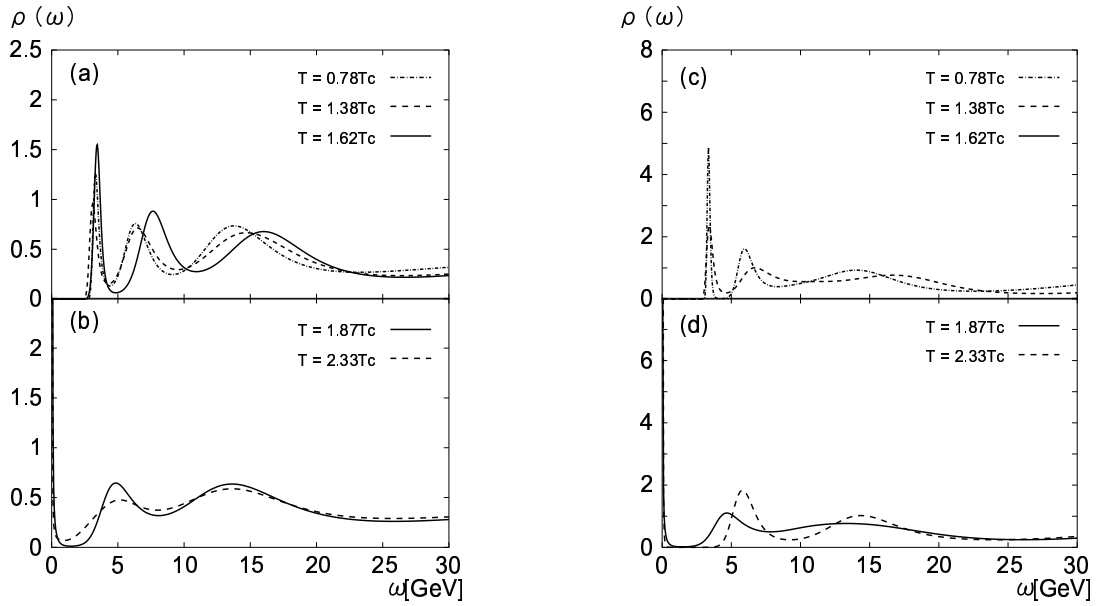

Figure 2.21: Spectral functions for J/ψ (a) and (b), and η_c (c) and (d) at temperature T/T_c of 0.78, 1.38, 1.62 (a) and (c), and 1.87, 2.33 (b) and (d) [52].

increases faster with increase of $\sqrt{s}$ than that of hadrons and it may not be negligible at RHIC energy.

Comover Interactions with Charmonia

The comover scattering of charmonia is an additional absorption of charmonia by secondary hadrons called comover, which occurs in the hadronic phase. The survival probability of charmonia, S_{co}, can be expressed as follows:

$$S_{co} = \exp\left(-\int d\tau \rho_{co}(\tau)\sigma_{co}v\right), \tag{2.48}$$

where $\rho_{co}(\tau)$ is the comover density at the proper time τ, σ_{co} is the charmonium absorption cross section by comovers and v is the relative velocity of a charmonium to a comover. The interaction cross section of charmonia with hadrons are evaluated by various models [62]. Some of the predicted cross sections differ by orders of magnitude. One comover model can reproduce the J/ψ suppression data at the SPS with the dissociation cross section σ_{co} of 0.6–1 mb [63].

2.5.2 Cold Nuclear Matter Effects

The cold nuclear matter effects on the charmonium production such as nuclear shadowing, nuclear absorption and Cronin effect will be explained in this subsection.

The nuclear target dependence of hard processes in $A + B$ collisions is usually parameterized as a power law, based on empirical observations,

$$\sigma_{AB} = \sigma_{NN}(AB)^{\alpha}, \tag{2.49}$$

where the exponent α represents all nuclear effects. The exponent α depends on x_F, p_T and $\sqrt{s}$.

Nuclear Shadowing

It was discovered by the EMC group in 1982 in μ+Fe scattering that the structure function $F_2(x, Q^2)$ in Fe (iron) differs significantly from that of a free nucleon [64]. The modification of the parton distribution in a nucleus is usually quantified as the ratio of parton structure function in the nucleus to that in a deuteron or a carbon nucleus. Figure 2.22 shows the ratio of the structure functions in heavy nuclei and C (carbon), F_2^A/F_2^C [65]. Shadowing ($F_2^A/F_2^C < 1$ at $x < 0.1$), anti-shadowing ($F_2^A/F_2^C > 1$ at $0.1 < x < 0.3$) and EMC effect ($F_2^A/F_2^C < 1$ at $x > 0.3$) are seen.

Nuclear parton distribution functions (NPDF) are deduced from F_2^A and the parton distribution function (PDF) in a proton. Figure 2.23 shows the expectation of the parton distribution function of valence quarks (left), sea quarks (center) and gluons (right) in a calcium (Ca) nucleus relative to those in a proton. Solid lines are NDS parameterization of NPDF [65], dashed lines are EKS parameterization [66] and dotted lines are HKM parameterization [67]. These parameterizations agree well on valence and sea quark distribution, however, there are $\sim 20\%$ diffrences in gluon distribution. Figure 2.24 shows the ratio of gluon distribution in a gold (Au) nucleus over that in a proton at the J/ψ mass scale, $R_g^{\mathrm{Au}}(x, Q^2 = m_{J/\psi}^2)$, as a function of x using the different parameterizations [68].

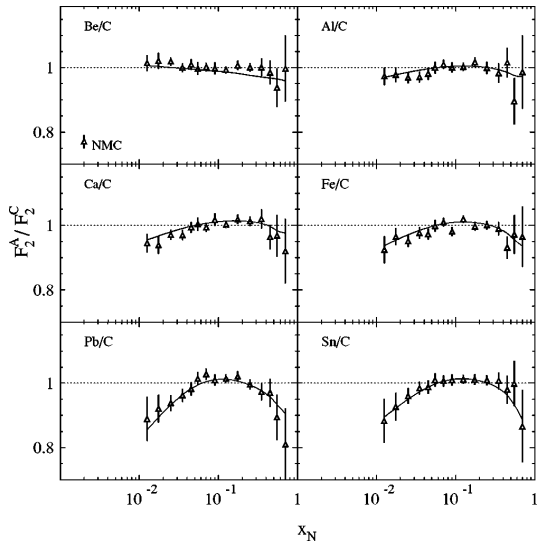

Figure 2.22: F_2^A/F_2^C data. The lines interpolate the values obtained with the NLO NPDF parameterization at the respective Q^2, and extrapolate to low x_N at the Q^2 leftmost point [65].

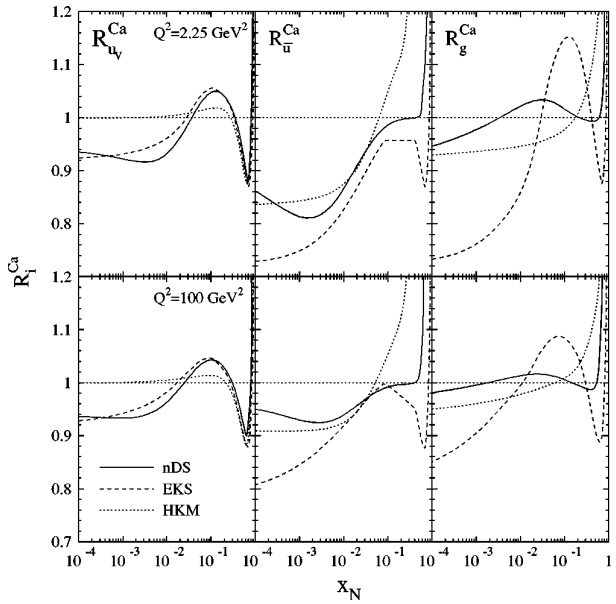

Figure 2.23: The ratios of nuclear parton distributions with different NPDF parameterization [65].

Since charmonia have similar mass, the x regions of charmonia are similar and the extent of nuclear shadowing is almost the same for all charmonia. Therefore, R_{χ_c} will

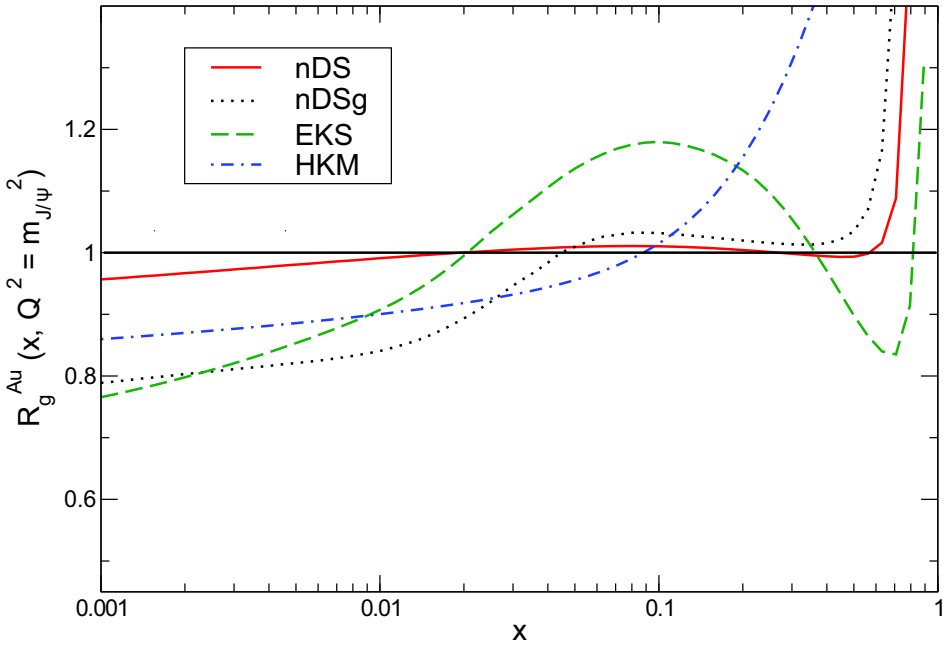

Figure 2.24: The ratio of the gluon distribution in a Au nucleus over that in a proton, $R_g^{\rm Au}(x, Q^2 = m_{J/\psi}^2)$, plotted as a function of Bjorken-x using the NDS, NDSG [65], EKS [66] and HKM [67] parameterizations [68].

not be changed largely by nuclear shadowing.

Nuclear Absorption

Physical picture of nuclear absorption of charmonium described in this subsection is based on Ref. [49].

Nuclear absorption of a charmonium C ($C = J/\psi, \chi_c, \psi', \cdots$) is described in terms of the singlet and octet components of the charmonium wave function:

$$|C\rangle \;=\; a_0|(c\bar{c})_1\rangle + a_1|(c\bar{c})_8 g\rangle + a_{2,1}|(c\bar{c})_1 gg\rangle + a_{2,8}|(c\bar{c})_8 gg\rangle + \cdots . \qquad (2.50)$$

In the CSM, only the first component is nonzero for direct J/ψ production. The $c\bar{c}$ pairs then pass through nuclear matter as small color singlet states and reach their final state size outside the nucleus.

If $c\bar{c}$ pairs are predominantly produced in color octet states, the $|(c\bar{c})_8 g\rangle$ states mainly interact with nucleons. After the color octet $c\bar{c}$ pair is produced, it can neutralize its color by a nonperturbative interaction with a gluon. The free energy of singlet $c\bar{c}$ pairs and octet $c\bar{c}$ pairs are attractive and repulsive, respectively [72]. This color octet state is fragile and a gluon exchanged between it and a nucleon would separate the $(c\bar{c})_8$ from the gluon. Since the $(c\bar{c})_8$ is unbound, it breaks up. If the $|(c\bar{c})_8 g\rangle$ state is free to evolve without interaction, such as in $p+p$ collisions, the additional gluon would be absorbed by the octet $c\bar{c}$ pair, evaporating the color. The effect of nuclear absorption alone on the charmonium production cross section in $p+A$ collisions may be expressed

as

$$\sigma_{pA} \;=\; \sigma_{pp} \int d\mathbf{b} \int_{-\infty}^{\infty} dz \rho_A(\mathbf{b}, z) S^{abs}(\mathbf{b}, z), \tag{2.51}$$

where $\mathbf{b}$ is the impact parameter, z is the longitudinal production point and ρ_A is the nucleon density of the nucleus A. If the production and absorption can be factorized and no other A dependent effects are included, the nuclear absorption survival probability, S^{abs}, is

$$S^{abs}(\mathbf{b}, z) \;=\; \exp\left\{ -\int_{z}^{\infty} dz' \rho_A(\mathbf{b}, z) \sigma_{abs}(z - z') \right\}, \tag{2.52}$$

where σ_{abs} is the absorption cross section of charmonia or preresonant $c\bar{c}$ states. The effective A dependence is obtained from Eqs. (2.51) and (2.52) by integrating over z, z' and $\mathbf{b}$. The dependence on A is related to α in Eq. (2.49) and α is only constant if σ_{abs} is constant and independent of the production mechanism.

Pure color singlet absorption is first discussed. In this case, σ_{abs} depends on the size of the $c\bar{c}$ pair as it traverses the nucleus. The $c\bar{c}$ pair is initially produced with a size, r_{init}, on the order of its production time τ_{pert}, $r_{init} \sim c\tau_{pert} \simeq 0.06$ fm and the r_{init} is negligibly small compared with the charmonium radii in Table 2.3. As described above, the charmonium formation time obtained from potential models is $\tau_C \sim 1$–2 fm/c. The absorption cross section of these small color singlet pairs grows as a function of proper time until τ_C when it saturates at its asymptotic value σ^s_{CN}:

$$\sigma^s_{abs}(z - z') \;=\; \begin{cases} \sigma^s_{CN} \left(\frac{\tau}{\tau_C}\right)^2 & \text{if } \tau < \tau_C, \\ \sigma^s_{CN} & \text{otherwise,} \end{cases} \tag{2.53}$$

where $\tau = (z' - z)/\gamma\beta$ and β and γ are the velocity and Lorentz factor of the charmonium relative to the nucleus and introduce x_F and $\sqrt{s}$ dependencies to σ_{abs}.

Assuming that the asymptotic cross sections scale in proportional to the squares of the charmonium radii [69], we have $\sigma^s_{\psi' N} \simeq 3.7\sigma^s_{J/\psi N}$ and $\sigma^s_{\chi_{cJ} N} \simeq 2.4\sigma^s_{J/\psi N}$ with the radii listed in Table 2.3. Figure 2.25 shows the proper time dependence of absorption cross sections of color singlet states, J/ψ, ψ' and χ_c.

As shown in Fig. 2.19, at $\sqrt{s_{NN}} = 200$ GeV, the crossing time of a gold nucleus is smaller than the J/ψ formation time even at backward rapidity of $y = -2$. Since χ_c has the smallest absorption cross section in the proper time range of $\tau < 1$ fm/c, R_{χ_c} will be increased by nuclear absorption in heavy-ion collisions at $\sqrt{s_{NN}} = 200$.

Figure 2.26 illustrates the energy dependence of color singlet absorption in $p + A$ interactions at fixed target energy ($\sqrt{s_{NN}} = 17.3$–41.6 GeV) with $\sigma^s_{J/\psi N}$=2.5 mb. The contributions from the four origins to inclusive J/ψ are assumed to be as follows in this calculation:

1. Directly produced J/ψ : 0.58
2. J/ψ produced from decay of three χ_c states : 0.30
3. J/ψ produced from decay of ψ' : 0.12
4. J/ψ produced from decay of bottom quark : 0

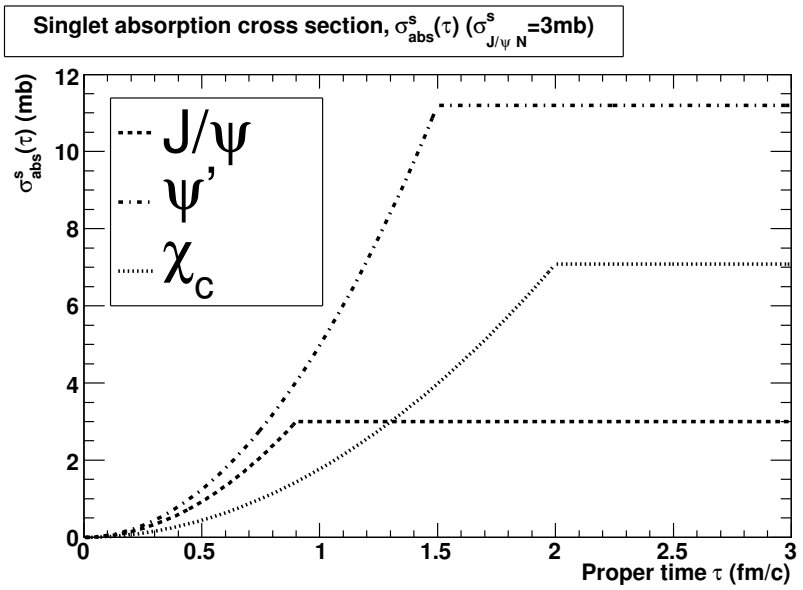

Figure 2.25: The proper time dependence of absorption (breakup) cross sections of color singlet states.

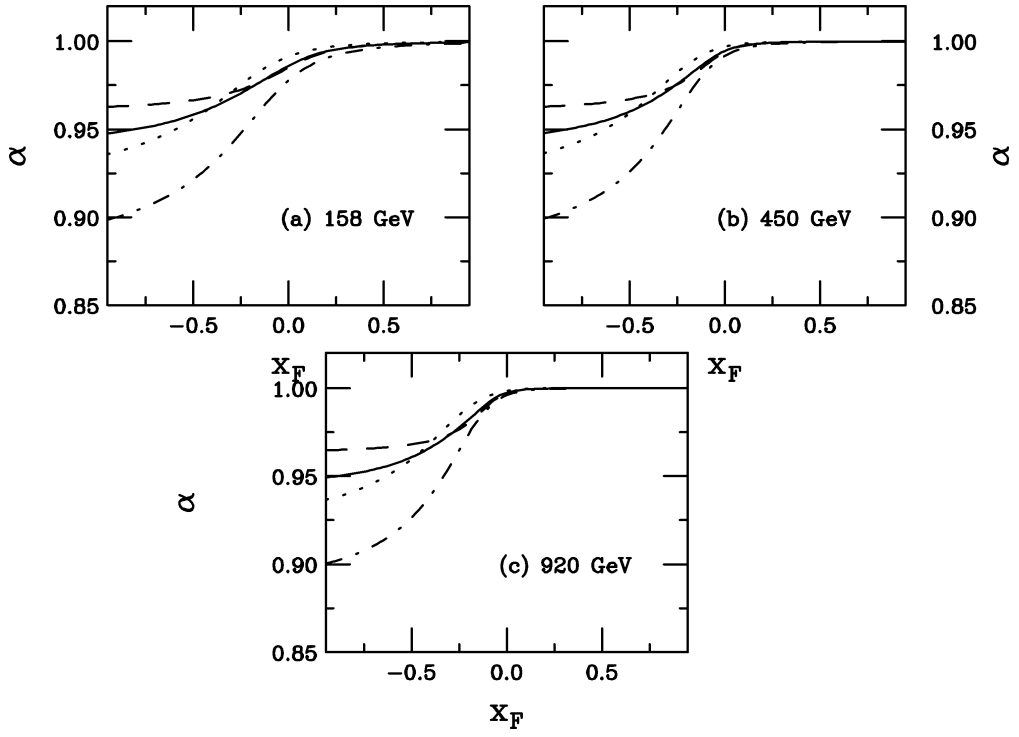

Figure 2.26: The A dependence for color-singlet absorption in $p + A$ collisions with $\sigma^s_{J/\psi N}$=2.5 mb is shown [49]. The results are calculated at beam energy of 158 GeV ($\sqrt{s_{NN}}$ = 17.3 GeV) (a), 450 GeV ($\sqrt{s_{NN}}$ = 29.1 GeV) (b) and 920 GeV ($\sqrt{s_{NN}}$ = 41.6 GeV) (c). The total J/ψ (solid), the direct J/ψ (dashed), the ψ' (dot-dashed) and the χ_c (dotted) A dependencies are given. Negative x_F is the nucleus going direction.

Since the crossing time of a charmonium (a $c\bar{c}$ pair) through a nucleus at large x_F is much smaller than the charmonium formation time, α is 1.

On the other hand, if $c\bar{c}$ pairs are produced only in color octet states, they should hadronize after $\tau_8 \sim 0.25$ fm in the $c\bar{c}$ rest frame. At large x_F, hadronization occurs after the $c\bar{c}$ has passed through the target as an octet. These fast $c\bar{c}$ pairs thus remain color octet states until they leave the nucleus. At negative x_F, however, it is possible for the octet states to neutralize their color inside the nucleus and interact as color singlets during the remainder of their path through the target. The produced color singlets are absorbed according to Eq. (2.53). While traveling through the nucleus as a preresonant $|(c\bar{c})_8 g\rangle$ state, the eventual identity of the final state resonance is undetermined and all charmonium states are absorbed with the same cross section, σ^o_{abs}. This physical picture agrees rather well with the empirical evidence that the J/ψ and ψ' dependencies are similar over the measured x_F range at $\sqrt{s_{NN}} = 39$ GeV [73] as shown in Fig. 2.27. To

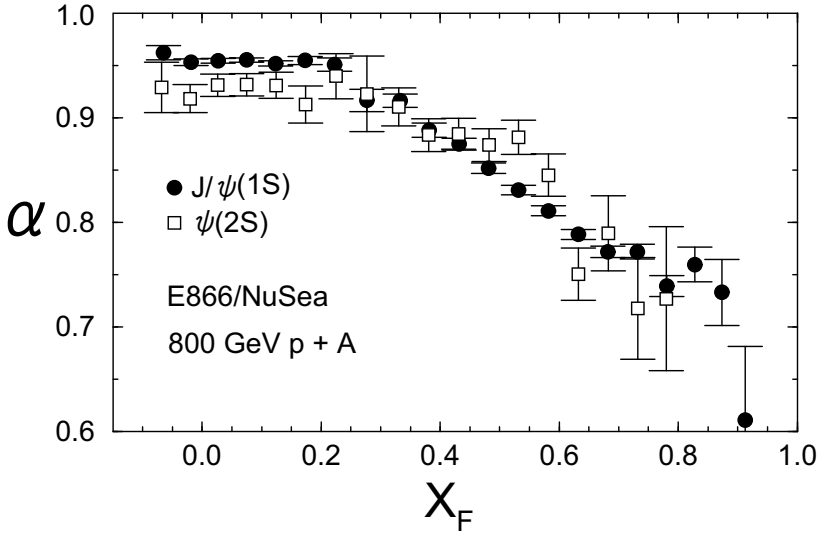

Figure 2.27: α for $J/\psi(1S)$ and $\psi'(2S)$ versus x_F in p+Be, p+Fe and p+W collisions at $\sqrt{s_{NN}} = 39$ GeV (800 GeV/c proton beams) at the E866/NuSea experiment [73].

agree with $\alpha \simeq 0.95$ for the J/ψ measured at x_F at $\sqrt{s_{NN}} = 39$ GeV [73] without other nuclear effects, $\sigma^o_{abs} = 3$ mb is chosen. Figure 2.28 shows the energy dependence of color octet absorption in $p + A$ interactions at fixed target energy ($\sqrt{s_{NN}} = 17.3$–41.6 GeV) with σ^o_{abs}=3 mb. The contributions to inclusive J/ψ is assumed as same as those in the color singlet case.

To determine the fraction of produced charmonium states in color singlets and color octets, NRQCD can be used. Table 2.5 shows the percentage of charmonium production from color octets in the NRQCD at the fixed target energy ($\sqrt{s_{NN}} = 17.3$–41.6 GeV).

In a nucleus-nucleus collision, the nuclear shadowing and nuclear absorption occur at both forward and backward rapidity. Figure 2.29 shows the ratio of J/ψ yield in Au+Au and Cu+Cu collisions at $\sqrt{s_{NN}} = 200$ and 62 GeV to J/ψ yield in $p + p$ collisions at the same energy with appropriate scaling. The color octet production and color singlet production are separately shown. The EKS shadowing parameterization is used. If there are no CNM effects, this ratio will be unity. The asymptotic absorption

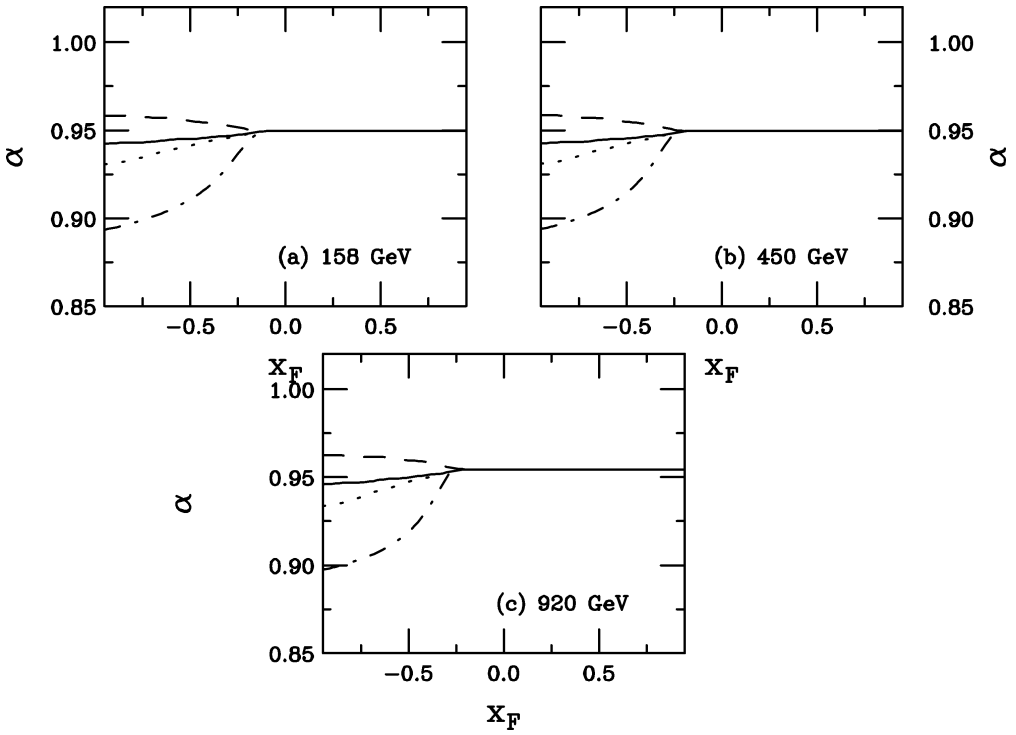

Figure 2.28: The A dependence for color-octet absorption in $p + A$ collisions with σ^o_{abs}=3 mb is shown [49]. The results are calculated at beam energy of 158 GeV (a), 450 GeV (b) and 920 GeV (c). The total J/ψ (solid), the direct J/ψ (dashed), the ψ' (dot-dashed) and the χ_c (dotted) A dependencies are given. Negative x_F is the nucleus going direction.

$\sqrt{s_{NN}}$ (GeV)	P_{beam} (GeV/c)	Total J/ψ (%)	Direct J/ψ (%)	ψ' (%)	$\sum_J \chi_{cJ} \to J/\psi\gamma$ (%)
17.3	158	66.6	90.7	75.2	8.9
29.1	450	62.6	86.7	66.2	6.3
41.6	920	60.4	84.7	61.9	5.0

Table 2.5: The percentage of charmonium production from color octets in the NRQCD at each energy [49].

cross section of color singlet J/ψ and the absorption cross section of color octet are assumed to be the same:

$$\sigma^{s}_{J/\psi N} \;=\; \sigma^{o}_{abs} \;=\; \sigma_{abs}. \tag{2.54}$$

The results with σ_{abs} =0, 1, 3 and 5 mb are shown in Fig. 2.29. Since the absorption cross section of color octet is assumed to be independent of the proper time, the effect of nuclear absorption for the octets is much larger than that for the singlets. At midrapidity ($y = 0$), there is absolutely no absorption for the singlet state. Even in Au+Au collisions at forward rapidity ($y = \pm 2$), singlets are reduced by only 9% but octets are reduced by 62% with $\sigma_{abs} = 5$ mb. Therefore, the contribution of color octets in the charmonium production is important to estimate the nuclear absorption.

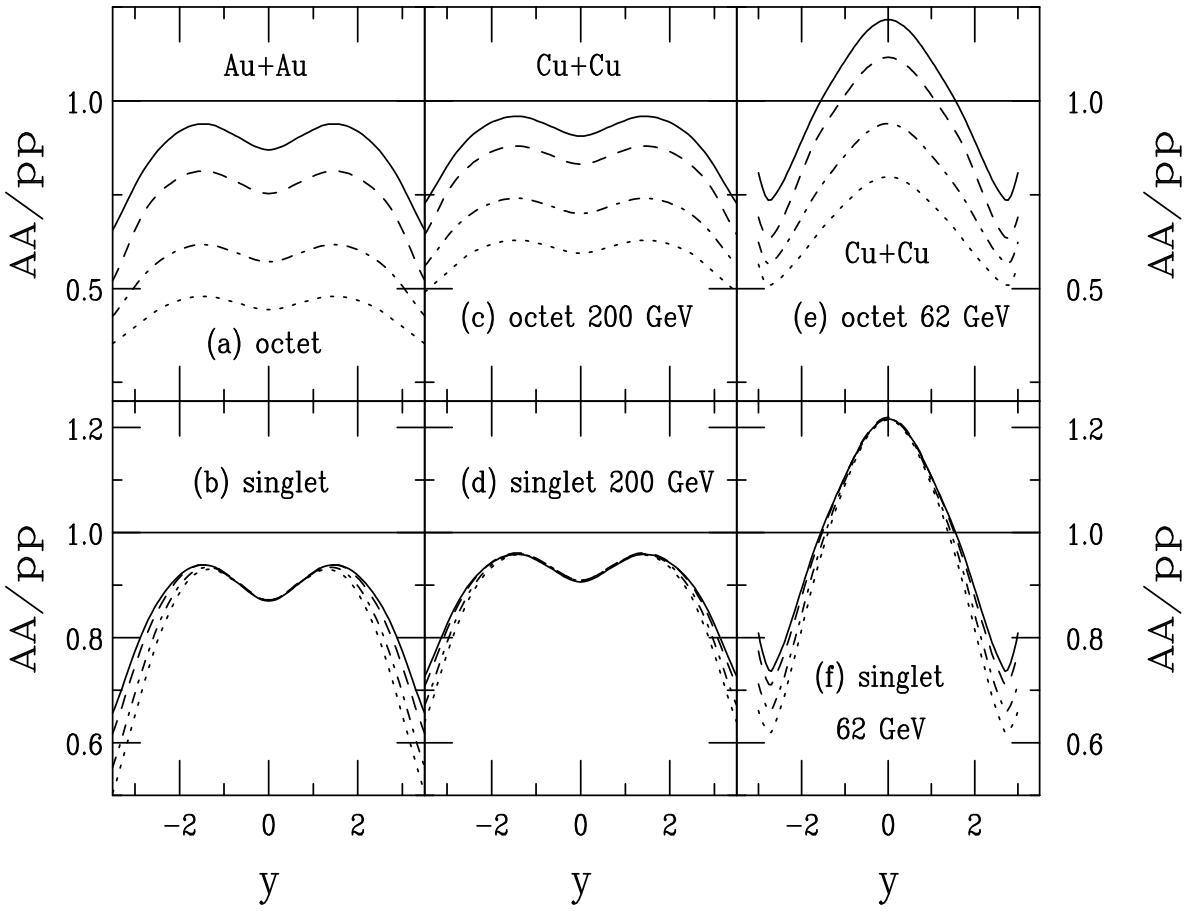

Figure 2.29: The AA/pp ratio with the EKS parameterization as a function of y for octet (upper) and singlet (lower) absorption [74]. In (a) and (b) the Au+Au results at $\sqrt{s_{NN}}$ = 200 GeV are shown while the Cu+Cu results are shown at 200 GeV (c) and (d) as well as at 62 GeV (e) and (f). The curves are σ_{abs} =0 (solid), 1 (dashed), 3 (dot-dashed) and 5 mb (dotted).

Cronin Effect

Partons suffer multiple scatterings while they traverse in nuclei before charmonium production. Partons from the projectile nucleus collide with various target nucleons exchanging a transverse momentum in each collision. This makes the p_T distribution of charmonia wider compared to that in $p+p$ collisions and is known as the Cronin effect [75].

The mean squared transverse momentum $\langle p_T^2 \rangle$ depends on the production point $\mathbf{x} = (\mathbf{b}, z)$,

$$\langle p_T^2 \rangle(\mathbf{b}, z) \;=\; \langle p_T^2 \rangle_{pp} + \langle p_T^2 \rangle_{gN} \sigma_{gN} \int_{-\infty}^{z} dz' \rho_A(\mathbf{b}, z'), \tag{2.55}$$

where $\langle p_T^2 \rangle_{pp}$ is the mean squared transverse momentum in $p+p$ collisions, σ_{gN} is gluon-nucleon cross section, $\langle p_T^2 \rangle_{gN}$ is the mean squared transverse momentum acquired per gluon-nucleon collision and ρ_A is the nucleon number density of a nucleus A. Eq. (2.55) can be written in terms of the pass length L using a coefficient a_{gN} which includes σ_{gN} and $\langle p_T^2 \rangle_{gN}$,

$$\langle p_T^2 \rangle \;=\; \langle p_T^2 \rangle_{pp} + a_{gN} L. \tag{2.56}$$

2.6 Measurement of J/ψ and ψ' in Heavy-Ion Collisions

The experimental study of charmonia in high-energy heavy-ion collisions has been started from experiments at the SPS accelerator and has been performed by the PHENIX experiment at RHIC at much higher energy.

2.6.1 Measurement of J/ψ and ψ' at SPS

The NA38, NA50, NA51 and NA60 experiments at the SPS performed experimental study of J/ψ and ψ' production in high-energy light- and heavy-ion collisions using $\mu^+\mu^-$ pairs. Table 2.6 summarizes the collision system and energy. The production cross sections of J/ψ and ψ' are divided by that of Drell-Yan process, since the Drell-Yan cross section is scaled with the number of collisions N_{coll} [88].

Figure 2.30 shows ratios of cross sections of J/ψ and Drell-Yan as a function of path length L in Pb+Pb and lighter ion collisions at $\sqrt{s_{NN}} = 17.3$ and 19.4 GeV at NA38 and NA50 at the SPS. From the path length dependence of the ratio of cross sections, the absorption cross section of J/ψ is determined to be $\sigma_{abs}^{J/\psi} = 4.2 \pm 0.5$ mb [94]. This absorption cross section $\sigma_{abs}^{J/\psi}$ is static and is not taken into account the proper time dependence discussed in subsection 2.5.2. The solid line in Fig. 2.30 shows the expected ratio of J/ψ including absorption. The absorption cross section of ψ' is similarly determined to be $\sigma_{abs}^{\psi'} = 7.7 \pm 0.9$ mb. These absorption cross sections correspond to the α parameters of $\alpha_{J/\psi} = 0.925 \pm 0.009$ and $\alpha_{\psi'} = 0.852 \pm 0.019$.

Figure 2.31 shows ratios of measured yields to expected yields of J/ψ and ψ' as a function of path length L in Pb+Pb and lighter ion collisions. In central Pb+Pb

Experiment $\sqrt{s_{NN}}$ (GeV)	P_{beam} (GeV/c)	System	Charmonium	Reference
NA38				
19.4	200	^{16}O+U	J/ψ	[76, 77]
19.4	200	p+Cu, p+U, ^{16}O+Cu, ^{16}O+U, ^{32}S+U	J/ψ	[78, 79, 80, 81]
19.4	200	p+W, p+U, ^{32}S+U	J/ψ, ψ'	[82]
29.1	450	p+C, p+Al, p+Cu, p+W	J/ψ, ψ'	[84]
19.4	200	^{16}O+Cu, ^{16}O+U, ^{32}S+U	J/ψ, ψ'	[83, 85, 86]
NA50				
17.3	158	^{208}Pb+Pb	J/ψ	[87, 88, 89, 5, 91, 93]
17.3	158	^{208}Pb+Pb	J/ψ, ψ'	[90]
29.1	450	p+Be, p+Al, p+Cu, p+Ag, p+W	J/ψ, ψ'	[92]
27.4	400	p+Be, p+Al, p+Cu, p+Ag, p+W, p+Pb	J/ψ, ψ'	[94]
17.3	158	^{208}Pb+Pb	ψ'	[95]
NA51				
29.1	450	$p+p$, $p+d$	J/ψ, ψ'	[96]
NA60				
17.3	158	^{115}In+In	J/ψ	[97]

Table 2.6: The collision system and energy of charmonium experiments at the SPS.

collisions, suppression of J/ψ yield beyond the CNM effect is seen. Suppression of ψ' is larger than that of J/ψ and is observed even in lighter system of S+U.

Figure 2.32 shows the ratios of measured yields to expected yields of J/ψ in In+In collisions at NA60. For collisions involving more than about 80 participant nucleons, suppression is seen. This result is in qualitative agreement with the Pb+Pb measurements by the NA50 experiment.

Figure 2.33 shows $\langle p_T^2 \rangle$ of J/ψ at $\sqrt{s_{NN}} = 17.3$ and 19.4 GeV as a function of path length L [90]. The results are fitted according to the formalism of the Cronin effect given in Eq. (2.56). The slope a_{gN} is 0.081±0.004((GeV/c)^{2}fm^{-1}) and 0.078±0.006 ((GeV/c)^{2}fm^{-1}) for $\sqrt{s_{NN}} = 17.3$ and 19.4 GeV, respectively.

2.6.2 Measurement of J/ψ at RHIC

At RHIC collider, the yields of J/ψ production in $p+p$, d+Au and Au+Au collisions at $\sqrt{s_{NN}} = 200$ GeV have been measured by the PHENIX experiment as tabulated in Table 2.7. The yield of J/ψ in $p+p$ collisions is used as baseline measurement and the yield of J/ψ in d+Au collision is used to estimate the CNM effects. At midrapidity $|y| < 0.35$, J/ψ is measured via e^+e^- pairs. At forward and backward rapidity $1.2 < |y| < 2.2$, J/ψ is measured via $\mu^+\mu^-$ pairs.

In $p+p$ Collisions

Figure 2.34 shows the J/ψ differential cross section times di-lepton branching ratio in $p+p$ collisions as a function of the rapidity of J/ψ [7]. The dashed curve is an NRQCD calculation [102]. The dot-dash curve is pQCD calculation that includes diagrams describing a third gluon which is necessary to neutralize the color [103]. This model

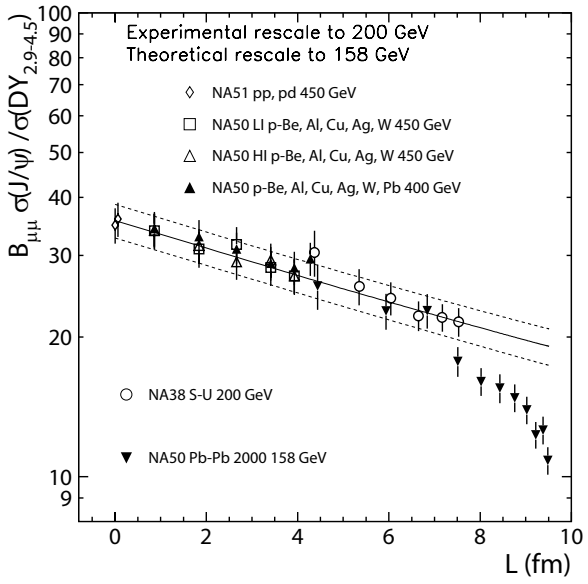

Figure 2.30: The ratios of cross sections of J/ψ and Drell-Yan at NA38, NA50 and NA51 [93].

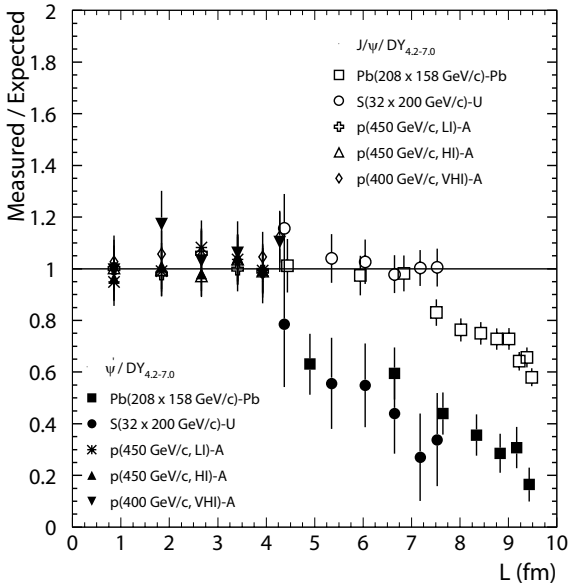

Figure 2.31: The ratios of measured yields to expected yields of J/ψ and ψ' at NA38, NA50 and NA51 [95].

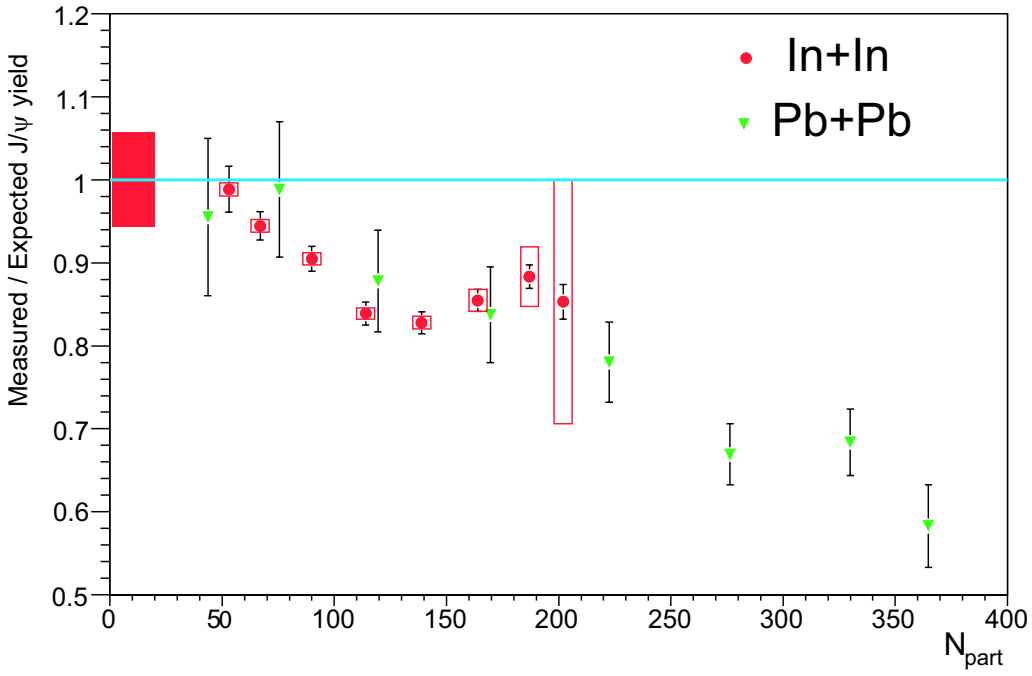

Figure 2.32: The ratios of measured yields to expected yields of J/ψ in In+In collisions at NA60 and in Pb+Pb collisions at NA50 at $\sqrt{s_{NN}} = 17.3$ GeV [97].

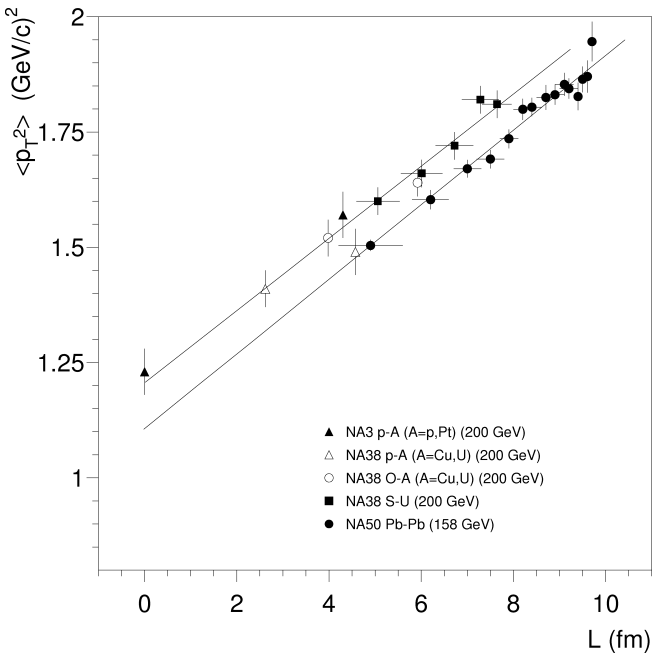

Figure 2.33: The mean squared transverse momentum $\langle p_T^2 \rangle$ of J/ψ at $\sqrt{s_{NN}} = 17.3$ GeV ($P_{beam} = 158$ GeV/c) and $\sqrt{s_{NN}} = 19.4$ GeV ($P_{beam} = 200$ GeV/c) at SPS as a function of path length L [90].

Run	Year	$\sqrt{s_{NN}}$ (GeV/c^2)	System	Charmonium	Reference
Run-1	2000	130	^{197}Au+^{197}Au		
Run-2	2001–2002	200	^{197}Au+^{197}Au	J/ψ	[98]
		200	$p+p$	J/ψ	[99]
Run-3	2002–2003	200	d+^{197}Au	J/ψ	[100, 8]
		200	$p+p$	J/ψ	[100]
Run-4	2004	200	^{197}Au+^{197}Au	J/ψ	[6]
Run-5	2005	200	^{63}Cu+^{63}Cu	J/ψ	[9], $*$
		200	$p+p$	J/ψ	[7]
				χ_c	$*$
Run-6	2006	200	$p+p$	J/ψ	
				χ_c	$*$
Run-7	2007	200	^{197}Au+^{197}Au		
Run-8	2008	200	d+^{197}Au		

Table 2.7: The collision system and energy of charmonium measurements by the PHENIX experiment at RHIC. The asterisks $*$ mean the topics of this thesis.

fails to reproduce the steeply falling cross section observed in the data at large rapidity. The dot curve is an empirical double Gaussian fit and is able to reproduce the data, but has no strong theoretical foundation. The data slightly favor a flatter distribution in the rapidity range $|y| < 1.5$ than most models. The total cross section times branching ratio determined for J/ψ production is $B_{ll} \cdot \sigma_{pp}^{J/\psi} = 178 \pm 3(\text{stat}) \pm 53(\text{syst}) \pm 18(\text{norm})$ nb. "norm" is the absolute normalization error.

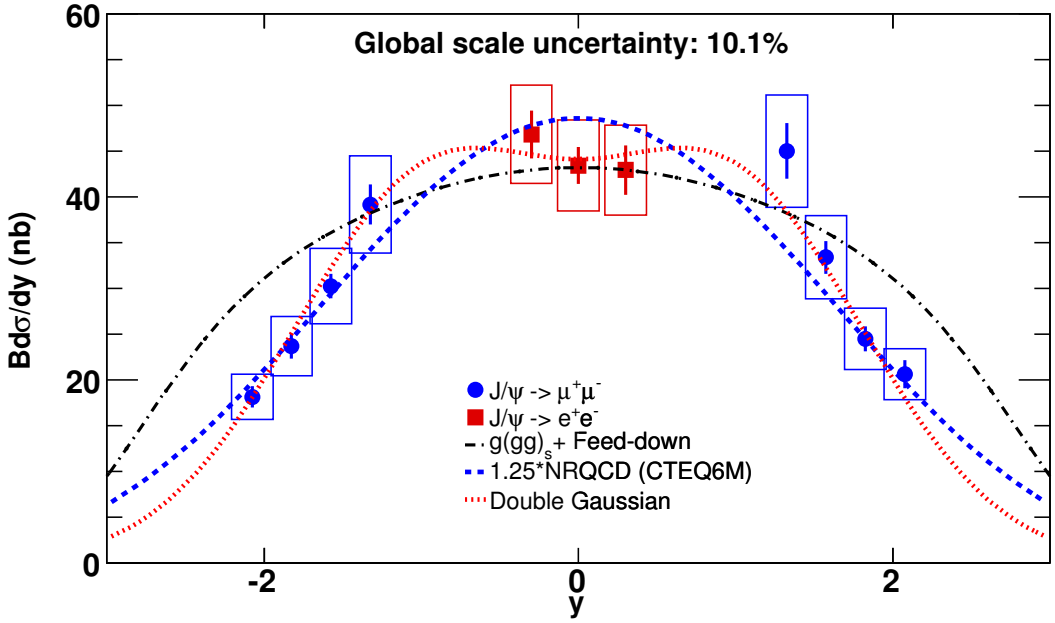

Figure 2.34: The J/ψ differential cross section times di-lepton branching ratio in $p+p$ collisions at $\sqrt{s} = 200$ GeV plotted versus rapidity [7]. The total production cross section of J/ψ times branching ratio is $B_{ll} \cdot \sigma_{pp}^{J/\psi} = 178 \pm 3(\text{stat}) \pm 53(\text{syst}) \pm 18(\text{norm})$ nb.

In d+Au Collisions

Figures 2.35 and 2.36 show the nuclear modification factor in d+Au collisions ($R_{d\text{Au}}$) at $\sqrt{s_{NN}} = 200$ GeV as a function of the rapidity of J/ψ with model predictions of the cold nuclear matter effect with the EKS and NDSG shadowing models, respectively [8]. These cold nuclear matter effect is based on the physical picture explained in subsection 2.5.2. The fraction of charmonium states produced in color singlets and color octets was determined by the NRQCD calculation [101]. The nuclear modification factor will be explained in section 5.1 and will be unity if there is no medium effect. If the J/ψ production is totally suppressed by the medium effects, the nuclear modification factor will be zero. A suppression of J/ψ in cold nuclear matter is observed as one goes in forward rapidity (in the d going direction), corresponding to a region sensitive to initial state low-x gluons in the Au nucleus. Breakup (absorption) cross sections of $\sigma_{breakup} = 2.8^{+1.7}_{-1.4}$ ($2.2^{+1.6}_{-1.5}$) mb are obtained by fitting to the data using the EKS (NDSG) nuclear shadowing. This $\sigma_{breakup}$ is the identical quantity to σ_{abs} in Eq. (2.54). These values of $\sigma_{breakup}$ are consistent within large uncertainties with $\sigma_{abs}^{J/\psi} = 4.2 \pm 0.5$ mb at the SPS, which is mentioned in the previous subsection.

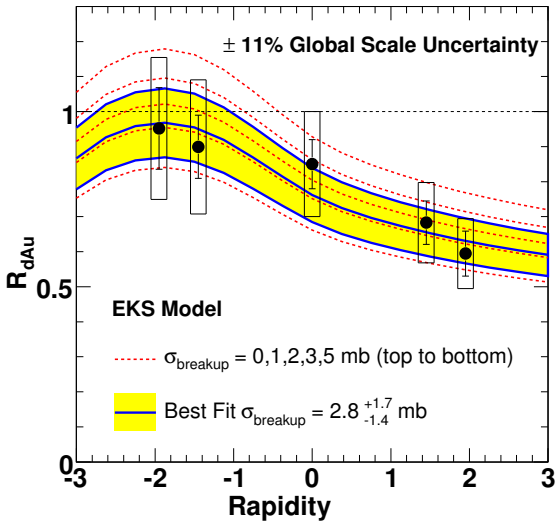

Figure 2.35: $R_{d\mathrm{Au}}$ data compared to the EKS curves for different $\sigma_{breakup}$ values [8]. The best fit value is $\sigma_{breakup} = 2.8^{+1.7}_{-1.4}$ mb.

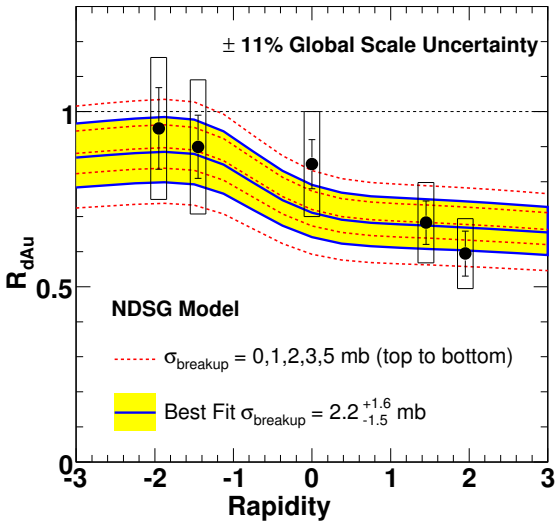

Figure 2.36: $R_{d\mathrm{Au}}$ data compared to the NDSG curves for different $\sigma_{breakup}$ values [8]. The best fit value is $\sigma_{breakup} = 2.2^{+1.6}_{-1.5}$ mb.

In Au+Au Collisions

Figure 2.37 shows the nuclear modification factor R_{AA} in Au+Au collisions at $\sqrt{s_{NN}} =$ 200 GeV as a function of the number of participating nucleons, N_{part} [6]. The strong suppression by a factor of about 4 and 6 is observed in central collisions at mid and forward rapidity, respectively. The ratio of forward/mid rapidity R_{AA} first decreases then reaches a plateau of about 0.6 for $N_{part} > 100$.

2.7 Motivation of This Study

The motivation of this study is to perform systematic study hot and dense matter using charmonia at the RHIC energy which is higher than the SPS energy by a factor of 10.

The motivation of the measurement of J/ψ production in Cu+Cu collisions is to perform more precise measurement in the small N_{part} region of < 100 with higher luminosity and a smaller system than in Au+Au collisions. In the small N_{part} region, the cold nuclear matter effect can be dominant and information of the effect might be extracted. The J/ψ data in Cu+Cu collisions will tell us where the starting point of the J/ψ suppression is.

The motivation of the measurement of χ_c production in $p+p$ collisions is to know the contribution of χ_c states to the inclusive J/ψ production. The χ_c contribution has the largest ambiguity of the inclusive J/ψ production. The fraction of J/ψ from χ_c decay feed-down is important by three reasons; the binding energy dependence of the charmonium dissociation temperature, the production mechanism of charmonia, which is not well understood by theories, and the sensitivity to the color octet contribution, which is important to the nuclear absorption. While the fraction of J/ψ from χ_c decay

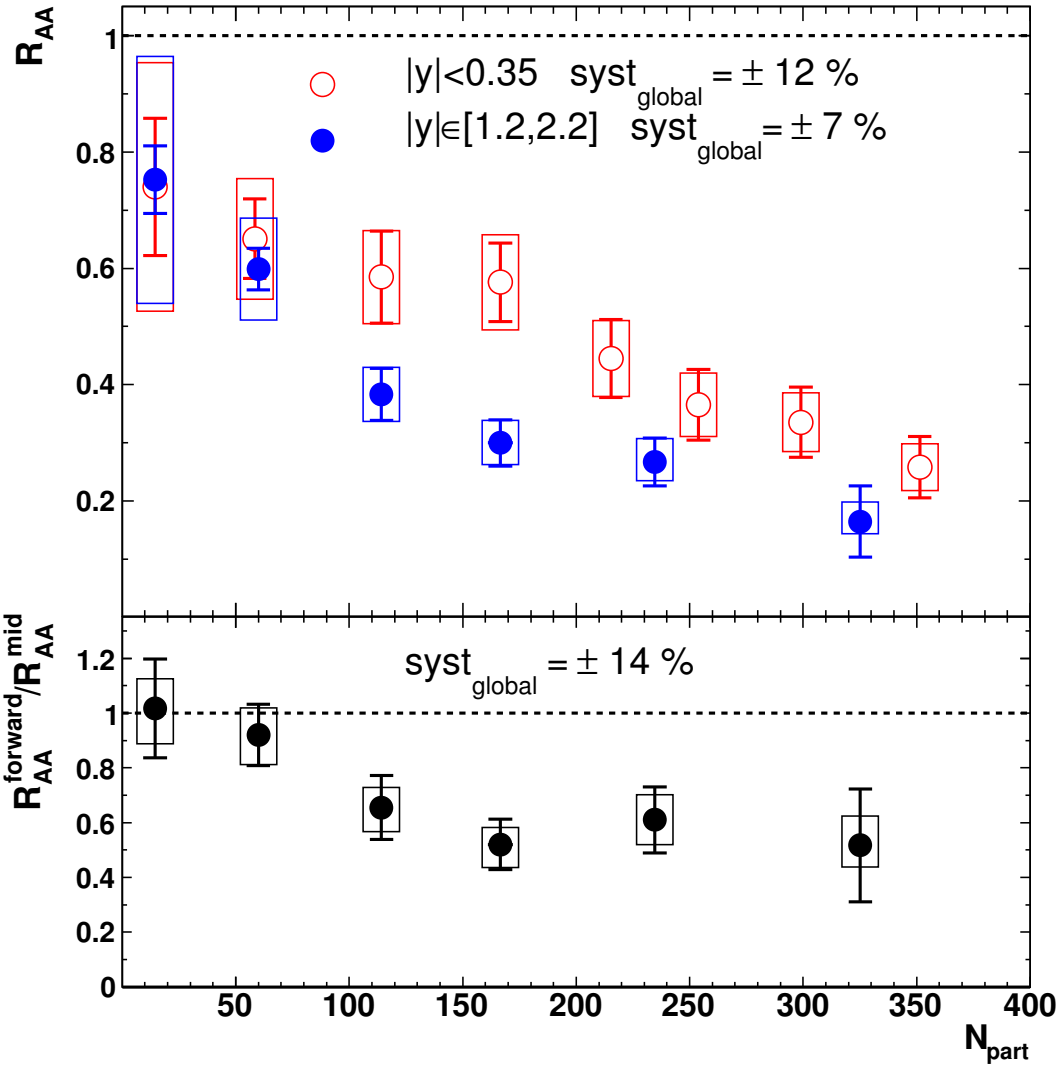

Figure 2.37: (Upper plot) J/ψ nuclear modification factor R_{AA} vs. the number of participants N_{part} for Au+Au collisions [6]. Mid (forward) rapidity data are shown with open (filled) circles. (Lower plot) Ratio of forward/mid rapidity J/ψ R_{AA} vs. N_{part}.

feed-down in $p + p$ collisions should be different from that in heavy-ion collisions by the nuclear absorption which is expected to depend on the charmonium radii, the χ_c measurement in $p + p$ collisions is important as a baseline measurement and to check the input fractions of the cold nuclear matter model.

Chapter 3

Experimental Setup

3.1 RHIC Accelerator Complex

The Relativistic Heavy Ion Collider (RHIC) is a colliding-type accelerator at Brookhaven National Laboratory (BNL) in the United States and started its operation in 2000 [104]. Figure 3.1 shows the layout of the RHIC accelerator complex. The RHIC accelerator complex consists of Tandem Van de Graaff accelerator, the proton linac, the booster synchrotron, Alternating Gradient Synchrotron (AGS) and RHIC whose circumference is 3834 m. RHIC can accelerate from protons (p) to gold (Au) ions at the maximum center of mass energy of 500 GeV in $p + p$ collisions and 200 GeV per nucleon pair in Au+Au collisions. RHIC has collied $p^+ + p^+$, $d^+ + {}^{197}\mathrm{Au}^{79+}$, ${}^{63}\mathrm{Cu}^{29+} + {}^{63}\mathrm{Cu}^{29+}$ and ${}^{197}\mathrm{Au}^{79+} + {}^{197}\mathrm{Au}^{79+}$ at 200 GeV per nucleon pair and lower energy. An acceleration cycle of heavy ion beam starts from a pulsed sputter ion source which extract negative ions, Cu^- (Au^-). The negative ions are injected into Tandem with a peak intensity of 250 μA and are accelerated from ground to +14 MV potential. They pass through a stripping foil in the high voltage terminal in the middle of Tandem. The partially stripped ions are accelerated back to ground potential and are selected charge state of Cu^{11+} (Au^{12+}). When Au ions are accelerated, another carbon foil at the exit of Tandem is used to strip electrons and to make higher charged ion, Au^{32+}. The ions traverse an 840 m long heavy ion transfer line to the Booster synchrotron without further stripping. The AGS booster accelerator is a small synchrotron whose circumference is 200 m. The 900 (600)-μs Tandem pulse yields 98 (45) booster turns for Cu (Au). After multi turn injections, beams are captured into six bunches and accelerated to a momentum of 445 (431) MeV/c per nucleon. The ions are stripped to Cu^{29+} (Au^{77+}) at the exit of the booster. The selected Cu^{29+} ion is the fully stripped charge state. The AGS accelerates Cu^{29+} (Au^{77+}) to a momentum of 11.2 (9.75) GeV/c. All beams are delivered through the AGS to RHIC (AtR) beam transfer line. The last two electrons of gold ions are removed to produce the fully stripped charge state, Au^{79+}, at the stripper foil in the AtR. RHIC has two rings; Blue Ring where beams circulate clockwise and Yellow Ring where beams circulate counterclockwise. Beams injection is done in box car fashion, one bunch at a time. The AGS cycle is repeated 14 times to establish the 41 (56) bunches. Acceleration and storage of beam bunches at RHIC use two RF systems. One RF operating at 28 MHz is used to capture the AGS bunches and accelerates to the top energy. Another RF operating at 197 MHz is used to limit the bunch length

growth due intra-beam scattering due to the Coulomb interaction, which scales with Z^4/A^2 (thereby limiting the collision diamond RMS length to 20 cm). Acceleration from injection energy to top energy takes 130 seconds. At the end of injection there are 4.5×10^9 (1.1×10^9) ions per bunch and the minimum bunch crossing time is 106 ns.

RHIC serves also as a polarized proton collider. Polarized protons extracted from the polarized proton source are accelerated by the 200 MeV linac and booster. The maximum polarized proton momentum is 24.3 GeV/c in the AGS and 250 GeV/c in RHIC.

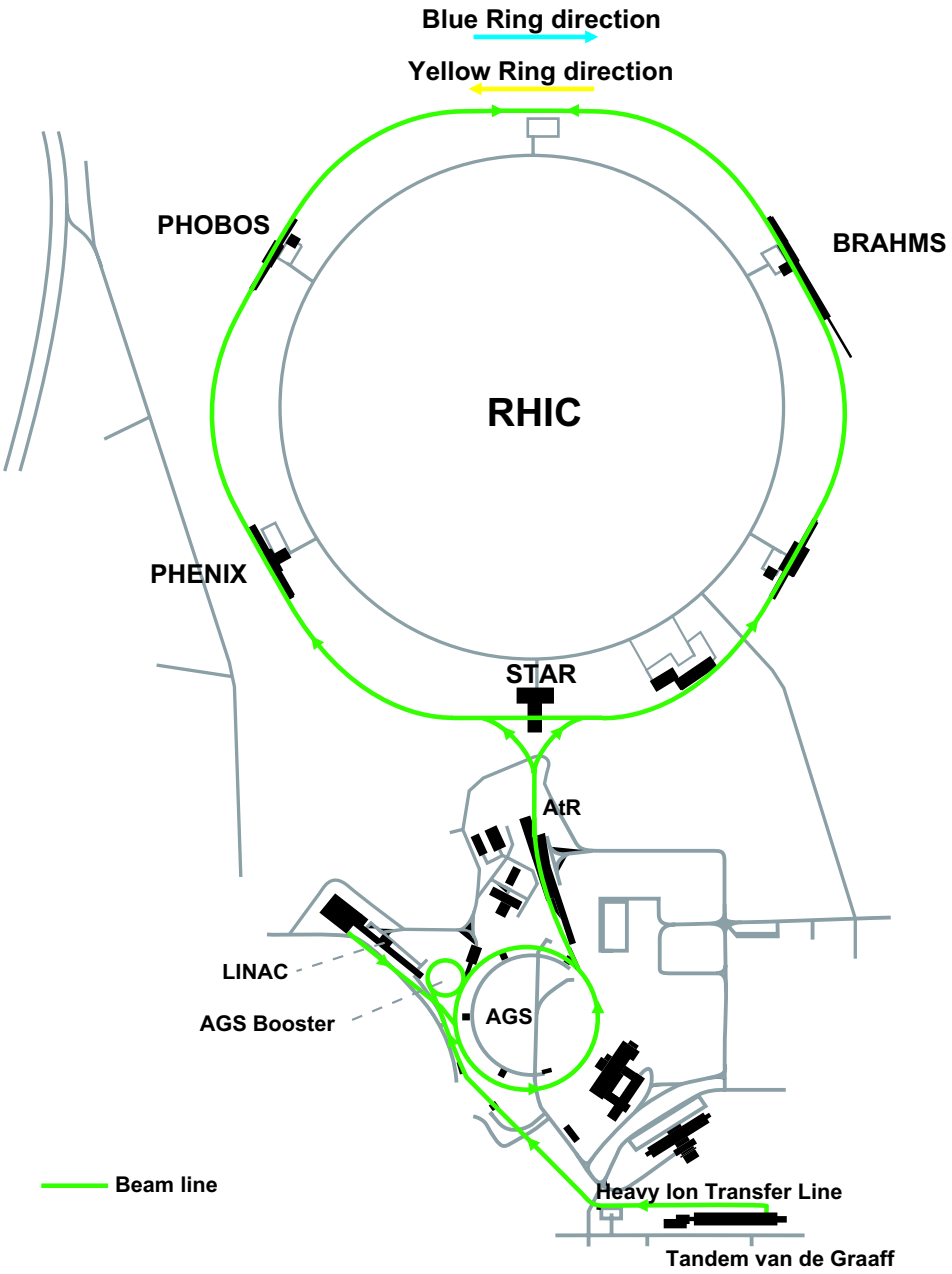

Figure 3.1: The RHIC accelerator complex and the arrangement of experiments.

3.2 PHENIX Detector Overview

There are four experiments, BRAHMS [105], PHENIX [106], PHOBOS [107] and STAR [108], at RHIC. The PHENIX detector was constructed to measure a wide variety of physics observables to address the signatures of QGP and study the QGP property.

In the following sections, the PHENIX subsystems used in 2005 (RHIC Run-5) and 2006 (RHIC Run-6) will be described. The layout of the PHENIX detectors and magnets is shown in Fig. 3.2. The definition of the global coordinate system in the PHENIX experiment is shown in Fig. 3.3. The origin of the coordinate system is the center of interaction region along the center of the cylindrical beam pipe. y-axis is defined as the altitude relative to the altitude of the origin. z-axis is defined as an axis along the center of the beam pipe. The positive z direction is the north side of detectors. x-axis is defined as x, y and z-axes form the right handed coordinate system. Thus the positive x direction is the west side of detectors. The PHENIX subsystems can be categorized into four groups, beam detectors, magnets, central arms and muon arms. The beam detectors are used for triggering and event characterization. The magnets, the central magnet and two muon magnets, realize the magnetic fields to measure momenta of charged particles. The central arms consist of east and west arms and are instrumented to detect electrons, photons and hadrons at midrapidity ($|\eta| < 0.35$). The muon arms are optimized for detection of dimuons in the forward and backward rapidity regions ($1.2 < |\eta| < 2.4$). Around the interaction point, the beryllium beam pipe is used and its diameter and thickness are 76 mm and 1.0 mm (0.28% of radiation length), respectively.

3.3 PHENIX Beam Detectors

The PHENIX beam detectors consists of Beam-Beam Counters (BBC) [109] and Zero-Degree Calorimeters (ZDC) [110, 111, 112] to measure the beam property such as the luminosity, the collision vertex and the collision centrality.

3.3.1 Beam-Beam Counters

The Beam-Beam Counter (BBC) provides information for triggering beam collisions and the collision vertex position along the beam axis with resolution of about 2 cm (1 mm) for $p + p$ (central Au+Au) collisions. The BBC is designed to measure the multiplicity of charged particles produced by a collision, the timing of the collision and the collision vertex. The information must be available at the trigger level to discriminate backgrounds. The timing information is also used to perform the time of flight (TOF) measurement combined with the information from the TOF detectors in the east arm for particle identification. The BBC consists of two arrays of counter elements, and each is placed at the south side and the north side of the beam crossing point ($z_{\rm BBC} = \pm 1.44$ m, η =3.0–3.9). Pictures in Fig. 3.4 show (a) one counter, (b) an array of counters and (c) the BBC mounted on the PHENIX detector. The average and difference of the arrival times (T_1 for the south array and T_2 for the north array) of the fast leading charged particles from a beam collision into the two BBC arrays provide

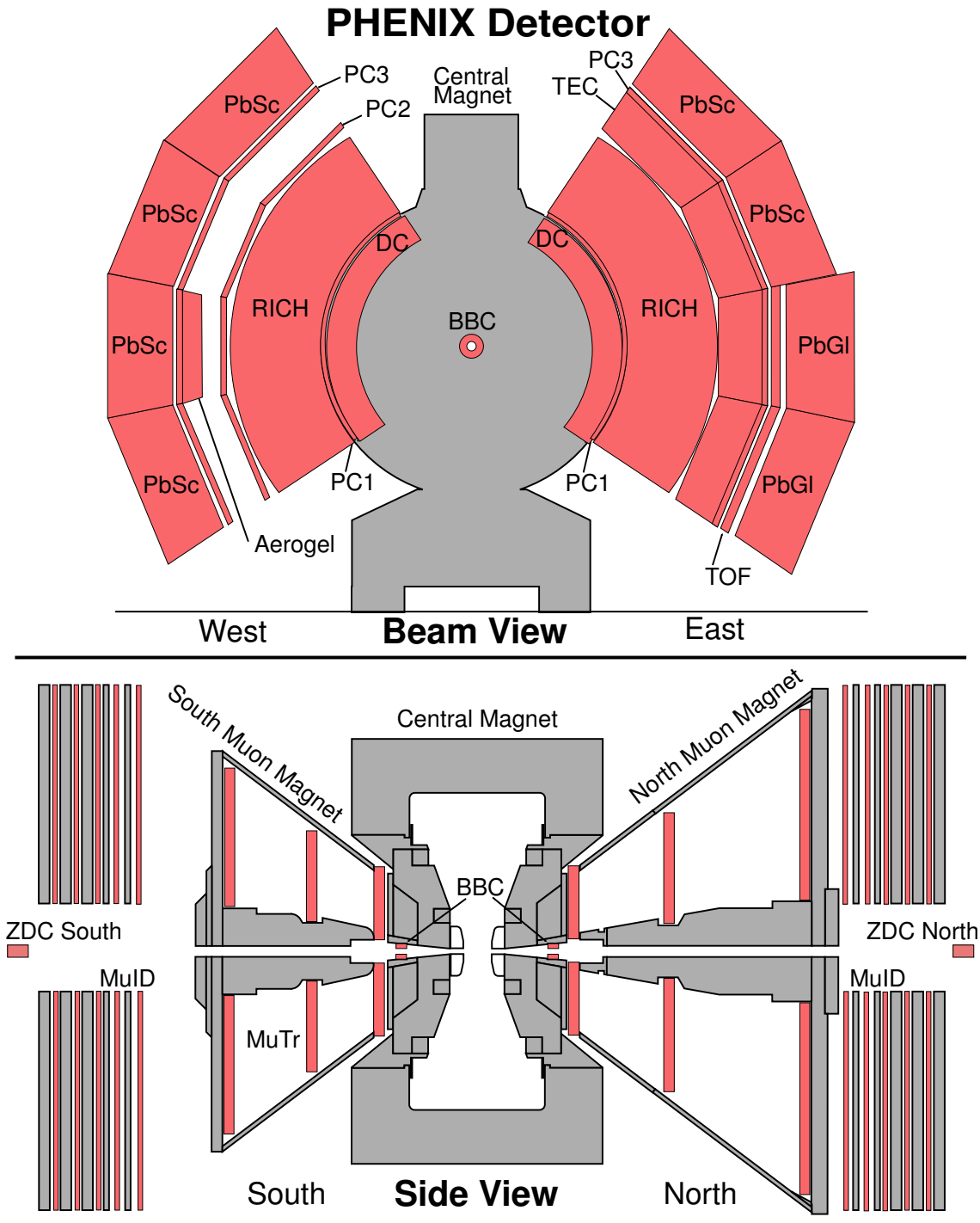

Figure 3.2: The PHENIX detector layout in 2005 and 2006. Upper panel shows a beam view. Two central arms and central magnet are shown. Lower panel shows a side view. Two muon arms, central magnet and muon magnets are shown.

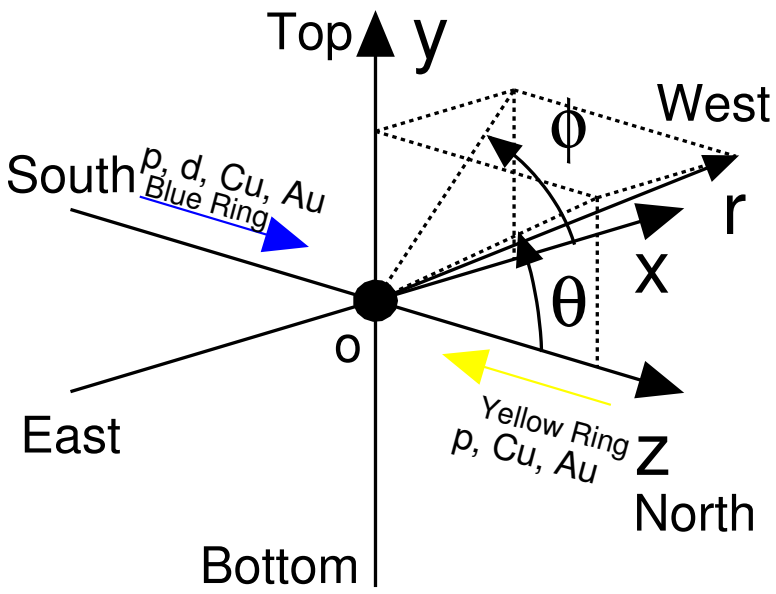

Figure 3.3: Definition of global coordinate system used in the PHENIX experiment.

the time origin (T_0) and the vertex position of the collision (BbcZvertex), as follows:

$$T_0 = \frac{T_1 + T_2}{2} - \frac{|z_{\rm BBC}|}{c} + t_{\rm offset}, \tag{3.1}$$

$$\text{BbcZvertex} = \frac{c \cdot (T_1 - T_2)}{2} + z_{\rm offset}, \tag{3.2}$$

where c is the speed of light ($c = 299792458$ m/s).

Each array consists of 64 modules of counter elements which are constructed from Cherenkov radiators of 30 mm long fused quartz and phototubes of 1 inch diameter. There is a magnetic field of ∼0.3 T almost parallel to the beam axis (Fig. 3.8). To operate under the magnetic field, mesh-dynode phototubes (Hamamatsu R6178) whose timing resolution is 50 ps are adopted.

3.3.2 Zero-Degree Calorimeters

The Zero-Degree Calorimeters (ZDC) are the common trigger device among the four RHIC experiments. The ZDC is a hadron calorimeter designed to detect neutrons and measure their total energy. Figure 3.5 shows the layout of the ZDC. Two ZDCs are positioned at $z_{\rm ZDC} = \pm 18.25$ m from the interaction point and just behind the DX dipole magnet. The angular acceptance of the ZDC is $|\theta| < 2$ mrad. The DX dipole magnets serve to bend the incoming beams to the colliding region and outgoing beams to the collider beam line. Because of the bending by the DX dipole magnet, only the

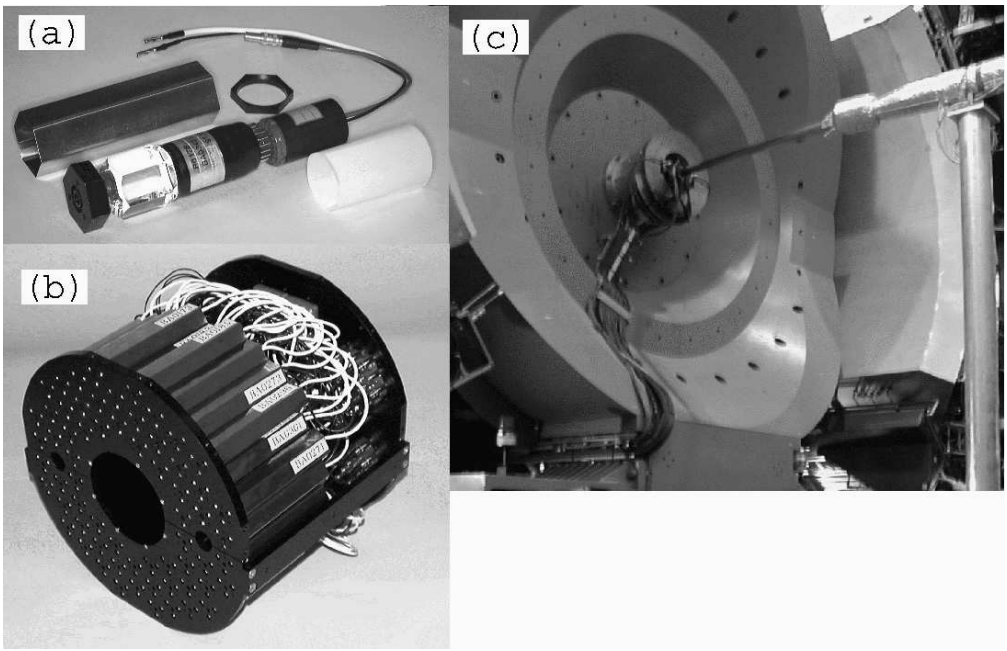

Figure 3.4: (a) Single BBC consisting of a 1 inch mesh dynode phototube mounted on a 3 cm quartz radiator; (b) A BBC array comprising 64 BBC elements; and (c) The BBC mounted on the PHENIX detector is shown. The beam pipe is seen in the middle of the picture. The BBC is installed on the mounting structure just behind the central spectrometer magnet.

neutrons can reach to each ZDC. Therefore, each ZDC provides the energy measurement of the forward neutrons unbound by coulomb excitation or evaporated from unstable spectators produced by hadronic interactions.

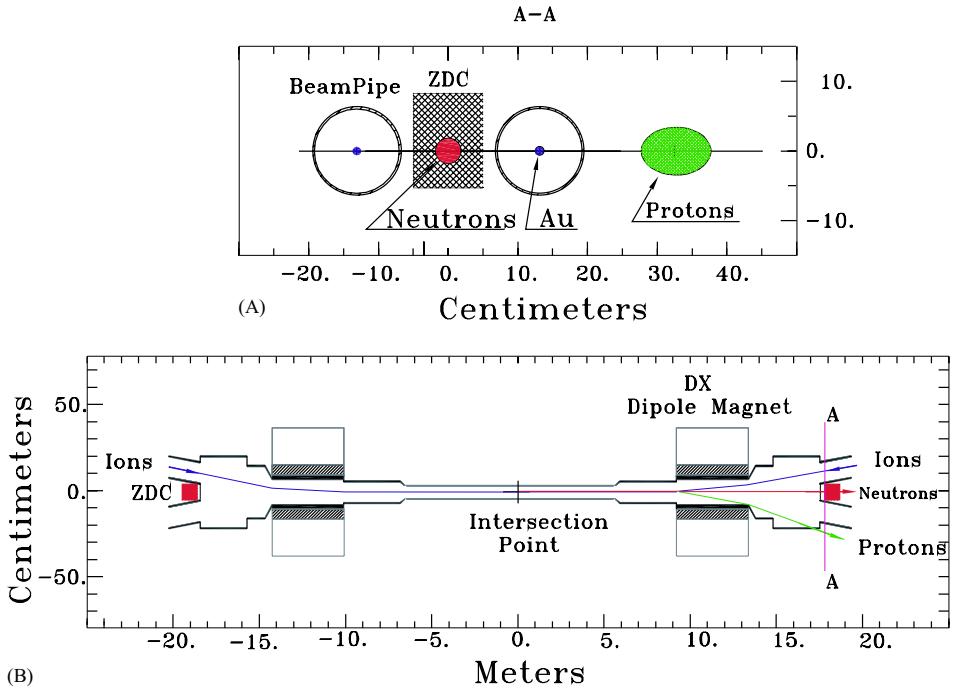

Figure 3.5: A plan view of the collision region and (section A-A) a beam view of the ZDC location indicating deflection of protons and charged fragments with Z/A ∼1 downstream of the DX dipole magnet.

Each ZDC is mechanically subdivided into three identical modules with two interaction lengths (weight∼50 kg) each. The mechanical design of one module is shown in Fig. 3.6. The active medium is clear PMMA fibers (ϕ = 0.5 mm) interleaved with tungsten absorber (27 plates) of 5 mm thickness. This sandwich structure is tilted at 45 degrees to the beam to align the optical fibers with the Cherenkov angle for forward particles in the shower. The fibers are connected to a phototube (Hamamatsu R329-2). Taking the correlation between the north and south ZDC provides the background rejection due to single beam interaction with the residual gas in the beam pipe. The energy resolution of the ZDC for 100 GeV neutrons is 21%. Time resolution is ∼120 ps corresponding the collision vertex resolution of ∼2.5 cm for 100 GeV neutrons.

3.4 PHENIX Magnet System

The PHENIX magnet system consists of three magnets, Central Magnet (CM), North Muon Magnet (MMN) and South Muon Magnet (MMS) [113]. The layout of the magnets is shown in Fig. 3.7 and the magnetic field produced by the magnets is shown in Fig. 3.8.

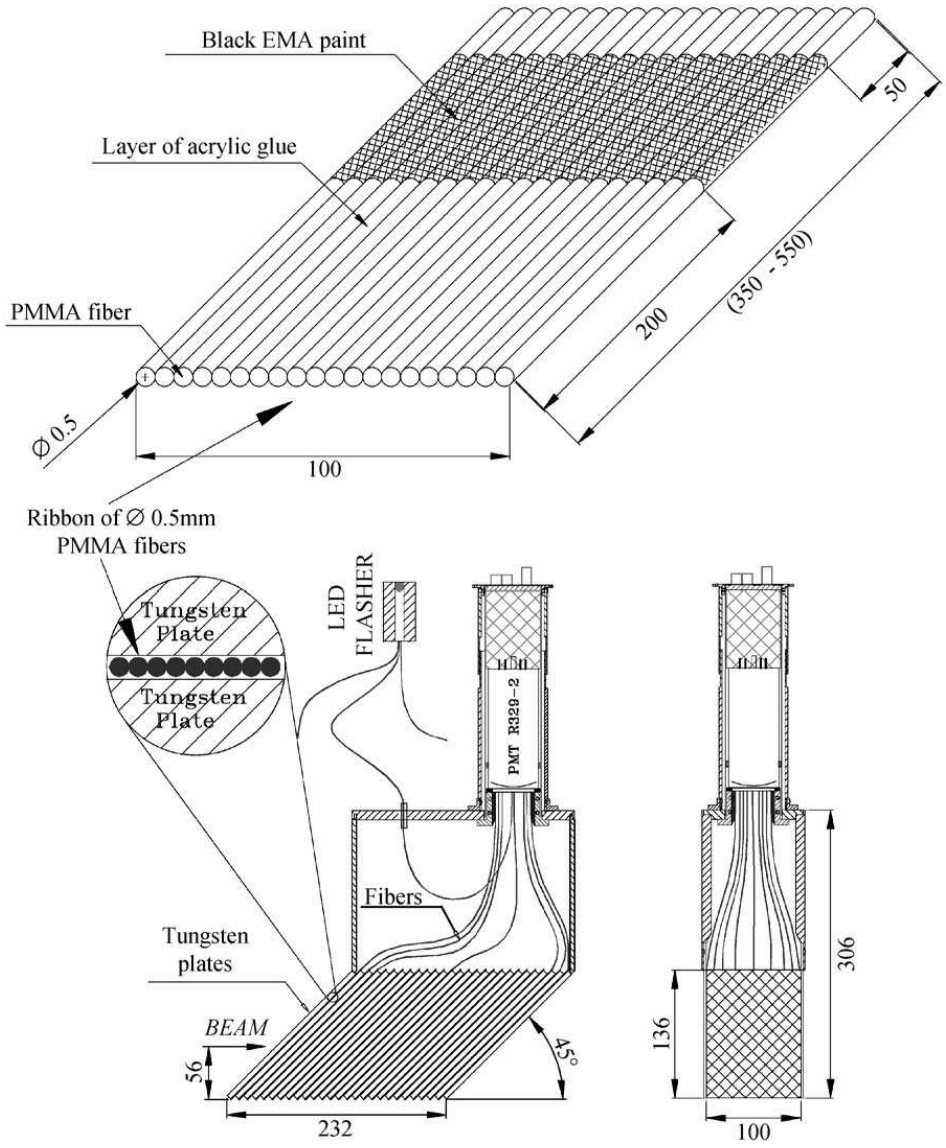

Figure 3.6: Mechanical design of the production tungsten module. Dimensions shown are in mm.

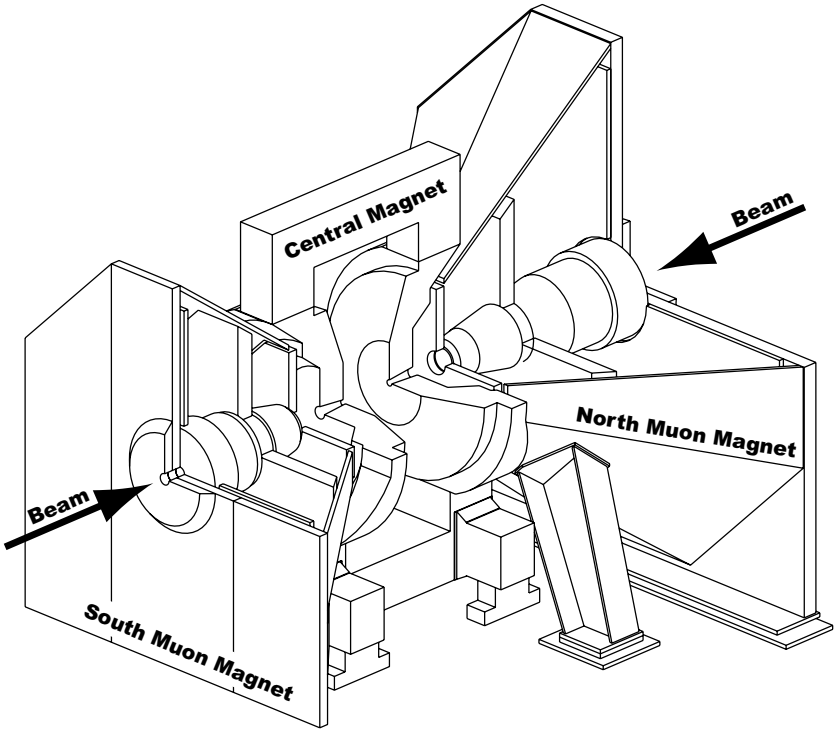

Figure 3.7: Line drawings of the PHENIX magnets, shown in perspective and cut away to show the interior structures. Arrows indicate the beam line of the colliding beams in RHIC.

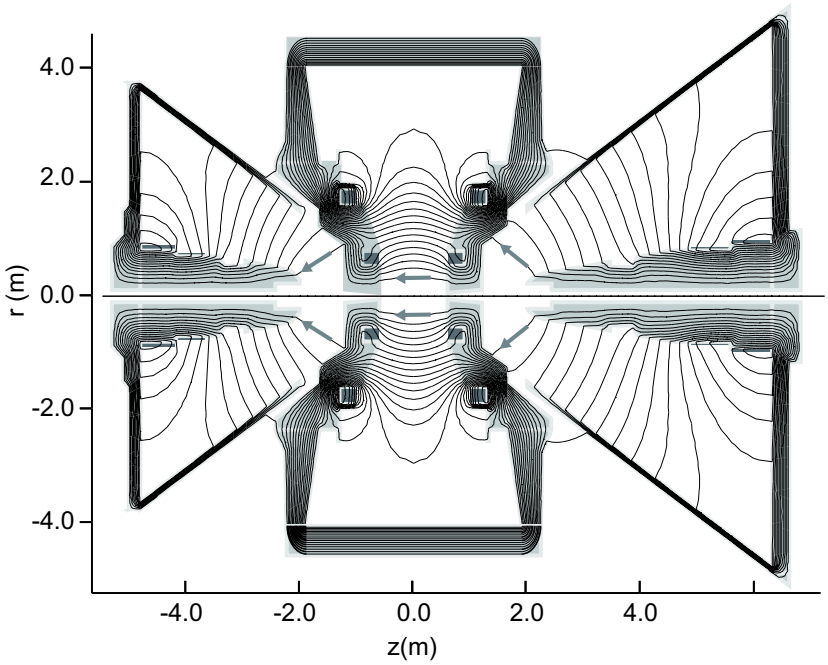

Figure 3.8: The field lines of the central magnet and muon magnets shown on a vertical cutaway drawing of the PHENIX magnets. The beams travel along the $r = 0$-axis in this figure and collide at $r = z = 0$. Arrows indicate the field direction.

3.4.1 Central Magnet

The PHENIX Central Magnet (CM) realizes an axial field and its integrated field is $\int B \cdot dl = 0.78$ T·m at $\theta = \pi/2$ rad. The CM is used for momentum determination of charged particles with magnetic bending. The CM is energized by two, inner and outer, pairs of concentric coils, which can be run separately, with the same polarities or opposite polarities. In Run-5 (2005) and Run-6 (2006), the same polarity operation was chosen. The operation is called as CM++ or CM−− according to the polarity of the magnetic field. The pole faces of the magnet are positioned at $z = \pm 0.45$ m covering the pseudo rapidity range of $\eta < 0.35$. The CM pole tips also serve as the hadron absorbers for the muon spectrometers.

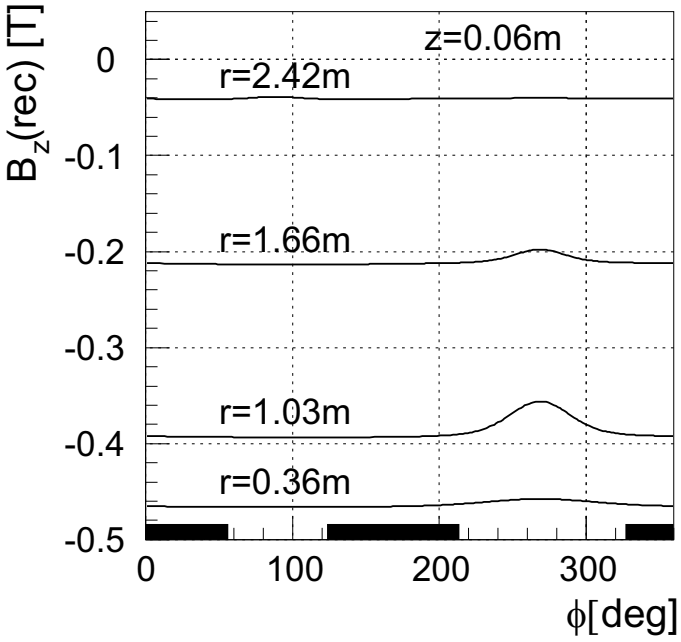

Figure 3.9: Reconstructed B_z values as a function of ϕ for various radii.

3.4.2 Muon Magnets

The PHENIX Muon Magnets use solenoid coils to produce radial magnetic field for muon analysis. The MMN (MMS) covers a pseudorapidity interval of 1.1–2.4 (−2.2–−1.1) and full azimuth. The coils are wound on cylindrical surface at the end of large tapered pistons. The iron yokes consist of 8-sided lampshades and back plates. Each of the muon magnets provides a field integral of 0.72 Tm. The magnet acceptance was maximized to have large acceptance of muon pair events.

3.5 PHENIX Central Arms

The PHENIX central arms are designed to detect charged particles and photons. The momentum measurement of charged particles is performed by drift chambers and pad

chambers [115]. The energy measurement of photons is performed by electromagnetic calorimeters [118]. Identification of the charged particle is also performed [115]. Ring imaging Cherenkov counters and electromagnetic calorimeters are the devices for the electron identification. Time of flight counters and aerogel Cherenkov counters are the devices for the hadron identification (π, K, p and d).

3.5.1 Drift Chambers

The Drift Chambers (DC) are used to measure charged particle trajectories in the $r-\phi$ direction and to determine the transverse momentum (p_T) of each particle. The DC system consists of two independent gas volumes located in the west and east arms, respectively. A gas mixture of 50% argon and 50% ethane is filled in the gas volumes. The east arm DC is the mirror image of the west arm DC. Each DC occupies radial budget from 2.02 to 2.46 m from the beam line and covers 1.8 m along the beam line direction as an active area. Each DC is placed in a region having high residual magnetic field up to 0.06 T at maximum. Each DC volume is constructed with a cylindrical titanium frame as shown in Fig. 3.10. Each frame is divided in 20 equal sectors covering 4.5° in ϕ.

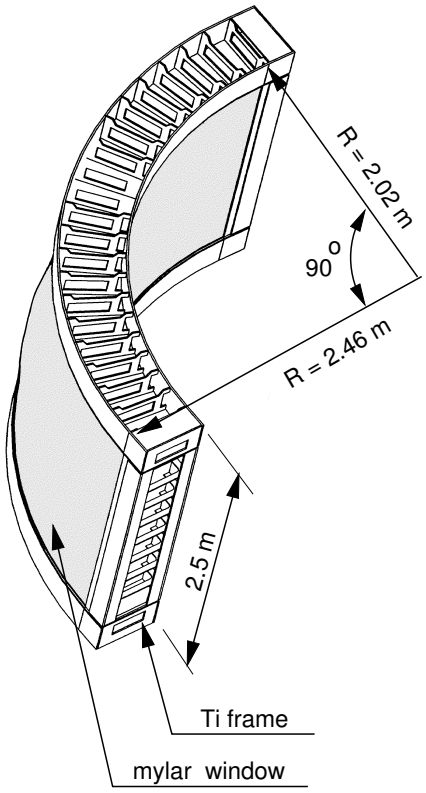

Figure 3.10: A frame of a drift chamber.

As shown in Fig. 3.11, there are six types of wire modules stacked radially in each sector: X1, U1, V1, X2, U2, V2. Each module contains 4 sense (anode) planes and

4 cathode planes forming cells with a 20–25 mm drift space in the ϕ direction. The sense (S) wires are separated by potential (P) wires, and surrounded by gate (G) and back (B) wires. The P wires form a strong electric field and separate sensitive regions of individual S wires. The G wires limit the track sample length to roughly 3 mm and terminate unwanted drift lines. The B wire has a rather low potential and terminates most of the drift lines from its side, essentially eliminating left-right ambiguity and decreasing the signal rate per electronics channel by a factor of two. Each X, U and V cell contains 12, 4 and 4 S wires, respectively. There are 40 drift cells in the DC located at different radii. The X1 and X2 wire cells run in parallel to the beam line to perform precise track measurement in $r - \phi$. Each X wire cell is followed by the of U and V wire cells used for pattern recognition. The U and V wires have stereo angles of about 6° relative to the X wires and measure the z coordinate of the track. The stereo angle was selected to minimize track ambiguities by matching the z coordinate of the pad chambers. To satisfy the requirement of efficient track recognition for up to 500 tracks in the whole PHENIX fiducial volume, each sense wire is separated at the center into two halves. The electrostatic field is adjusted to keep the mean pulse width to near 35 ns and therefore achieve the double track resolution better than 2 mm. The single wire resolution is 165 μm.

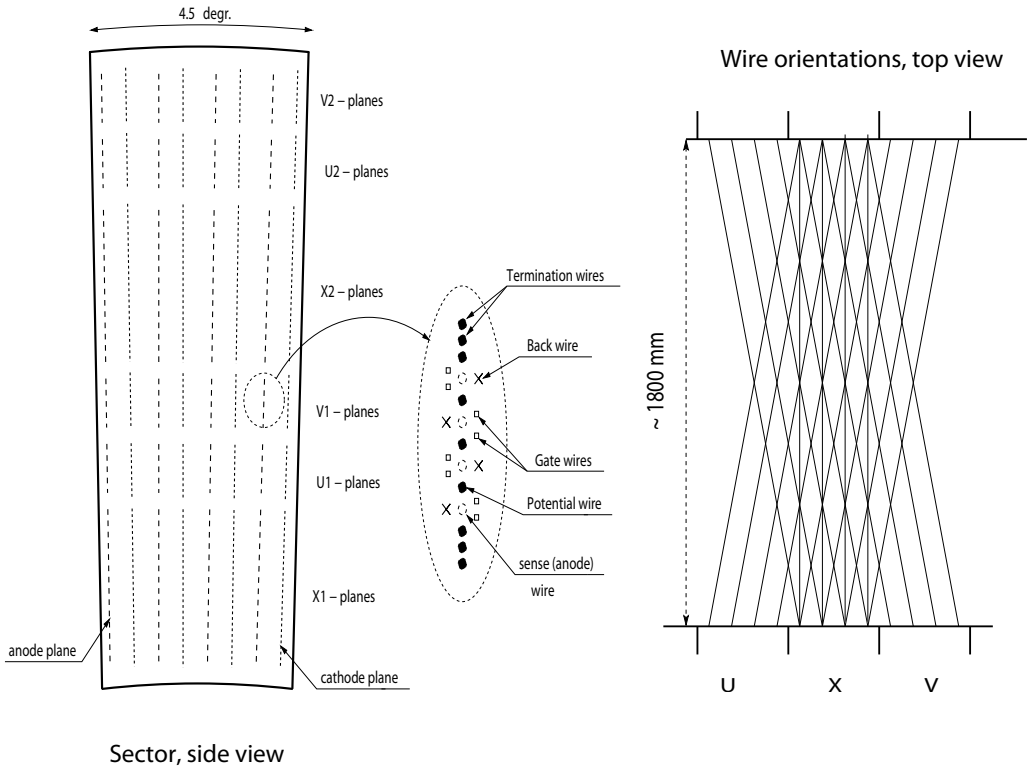

Figure 3.11: The layout of wire position within one sector and inside the anode plane (left). A schematic diagram, top view, of the stereo wire orientation (right).

3.5.2 Pad Chambers

Pad Chambers (PC) is used to determine three dimensional spatial positions which are used for momentum determination in the z direction (p_z). The PC is a multi-wire proportional chamber with cathode readout and forms three separate layers (PC1, PC2 and PC3) as shown in Fig. 3.12. The PC1 is the innermost chamber occupying 2.47–2.52 m in radial distance from the interaction point, located between the DC and the ring imaging Cherenkov detectors on both east and west arms. The PC2 layer exists only the west arm and is placed behind the RICH at r =4.15–4.21 m. The PC3 is located in front of the electromagnetic calorimeter and occupies r =4.91–4.98 m. The PC1 is essential for determination of the three dimensional momentum by providing the z coordinate at the exit of the DC. The DC and PC1 information gives the straight line particle trajectories outside the magnetic field. The PC2 and PC3 are needed to resolve ambiguities in outer detectors where about 30% of particles striking the EMCal are produced by either secondary interaction and decays outside the aperture of DC and PC1.

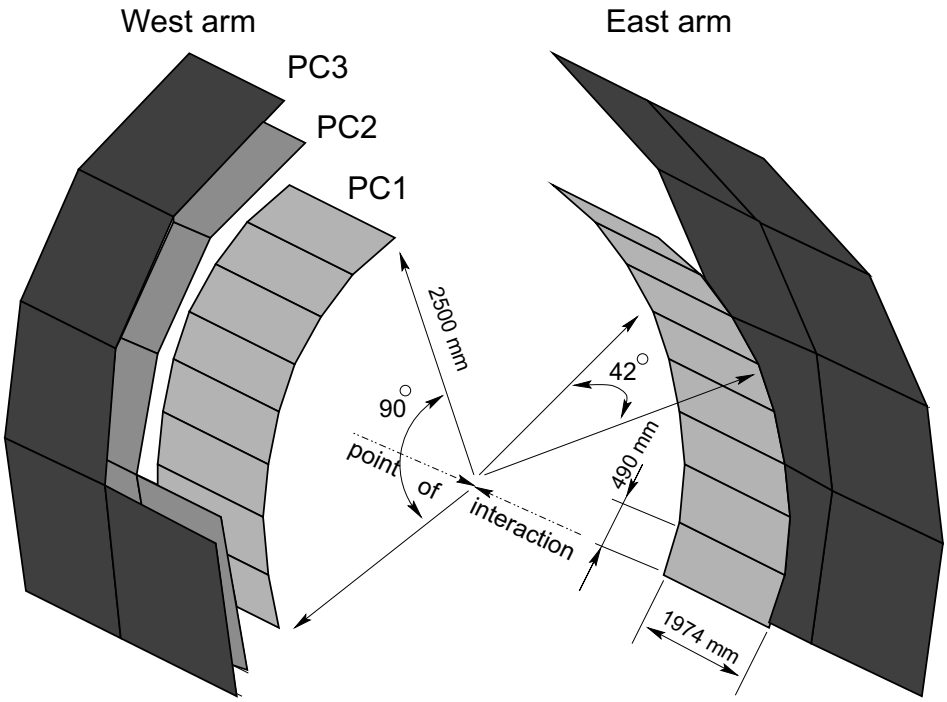

Figure 3.12: Pad chambers (PC1, PC2 and PC3). Several sectors of PC2 and PC3 in the west arm are removed for clarity of the picture.

Each detector consists of a cathode panel and a signal plane of anode and field wires. One cathode is finely segmented into an array of pixels as shown in Fig. 3.13. The gas is chosen to be a mixture of 50% argon and 50% ethane at atomospheric pressure. The specifications of the PCs are listed in Table 3.1.

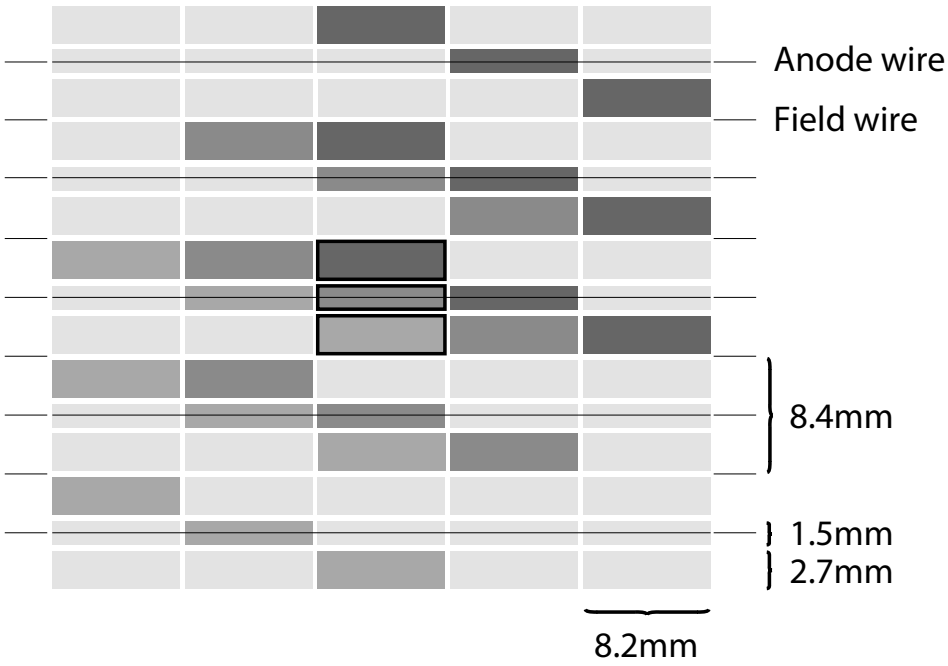

Figure 3.13: The pad and pixel geometry (left). A cell defined by three pixels is at the center of the right picture.

Parameters	PC1	PC2	PC3
Pad size ($\phi \times z$) (mm^2)	8.4×8.4	13.6×14.4	16.0×16.7
Single hit resolution in z (mm)	1.7	3.1	3.6
Efficiency	$\geq 99\%$	$\geq 99\%$	$\geq 99\%$

Table 3.1: Performance of pad chambers in Run-2 (2001–2002) and cosmic ray test.

3.5.3 Ring Imaging Cherenkov Detectors

Each of the PHENIX central arms equips a Ring Imaging Cherenkov detector (RICH) [116]. The RICH detector is one of the primary devices to identify electrons among the large number of charged hadrons. The RICH detectors are placed in back-to-back fashion on both sides of the beam line in the radial position between 2.5–4.1m, covering θ =70–110 degrees and 90 degrees per arm in the azimuth. Figure 3.14 shows a cutaway view of one of the RICH detectors. Each detector has a volume of 40 m^3, with an entrance window area of 8.9 m^2 and an exit window area of 21.6 m^3. Each detector contains 48 composite mirror panels, forming two intersecting spherical surfaces, with a total reflecting area of 20 m^2. The mirror panel substrates have a radius of curvature of $\sim$4.01 m and the panel shapes are defined by lines of latitude and longitude on a spherical surface. The panels are 0.812 m long with widths that vary from 0.432 to 0.505 m. They consists of 12.5 mm of Rohacell foam with four layers of graphite epoxy on each side. The combined thickness of the four layers of graphite epoxy is 0.7 mm. The reflectivity was found 83% at 200 nm and 90% at 250 nm. The spherical mirrors focus Cherenkov light onto two arrays of 1280 Hamamatsu H3171S UV phototubes with the cathode diameter of 25 mm, each located on either side of the RICH entrance window. The phototubes are fitted with 2 inch diameter Winston cones and have magnetic shields that allow them to operate at up to the magnetic field of 0.01 T. The phototube UV glass windows absorb photons with wavelengths below 200 nm. The phototube has a bi-alkaline photocathode and a linear focus 10 stage dynode. The quantum efficiency is 27% at peak ($>$ 19% at λ=300 nm and $>$ 5% at λ=200 nm), the typical dark current is 10 nA. The typical operation voltage and gain are 1.5 kV and 10^7, respectively.

The minimum and maximum thicknesses of radiator gas seen by any particle is 0.87 m and 1.50 m, respectively. The radiator gas is maintained at a pressure of 0.5 inch of water above ambient. The large aluminized Kapton entrance and exit windows are 125 μm thick, and are supported against the internal pressure by graphite-epoxy beams. The preamplifiers whose gain is $\sim$10 for the signals from the phototubes are mounted directly on the RICH detectors.

Figure 3.15 shows a schematic view of the RICH. In the RICH gas vessel, charged particles moving faster than the speed of light in the gas emit Cherenkov photons. The emitted photons are reflected and focused by the spherical mirror on the plane of phototube array. Radiator gas filled in the RICH is CO_2 gas whose index is 1.000410 at 20 °C and 1 atm [19]. A charged particle with $\beta\gamma > 35$ emits Cherenkov photons. This corresponds to 18 MeV/c for electrons and 4.9 GeV/c for pions. The ring diameter for is about 118 mm for $\beta = 1$ particles and CO_2 gas.

The RICH Front-End Electronics (FEE) processes the phototube signals at each bunch crossing (9.4 MHz) and transmits digitized data to the PHENIX data acquisition system on the trigger signal supplied by the PHENIX global trigger system ($\sim$25 kHz) [117]. The acceptable charge range is from 0 to 10 photoelectrons, which corresponds to the input charge from 0 to 160 pC preceded by the preamplifier. Charge resolution is $\sim$ 1/10 photoelectron and timing resolution is $\sim$ 240 ps. Both of the charge and timing outputs are stored in Analog Memory Unit (AMU) clocked at the RHIC bunch crossing frequency. The analog date stored in the AMU are digitized only after the receipt of an acceptance from the PHENIX global trigger system.

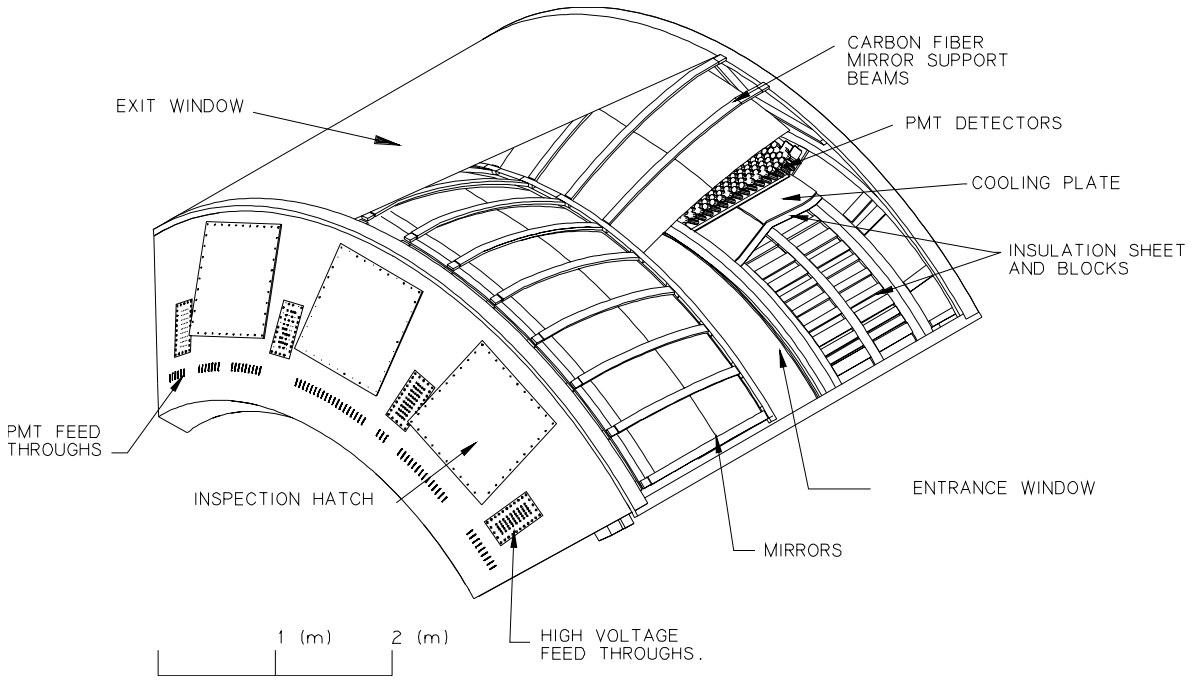

Figure 3.14: A cutaway view of one arm of the RICH detector.

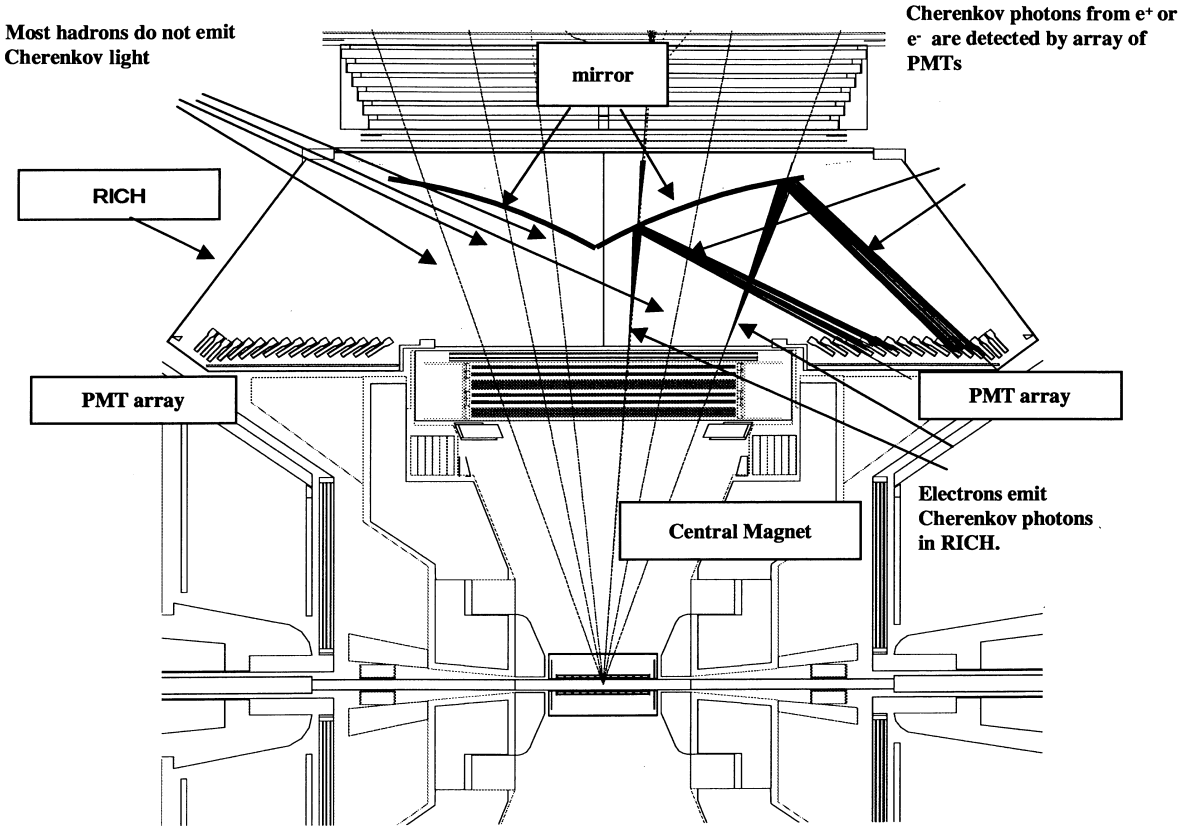

Figure 3.15: A cut through view if the RICH detector.

3.5.4 Electromagnetic Calorimeters

The Electromagnetic Calorimeter (EMCal) is used to measure the energy and spatial position of electrons and photons produced in beam collisions. It covers the full central spectrometer acceptance of $70^\circ \leq \theta \leq 110^\circ$ with two walls, each subtending 90° in the azimuth. One wall comprises four sectors of a lead scintillator sampling calorimeter (PbSc) and the other has two sectors of PbSc and a lead glass Cherenkov calorimeter (PbGl). The coverage in pseudo rapidity is $-0.35 < \eta < 0.35$ for both PbSc and PbGl. The coverage in the azimuthal angle is $6 \times \pi/4$ for PbSc and $2 \times \pi/4$ for PbGl.

Lead Scintillator Calorimeters

The lead scintillator calorimeter (PbSc) is a shashlik type sampling calorimeter consisting of 15552 individual towers and covering area of $\sim$ 50 m^2. Each PbSc tower contains 66 sampling cells consisting of alternating tiles of Pb and scintillator. These cells are optically connected by 36 longitudinally penetrating wavelength shifting fibers for light connection. Light is read out by 30 mm FEU115M phototubes at the back of the towers. Optically isolated four towers are mechanically grouped together into a single structural entity called a module as shown in Fig. 3.16. Thirty six modules are attached to a backbone and held together by welded stainless steel skins on the outside to form a rigid structure called a supermodule. Eighteen supermodule make a sector, a 2×4 m^2 plane with its own rigid steel frame. The energy resolution of PbSc obtained from the tests using electron beams is given by

$$\frac{\sigma_E}{E} = \frac{8.1\%}{E(\mathrm{GeV})} \oplus 2.1\%. \tag{3.3}$$

Lead Glass Calorimeters

The lead glass calorimeter (PbGl) array comprises 9216 modules. Each module has a lead glass crystal of 40 mm×40 mm×400 mm. The active depth of 400 mm corresponds to 16 radiation length. The Cherenkov photons emitted by the electrons and positrons in the electromagnetic shower process are read out by an FEU84 phototube in the back end. The modules are individually wrapped with aluminized mylar and shrink tube and 24 modules are glued together with carbon fiber and epoxy resin to form a self-supporting supermodules (Fig. 3.17). Each PbGl sector comprises 192 supermodules (16 supermodule wide by 12 supermodule high). The energy resolution of PbGl obtained from the tests using electron beams is given by

$$\frac{\sigma_E}{E} = \frac{5.9\%}{E(\mathrm{GeV})} \oplus 0.8\%. \tag{3.4}$$

3.5.5 Other Detectors

Time of Flight Counters

The time of flight counter (TOF) serves as a particle identification devices for charged hadrons in PHENIX. It is designed to have ∼100 ps timing resolution to achieve particle

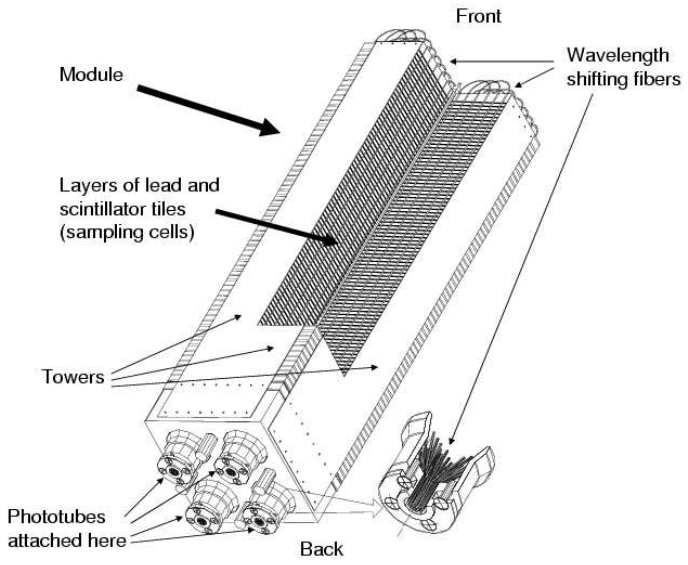

Figure 3.16: Interior view of a lead scintillator calorimeter module showing a stack of scintillator and lead plates, wavelength shifting fiber readout and leaky fiber inserted in the central hole. Its active depth is 375 mm (18 radiation length) and lateral segmentation size is 55.35×55.35 mm^2.

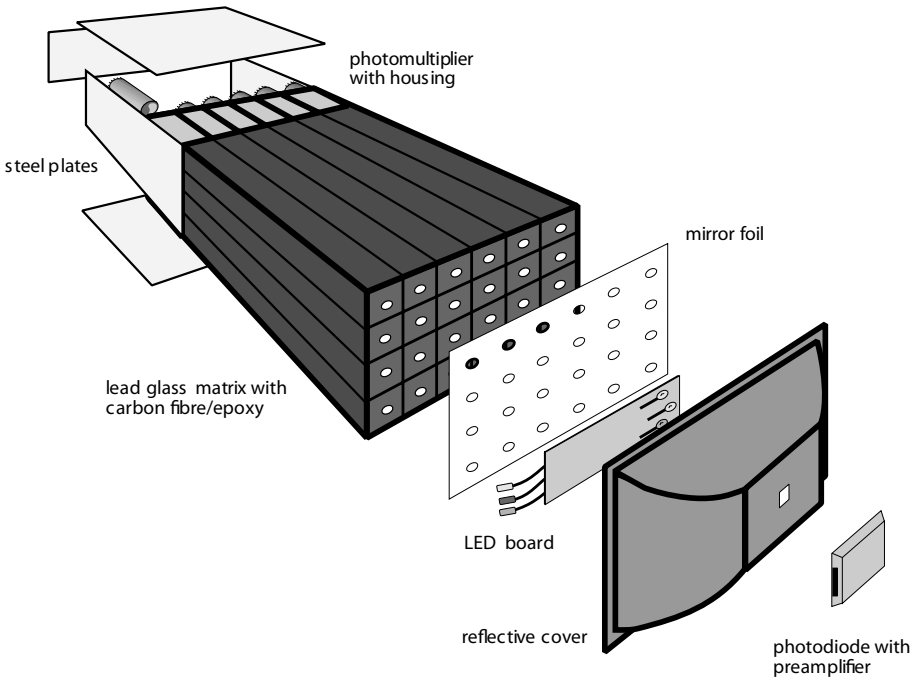

Figure 3.17: Exploded view of a lead glass calorimeter supermodule.

separation up to a high momentum region (pion/kaon < 2.4 GeV/c, kaon/proton $<$ 4.0 GeV/c). The TOF counter consists of 10 of TOF walls. Figure 3.18 shows a schematic view of a TOF wall. One TOF wall consists of 96 segments, each equipped with a plastic scintillator slat and one phototubes at each end. The plastic scintillator is Bicron BC404, 1.5 cm in width, 1.5 cm in depth and 63.8 or 43.4 cm in length. The phototube is Hamamatsu R3478S and its diameter is 3/4 inch. The TOF counter covers the region of $\pi/8(\phi) \times 0.7(\eta)$ in the east arm.

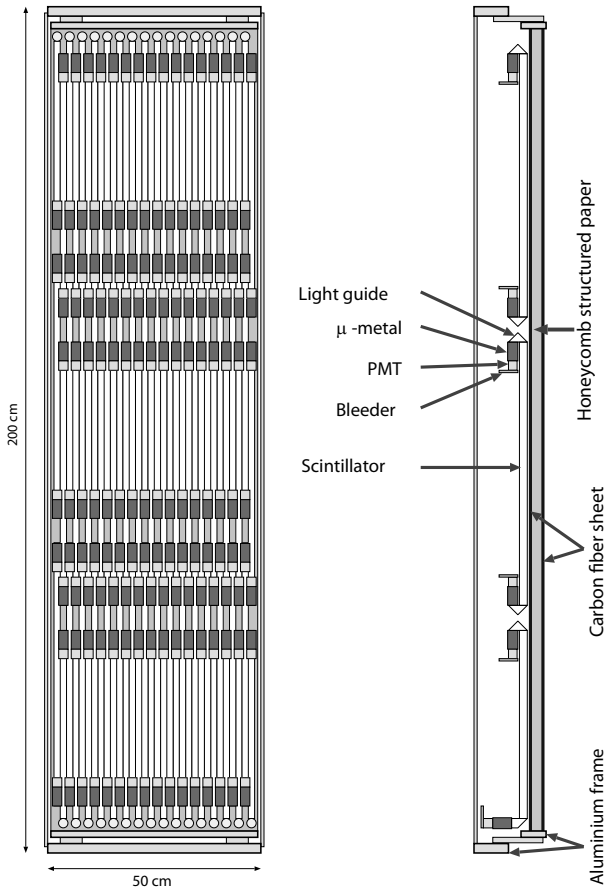

Figure 3.18: Schematic diagram of the components of a single TOF panel, which consists of 96 plastic scintillation counters with phototubes at both ends, light guides and supports.

Aerogel Cherenkov Counters

A cell of the aerogel Cherenkov counters consists of $22(z)\times11(\phi)\times12(r)$ cm^3 aerogel with a refractive index of $\sim$1.01, an integration cube and two 3-inch phototubes. Figure 3.19 shows an aerogel cell and the stack of aerogel cells. The intermediate refractive index of aerogel enables us to distinguish pion and kaon, kaon and proton. The aerogel Cherenkov counter covers the region of $\pi/8(\phi) \times 0.7(\eta)$ in the west arm.

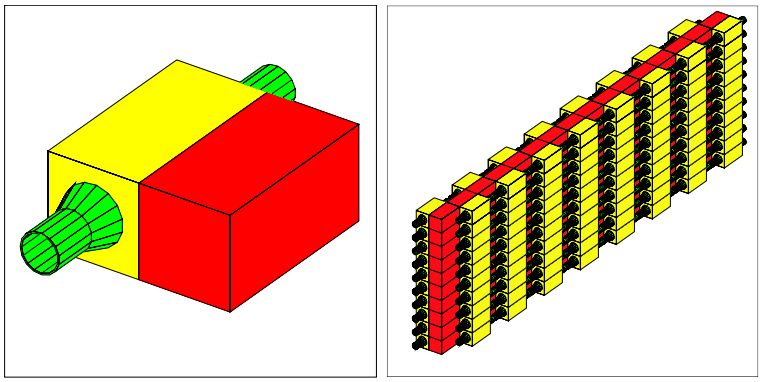

Figure 3.19: An aerogel cell with an aerogel radiator and two phototubes (left). Stack of aerogel cells (right).

Time Expansion Chambers

The time expansion chamber (TEC) is a transition radiation detector and gives information of charged particle tracking and electron identification by dE/dx and transition radiation information. The TEC covers $\pi/2$ in azimuth and ± 0.35 in η. One TEC sector has an active area of 3.1–3.5 m (z) $\times$ 1.7–1.9 m (ϕ) and consists of 6 individual chambers. Each chamber is build in two layers; a lower layer containing window support and radiator foils, and an upper layer containing the active elements of the wire chamber. The upper layer is filled with a Xe/CO_2 gas mixture and is composed of a Cu-mylar cathode window, 3 cm drift space, three wire planes (field, anode, field) oriented parallel to the z axis of the detector, and a final Cu-mylar cathode window.

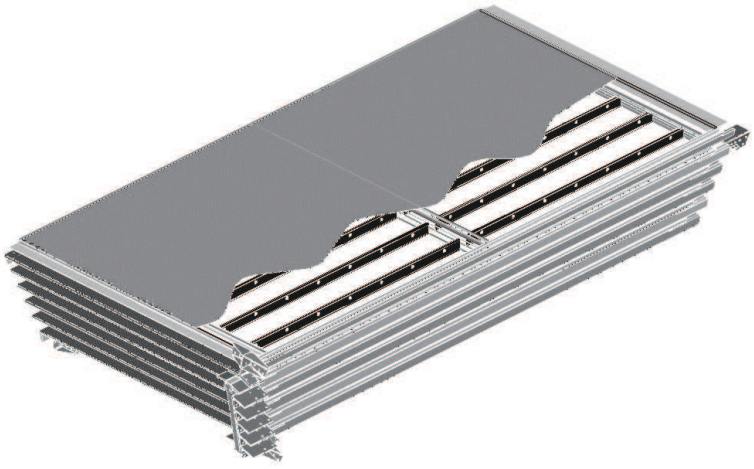

Figure 3.20: A TEC sector consisting of 6 chambers.

3.6 PHENIX Muon Arms

The PHENIX muon arms are built to detect muons at forward rapidities of $y = 1.2$–2.4 with full azimuthal acceptance [119]. Both North and South muon arm must have capability to track and identify muons and provide rejection of pions and kaons ($\sim 10^2$). In order to accomplish these requirement, we employ a radial field magnetic spectrometer with precision tracking (Muon Tracker) followed by a stack of absorber/low resolution tracking layers (Muon Identifier) is employed.

3.6.1 Muon Tracker

A Muon Tracker design consists of three stations of cathode strip readout tracking chambers filled with a gas mixture of $Ar/CO_2/CF_4$ (50%/30%/20%). They are mounted inside the conical shaped muon magnets, with multiple cathode strip orientations and readout planes in each station. Position resolution in cosmic ray tests was 130 μm and the relative mass resolution from the reconstruction of a muon pair is approximately given by $\sigma(M)/M = 9\%/\sqrt{M}$, where M is in GeV/c^2.

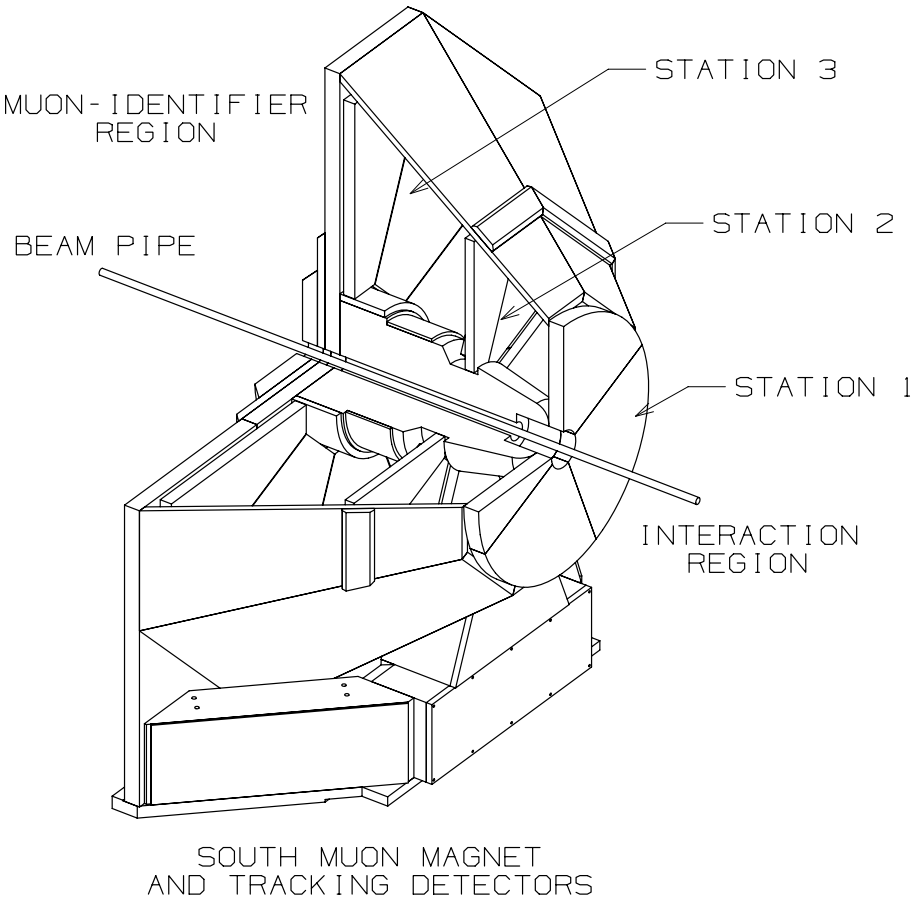

Figure 3.21: The south muon arm tracking spectrometer. Muons from the intersection region, to the right, intercept the station 1, 2 and 3 detectors and proceed to the muon identifier detectors to the left (not shown).

3.6.2 Muon Identifier

The muon identifier (MuID) consists of five layers of drift tubes and four layers of steel absorbers. A drift tube consists of eight 100-μm gold coated CuBe anode wires at the center of long channels of a graphite coated plastic cathode. A gas mixture of CO_2 (92%) and i-C_4H_{10} (8%) is filled in the tubes. Tubes with 9 mm$\times$9 mm channels satisfy the counter rate and localization requirements. Each wire is held at the center of its channel by means of plastic wire spacers positioned every 50 cm along the tube. A two-pack is a pair of tubes connected together and staggered by half a channel. Groups of two-packs oriented both horizontally and vertically are held inside an aluminum box so that both projections are measured. The tubes are operated in the proportional mode at 4500 V to increase longevity. The chosen segmentation of absorbers is four steel absorbers of thickness 10, 10, 20, 20 cm after the 30 cm thick muon magnet backplate.

3.7 Trigger

The Level-1 trigger (LVL1) is responsible to select interested events and provide sufficient rejection of uninterested events to reduce the data rate to a level which can be handled by the PHENIX data acquisition system [120]. The LVL1 trigger is a parallel, pipelined and deadtimeless system.

The trigger system consists of two separate subsystems. One is the Local Level-1 (LL1) system and the other is the Global Level-1 (GL1) system. LL1 system communicates directly with participating detectors such as BBC, EMCal and RICH. The input data from these detectors is processed by the following LL1 algorithms to produce a set of reduced-bit input data for each RHIC beam crossing.

BBC LL1 trigger (BBCLL1) is an event trigger to record collision data. The timing information of BBC is used to select events which occur in beam crossings and within nominal interaction region ($|z| < 50$ cm). The digitized timing information of both north and south BBC is sent to the BBCLL1 module which makes trigger decision.

EMCal-RICH LL1 trigger (ERTLL1) is used as the electron and photon triggers. For the photon trigger, only the EMCal information is used. Acceptance coverage of each of the EMCal and RICH is divided into 16 trigger segments. Each segment consists of 9(PbSc)/16(PbGl, RICH) trigger tiles. Each trigger tile consists of 144 EMCal towers (20 RICH phototubes). EMCal has two different methods, 2$\times$2 tower sum and 4$\times$4 tower sum, to sum the energy of towers. The energy threshold value of EMCal for the hit definition can be changed. If there is a hit tile defined by 4$\times$4 sum (2$\times$2 sum) in the EMCal part, ERTLL1_4x4 (ERTLL1_2x2) is issued. These triggers are photon triggers. If there are an EMCal hit tile defined by 2$\times$2 sum and an associated RICH hit tile, an electron trigger, ERTLL1_E is issued. Association of EMCal and RICH tiles is performed using the look-up table in the ERTLL1 module.

The GL1 receives and combines the LL1 data to make a trigger decision. The GL1 also manages busy signals.

The PHENIX experiment defines BBCLL1 as the Minimum Bias (MB) trigger which is used for taking minimum bias events, and the studies of global variables, trigger efficiency etc.

3.8 Data Acquisition System

The PHENIX data acquisition (DAQ) system processes the signals from each detector subsystem, produces the trigger decision, and stores the triggered data [120]. The typical data logging rates of Cu+Cu and $p+p$ collisions were 3 kHz and 5 kHz in Run-5 (2005), respectively. The zero suppressed event sizes are 160 kbytes for Au+Au, 110 kbytes for Cu+Cu and 40 kbytes for $p+p$. The schematic of the data acquisition flow is shown in Fig. 3.22.

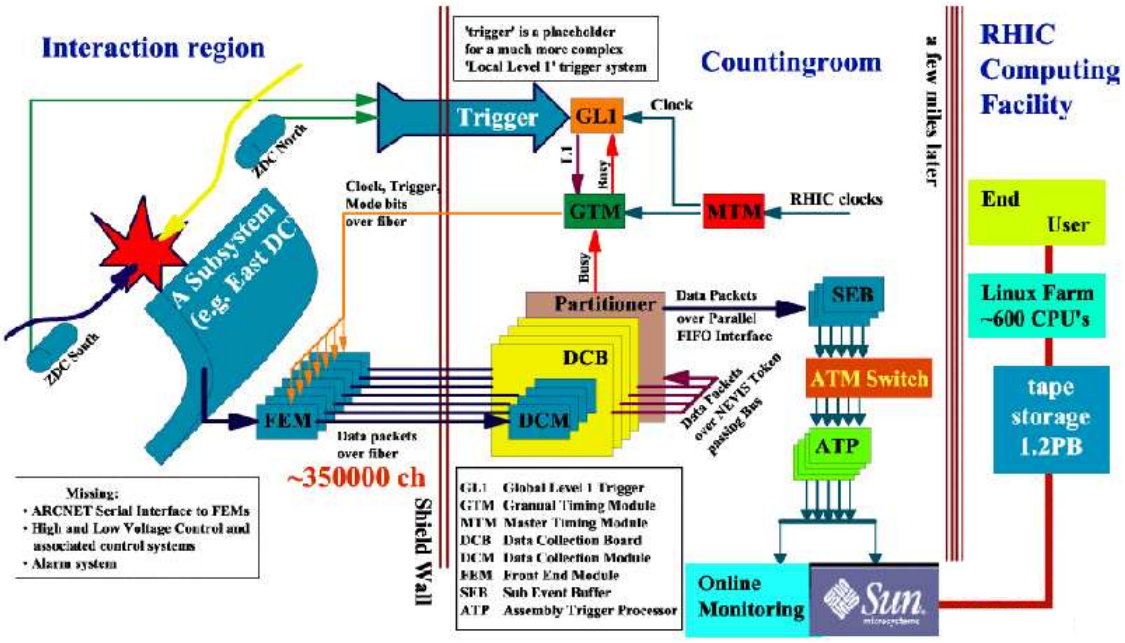

Figure 3.22: Schematic diagram of the data acquisition system.

Overall control of the DAQ is provided by the Master Timing Module (MTM), the Granule Timing Module (GTM), and the GL1. The MTM receives 9.4 MHz RHIC clock and delivers it to the GTM and GL1. The GTM delivers the clock, the control commands (Mode Bits), event accept signal to the Front End Modules (FEMs) of each detector. The GTM equips a fine delay tuning of the clock with ∼50 ps step, in order to compensate the timing difference among the FEMs. The GL1 produces the first LVL1 trigger decision, combining LVL1 signals from detector components.

The FEM of each detector is designed to convert the analog response of the detectors into the digitized signal. The LVL1 trigger signals are simultaneously generated. The generation of global decision, whether an event should be taken or not, takes ∼30 bunch crossings. While the GL1 system is making decision, the event data is stored in the FEM. After receiving the accept signal, each FEM starts to digitize the data.

The data collection from each FEM is performed by a Data Collection Module (DCM) via an optical fiber cable. The DCMs provide data buffering, zero suppression,

error checking and data formatting. The DCMs send the compressed data to Event Builder (EvB).

The EvB is the system which consists of 39 Sub Event Buffers (SEBs), Asynchronous Transfer Mode (ATM) switch and 52 Assembly Trigger Processors (ATPs). The SEBs are the front end of the EvB and communicate with each granule. The SEBs transfer the data from granule to the ATP via the ATM, where event assembly is performed. The combined data is stored to the disk with the maximum logging rate of 400 Mbytes/s and is used for online monitoring.

Chapter 4

Experiment

This analysis is based on the data collected with the PHENIX experiment during RHIC Run-5 (in 2005) and Run-6 (in 2006). The analyses of J/ψ and χ_c use the data in Cu+Cu collisions at $\sqrt{s_{NN}}$ =200 GeV and the data in p+p collisions at $\sqrt{s}$ = 200 GeV, respectively. The beam and trigger conditions are described briefly in this chapter.

4.1 Collisions of Cu+Cu at $\sqrt{s_{NN}} = 200$ GeV in 2005

During the heavy ion run period in the RHIC Run-5 (January 18, 2005–March 6, 2005), Cu+Cu collisions at $\sqrt{s_{NN}} = 200$ GeV were collected with the PHENIX detector. The peak luminosity was 2×10^{28} cm^{-2}s^{-1}. The delivered integrated luminosity is shown in Fig. 4.1 as a function of date and the recorded integrated luminosity is 3.1 nb^{-1}. The cross section of inelastic Cu+Cu collisions is $\sigma_{\mathrm{Cu+Cu}}$=2.9 b.

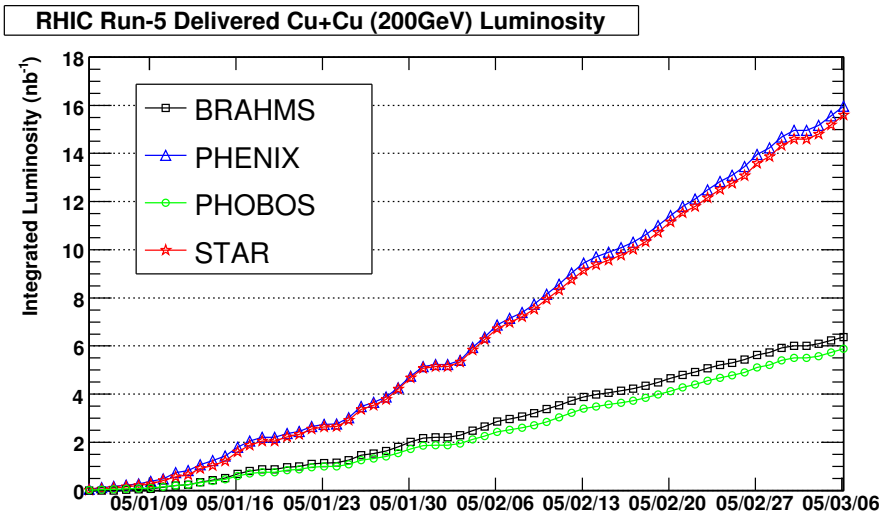

Figure 4.1: The delivered integrated luminosity of Cu+Cu at $\sqrt{s_{NN}}$ = 200 GeV in RHIC Run-5 as a function of the date.

The data was taken with the "Minimum Bias (MB)" trigger and the "ERT electron" trigger. The trigger logic of the MB and ERT electron triggers for the Cu+Cu collisions

are defined as:

$$\text{Minimum Bias} \equiv \text{BBCLL1}(>0\text{tubes}), \quad (4.1)$$

$$\text{ERT electron} \equiv \text{ERTLL1\_E} \cap \text{BBCLL1}(>0\text{tubes}), \quad (4.2)$$

where BBCLL1(>0 tubes) means that at least one hit is required in each BBC and the vertex position obtained by BBCLL1 online in z direction, z_{BBCLL1}, required to be less than 37.5 cm. ERTLL1_E denotes the coincidence of a EMCal hit with energy deposit above the ERTLL1_2x2 threshold and a RICH hit of ≥ 3 photoelectrons.

Table 4.1 shows the configurations of detector; magnet polarity, existence of a photon converter and the ERTLL1_2x2 energy threshold. The photon converter is made of brass with thickness of 1.7% of radiation length and is used for the study of semi-leptonic decays of heavy quarks [47, 152]. Based on the configurations, the entire Cu+Cu runs are divided in to four run groups, G0–G3.

Run group	Run number	Magnet polarity	Converter	ERTLL1_2x2 energy threshold
G0	149539–155706	CM++	Without	1.1GeV
G1	155920–155931	CM−−	Without	1.1GeV
G2	156307–157324	CM−−	With	1.1GeV
G3	157419–160487	CM−−	Without	0.8GeV

Table 4.1: The configurations in the Run-5 Cu+Cu 200 GeV period.

The collision vertex along the beam axis (z direction) is determined by the BBC information in the offline analysis and the determined position is called BbcZvertex. The BbcZvertex distribution in Cu+Cu collisions at $\sqrt{s_{NN}} = 200$ GeV is shown in Fig. 4.2.

4.2 Collisions of $p+p$ at $\sqrt{s} = 200$ GeV in 2005 and 2006

During the polarized proton run period in the RHIC Run-5 (April 16, 2005–June 24, 2005) and the RHIC Run-6 (March 4, 2006–June 5, 2006), $p+p$ collisions at $\sqrt{s} =$ 200 GeV were collected with the PHENIX detector. The mode of 111 bunch was used and there were 1.35×10^{11} protons in each bunch. The peak luminosity was 3.5×10^{31} cm^{-2}s^{-1}. The delivered integrated luminosities of $p+p$ collisions in Run-5 and Run-6 are shown as a function of date in Fig. 4.3 and Fig. 4.4, respectively. The recorded integrated luminosities are 3.8 pb^{-1} (Run-5) and 10.7 pb^{-1} (Run-6).

The definitions of the MB and ERT electron triggers for $p+p$ collisions are the same as ones for Cu+Cu collisions (Eqs. (4.1) and (4.2)). The following photon triggers were also used.

$$\text{ERT photon(i)} \equiv \text{ERTLL1\_4x4i} \cap \text{BBCLL1}(>0\text{tubes}) \ \ (\text{i} = \text{a}, \text{b}, \text{c}), \quad (4.3)$$

where 4x4a, 4x4b and 4x4c mean different energy thresholds for 4x4 tower sum. The threshold values of these ERTLL1_4x4 triggers were 2.1 GeV (4x4a), 2.8 GeV (4x4b)

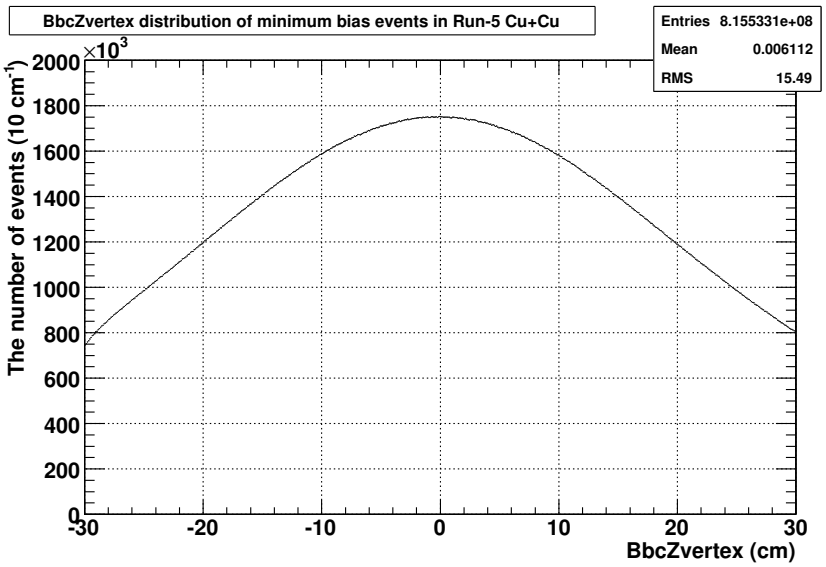

Figure 4.2: The distribution of BbcZvertex in the minimum bias Cu+Cu events at $\sqrt{s_{NN}}=200$ GeV in Run-5. An online vertex cut of $|z_{\mathrm{BBCLL1}}|<37.5$ cm and an offline vertex cut of $|\mathrm{BbcZvertex}|<30$ cm is applied.

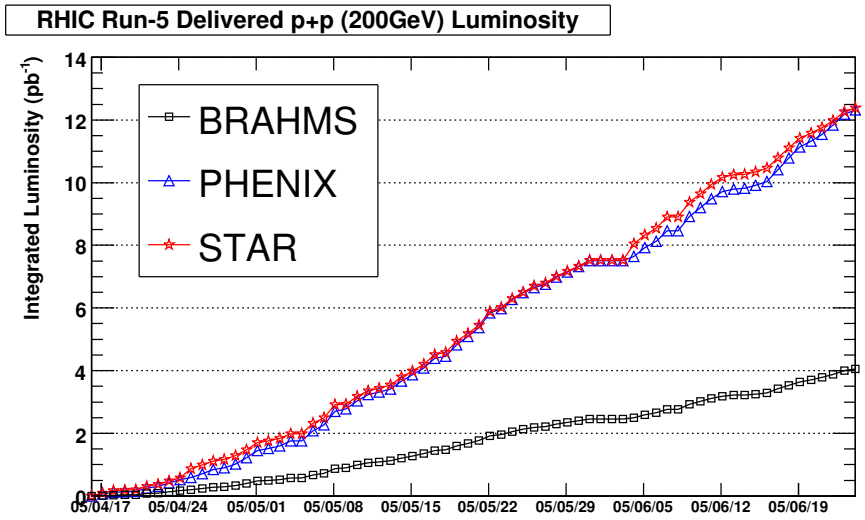

Figure 4.3: The delivered integrated luminosity of $p+p$ collisions at $\sqrt{s}=200$ GeV in RHIC Run-5 as a function of the date.

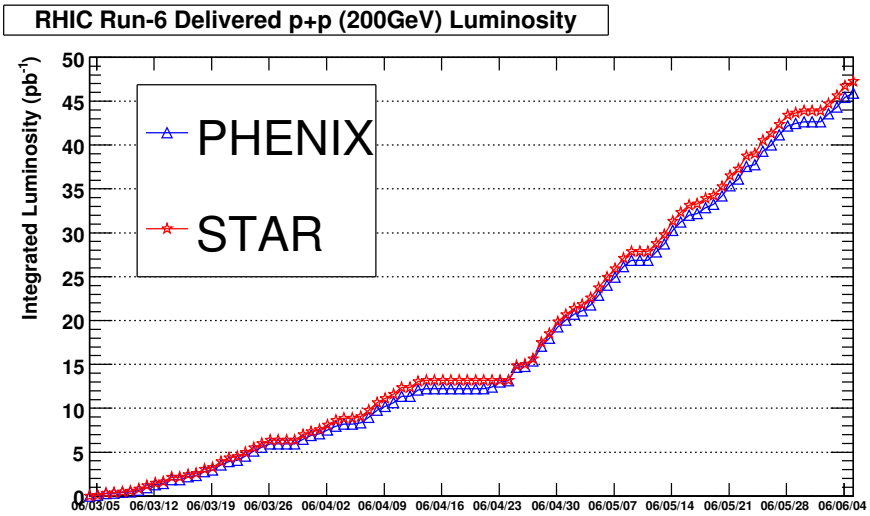

Figure 4.4: The delivered integrated luminosity of $p+p$ collisions at $\sqrt{s} = 200$ GeV in RHIC Run-6 as a function of the date.

Run	Polarization	Run number	Magnet polarity	ERTLL1_2x2 energy threshold
Run-5	Longitudinal	166030–179846	CM−−	0.4 GeV
Run-6	Transverse	188216–197795	CM++	0.4 GeV
	Longitudinal	198061–199767	CM++	0.4 GeV
	Longitudinal	200240–204639	CM++	0.6 GeV

Table 4.2: The beam polarizations, run numbers and the ERTLL1_2x2 energy threshold in the Run-5 and Run-6 $p+p$ 200 GeV periods.

and 1.4 GeV (4x4c) during Run-5 and Run-6 $p+p$ 200 GeV periods. The threshold value of ERTLL1_2x2 trigger is shown in Table 4.2.

The BbcZvertex distribution in $p+p$ collisions at $\sqrt{s}=200$ GeV is shown in Fig. 4.5.

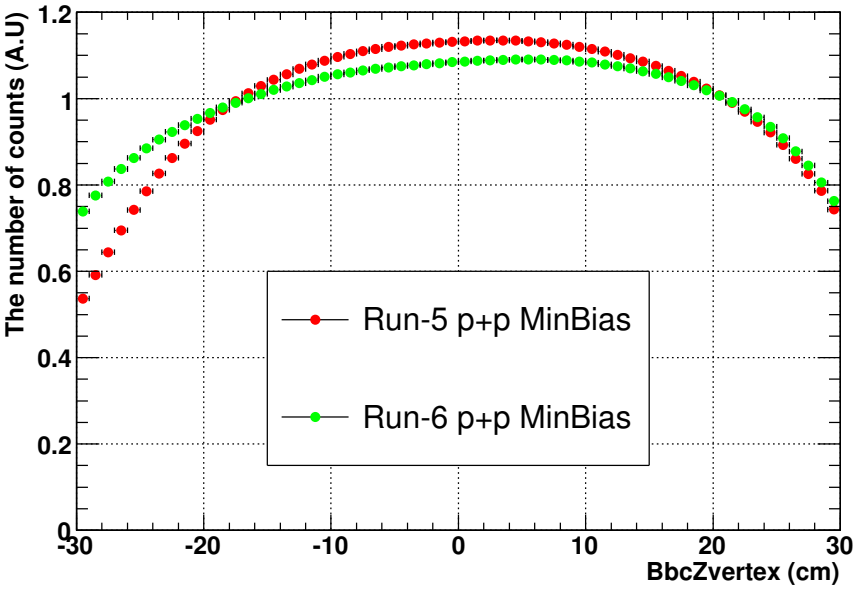

Figure 4.5: The distribution of BbcZvertex in the minimum bias data of Run-5 $p+p$ (red) and Run-6 $p+p$ (green).

Chapter 5

Data Analysis 1 - J/ψ Meson in Cu+Cu Collisions

The invariant yield of J/ψ in Cu+Cu collisions at $\sqrt{s_{NN}} = 200$ GeV has been measured. In this chapter, the analysis of J/ψ in Cu+Cu collisions will be described. In section 5.1, the procedure of yield extraction is introduced. Section 5.2 describes the method of event classification. Track reconstruction and momentum determination are described in section 5.3 and electron identification is described in section 5.4. The used fiducial cut is explained in section 5.5. In section 5.6, the run selection is described. The signal extraction of J/ψ is described in section 5.7. Correction factors and systematic errors are evaluated in section 5.8 and section 5.9, respectively.

5.1 Invariant Yield and Nuclear Modification Factor

The J/ψ particle in the e^+e^- decay mode (branching ratio, BR =5.94±0.06% [19]) is identified as a prominent peak in the invariant mass spectrum of the e^+e^- pair, $M_{e^+e^-}$, calculated with the following equation,

$$M_{e^+e^-} = \sqrt{(E_{e^+} + E_{e^-})^2 - (\vec{p}_{e^+} + \vec{p}_{e^-})^2}, \tag{5.1}$$

where E_{e^+} and E_{e^-} are the total energies, and $\vec{p}_{e^+}$ and $\vec{p}_{e^-}$ are the momenta of the positron and electron, respectively.

The invariant cross section of J/ψ with the momentum p is expressed in terms of the rapidity y and momentum $p_T(=\sqrt{p_x^2 + p_y^2})$ transverse to the beam direction:

$$E\frac{d^3\sigma_{J/\psi}}{dp^3} = \frac{d^3\sigma_{J/\psi}}{d\phi dy p_T dp_T} = \frac{1}{2\pi p_T}\frac{d^2\sigma_{J/\psi}}{dp_T dy}, \tag{5.2}$$

where E and ϕ are the total energy and azimuthal angle of J/ψ, respectively.

The invariant cross section of J/ψ via the e^+e^- decay mode can be extracted experimentally as follows:

$$\frac{BR}{2\pi p_T}\frac{d^2\sigma_{J/\psi}}{dp_T dy} = \frac{1}{2\pi p_T}\frac{n_{J/\psi}(p_T)}{\int L dt \varepsilon(p_T)\Delta p_T \Delta y}, \tag{5.3}$$

where $n_{J/\psi}$ is the number of reconstructed J/ψ via the e^+e^- decay mode, ε is the overall efficiency including acceptance, Δy is the rapidity bin width and is set to $\Delta y = 1$, Δp_T is the p_T bin width and $\int Ldt$ is the integrated luminosity.

The integrated luminosity can be expressed using the number of minimum bias (MB) triggered events, $N_{\rm MB}$,

$$\int Ldt = \frac{N_{\rm MB}}{\sigma_{A+A}\varepsilon_{\rm MB}^{A+A}} = \frac{N_{\rm MB}}{\langle N_{coll}^{\rm MB}\rangle \sigma_{p+p}\varepsilon_{\rm MB}^{A+A}}, \tag{5.4}$$

where σ_{A+A} and σ_{p+p} are the cross sections of inelastic $A+A$ and $p+p$ collisions, $\varepsilon_{\rm MB}^{A+A}$ and $\langle N_{coll}^{\rm MB}\rangle$ are the MB trigger efficiency and the number of binary collisions for MB $A+A$ collisions, respectively. The cross section of inelastic $p+p$ collisions triggered by the MB trigger is $\sigma_{p+p} \times \varepsilon_{\rm MB}^{p+p}$=23.0 $\pm$ 2.2 mb [121]. Estimation of $\varepsilon_{\rm MB}^{A+A}$ and $\langle N_{coll}\rangle$ for Cu+Cu collisions is described in section 5.2.

The invariant yield is defined as follows:

$$\frac{BR}{2\pi p_T}\frac{d^2N_{J/\psi}}{dp_T dy} = \frac{1}{2\pi p_T}\frac{n_{J/\psi}(p_T)}{N_{\rm MB}\Delta p_T \Delta y \varepsilon(p_T)}, \tag{5.5}$$

$$= \frac{1}{\sigma_{A+A}\varepsilon_{\rm MB}^{A+A}} \times \frac{BR}{2\pi p_T}\frac{d^2\sigma_{J/\psi}}{dp_T dy}. \tag{5.6}$$

The integrated J/ψ yield is calculated as follows:

$$BR\frac{dN_{J/\psi}}{dy} = BR\sum_{p_T}\frac{d^2N_{J/\psi}}{dp_T dy}\Delta p_T. \tag{5.7}$$

The nuclear modification factor, R_{AA}, is used to quantify the difference between the superposition of nucleon-nucleon collisions and a nucleus-nucleus collisions. The definition of R_{AA} is as follows:

$$R_{AA}(p_T) = \frac{BR\frac{d^2N_{J/\psi}^{A+A}}{dp_T dy}}{BR\frac{d^2\sigma_{J/\psi}^{p+p}}{dp_T dy} \times T_{AA}} = \frac{BR\frac{d^2N_{J/\psi}^{A+A}}{dp_T dy}}{\langle N_{coll}\rangle BR\frac{d^2N_{J/\psi}^{p+p}}{dp_T dy}}, \tag{5.8}$$

$$R_{AA} = \frac{BR\frac{dN_{J/\psi}^{A+A}}{dy}}{BR\frac{d\sigma_{J/\psi}^{p+p}}{dy} \times T_{AA}} = \frac{BR\frac{dN_{J/\psi}^{A+A}}{dy}}{\langle N_{coll}\rangle BR\frac{dN_{J/\psi}^{p+p}}{dy}}, \tag{5.9}$$

$$T_{AA} = \frac{\langle N_{coll}\rangle}{\sigma_{p+p}}, \tag{5.10}$$

where T_{AA} is called as a nuclear overlap function.

The nuclear modification factor R_{AA} is the ratio of the J/ψ yield in $A+A$ collisions to the J/ψ yield in $p+p$ collisions scaled by the average number of binary collisions. If there is no medium effect on the J/ψ production in $A+A$ collisions, the J/ψ production in $A+A$ collisions will be described by the superposition of independent nucleon-nucleon collisions and R_{AA} will be unity.

5.2 Event Classification

In this section, the event classification method in PHENIX is described. Geometrical parameters, the impact parameter of two colliding nuclei, the number of participant nucleons and the number of binary nucleon-nucleon collisions, characterize the collision. These parameters are calculated with the Glauber model, which is described in subsection 2.2.1. Determination of the MB trigger efficiency for Cu+Cu collision is also described in this section.

5.2.1 Determination of Minimum Bias Trigger Efficiency

The efficiency of inelastic Cu+Cu collisions by the MB trigger, $\varepsilon_{\rm MB}^{\rm Cu+Cu}$, was estimated by the full detector simulation with event generators [122] and the BBC charge distribution of the real data using the negative binomial distribution with the assumption of N_{part} scaling of the BBC hit distribution [123]. Detector simulation was performed using the GEANT3 simulator [124] of the PHENIX detector, PISA, and two event generators, HIJING [125] and JAM [126], were used. The values of obtained efficiency by the three methods are as follows:

- HIJING and PISA : $\varepsilon_{\rm MB}^{\rm Cu+Cu} = 92.7 \pm 1.8$ (stat)%
- JAM and PISA : $\varepsilon_{\rm MB}^{\rm Cu+Cu} = 94.2 \pm 1.5$ (stat)%
- Negative binomial distribution of the BBC hits : $\varepsilon_{\rm MB}^{\rm Cu+Cu} = 94.6 \pm 0.3$ (stat)%

Based on these three calculations, the efficiency of inelastic Cu+Cu collisions by the MB trigger is estimated to be $\varepsilon_{\rm MB}^{\rm Cu+Cu} = 94 \pm 2$ (syst)%.

5.2.2 Centrality Determination

Collision centrality of each event in Cu+Cu collisions is determined from the charge measured by the BBC. Figure 5.1 shows the distribution of the BBC total charge. The amount of total charge of the BBC is proportional to the particle multiplicity. The particle multiplicity is correlated to the overlapping area of two colliding nuclei. Thus, the BBC total charge has negative correlation with the impact parameter of the collision. The centrality class of an event is determined by the BBC charge; the events have the maximum BBC charge and the minimum BBC charge are assigned to centrality of 0% (smallest impact parameter) and 94% (largest impact paramter), respectively, as shown in Fig. 5.1. Intermediate region is sliced with a binning of 10%, that is, 0–10%, 10–20%, 20–30%, $\cdots$, 70–80% and 80–90%. The most peripheral bin is 90–94%. Since the observed charge of BBC depends on the collision vertex position, BbcZvertex, the centrality determination was performed with a 5 cm binning of BbcZvertex, that is -40–-35 cm, -35–-30 cm, -30–-25 cm, $\cdots$, 30–35 cm and 35–40 cm. Figure 5.2 shows the Centrality percentile distribution in MB events with a |BbcZvertex < 30| cm. The non-flatness of the Centrality percentile distribution in Cu+Cu collisions at $\sqrt{s_{NN}} = 200$ GeV is less than 1%.

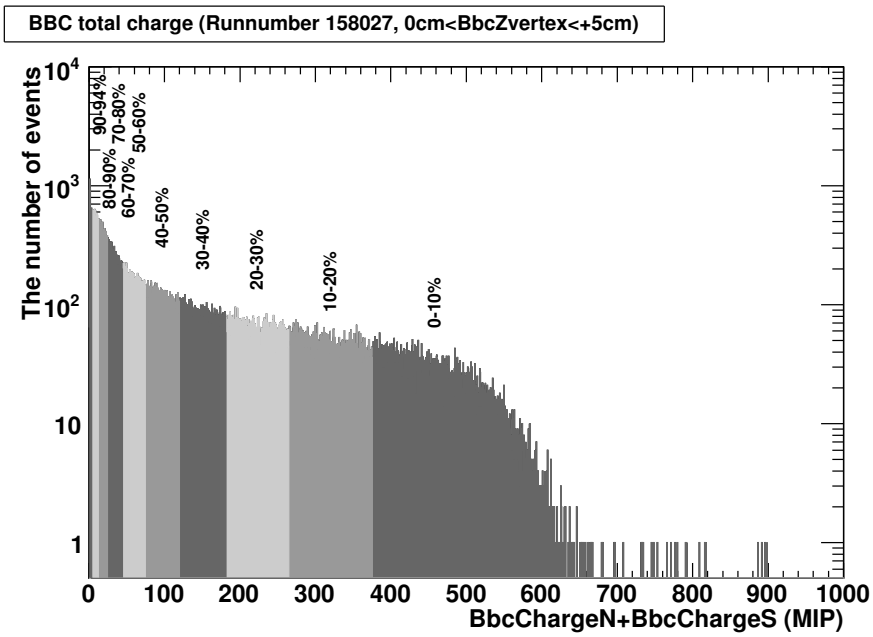

Figure 5.1: Distribution of the BBC total charge, (BbcChargeN + BbcChargeS), in minimum bias events of a run (run 158027) with a $0 <$ BbcZvertex < 5 cm cut.

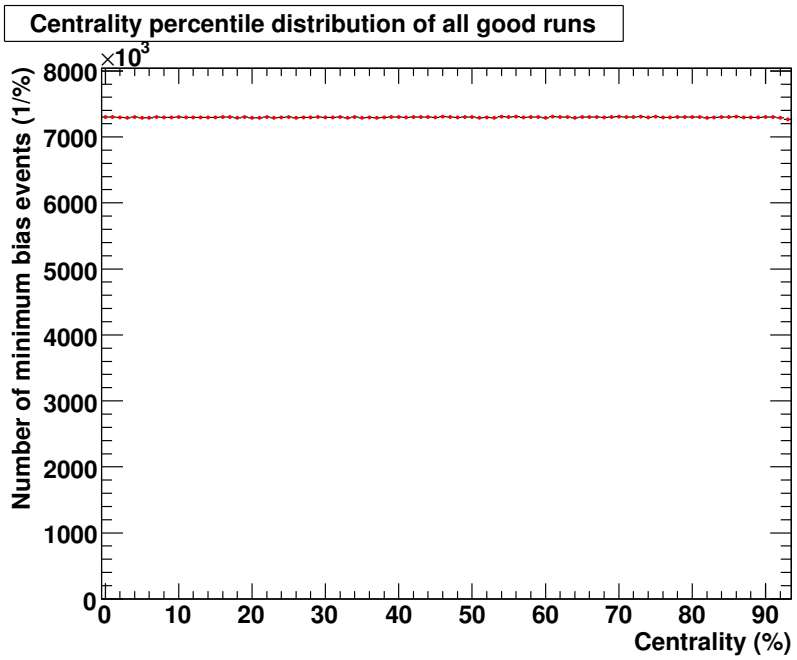

Figure 5.2: Centrality percentile distribution in minimum bias events of all good runs in Cu+Cu collisions at $\sqrt{s_{NN}} = 200$ GeV. The non-flatness of Centrality distribution is less than 1%.

5.2.3 Glauber Calculation

In the case of ^{63}Cu+^{63}Cu collisions, input parameters for Eqs. (2.18) and (2.19) are as follows [123, 127]:

- $R = 4.2 \pm 0.2$ fm
- $d = 0.60 \pm 0.03$ fm
- $\sigma_{NN} = 42 \pm 3$ mb
- $t(\mathbf{b})$: black disk nucleon-nucleon overlap function (1 if $|\mathbf{b}| \leq \sqrt{\sigma_{NN}/\pi}$, 0 otherwise)

The errors of R, d and σ_{NN} were used for the systematic error estimation.

Table 5.1 summarizes the average N_{part}, N_{coll}, $T_{\rm CuCu}$, b and those systematic errors for each Centrality class.

Centrality class (%)	$\langle N_{part} \rangle$	$\langle N_{coll} \rangle$	$T_{\rm CuCu}$ (mb^{-1})	$\langle b \rangle$ (fm)
0–10	98.2±2.4	182.7±20.7	4.35±0.40	2.4±0.1
10–20	73.6±2.5	121.1±13.6	2.88±0.26	4.0±0.2
20–30	53.0±1.9	76.1± 8.5	1.81±0.17	5.2±0.3
30–40	37.3±1.6	47.1± 5.3	1.12±0.11	6.2±0.3
40–50	25.4±1.3	28.1± 3.4	0.67±0.08	7.1±0.4
50–60	16.7±0.9	16.2± 1.9	0.39±0.04	7.8±0.4
60–70	10.4±0.6	9.0± 1.0	0.21±0.02	8.6±0.4
70–80	6.4±0.5	4.9± 0.6	0.12±0.02	9.3±0.5
80–94	3.6±0.3	2.4± 0.3	0.06±0.01	10.0±0.5

Table 5.1: N_{part}, N_{coll}, $T_{\rm CuCu}$ and b by Glauber calculation for Cu+Cu collisions at $\sqrt{s_{NN}} = 200$ GeV. Errors are systematic errors.

5.3 Track Reconstruction and Momentum Determination

The track reconstruction technique in the PHENIX central arm is described in Ref. [128] and is briefly presented in this section.

Figure 5.3 and Fig. 5.4 show schematic views of the trajectory of a charged particle traveling through the axial magnetic field in PHENIX in the x-y plane and the z-r plane, respectively. To determine the particle trajectory and momentum, the following variables are measured.

- α : The angle between the projection of the trajectory in the x-y plane and the radial direction at the DC reference radius of 220 cm.
- ϕ : The azimuthal angle of the intersection point at the DC reference radius of 220 cm.

- β : The polar angle of the intersection point at the DC reference radius of 220 cm.
- zed : The z coordinate of the intersection point at the DC reference radius of 220 cm.
- z_{vertex} : The interaction vertex position along the z axis.
- p_T : The transverse momentum.
- θ_0 : The polar angle of the initial direction.
- ϕ_0 : The azimuthal angle of the initial direction.

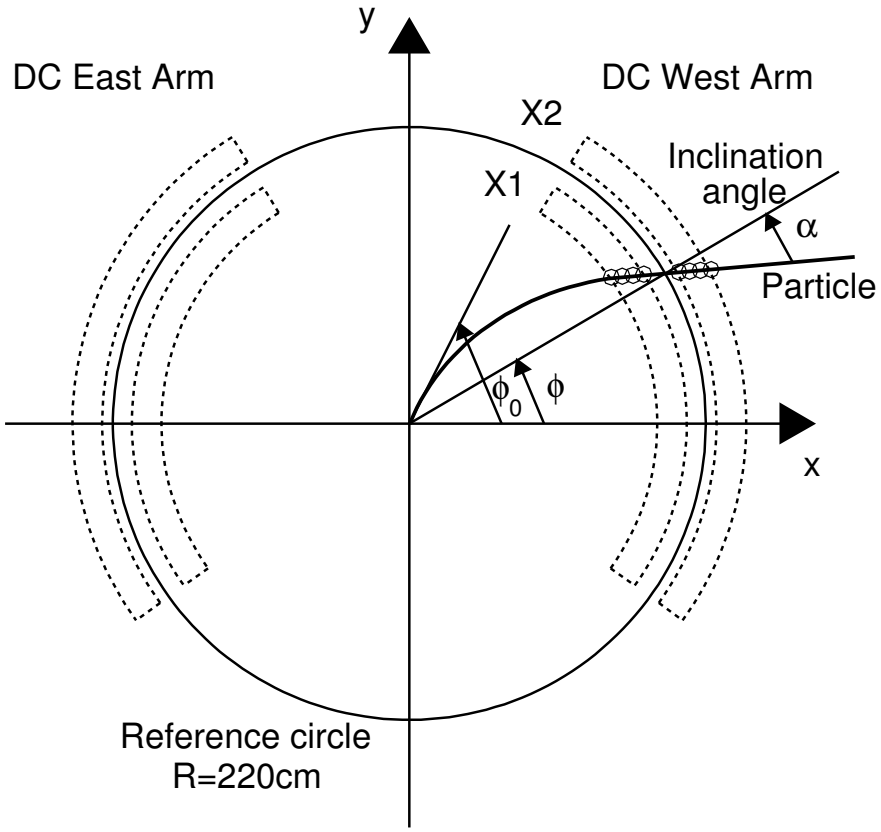

Figure 5.3: An illustration of the Hough transform parameters, ϕ_0, ϕ and α, for the drift chamber (DC) track reconstruction in the x-y plane. The outline shows the DC active volume. The small circles represent DC hits along the particle trajectory. (Not to scale)

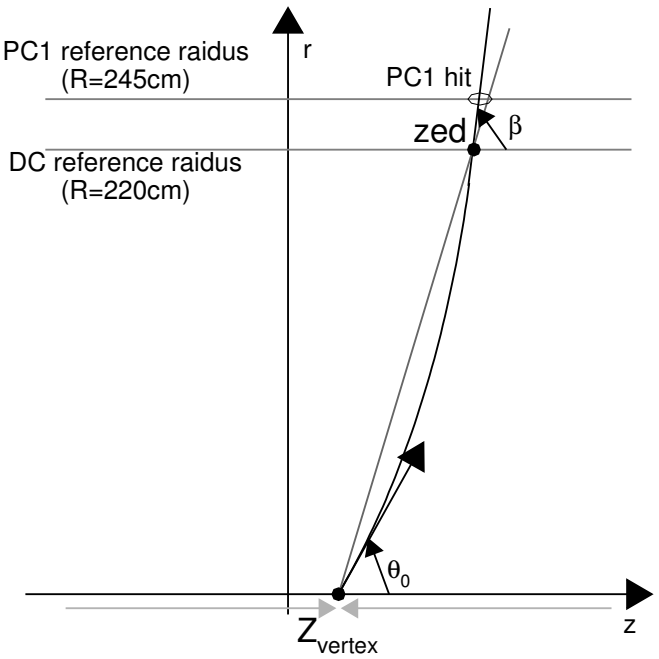

Figure 5.4: A schematic view of a track in the $r - z$ plane.

5.3.1 Track Reconstruction Technique

The trajectory of a particle is uniquely determined by the four variables, p_T, θ_0, ϕ_0 and z_{vertex}. These variables are reconstructed from the measured variables α, ϕ, *zed* and z_{vertex}.

The track reconstruction starts from finding the hits in X1 and X2 wires of the DC in the x-y plane. The angles of α and ϕ are determined from the X1 and/or X2 hit positions by the Hough transformation with the assumption that tracks are straight in the DC. The Hough transformation is a general algorithm for finding straight lines. Any pair of hits can be mapped to a point in the space defined by α and ϕ. All hit pairs from a given track have the same α and ϕ, and result in a local maximum in the feature space. Figure 5.5 shows the example of a part of the DC hits and the amplitude in the feature space from PISA simulation of a central Au+Au collision. The reconstructed track by the Hough transformation is associated with the X1 and X2 hits.

Then, the tracks are reconstructed in the z-r plane by combining the information of PC1 hits, UV-wire hits and collision vertex (z_{vertex}) measured by the BBC. The straight line of the track in the x-y plane is extended to the PC1. If there is an unambiguous associated PC1 hit within 2 cm in the x-y plane, the track vector in the z-r plane is fixed by the z-coordinate of the PC1 hit and z_{vertex}. The intersection points at the UV wires of the DC are calculated. If UV hits are within 5 cm from the track in the $r - z$ plane, the UV hits are associated.

Each reconstructed track is associated with hit information of outer detectors (PC2, PC3, EMCal and RICH). In the association with the outer detectors, the residual magnetic field is not taken into account and the track is assumed to be a straight line.

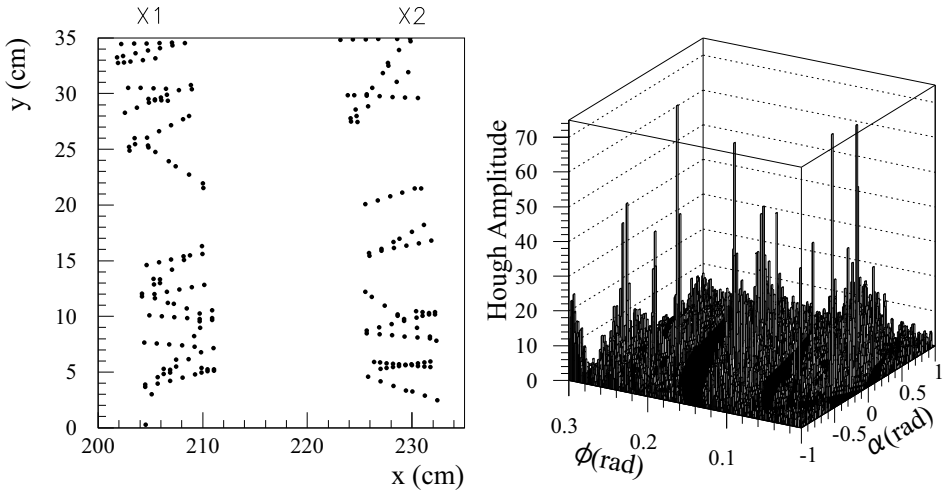

Figure 5.5: The Hough transformation of the DC hits in the $x-y$ plane to the feature space of α and ϕ. The left panel shows simulated hits from a central Au+Au collision for a small physical region of the drift chamber. The right panel shows the Hough transform feature space for this region. Tracks appear as peaks in this plot.

Track Quality

The quality of a reconstructed charged track is defined using hit information of X and UV wires in the DC and the associated PC1 hit. This information is implemented in the data as the 6-bit variable, quality, for each track. Table 5.2 is the definition of quality. The best case is quality == 63 and the second best case is quality == 31, wherein the PC1 hit is ambiguous, but the UV hit is unique.

	bit	decimal	description
LSB	0	1	X1 hit is used
	1	2	X2 hit is used
	2	4	UV hit is found
	3	8	UV hit is unique (No hit sharing)
	4	16	PC1 hit is found
MSB	5	32	PC1 hit is unique (No hit sharing)

Table 5.2: The bit definition of quality variable.

5.3.2 Momentum Determination

To determine the initial kinematic parameters of charged particles passing through the magnetic field, the technique of non-linear grid interpolation table is applied in PHENIX. The speed of the technique is faster than that of an analytical method.

The variables in the field-integral grid are z_{vertex}, θ_0, the total momentum of p and the radius r at which the field integral $f(p, r, \theta_0, z_{vertex})$ is calculated. The field integral

grid is generated by explicitly swimming particles through the measured magnetic field map and numerically integrating to obtain $f(p, r, \theta_0, z_{vertex})$ for each grid point.

The transverse momentum p_T (GeV/c) and the angle α (rad) have the following relation:

$$p_T \simeq \frac{K}{\alpha}, \tag{5.11}$$

where $K \simeq 0.10$ rad GeV/c is the effective field integral in the central arm expressed as:

$$K = \frac{e}{R}\int lBdl, \tag{5.12}$$

where, e is the elementary charge in the hybrid unit (e=0.2998 GeV/c T^{-1}m^{-1}) and R is the DC reference radius (R=220 cm).

An iterative procedure is used to determine the initial kinematic parameters of the reconstructed tracks with the initial assumption of Eq. (5.11). The momentum resolution is about 1% for tracks with p_T=1 GeV/c.

5.3.3 Nano Data Summary Tape (nDST)

The information of the reconstructed track and the associated hits of the detectors are recorded in the Nano Data Summary Tape (nDST). Parameters which characterize events, such as the collision vertex and centrality, are also recorded in the nDST. The average data size of the nDST, which contains charged tracks in the central arm and associated hit information, of a MB Cu+Cu collision event is 8 kbytes.

In this thesis, the variables in the nDST are written in Sans serif font. The momentum of a track is calculated from the total momentum mom, initial polar angle the0 and initial azimuthal angle phi0:

$$p_z = \mathsf{mom} \cdot \cos(\mathsf{the0}), \tag{5.13}$$
$$p_T = \mathsf{mom} \cdot \sin(\mathsf{the0}), \tag{5.14}$$
$$p_x = p_T \cdot \cos(\mathsf{phi0}), \tag{5.15}$$
$$p_y = p_T \cdot \sin(\mathsf{phi0}). \tag{5.16}$$

5.4 Electron Identification

Electron identification is performed by RICH and EMCal and is described in this section. Table 5.3 is the summary of the variables used in the electron identification and describes those specifications.

5.4.1 Electron Identification with RICH

After the track reconstruction by the DC and PC1 (DC-PC1 track), the tracks are associated with the PC2, PC3 and EMCal. Track association with RICH is performed with the hit information of the PC1 and PC2 (PC1-PC2 track) in the west arm and the PC1 and PC3 (PC1-PC3 track) in the east arm. If any associated hit is not found

Variables	Description
RICH	
n0	The number of fired phototubes in the nominal ring area ($3.8 \leq r \leq 8.0$ (cm))
n1	The number of fired phototubes in the larger disk ($r \leq 11.0$ (cm))
npe0	The number of photo-electrons detected in the nominal ring area
npe1	The number of photo-electrons detected in the larger disk
disp	Displacement between the projection point on the RICH phototube plane and the centroid of the associated fired phototubes
chi2	Ring shape parameter
EMCal	
ecore	The EMCal shower core energy (GeV)
dep	The normalized energy and momentum matching parameter (ecore/mom $-$ $\langle$ecore/mom$\rangle$)/σ(ecore/mom)
emcsdphi_e	The difference between the track projection and the EMCal cluster position in the ϕ direction at the EMCal surface normalized to σ
emcsdz_e	The difference between the track model projection and the EMCal cluster position in the z direction at the EMCal surface normalized to σ

Table 5.3: Summary of the variables for electron identification.

in the PC2 and PC3, the hit position of the outer detectors (the PC3/EMCal for the west arm and EMCal for the east arm) or projection points of the DC-PC1 track are used for the association with RICH. The tracks are reflected with respect to the RICH mirror and the reflected tracks are projected onto the RICH phototube plane. Then, fired phototubes around the projection points of the reflected tracks are associated with the tracks. Figure 5.6 shows a schematic view of the definition of variables used for RICH variables.

The parameter r^i_{cor} is the distance between the center of the phototube i and the track projection. The definitions of n0 and n1 are as follows:

$$\mathsf{n0} = \text{the number of fired phototubes of } 3.4 \leq r^i_{cor} \leq 8.4 \text{ cm}, \quad (5.17)$$

$$\mathsf{n1} = \text{the number of fired phototubes of } r^i_{cor} \leq 11.0 \text{ cm}, \quad (5.18)$$

where the fired phototube in RICH is defined to have greater than 0.2 photo-electron. For the association with RICH, n1 $\geq$ 2 is required. The variables nep0 and npe1 are the summation of the number of photo-electrons, $N_{p.e.}(i)$, of fired phototubes of $3.4 \leq r^i_{cor} \leq 8.4$ cm and $r^i_{cor} \leq 11.0$ cm, respectively.

$$\mathsf{npe0} = \sum_{3.4 \leq r^i_{cor} \leq 8.4 \text{ cm}} N_{p.e.}(i), \quad (5.19)$$

$$\mathsf{npe1} = \sum_{r^i_{cor} \leq 11.0 \text{ cm}} N_{p.e.}(i). \quad (5.20)$$

The position of the ring center, $\vec{R}_{center}$, is calculated from the weighted average of

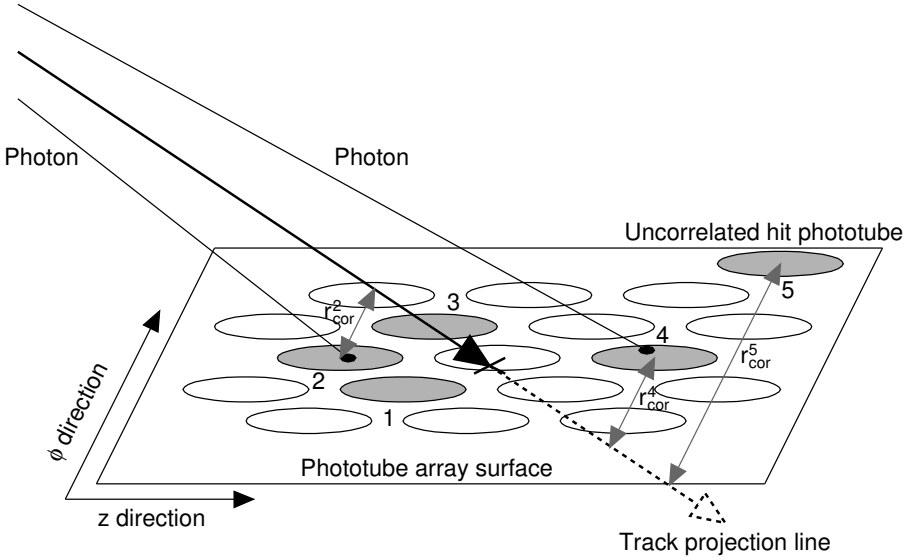

Figure 5.6: A schematic view of the definition of variables characterizing a RICH ring. A track projection, five associated fired phototubes and one correlated fired phototube are shown as an example. The distances between the center of the fired phototubes 2, 4 and 5, and the track projection vector are represented as r^2_{cor}, r^4_{cor} and r^5_{cor}, respectively.

the positions of fired phototubes, $\vec{R}_i$, where the weights are taken to be $N_{p.e.}(i)$,

$$\vec{R}_{center} = \frac{\sum_{3.4 \leq r^i_{cor} \leq 8.4 \text{ cm}} N_{p.e.}(i) \cdot \vec{R}_i}{\mathsf{npe0}}. \tag{5.21}$$

The distance between $\vec{R}_{center}$ and the track projection line is defined as the variable disp. The variable chi2 is the weighted average of the deviation of the fired phototube from the ideal ring radius, r_0=5.9 cm. The weight is the number of photo-electrons in each phototube.

$$\mathsf{chi2} = \frac{\sum_{r^i_{cor} \leq 11.0 \text{ cm}} N_{p.e.}(i) \cdot (r^i_{cor} - r_0)^2}{\mathsf{npe1}}. \tag{5.22}$$

Accidental Association with RICH

To estimate the background due to the accidental association of charged hadron tracks to the fired phototubes, the track projection point $\vec{R}_0 = (x_0, y_0, z_0)$ is flipped in the z direction and the z-swapped point $\vec{R}_0^{z-swap} = (x_0, y_0, -z_0)$ is defined. The associated fired phototubes are searched around the z-swapped point $\vec{R}_0^{z-swap}$. The variables of sn0, sn1, snpe0, snpe1, sdisp and schi2 of $\vec{R}_0^{z-swap}$ correspond to the n0, n1, npe0, npe1, disp and chi2 of $\vec{R}_0$, respectively. The subtraction of electron candidates with the swapped variables from electron candidates with the normal (non-swapped) variables gives the net electron candidates without accidental association.

Figure 5.7 shows the distribution of the RICH variables, n0, n1, npe0, npe1, disp and chi2/npe1, in MB Cu+Cu collisions at $\sqrt{s_{NN}} = 200$ GeV. The raw distribution, z-swapped distribution and net (subtracted) distribution are shown as solid and dashed lines, and shaded histograms, respectively. These tracks are selected with the following cut parameters:

- $p_T > 0.2$ GeV/c
- mom < 5 GeV/c
- quality $== 63$
- n1 ≥ 2 || sn1 ≥ 2

RICH Calibration

Gain calibration of RICH phototubes and alignment of RICH mirrors are important for the electron identification.

Gain calibration was performed for each phototube by fitting of the raw ADC spectrum. Gaussian functions were used to fit to the pedestal peak and the one photo-electron peak, and those peak positions ($ADC_{pedestal}$ and $ADC_{1p.e.}$) were obtained. Using these values, the number of photo-electrons ($N_{p.e.}$) of the phototube is calculated from its ADC value (ADC) as follows:

$$N_{p.e.} = \frac{ADC - ADC_{pedestal}}{ADC_{1p.e.} - ADC_{pedestal}}. \tag{5.23}$$

Figure 5.8 shows the distribution of the number of photo-electrons for a phototube after the gain calibration.

The spherical mirrors reflect Cherenkov photons to the phototubes in RICH, as shown in Fig. 3.15. There are 24 mirrors per arm per side, and the total of 96 (=24 $\times$ 2 $\times$ 2) mirrors are used. The alignment of 96 mirrors was done with electron candidates selected with the following conditions:

- n0 ≥ 3
- $0.5 <$ mom < 5 GeV/c
- $0.7 <$ ecore/mom < 1.3
- |pc3sdphi| < 2
- |pc3sdz| < 2

where pc3sdz and pc3sdphi mean the normalized matching variables between the hit cluster centroid and projected point of the track in the z and ϕ directions in PC3, respectively.

The straight line between the associated cluster potions of PC1 and PC3 is used as the particle trajectory. The trajectory is reflected with respect to the RICH mirror

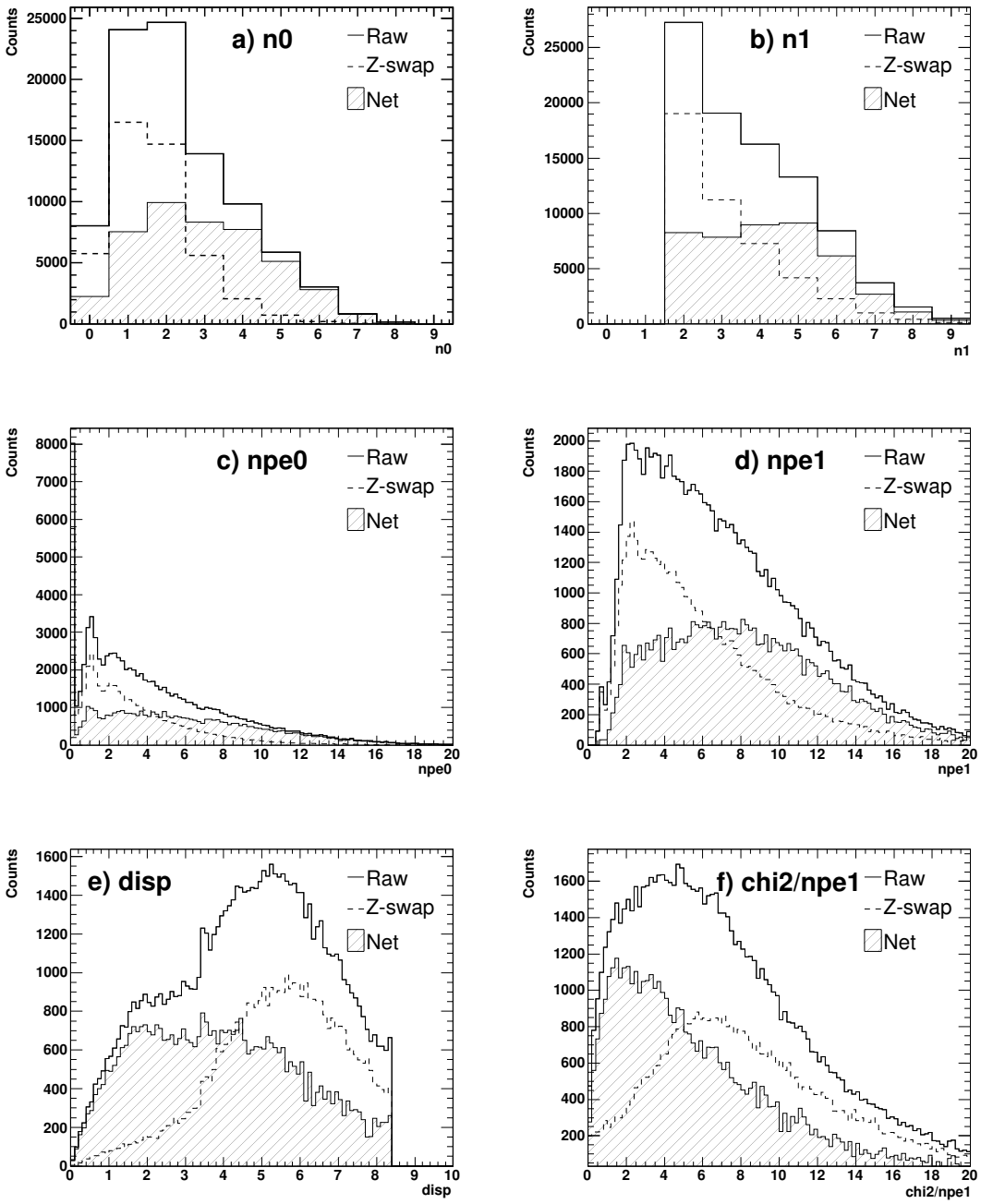

Figure 5.7: Distribution of RICH variables in MB Cu+Cu collisions at $\sqrt{s_{NN}}$ = 200 GeV. a), b), c), d), e) and f) show n0, n1, npe0, npe1, disp and chi2/npe1, respectively. The raw distribution, z-swapped distribution and net (subtracted) distribution are shown as solid, dashed lines and shaded histograms, respectively.

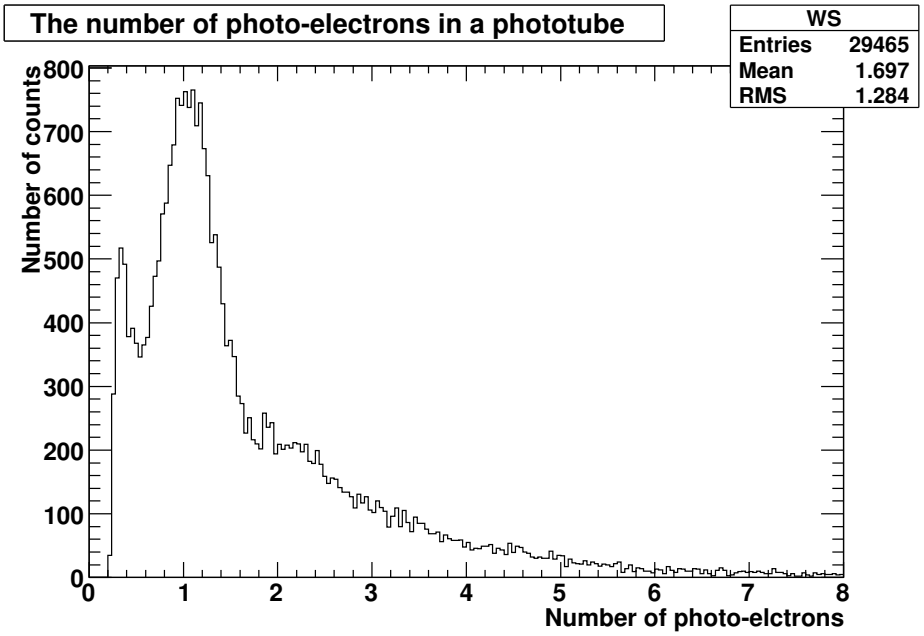

Figure 5.8: The number of photo-electron distribution after the gain calibration.

surface and projected to the RICH phototube surface. The mirror alignment was performed by adjusting the position of the mirror in the z and ϕ directions so that the projection point matches the ring center obtained from the positions of fired phototubes. The displacement of a mirror corresponds to the displacement of the projection point of a particle passing through the mirror. Figure 5.9 shows the fired phototube positions on the plane perpendicular to the reflected tracks after the mirror alignment.

5.4.2 Electron Identification with EMCal

EMCal measures the energy and hit position of electrons and photons. EMCal has eight sectors, W0–W3 (in the west arm, from bottom to top) and E0–E3 (in the east arm, from bottom to top). The sectors E0 and E1 are PbGl and the rest are PbSc. Energy calibration of each EMCal tower was performed using the π^0 peak mass reconstructed from two photons.

Since the electron mass is negligible compared to the momentum interested in high-energy heavy-ion collisions and the electron deposits all of its energy in EMCal, the ratio of the energy (ecore) measured by EMCal and the total momentum (mom) measured by the DC is about 1. Thus, the ratio ecore/mom can be used for the electron identification.

Figure 5.10 shows the ecore/mom distribution for all charged particles (dotted line), for the particles which passed a RICH cut (n0 ≥ 2, solid line) and for the particles with a z-swapped RICH cut (sn0 ≥ 2, dashed line). The shaded histogram in the right panel of Fig. 5.10 is the net distribution after the subtraction of the accidental association with RICH. These charged particles are selected with the following cut parameters:

- $p_T > 0.2$ GeV/c
- mom < 5 GeV/c

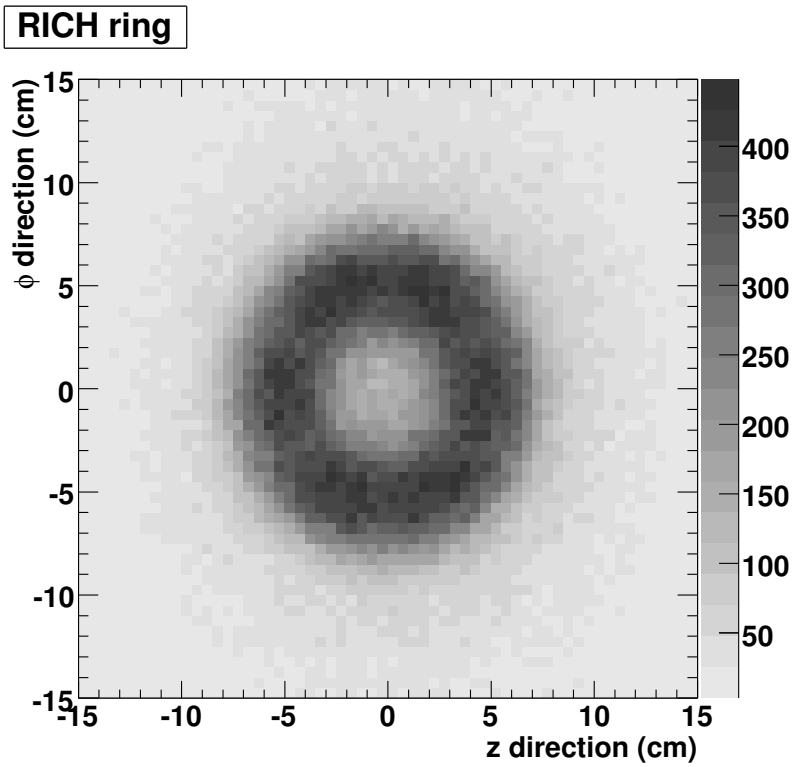

Figure 5.9: Accumulated RICH ring image after the mirror alignment.

- quality $== 63$

Distances between the projection point of a reconstructed track at the EMCal surface (pemcz, pemcphi) and the hit position (the centroid of the electromagnetic shower) (emcz, emcphi) are expressed by emcdz and emcdphi in the z and ϕ directions, respectively.

$$\mathsf{emcdz} = \mathsf{emcz} - \mathsf{pemcz}, \tag{5.24}$$

$$\mathsf{emcdphi} = \mathsf{emcphi} - \mathsf{pemcphi}. \tag{5.25}$$

The parameters ecore/mom, emcdz and emcdphi depend on the total momentum, the momentum direction and the electric charge of electrons/positrons and the sector and position of EMCal by the residual field. The parameters are normalized to the standard normal distribution with a mean of 0 and a σ of 1 for convenience of the analysis. The normalized variables are called dep, emcsdphi_e and emcsdz_e:

$$\mathsf{dep} = \frac{\frac{\mathsf{ecore}}{\mathsf{mom}} - \left\langle \frac{\mathsf{ecore}}{\mathsf{mom}} \right\rangle}{\sigma\left(\frac{\mathsf{ecore}}{\mathsf{mom}}\right)}, \tag{5.26}$$

$$\mathsf{emcsdphi\_e} = \frac{\mathsf{emcdphi} - \langle \mathsf{emcdphi} \rangle}{\sigma(\mathsf{emcdphi})}, \tag{5.27}$$

$$\mathsf{emcsdz\_e} = \frac{\mathsf{emcdz} - \langle \mathsf{emcdz} \rangle}{\sigma(\mathsf{emcdz})}. \tag{5.28}$$

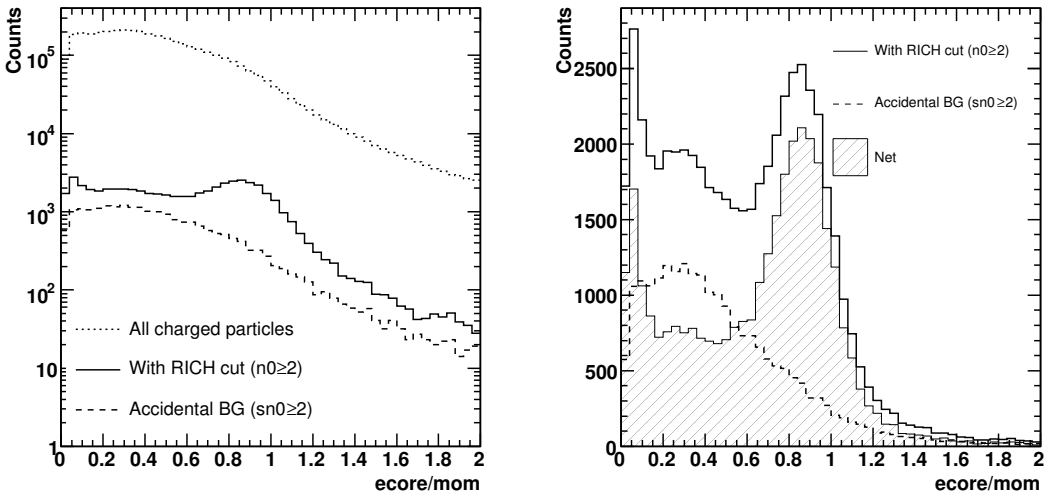

Figure 5.10: Distribution of ecore/mom. Left: ecore/mom distribution for all charged particles (dotted line), for the particles passed with a RICH cut (n0 $\geq$ 2, solid line) and for the particles with a z-swapped RICH cut (sn0 $\geq$ 2, dashed line), which correspond to the particles associated with RICH accidentally. Right: ecore/mom distribution for the particles passed with a RICH cut (n0 $\geq$ 2, solid line), for the particles with a z-swapped RICH cut (sn0 $\geq$ 2, dashed line) and for the net distribution of the subtraction of the accidental association with RICH (shaded histogram).

The dependence listed in Table 5.4 of the parameters was corrected for both the real data and the PISA simulation with the electron candidates selected with the following cuts:

- $0.4 <$ ecore/mom < 2
- $p_T >$0.2 GeV/c
- quality ≥ 29
- $4 \leq$ n1 ≤ 6
- disp < 5
- chi2/npe1 < 10

Since electrons with the CM++ magnet polarity and positrons with the CM−− magnet polarity feel the Lorentz force in the same direction, they are treated as the same particles in the EMCal matching parameters. Positrons with the CM++ and electrons with the CM−− magnet polarity are also treated as the same particles. The contribution of accidental association with RICH was subtracted by the z-swapped electron candidates with the cuts of $4 \leq$ sn1 ≤ 6, sdisp < 5 and schi2/snpe1 < 10. For the correction, convoluted functions of polynomial, exponential and power functions were used.

The distribution of the matching parameters, dep, emcsdphi_e and emcsdz_e, of both the real data and simulation is shown in Fig. 5.11, Fig. 5.12 and Fig. 5.13, respectively. Electrons and positrons were selected with the set of cut parameters listed in Table 5.5 and a $p_T > 0.7$ GeV/c cut. The set of cut parameters listed in Table 5.5 is called the "standard eID (electron identification) cut" and is used for the J/ψ signal extraction, the correction factor estimation and the run selection.

The input distribution of single electrons and positrons in the PISA simulation are as follows:

- Zvertex: Measured BbcZvertex distribution of the MB events in Run-5 Cu+Cu collisions within ±30 cm (Fig. 4.2)
- Rapidity: $-0.5 < y < 0.5$ (flat)
- Azimuthal angle: $0 \leq \phi < 2\phi$ (flat)
- Transverse momentum: $0.7 < p_T < 5$ GeV/c (exponential, $\frac{dN}{dp_T} \propto \exp(-\frac{p_T}{0.5 \text{ GeV}/c})$)

The output distribution of p_T and BbcZvertex in the simulation was weighted so that the real data and simulation have the same distribution in p_T and BbcZvertex.

The distribution of the matching parameters has almost ideal shapes, but there are small distortions from Gaussian and there are differences between the real data and simulation. The corrections for the differences will be estimated with J/ψ in section 5.8.

The hadron rejection factor of RICH and EMCal is about 300 at the electron efficiency of about 95%.

Data	Parameters	Dependence
Real data	dep	Total momentum (mom)
		EMCal sector (sector, dcarm)
	emcsdphi_e	Electric charge (charge)
		Total momentum (mom)
		EMCal sector (sector, dcarm)
		The polar angle (beta)
		The z coordinate at the DC reference radius (zed)
		The ϕ coordinate of the EMCal cluster (emcphi)
	emcsdz_e	Electric charge (charge)
		Total momentum (mom)
		EMCal sector (sector, dcarm)
		The polar angle at the DC reference radius (beta)
Simulation	dep	Total momentum (mom)
		EMCal sector (sector, dcarm)
	emcsdphi_e	Electric charge (charge)
		Total momentum (mom)
		EMCal sector (sector, dcarm)
		The ϕ coordinate of the EMCal cluster (emcphi)
	emcsdz_e	Electric charge (charge)
		Total momentum (mom)
		EMCal sector (sector, dcarm)
		The polar angle at the DC reference radius (beta)
		The z coordinate at the DC reference radius (zed)

Table 5.4: The corrected dependence of EMCal matching parameters in the real data and PISA simulation. The names of variables in nDST are written in parentheses.

Event cut	BBC	$\lvert$BbcZvertex$\rvert < 30$ cm
		$0 \leq$ Centrality <94
	Trigger	BBCLL1(>0 tubes) (Minimum Bias)
		ERTLL1_E&BBCLL1 (ERT electron)
Electron Cut	DC and PC1	quality $== 29\|\|30\|\|31\|\|49\|\|50\|\|51\|\|61\|\|62\|\|63$
		$p_T > 0.2$ GeV/c
		mom < 5 GeV/c
		Fiducial cut
	RICH	n0 ≥ 2
		Fiducial cut
	EMCal	dep > -2
		$\lvert$emcsdphi_e$\rvert < 4$
		$\lvert$emcsdz_e$\rvert < 4$
		Fiducial cut

Table 5.5: Standard eID cut used for the J/ψ signal extraction, the correction factor estimation and the run selection.

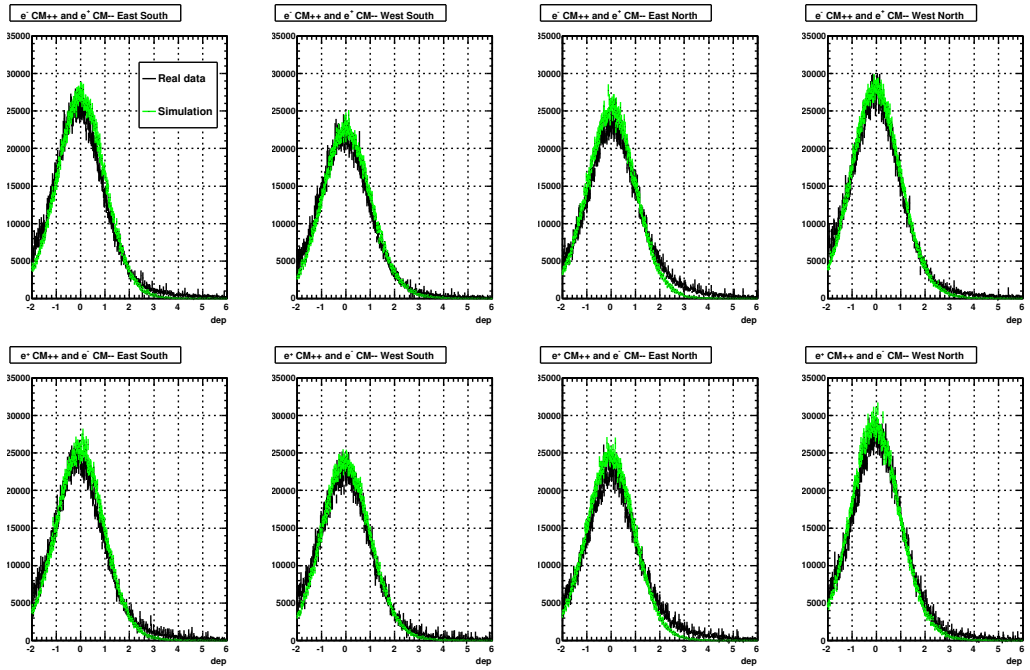

Figure 5.11: Distribution of the energy-momentum matching parameter, dep, of the real data (black) and simulation (green) with the standard eID cut and the $p_T > 0.7$ GeV/c cut for each sector.

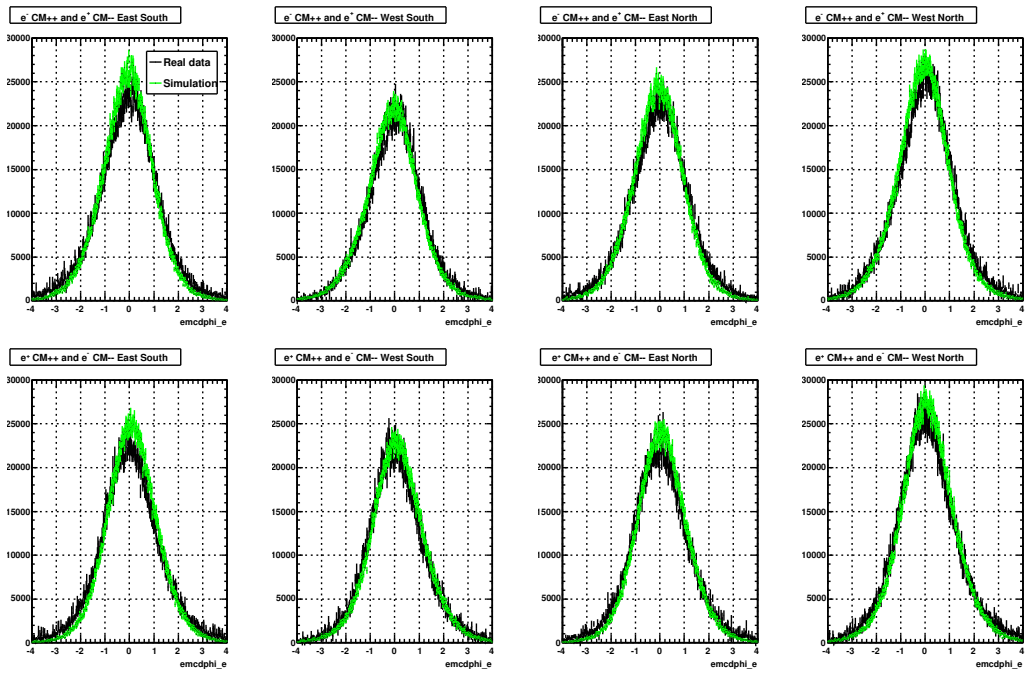

Figure 5.12: Distribution of the position matching parameter in the ϕ direction, emcsdphi_e, of the real data (black) and simulation (green) with the standard eID cut and the $p_T > 0.7$ GeV/c cut for each sector.

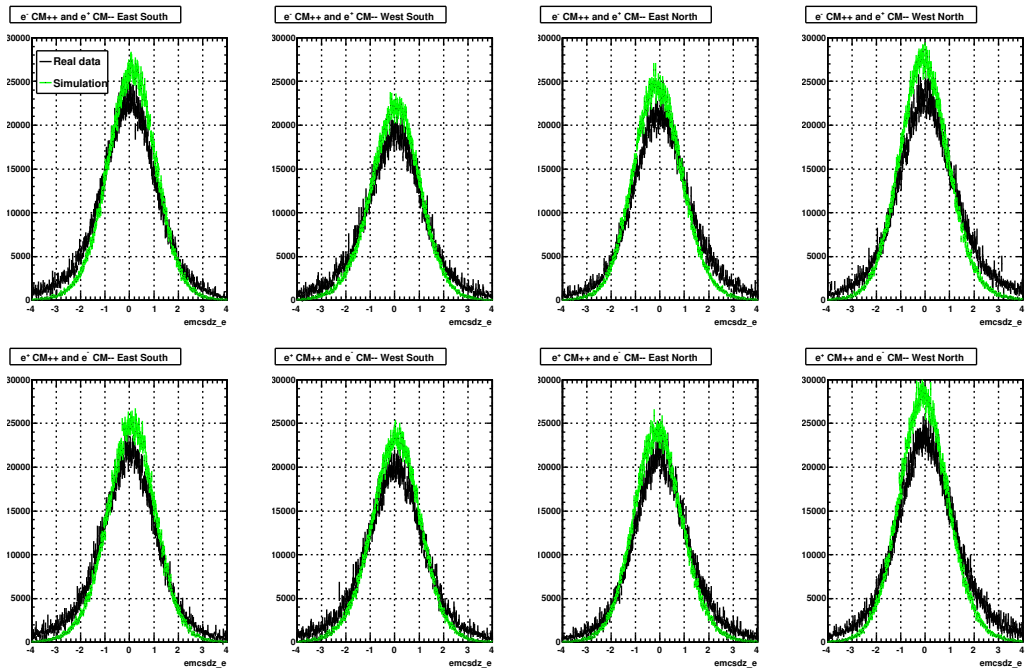

Figure 5.13: Distribution of the position matching parameter in the z direction, emcsdz_e, of the real data (black) and simulation (green) with the standard eID cut and the $p_T > 0.7$ GeV/c cut for each sector.

5.5 Fiducial Cut

To select active areas of detectors as fiducial volumes, the following hit maps were made.

- Hit maps of the z-coordinate of the collision vertex and the polar angle of the track at the DC reference radius for negative and positive particles: BbcZvertex-cos(beta)
  - The low efficiency parts in this correlation correspond to boundary regions, which separate the north and south sides, of the DC, PC1 and RICH.
- A map of DC hits in the z-ϕ plane: zed-phi
- A map of track hit points projected to the PC1 plane in the z and ϕ directions : ppc1z-ppc1phi
- A map of track hit points projected to the RICH phototube plane in the z and ϕ directions : cross_z-cross_phi
- A map of track hit points projected to the EMCal surface in the z and ϕ directions : pemcz-pemcphi

The following cuts were used to select charged tracks for making the hit maps.

- $0.6 < p_T < 5$ GeV/c (common cut)

- quality == 31 || 63 (applied for BbcZvertex-cos(beta))
- pc1id ≥ 0 (applied for PC1, an associated PC1 cluster is required)
- n1 ≥ 2 (applied for RICH)
- ecore/mom > 0.4 (applied for EMCal)

The obtained hit maps are shown in Fig. 5.14.

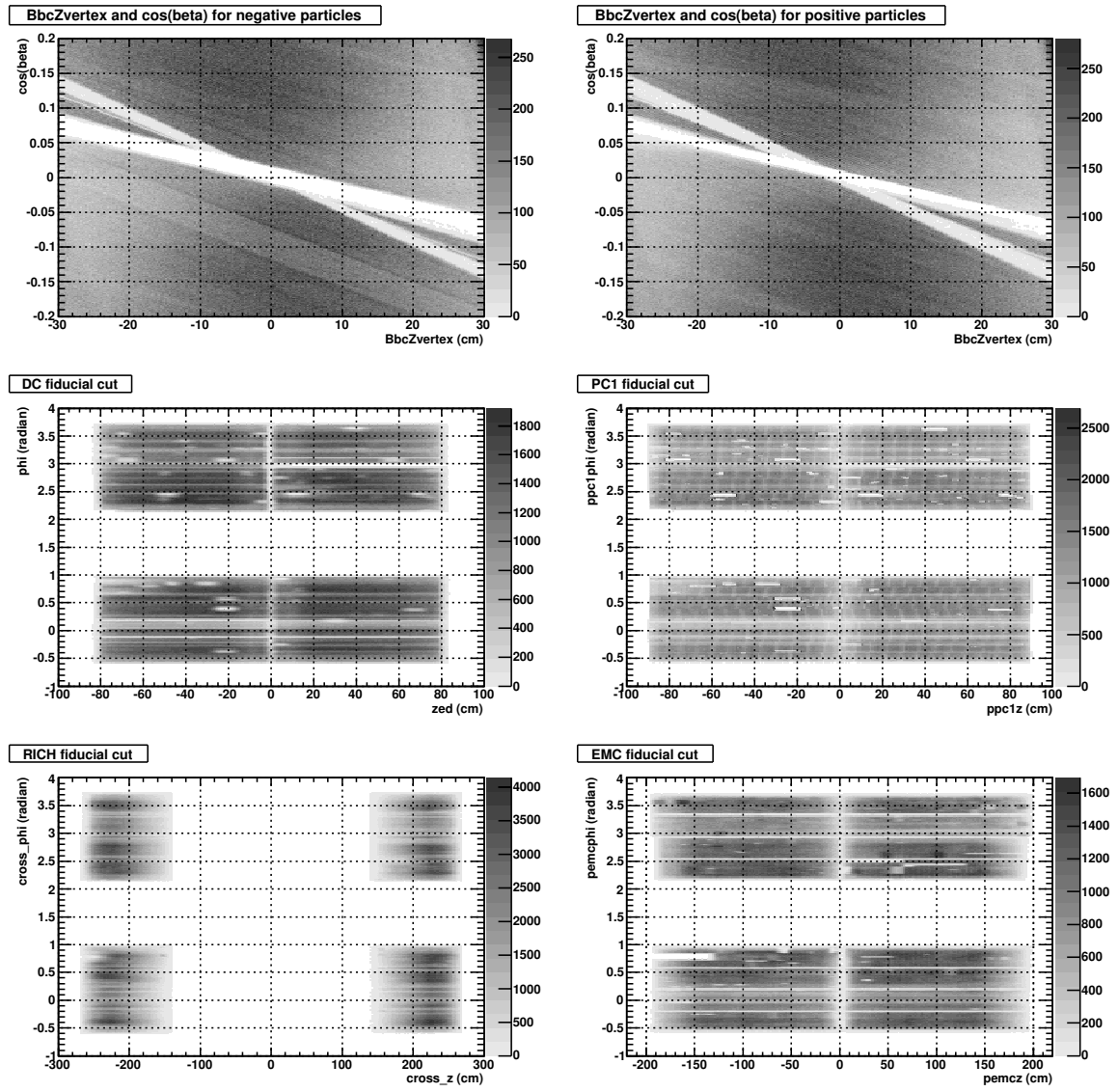

Figure 5.14: Hit maps of the correlation between BbcZvertex and cos(beta) for negative particles (top left) and positive particles (top right), DC (middle left), PC1 (middle right), RICH (bottom left) and EMCal (bottom right).

The whole area of each detector was divided into 250×250 sub areas. The number of hits was calculated for each sub area of the detector. If the number of hits of a sub

area is within $\pm 5\sigma$ from the mean value of the detector, the sub area is assigned as active. The obtained active areas of the detectors are shown in Fig. 5.15 and these areas were used as the fiducial volume.

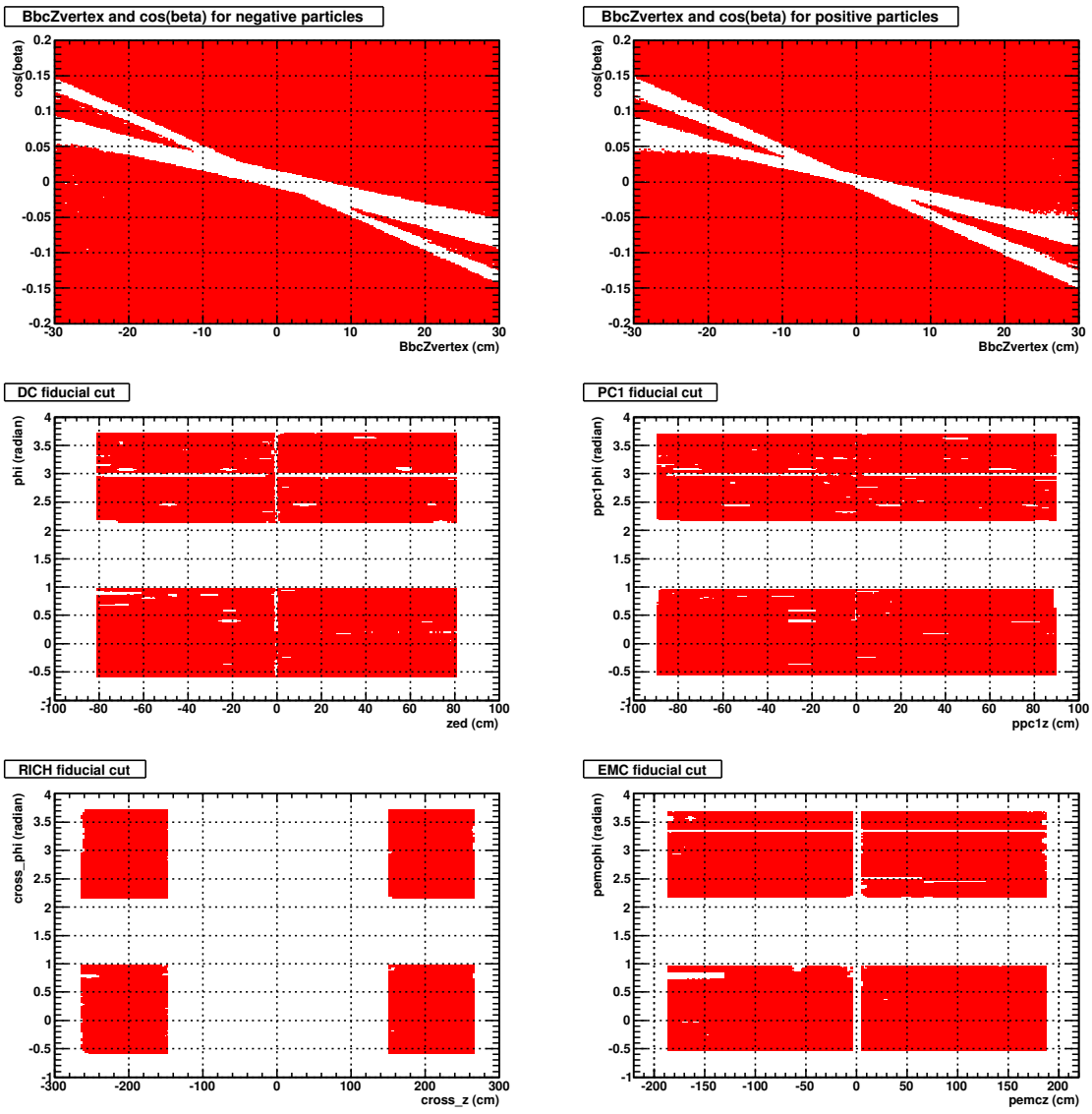

Figure 5.15: Fiducial cuts of the correlation between BbcZvertex and cos(beta) for negative particles (top left) and positive particles (top right), DC (middle left), PC1 (middle right), RICH (bottom left) and EMCal (bottom right).

Additional phi Cut in DC

Remaining noisy and low efficient areas were found in the DC after the $\pm 5\sigma$ cut by comparison between the real data and simulation. A charge dependent phi cut listed in Table 5.6 was added to reject these areas. This additional phi cut is included in the standard eID cut as well as the $\pm 5\sigma$ fiducial cut.

Charge (charge)	Arm (dcarm)	Side (dcside)	DC phi (rad)
− (charge = −1) (CM++)	East (dcarm = 0)	South (dcside = 0)	
+ (charge = +1) (CM−−)		North (dcside = 1)	2.92– 2.94
			3.04– 3.06
	West (dcarm = 1)	South (dcside = 0)	−0.44–−0.42
			−0.22–−0.18
			0.04– 0.14
			0.16– 0.22
			0.58– 0.60
			0.80– 0.82
		North (dcside = 1)	−0.34–−0.32
			−0.06–−0.04
			0.04– 0.12
			0.14– 0.16
			0.44– 0.46
+ (charge = +1) (CM++)	East (dcarm = 0)	South (dcside = 0)	2.14– 2.16
− (charge = −1) (CM−−)			2.18– 2.20
		North (dcside = 1)	2.14– 2.18
			3.02– 3.04
			3.08– 3.12
			3.22– 3.24
	West (dcarm = 1)	South (dcside = 0)	−0.58–−0.56
			−0.50–−0.44
			−0.26–−0.18
			−0.14–−0.12
			−0.10–−0.08
			0.04– 0.10
			0.14– 0.18
			0.20– 0.26
			0.44– 0.46
		North (dcside = 1)	−0.58–−0.56
			−0.30–−0.28
			−0.26–−0.18
			−0.14–−0.12
			−0.10–−0.08
			0.06– 0.10
			0.14– 0.18
			0.20– 0.22
			0.52– 0.54

Table 5.6: The additional fiducial cut of the DC phi angle.

Comparison Between Real Data and Simulation

The distribution of phi and zed from the simulation was compared to that of the real data. The simulation sample described in subsection 5.4.2 was used. The cut parameters were for the standard eID and a transverse momentum with $p_T > 0.7$ GeV/c was selected. The normalization between the simulation and the real data was determined by the number of entry electrons with the CM++ polarity and positrons with the CM−− polarity in the east south sector. This normalization factor was applied to other sectors.

Figure 5.16, Fig. 5.17 and Fig. 5.18 show the distribution of phi, zed and n0, respectively. The black and green histograms show the real data and simulation, respectively. The distribution of the real data and that of the simulation match well.

Figure 5.19 shows the ratio of the number of electrons in a sector to the number of electrons (CM++) in the east south sector for both the real data and simulation. Although the real data and simulation agree within error, the simulation has the larger number of entries. The square of the mean deviation of the ratio between the real and simulation is 4.3% and is used as the systematic error of the fiducial cut for J/ψ measured via di-electrons.

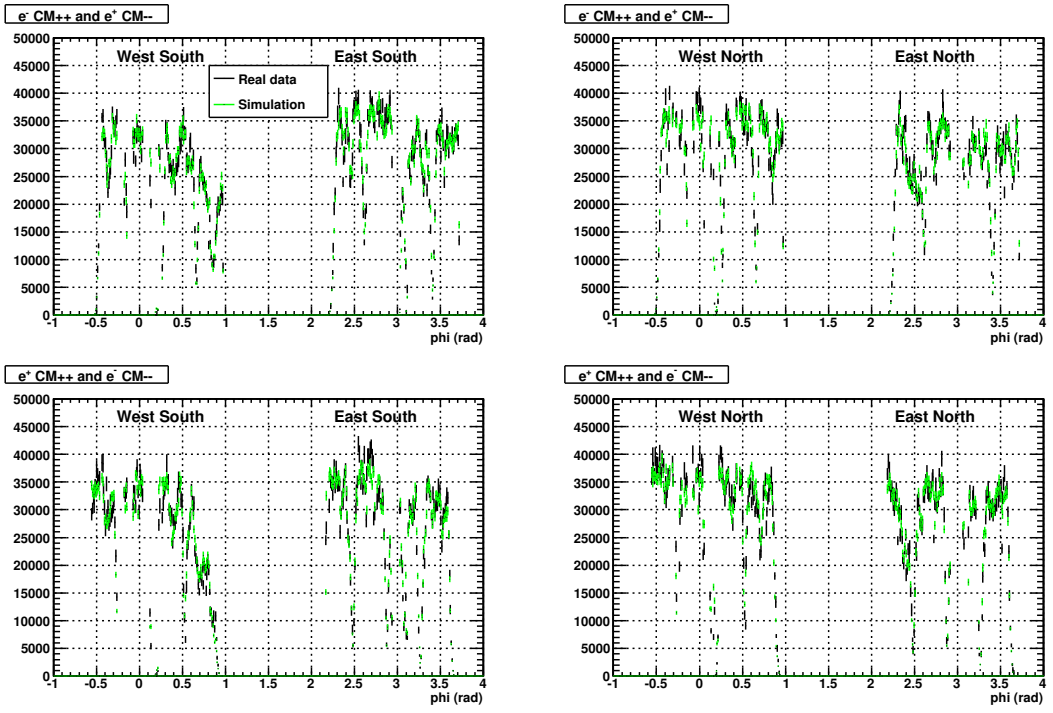

Figure 5.16: Distribution of phi with the standard eID cut and the $p_T > 0.7$ GeV/c cut in the real data (black) and simulation (green).

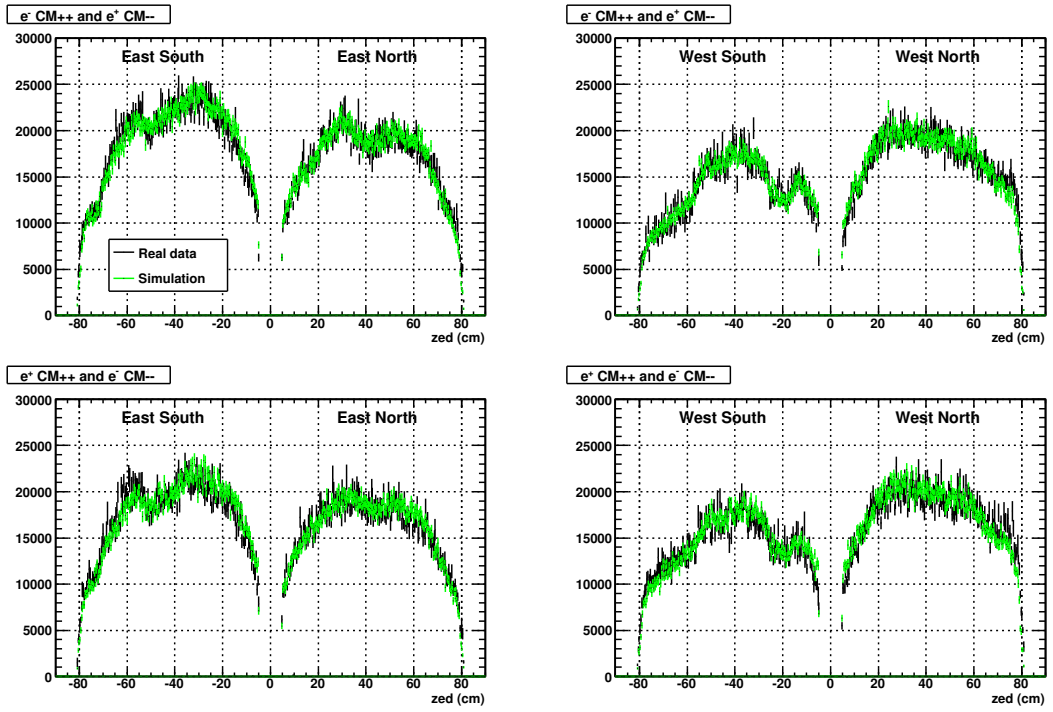

Figure 5.17: Distribution of zed with the standard eID cut and the $p_T > 0.7$ GeV/c cut in the real data (black) and simulation (green).

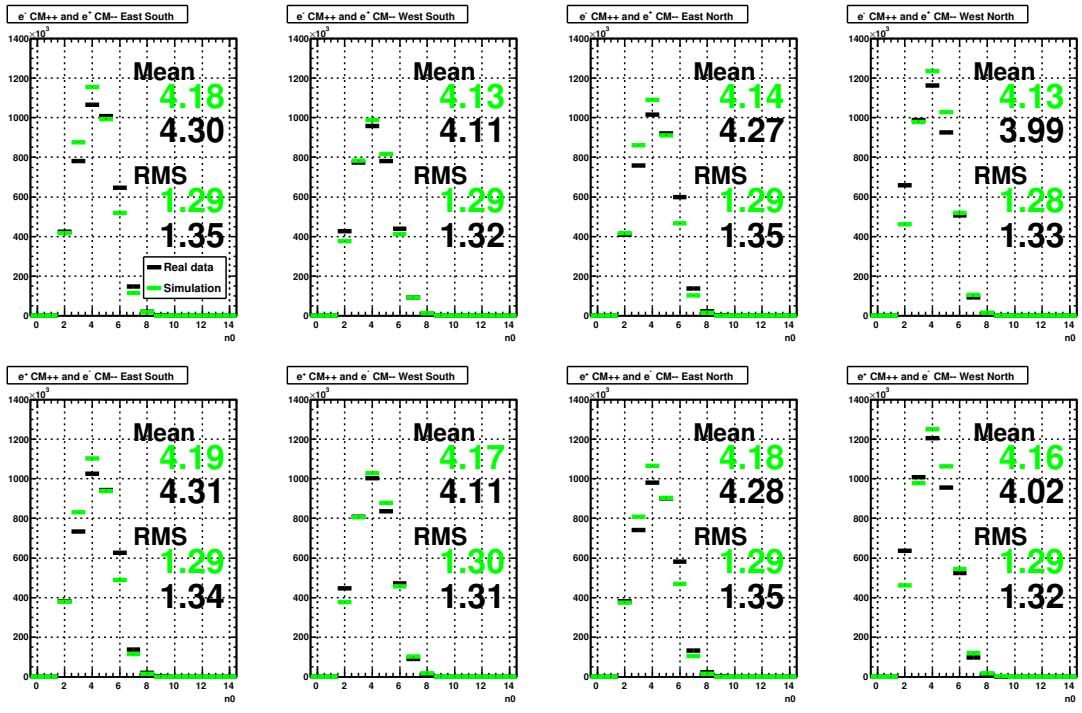

Figure 5.18: Distribution of n0 with the standard eID cut and the $p_T > 0.7$ GeV/c cut in the real data (black) and simulation (green).

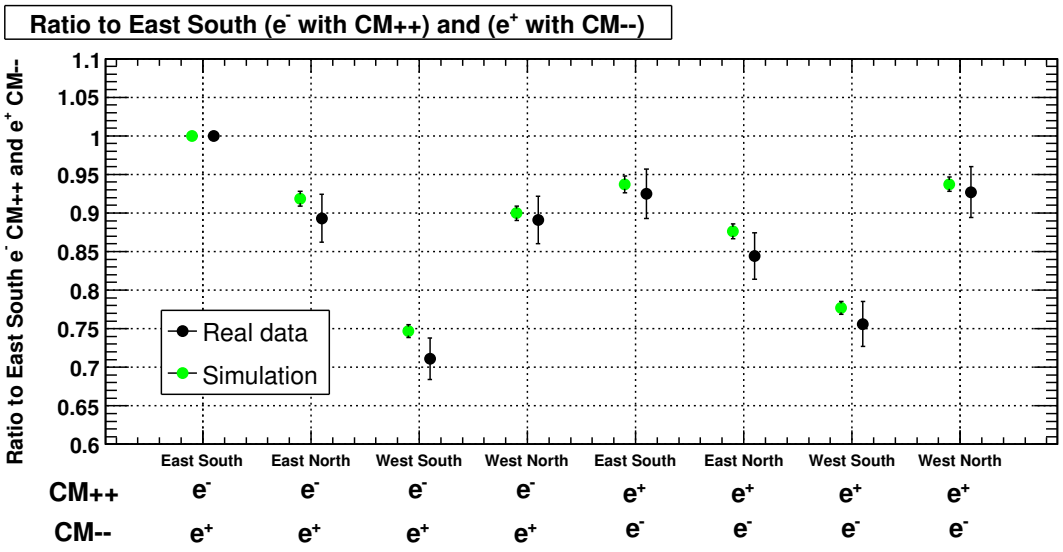

Figure 5.19: Ratio of the number of electrons/positrons in a sector to one of electrons in the east south sector.

5.6 Run Selection

Run selection to be used for the J/ψ analysis was performed based on the number of electrons per event with the standard eID cut. Average numbers of electrons and positrons per event were calculated for sector-by-sector without and without 0.7 GeV/c cuts for both MB and ERT electron triggered data in each run. The runs were divided into four groups (G0–G3) depending on the detector configuration as listed in Table 4.1. If the value for a category of a run is within $\pm 6\sigma$ from the mean value of the run group, the run is marked OK for the category. If a run passes all 64-fold categories (8 sectors (W0–W3 and E0–E3), 2 species (e^- and e^+), 2 p_T cuts (without and with the 0.7 GeV/c cut), 2 trigger sets (MB and ERT electron)), the run is assigned as a good run.

After the 64-fold selection, 357 runs out of 460 runs were left for the J/ψ analysis.

As an example, the results of electrons in the W0 sector are shown. Figure 5.20 and Fig. 5.21 show the average numbers of electrons per event in the W0 sector without and with the p_T cut of 0.7 GeV/c in the MB data, respectively. Blue and red points show the runs which passed and did not pass the 1-fold selection. Figure 5.22 and Fig. 5.23 show the average numbers of electrons per event in the W0 sector without and with the p_T cut of 0.7 GeV/c in the ERT data, respectively.

5.7 Signal Extraction of J/ψ

The J/ψ signals were extracted from the invariant mass spectrum of e^+e^- with the following mass cut:

$$2.9 \text{ GeV}/c^2 < M_{e^+e^-} < 3.3 \text{ GeV}/c^2, \tag{5.29}$$

where $M_{e^+e^-}$ means the invariant mass of an e^+e^- pair.

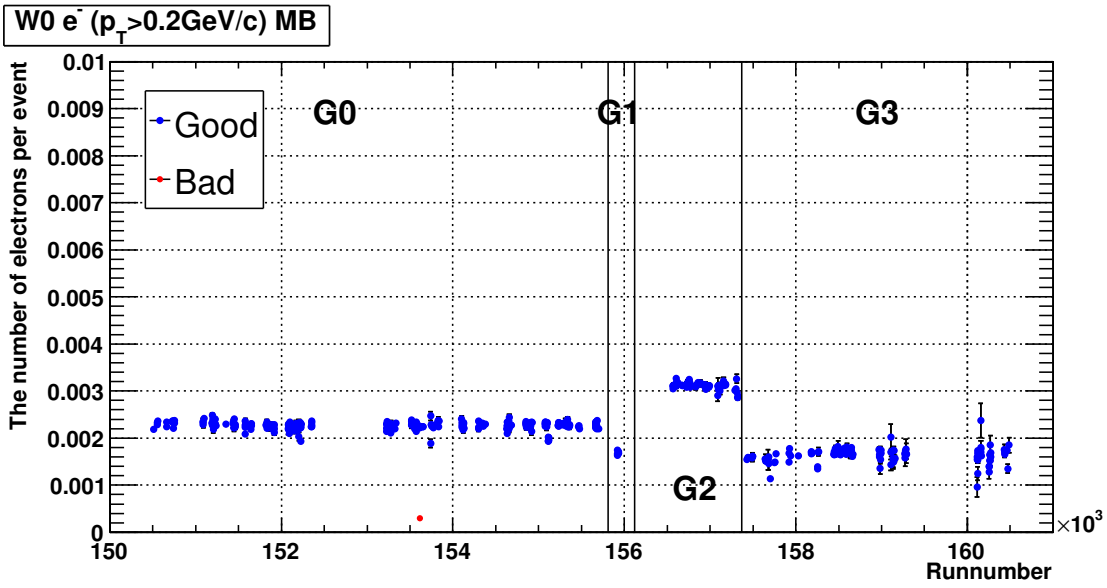

Figure 5.20: The number of electrons per event of W0 sector with the $p_T > 0.2$ GeV/c cut in MB data as a function of runnumber.

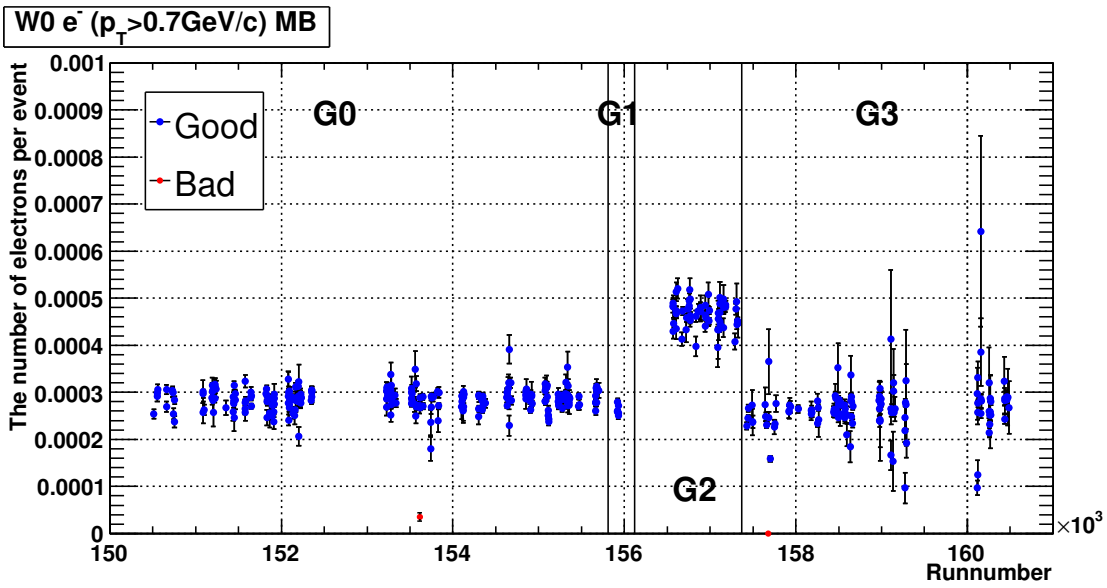

Figure 5.21: The number of electrons per event of W0 sector with the $p_T > 0.7$ GeV/c cut in MB data as a function of runnumber.

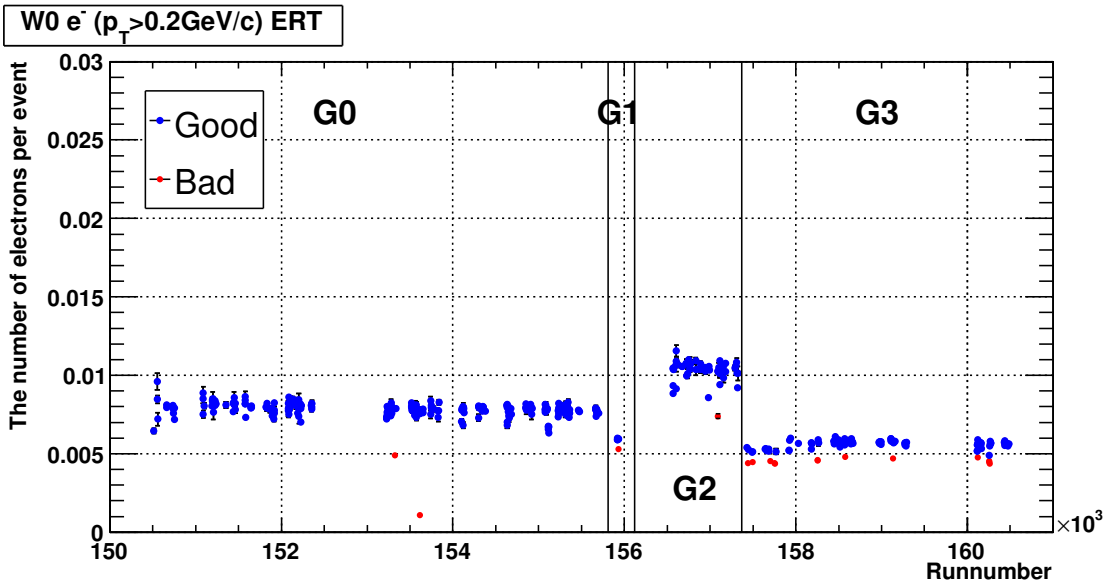

Figure 5.22: The number of electrons per event of W0 sector with the $p_T > 0.2$ GeV/c cut in ERT electron data as a function of runnumber.

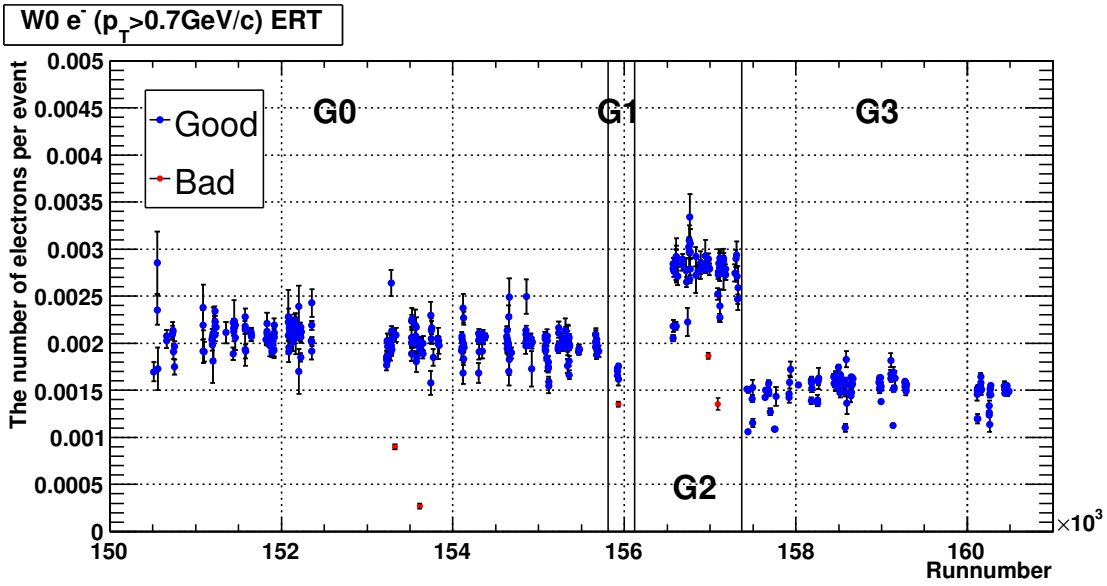

Figure 5.23: The number of electrons per event of W0 sector with the $p_T > 0.7$ GeV/c cut in ERT electron data as a function of runnumber.

The total energy of the electron and positron, E_e, in Eq. (5.1) is calculated from not the energy measured by EMCal but the total momentum measured by the DC and PC1 (mom),

$$E_e \;=\; \sqrt{m_e^2 + \mathsf{mom}^2}, \tag{5.30}$$

where m_e is the electron mass (m_e=0.0005109989 GeV/c^2 [19]).

The combinatorial background in e^+e^- (unlike sign) pairs is estimated using e^+e^+ and e^-e^- (like sign) pairs. The number of net counts, N_{net}, is used as the number of J/ψ without correction:

$$N_{net} \;=\; N_{+-} - (N_{++} + N_{--})\,, \tag{5.31}$$

where N_{+-}, N_{++} and N_{--} are the numbers of e^+e^-, e^+e^+ and e^-e^- pairs in the J/ψ mass region of 2.9–3.3 GeV/c^2.

Figure 5.24 shows the invariant mass spectrum and raw p_T spectrum of the MB events of the whole run group (G0–G3). The numbers of counts are $N_{+-} = 2005$, $N_{++} + N_{--} = 619$ and $N_{net} = 1386 \pm 51$. The invariant mass spectrum for each run group and for each Centrality bin is shown in Appendix C.

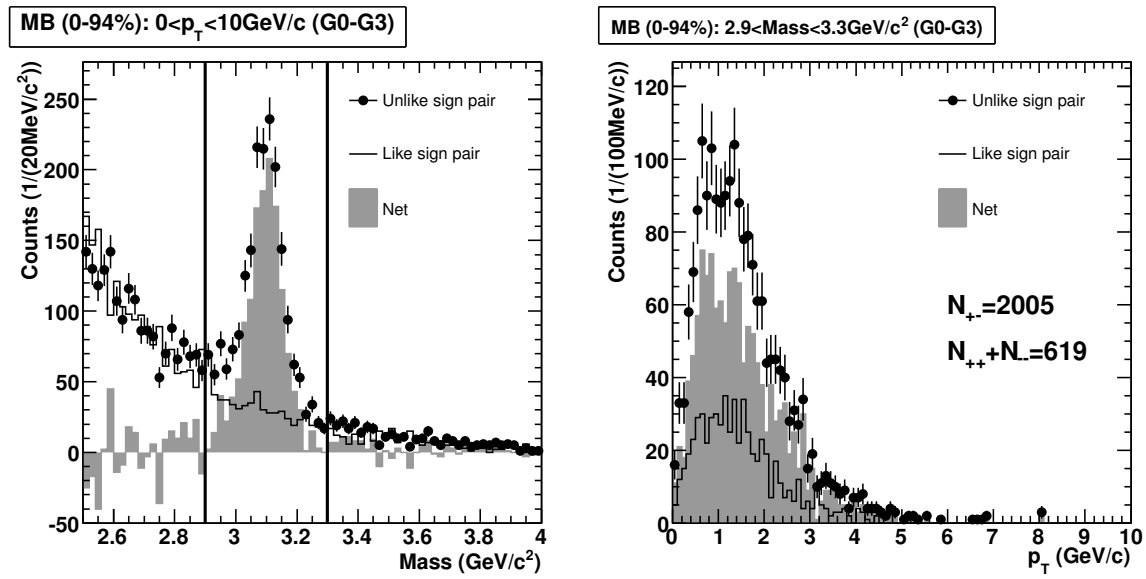

Figure 5.24: The invariant mass spectrum (left) and the raw p_T spectrum in the J/ψ mass region (2.9< $M_{e^+e^-}$ <3.3 GeV/c^2) (right) in MB (0–94%) data in all the run groups (G0–G3).

5.7.1 Continuum Contribution

Correlated pairs of electrons and positrons with the continuous mass distribution are produced from $c\bar{c}$, $b\bar{b}$ and Drell-Yan production whose contributions remain after subtracting the like sign pairs. These pairs are called as the continuum pairs. The ratio

of the yield of the continuum pairs, Y_{cont}, to the yield of J/ψ, $Y_{J/\psi}$, was estimated by an event generator, PYTHIA [129], and the ratio, R_{cont}, was evaluated to be as follows [132]:

$$R_{cont} = \frac{Y_{cont}}{Y_{J/\psi} + Y_{cont}} = 0.10 \pm 0.05(\text{syst}). \tag{5.32}$$

5.7.2 Internal Bremsstrahlung

Since the PISA simulation does not include the internal bremsstrahlung of J/ψ ($J/\psi \to e^+e^-\gamma$), the correction for the loss of the low mass tail due the mass cut of $2.9 < M_{e^+e^-} < 3.3$ GeV/c^2 is needed [130, 131]. With the parameterization described in Ref [131], the loss due to the internal bremsstrahlung with the mass cut of $2.9 < M_{e^+e^-} < 3.3$ GeV/c^2 was estimated to be 0.12±0.01 (syst) [132].

5.8 Correction Factors

As described in Eq. (5.5), the invariant yield can be determined with the total efficiency including acceptance, ε, and the number of MB events, $N_{\rm MB}$. The total efficiency is decomposed into three parts:

$$\begin{aligned} \varepsilon(p_{T,J/\psi}, \mathsf{Centrality}) &= \varepsilon_{acc,J/\psi\to e^+e^-}(p_{T,J/\psi}) \times \\ &\quad \varepsilon_{embed}(p_{T,J/\psi}, \mathsf{Centrality}) \times \varepsilon_{LVL1,J/\psi}(p_{T,J/\psi}, \mathsf{Centrality}), \end{aligned} \tag{5.33}$$

where $\varepsilon_{acc,J/\psi\to e^+e^-}$ is the J/ψ reconstruction efficiency including acceptance in the e^+e^- decay mode, ε_{embed} is the embedding efficiency which represents the inefficiency due to high particle multiplicity and $\varepsilon_{LVL1,J/\psi}$ is the ERT electron trigger efficiency for J/ψ.

In this section, the determinations of these three kinds of efficiency and $N_{\rm MB}$ are described.

5.8.1 Reconstruction Efficiency Including Acceptance

The J/ψ reconstruction efficiency including acceptance $\varepsilon_{acc,J/\psi\to e^+e^-}$ is defined as follows:

$$\varepsilon_{acc,J/\psi\to e^+e^-}(p_{T,J/\psi}) = \frac{n^{reco}_{J/\psi}(p_{T,J/\psi})}{n^{input}_{J/\psi}(p_{T,J/\psi})}, \tag{5.34}$$

where $n^{input}_{J/\psi}$ and $n^{reco}_{J/\psi}$ are the numbers of generated and reconstructed J/ψ, respectively.

The conditions in the generation of J/ψ are as follows:

- Zvertex: Measured BbcZvertex distribution of the MB events in Run-5 Cu+Cu collisions within ±30 cm (Fig. 4.2)
- Rapidity: $-0.5 < y < 0.5$ (flat)
- Azimuthal angle: $0 \le \phi < 2\phi$ (flat)

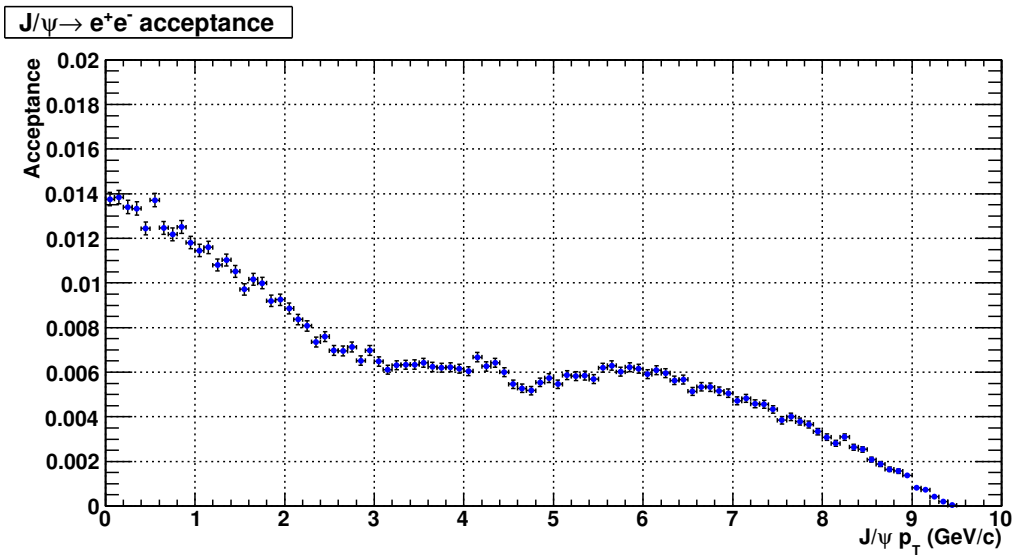

Figure 5.25: The J/ψ reconstruction efficiency including acceptance in Cu+Cu collisions.

- Transverse momentum: $0 < p_T < 10$ GeV/c (flat)

The obtained J/ψ reconstruction efficiency including acceptance with the standard eID cut is shown in Fig. 5.25.

At $p_{T,J/\psi} = 0$ GeV/c, $\varepsilon_{acc,J/\psi\to e^+e^-} = 1.4\%$. The fall in $\varepsilon_{acc,J/\psi\to e^+e^-}$ from 0 GeV/c to 3 GeV/c is due to the open geometry of the central arm. The fall in $\varepsilon_{acc,J/\psi\to e^+e^-}$ from 6 GeV/c to 9.5 GeV/c is due to the $\mathsf{mom} < 5$ GeV/c cut in the standard eID cut. The flat structure from 3 GeV/c to 6 GeV/c is created by these two reasons.

5.8.2 Embedding Efficiency

The high multiplicity in high-energy heavy-ion collisions causes wrong track reconstruction and hit association. The inefficiency caused by these wrong reconstruction and association is called embedding efficiency, ε_{embed}, in PHENIX. The embedding efficiency is estimated by embedding simulated single J/ψ events into the real data and reconstructing them. The efficiency is calculated as follows:

$$\varepsilon_{embed}(p_T, \mathsf{Centrality}) = \frac{n^{embed}_{J/\psi}(\mathsf{Centrality}, p_T)}{n^{single}_{J/\psi}(p_T)}, \tag{5.35}$$

where Centrality is the centrality of an event of the real data, p_T is the transverse momentum of J/ψ of single J/ψ simulation, and $n^{single}_{J/\psi}$ and $n^{embed}_{J/\psi}$ are the number of reconstructed J/ψ with the standard eID cut in single J/ψ simulation events and embedded events, respectively. Figure 5.26 shows the obtained embedding efficiency as a function of Centrality for all p_T range (left) and p_T for all Centrality range (MB) (right). The embedding efficiency of the most central events is 97% and the inefficinecy is 3%. The p_T dependence of the embedding efficiency is less than 2% and is neglected

in this analysis. In Fig. 5.26, the following fit function is shown:

$$\varepsilon_{embed}(\mathsf{Centrality}) \;=\; p_0 \cdot \left[1 - p_1 \cdot \exp\left(-\frac{\mathsf{Centrality}}{p_2}\right)\right], \tag{5.36}$$

where $p_0 = 1.005 \pm 0.019$, $p_1 = 0.033 \pm 0.016$ and $p_2 = 39 \pm 60$. The embedding efficiency obtained from the fit function is used for the analysis. The maximum deviation of the embedding efficiency by the statistical errors of the fit function is 1.9% and the systematic error of the embedding efficiency is assigned to be 1.9%.

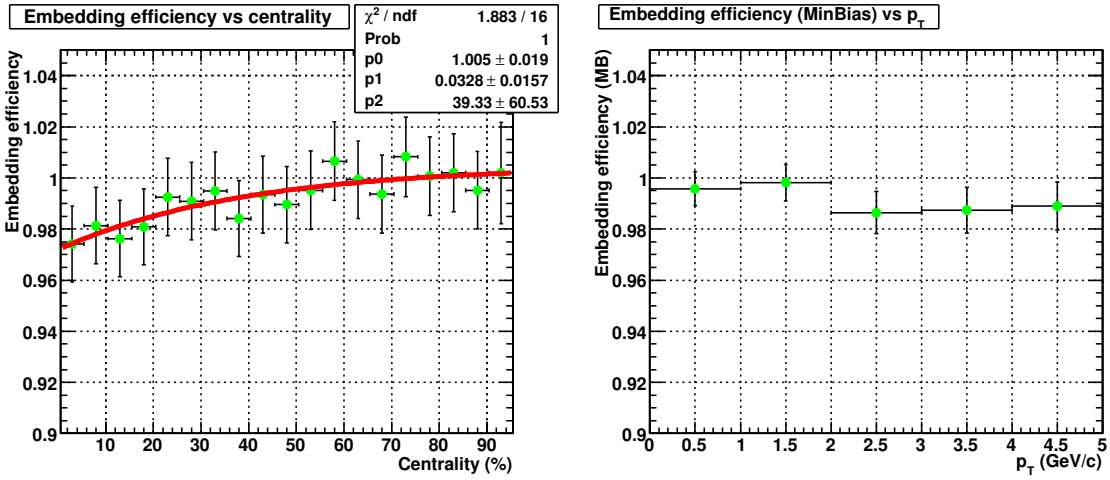

Figure 5.26: J/ψ embedding efficiency as a function of Centrality (left) and p_T (right).

5.8.3 ERT Electron Trigger Efficiency

The ERT electron trigger efficiency for J/ψ, $\varepsilon_{LVL1,J/\psi}$, is evaluated from the ERT electron trigger efficiency for single electrons, $\varepsilon_{LVL1,e}$. The ERT electron trigger efficiency for single electrons is evaluated with the MB triggered data. The ratio of the number of electrons in events where the ERT electron trigger (BBCLL1($>$ 0tubes)$\cap$ERTLL1_E) was fired to that in events where the MB trigger (BBCLL1($>$ 0tubes)) was fired in the MB triggered data is used as the ERT electron trigger efficiency for single electrons:

$$\begin{aligned} &\varepsilon_{LVL1,e}(\mathsf{mom}, \mathsf{sector}, \mathsf{Centrality}) \\ =\; &\frac{n_e(\mathsf{mom}, \mathsf{sector}, \mathsf{Centrality})\{\text{standard eID cut} \cap \text{BBCLL1}(>0\text{tubes}) \cap \text{ERTLL1\_E}\}}{n_e(\mathsf{mom}, \mathsf{sector}, \mathsf{Centrality})\{\text{standard eID cut} \cap \text{BBCLL1}(>0\text{tubes})\}}. \end{aligned} \tag{5.37}$$

Since it is not checked which electron fired the ERT electron trigger in this definition, the ERT electron trigger efficiency includes random benefit (RB), which depends on Centrality. The ERT electron trigger efficiency for single electrons without random benefit, $\varepsilon_{LVL1,e}^{\text{w/o RB}}$, is defined as follows:

$$\begin{aligned} &\varepsilon_{LVL1,e}^{\text{w/o RB}}(\mathsf{mom}, \mathsf{sector}) \\ =\; &\frac{n_e(\mathsf{mom}, \mathsf{sector})\{\text{standard eID cut} \cap \text{BBCLL1}(>0\text{tubes}) \cap \text{ERTLL1\_E} \cap \text{FiredTile}\}}{n_e(\mathsf{mom}, \mathsf{sector})\{\text{standard eID cut} \cap \text{BBCLL1}(>0\text{tubes})\}}, \end{aligned} \tag{5.38}$$

where "FiredTile" means the requirement that the electron fired both the RICH and EMCal trigger tiles which are associated in the look-up table in ERTLL1_E. As an example, the ERT electron trigger efficiency for single electrons with and without random benefit in Centrality of 0–10% in G0 (ERTLL1_2x2 trheshold is 1.1 GeV) and G3 (ERTLL1_2x2 trheshold is 0.8 GeV) is shown in Fig. 5.27. Due to the limited statistics, the electron momentum range of 2.5–5.0 GeV/c is combined to one bin. The random benefit in the low momentum region (mom $<$ 1 GeV/c) is 15% in G0 and 40% in G3. The ERT electron trigger efficiency for single electrons with and without random benefit for each run group and for each Centrality bin is shown in Appendix D.

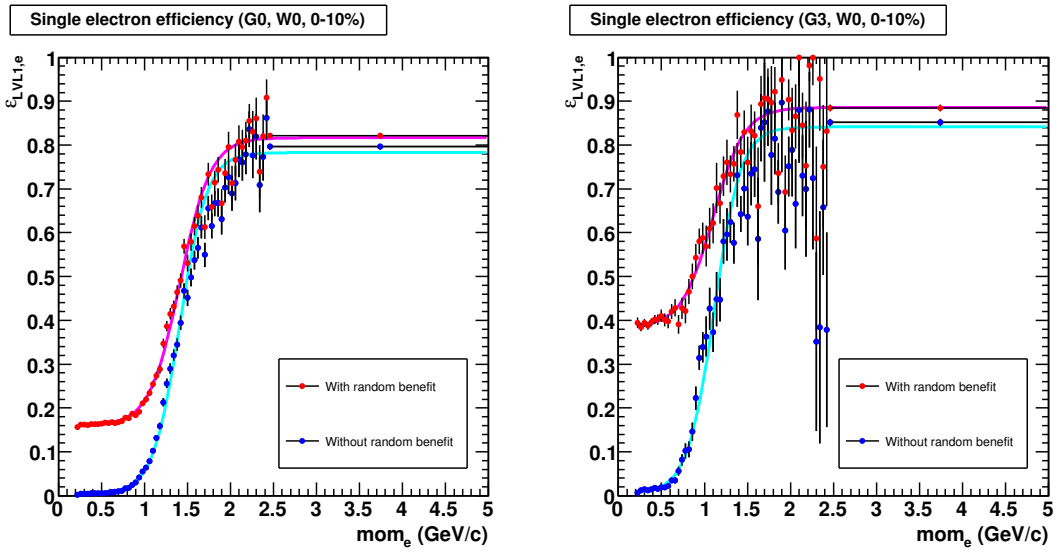

Figure 5.27: The ERT electron trigger efficiency for single electrons with (red) and without (blue) random benefit of W0 sector in centrality of 0–10% in G0 (left, ERTLL1_2x2 trheshold is 1.1 GeV) and G3 (right, ERTLL1_2x2 trheshold is 0.8 GeV). The single electron trigger efficiency is shown as a function of the electron momentum, mom_e.

The solid curves in Fig. 5.27 are the fitted functions with the following parameterization:

$$\varepsilon_{LVL1,e}^{(\text{w/o RB})}(\mathsf{mom}) \;=\; p_0 + \frac{p_1}{1+\exp\left(-\frac{\mathsf{mom}-p_2}{p_3}\right)}. \tag{5.39}$$

These fitted functions were used for the systematic error evaluation.

To obtain the larger number of J/ψ for a small statistical error, the ERT electron trigger and the ERT electron trigger efficiency including random benefit is used in this analysis.

The ERT electron trigger efficiency for J/ψ ($\varepsilon_{LVL1,J/\psi}$) is estimated from the sector and Centrality dependent ERT electron trigger efficiency for single electrons, $\varepsilon_{LVL1,e}$. Since the ERT electron trigger is the single electron trigger, it works for J/ψ as a logical OR. Therefore, $\varepsilon_{LVL1,J/\psi}$ can be obtained with the accepted J/ψ simulation events as follows:

$$\varepsilon_{LVL1,J/\psi}(p_{T,J/\psi}, \mathsf{Centrality})$$

$$= \frac{1}{N^{sim}_{J/\psi}} \sum_{N^{sim}_{J/\psi}} \{1 - [1 - \varepsilon_{LVL1,e}(\mathsf{mom}_{e^+}, \mathsf{sector}_{e^+}, \mathsf{Centrality})] \times [1 - \varepsilon_{LVL1,e}(\mathsf{mom}_{e^-}, \mathsf{sector}_{e^-}, \mathsf{Centrality})]\}, \quad (5.40)$$

where $N^{sim}_{J/\psi}$ is the number of accepted J/ψ simulation events, e^+ and e^- are the daughter particles of the accepted J/ψ, and mom_e and sector are the momentum and EMCal sector of the electron. The obtained ERT electron trigger efficiency for J/ψ with the histograms for each run group and for each $\mathsf{Centrality}$ is shown in Fig. 5.28. Since the statistics of the run group G1 are limited, G1 is combined with G0. The statistics of peripheral events ($\mathsf{Centrality} \geq 40\%$) are also limited and the $\mathsf{Centrality}$ bin of 40–94% is used. The efficiency is greater than 0.6 for all $\mathsf{Centrality}$ bins and all run groups.

The difference between the efficiency obtained from the histograms and the efficiency obtained from the fitted functions is shown in Fig. 5.29. The difference is about 4% and is used as the systematic error of the ERT electron trigger efficiency for J/ψ.

Look-Up Table

A hardware look-up table in ERTLL1_E is used for the association of RICH and EMCal trigger tiles. Due to the wrong configuration and electric noises, table look-up sometimes fails to pick up the events where the fired RICH and EMCal tiles have the association and ERTLL1_E should be fired. Figure 5.30 shows the efficiency of the look-up table. While the low efficient runs are seen, those runs were rejected by the run selection described in section 5.6.

Rejection Factor and Number of Minimum Bias Events

To obtain the invariant yield of J/ψ, the number of minimum bias events, $N_{\rm MB}$, should be known. Since the ERT electron triggered data is used for the signal extraction of J/ψ, the rejection factor of the ERT electron trigger, $RF_{\rm ERT\ electron}$, is needed to obtain the equivalent number of minimum bias events, $N^{\rm equiv}_{\rm MB}$. The rejection factor is obtained from the number of scaled (recorded) MB triggered events, $N^{\rm scaled}_{\rm MB}$, the number of scaled (recorded) ERT electron triggered events in the scaled MB triggered events, $N^{\rm scaled}_{\rm ERT\ electron}$, and the scale down factor of the ERTLL1_E trigger, $SF_{\rm ERT\ electron}$:

$$RF_{\rm ERT\ electron} = \frac{N^{\rm scaled}_{\rm MB}}{N^{\rm scaled}_{\rm ERT\ electron} \times (SF_{\rm ERT\ electron} + 1)}. \quad (5.41)$$

Figure 5.31 shows the rejection factor of the ERT electron trigger for each run. Blue points are the runs passing through the run selection and red points are the runs rejected by the run selection.

Using the number of analyzed ERT electron triggered event and the rejection factor, the equivalent number of MB events is obtained as follows:

$$N^{\rm equiv}_{\rm MB} = RF_{\rm ERT\ electron} \times N^{\rm analyzed}_{\rm ERT\ electron}. \quad (5.42)$$

The obtained equivalent number of MB events for each run group is shown in Table 5.7. The total equivalent number of MB events is 5.421×10^9 and it corresponds to a sampled luminosity of about 1.9 nb^{-1}.

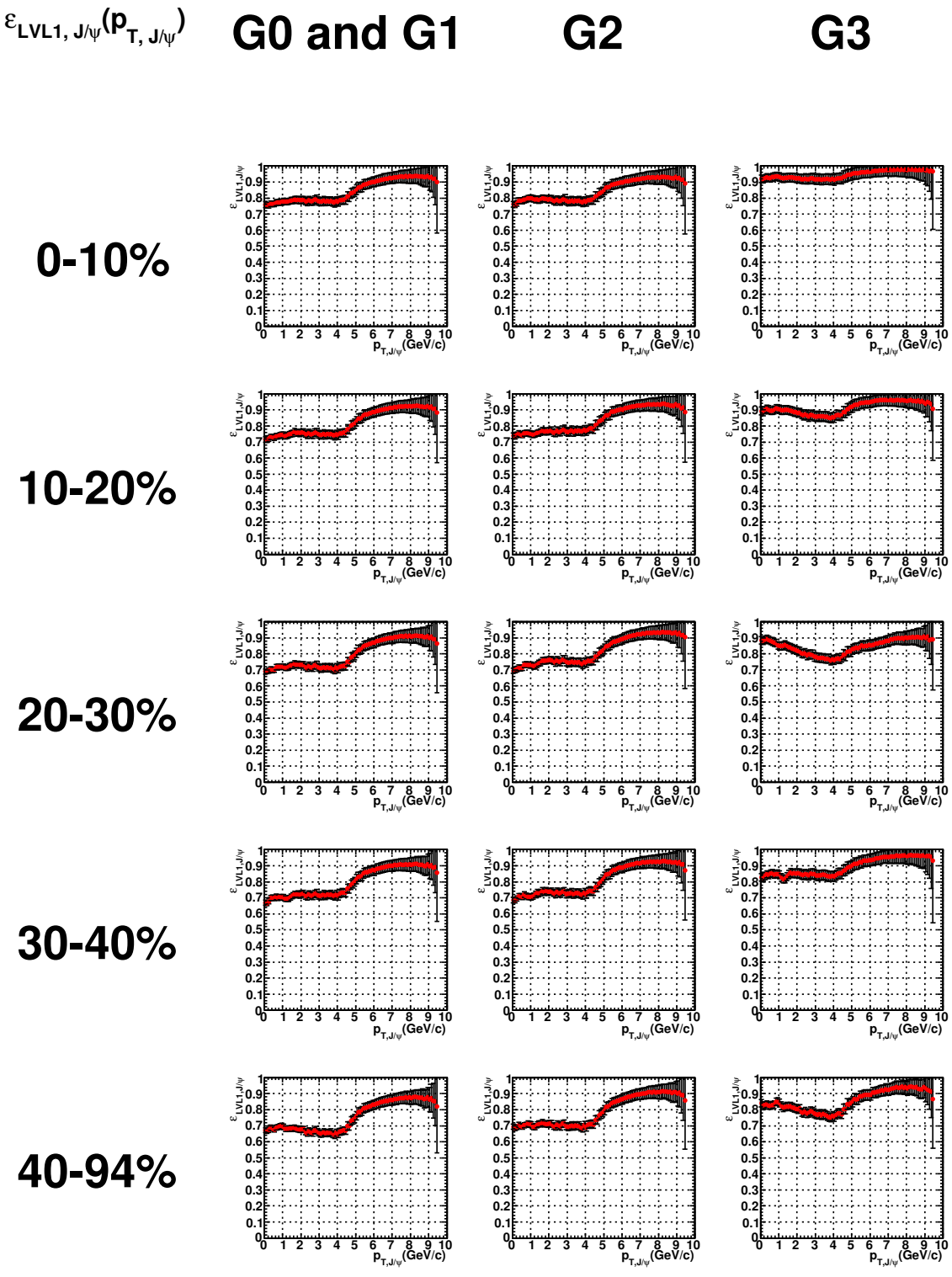

Figure 5.28: J/ψ trigger efficiency including random benefit for each Centrality and run group.

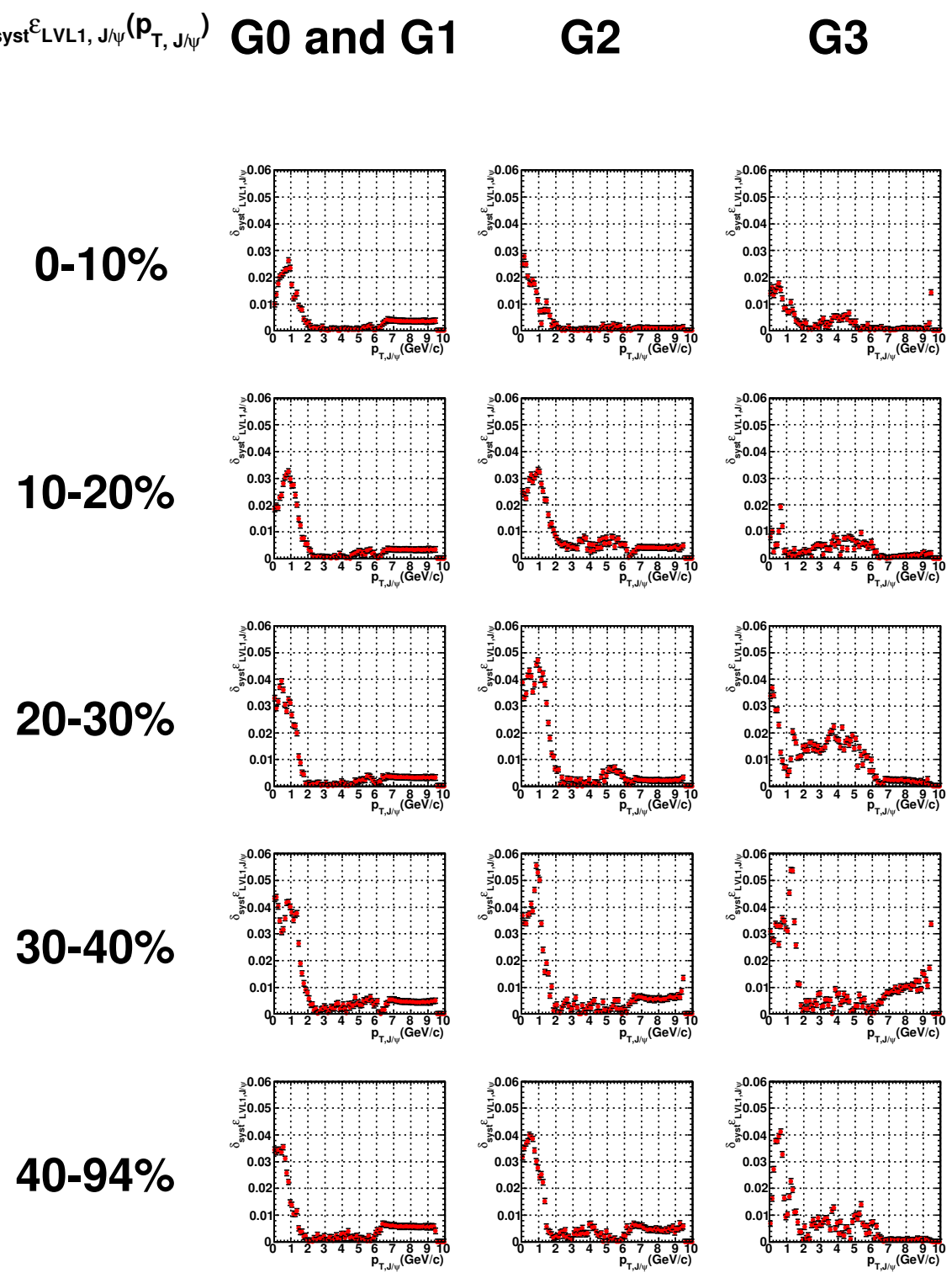

Figure 5.29: Difference between the J/ψ trigger efficiency including random benefit obtained from the histograms of the single electron trigger efficiency and that from the fitted functions of the single electron trigger efficiency.

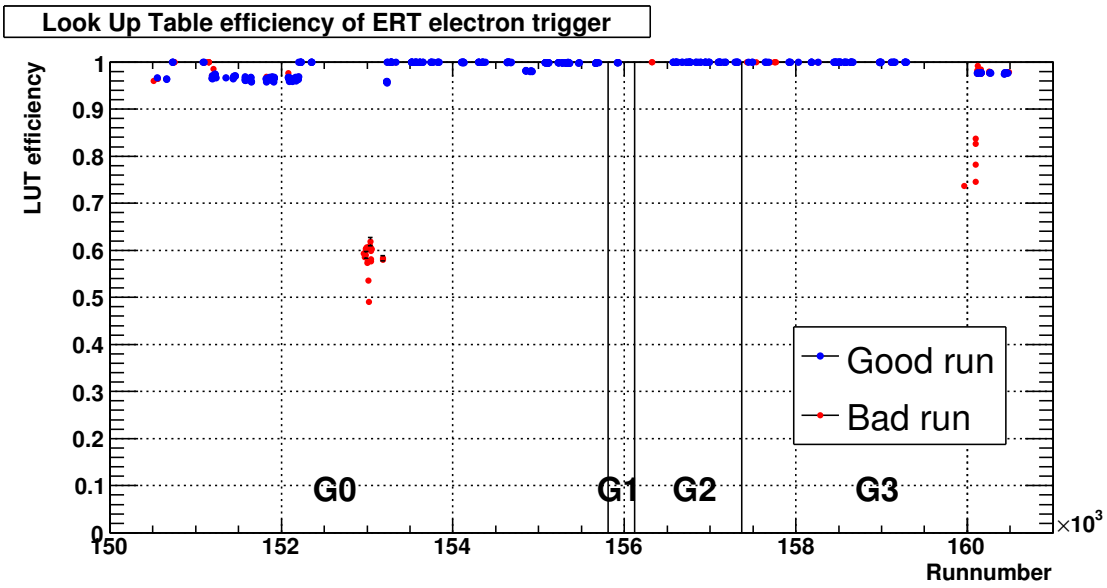

Figure 5.30: Efficiency of the look-up table of the ERT electron trigger.

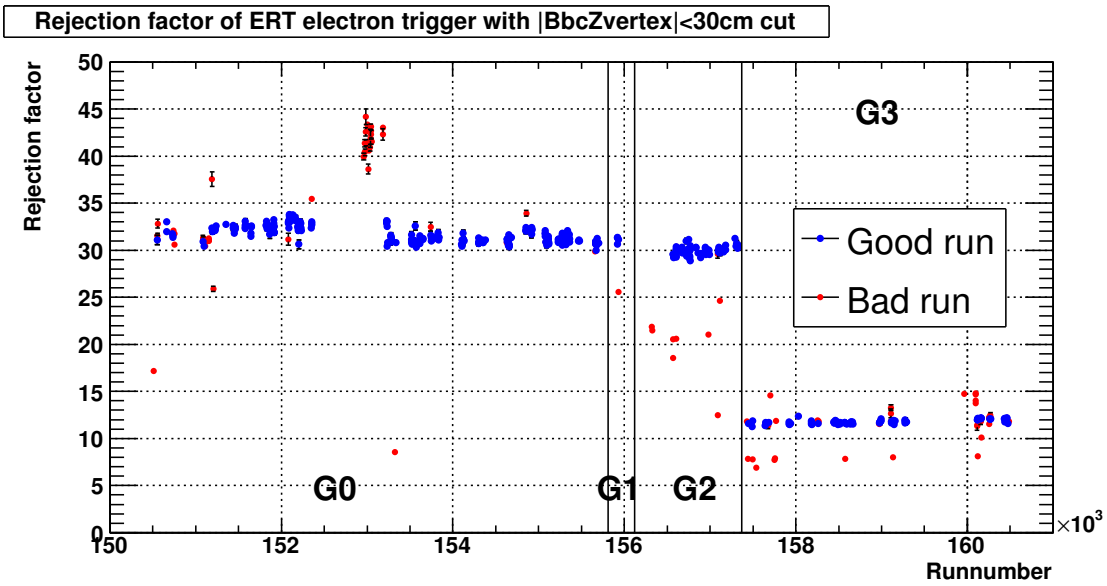

Figure 5.31: The rejection factor of the ERT electron trigger.

Run group	The number of good runs	$N_{\mathrm{ERT}}^{\mathrm{analyzed}}$	$N_{\mathrm{MB}}^{\mathrm{equiv}}$
G0	220	1.094×10^{8}	3.371×10^{9}
G1	4	0.051×10^{8}	0.158×10^{9}
G2	50	0.228×10^{8}	0.684×10^{9}
G3	83	0.938×10^{8}	1.109×10^{9}
Total	357	2.311×10^{8}	5.421×10^{9}

Table 5.7: The equivalent number of MB events, $N_{\mathrm{MB}}^{\mathrm{equiv}}$.

5.8.4 Difference of EMCal Matching Parameters between Real Data and Simulation

The differences of EMCal matching parameters, dep, emcsdphi_e and emcsdz_e, between the real data and simulation were estimated with the number of J/ψ by varying the cut threshold for each matching parameter. Keeping other cuts, the cut threshold for dep was varied from -5 to 5 as shown in Fig. 5.32. The numbers of J/ψ of the real data and simulation were normalized with the dep > -5 cut. With the standard cut (dep > -2), the number of J/ψ of the real data is greater than that of the simulation by $+2.8\%$ and this value is used for the correction. As well as the case of dep, the differences of emcsdphi_e and emcsdz_e were estimated with the normalizations with the emcsdphi_e < 5 and emcsdz_e < 5 cuts. The difference between the real data and simulation with the standard cut (emcsdphi_e < 4 and emcsdz_e < 4) is -0.2% for emcsdphi_e and -1.6% for emcsdz_e. The total correction factor is 1.0% and this total correction factor, 1.0%, is assigned as the systematic error of EMCal matching parameters.

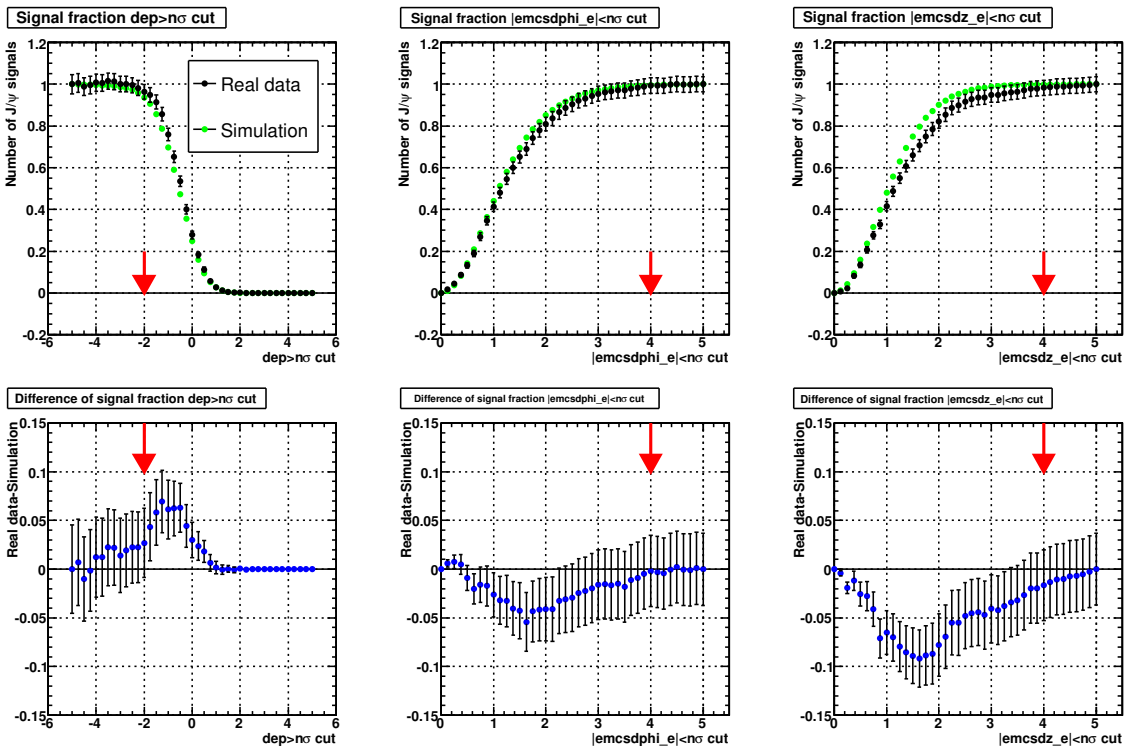

Figure 5.32: Difference of matching parameters between real data and simulation using reconstructed J/ψ.

5.8.5 Difference of RICH n0 and n1 between Real Data and Simulation

The reconstructed invariant mass spectrum of e^+e^- pairs has a peak at $\sim$20 MeV/c^2. This peak is produced by the γ conversion by the Be beam pipe. This highly pure electron sample is used to study the electron identification parameter.

Since the track reconstruction algorithm assumes that all primary and secondary tracks come from the collision vertex, electrons and positrons produced at off-vertex are reconstructed with wrong momenta. This situation is schematically shown in Fig. 5.33. As a result, the conversion pair acquires the fake invariant mass proportional to the

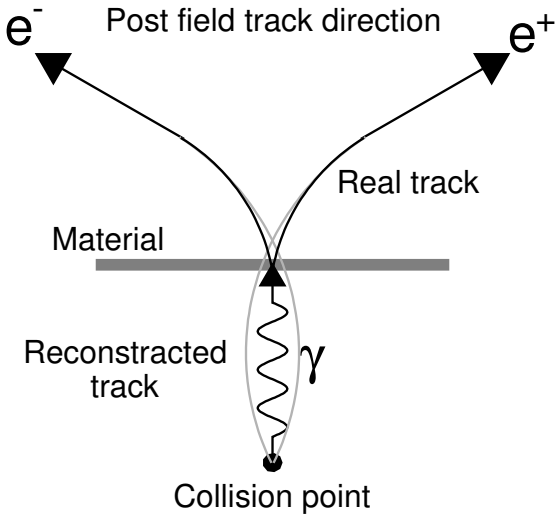

Figure 5.33: Production of a conversion electron pair.

radial distance between the photon conversion point and the collision vertex. The solid histogram in the left panel of Fig. 5.34 shows the invariant mass spectrum of e^+e^- pairs with the standard eID cut. The peak around 0.020 MeV/c^2 is the conversion pairs from the beam pipe and the residual components with the lighter mass than the conversion pairs are mainly from π^0 Dalitz decay ($\pi^0 \to e^+e^-\gamma$). Since the decay plane of the conversion pair is perpendicular to the magnetic field along the z-axis, the conversion component is separated from the π^0 Dalitz decay component using the angle between the decay plane and the z-axis, ϕ_v. The angle ϕ_v is obtained from as follows:

$$\vec{u} = \frac{\vec{p}_{e^+} + \vec{p}_{e^-}}{|\vec{p}_{e^+} + \vec{p}_{e^-}|}, \tag{5.43}$$

$$\vec{v} = \frac{\vec{p}_{e^+} \times \vec{p}_{e^-}}{|\vec{p}_{e^+} + \times\vec{p}_{e^-}|}, \tag{5.44}$$

$$\vec{w} = \vec{u} \times \vec{v}, \tag{5.45}$$

$$\vec{e}_z = (0,\ 0,\ 1), \tag{5.46}$$

$$\vec{a} = \frac{\vec{u} \times \vec{e}_z}{|\vec{u} \times \vec{e}_z|}, \tag{5.47}$$

$$\phi_v = \cos^{-1}(\vec{u} \cdot \vec{a}). \quad (5.48)$$

The shaded histogram in the left panel of Fig. 5.34 shows the invariant mass spectrum of e^+e^- pairs with the standard eID cut and the $\phi_v < 0.25$ cut. A clear peak from the conversion pairs is can be seen with the ϕ_v cut. The vertical lines in the panel indicates the signal region ($0.012 < M_{e^+e^-} < 0.029$ GeV/c^2) and the side band regions ($0.004 < M_{e^+e^-} < 0.012$ GeV/c^2 and $0.029 < M_{e^+e^-} < 0.037$ GeV/c^2). The middle and right panels of Fig. 5.34 shows the n0 and n1 of the conversion electrons in the real data and the single electrons in the simulation. In the real data, the contribution from combinatorial background is subtracted using the side band components. The p_T distribution in the simulation was weighted so that the real data and simulation have the same p_T distribution.

The n0 ≥ 2 cut is not applied in the middle panel to estimate the loss by the n0 ≥ 2 cut. The fraction of n0 < 2 is 3.8% for the real data and 2.4% for the simulation. The loss by the n1 ≥ 2 cut is estimated by fitting of Gaussian to the distribution. The estimated fraction of n1 < 2 is 0.6% for the real data and 0.1% for the simulation. The combined difference between the real data and simulation in n0 and n1 is 1.9% and this 1.9% is corrected in the J/ψ yield and is used as the systematic error of RICH parameters.

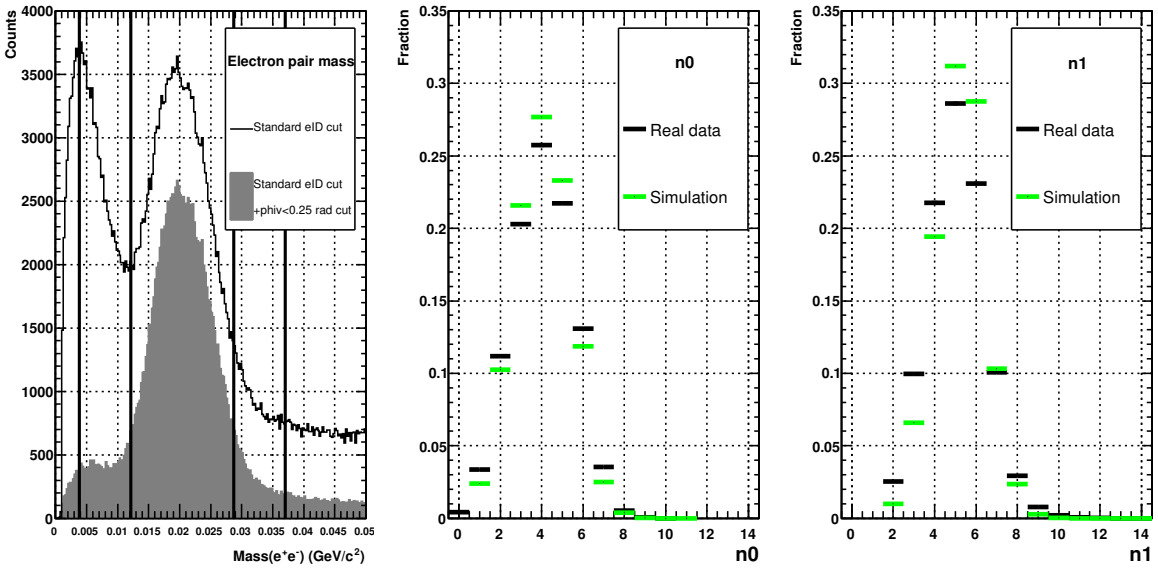

Figure 5.34: Difference of RICH n0 and n1 parameters between real data and simulation using conversion electrons.

5.9 Systematic Error Evaluation

5.9.1 Rapidity Distribution

Since the $\varepsilon_{acc,J/\psi\to e^+e^-}$ was calculated with the flat rapidity distribution, the systematic error due to the uncertainty of the rapidity distribution of J/ψ was evaluated. In

this evaluation, two types of the J/ψ rapidity distribution were assumed, which were obtained from PYTHIA with two kinds of parton distribution functions GRV 94L and CTEQ 5L. The differences the $\varepsilon_{acc,J/\psi\to e^+e^-}$ with GRV 94L and CTEQ 5L from that with the flat rapidity distribution were found to be +0.9% and +1.3%, respectively. The systematic error of the J/ψ rapidity distribution is assigned to be 1.3%.

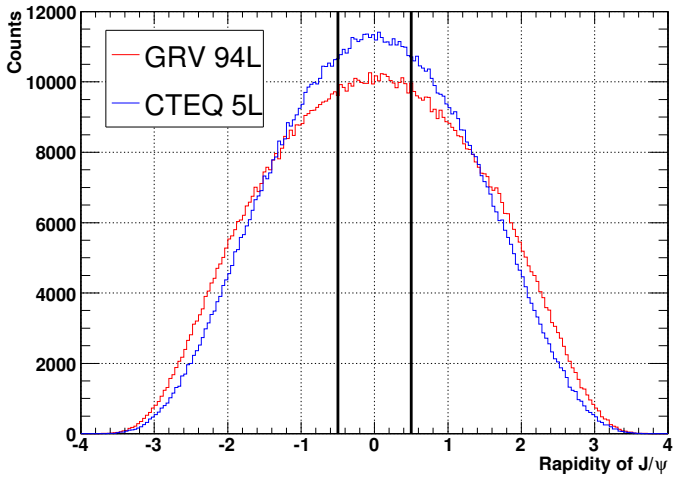

Figure 5.35: The rapidity distribution obtained from PYTHIA with the two kinds of parton distribution functions, GRV 94L and CTEQ 5L.

5.9.2 Momentum Smearing

Since the momentum resolution of the DC and PC1 is limited, the reconstructed p_T distribution of J/ψ is smeared from the initial p_T distribution. The measured p_T distribution was used as an initial p_T distribution and the smearing effect was evaluated by the PISA simulation. The RMS of the ratio of the reconstructed yield to the initial yield is found to be 2% and this RMS value of 2% is accepted as the systematic error of the momentum smearing.

5.9.3 Run-by-Run Fluctuation

The run-by-run fluctuation of the acceptance and reconstruction efficiency was estimated by the number of electron and positron pairs per event with the standard eID cut and the $p_T > 0.7$ GeV/c cut. The number of electron and positron pairs is defined as the sum of the number of pairs with electrons in the west arm and positrons in the east arm, and the number of pairs with electrons in the east arm and positrons in the west arm.

Figure 5.36 and Fig. 5.37 show the number of pairs in the MB data and the ERT electron data as a function of runnumber, respectively.

Table 5.8 shows the RMS values of the number of pairs for each data set and each run group. The average RMS of the ERT electron data, 3.5%, is assigned as the systematic error of the run-by-run fluctuation of the acceptance and reconstruction efficiency.

Run group	RMS of the number of electron pairs	
	MB	ERT electron
G0 and G1	3.0%	3.6%
G2	2.4%	2.9%
G3	5.2%	3.9%
Average	3.3%	3.5%

Table 5.8: Run-by-run fluctuation.

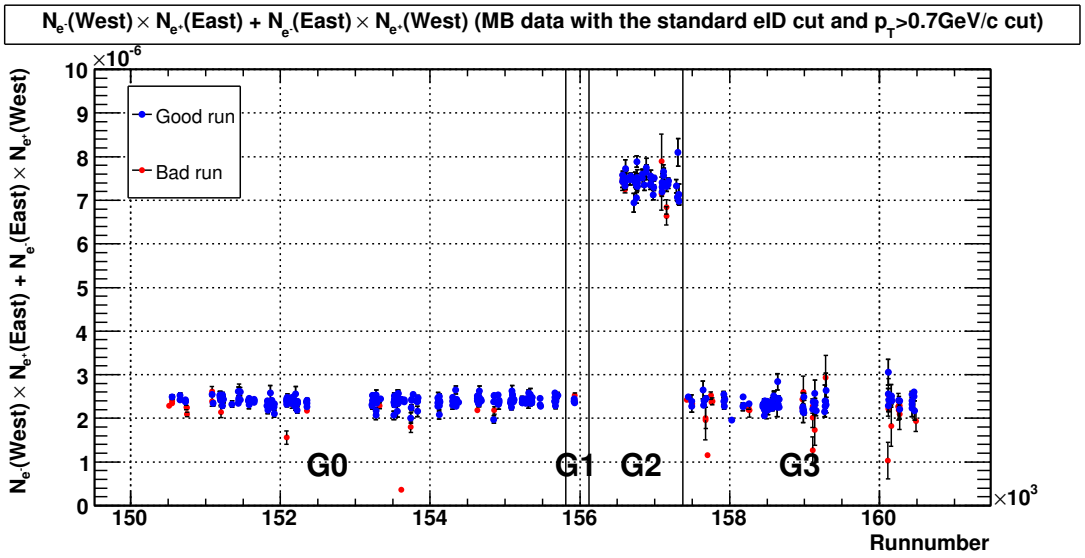

Figure 5.36: The number of electron pairs in the MB triggered data with the standard cut and the $p_T > 0.7$ GeV/c cut.

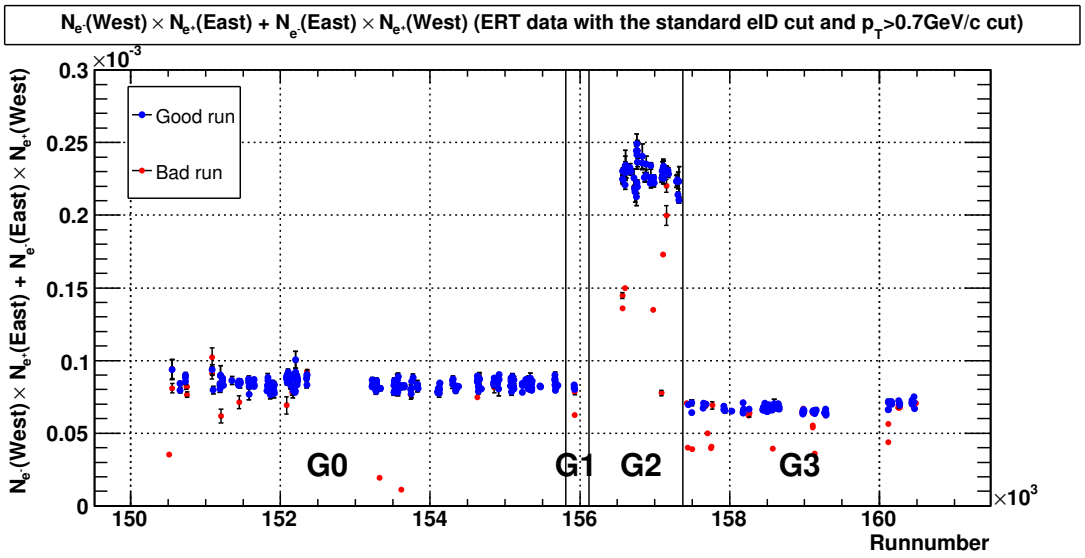

Figure 5.37: The number of electron pairs in the ERT electron triggered data with the standard cut and the $p_T > 0.7$ GeV/c cut.

5.9.4 Systematic Error Summary

The systematic error are summarized in Table 5.9. The systematic errors were classified into two groups, "Type A" and "Type B". "Type A" is the point-to-point uncorrelated systematic error, which is independent for Centrality and p_T. "Type B" is the point-to-point correlated systematic error with respect to the Centrality and/or p_T for which the points can move coherently by the same amount.

Source	Systematic error	Type
Signal extraction	5%	A
N_{coll}	11.1–12.5%	B
Fiducial cut	4.3%	B
Internal bremsstrahlung	1%	B
Embedding efficiency	1.9%	B
ERT electron trigger efficiency	4%	B
EMCal matching parameters	1.0%	B
RICH parameters	1.9%	B
Rapidity distribution	1.3%	B
Momentum smearing	2%	B
Run-by-run fluctuation	3.5%	B

Table 5.9: Summary of the systematic errors.

5.10 Results

5.10.1 Invariant Yield

Invariant yield of J/ψ as a function of p_T was obtained for 0–94%(MB)/0–20%/20–40%/40–60%/60-94% Centrality bins based on Eq. (5.5). Figure 5.38 shows the invariant yield for MB (black, $\times 10^2$ scale up), 0–20$ (red), 20–40% (gree $\times 10$ scale down), 40–60% (blue $\times 10^2$ scale down) and 60–94% (yellow, $\times 10^3$ scale down). The values of mean value, statistical error and systematic error are summarized in Table E.1 in Appendix E.

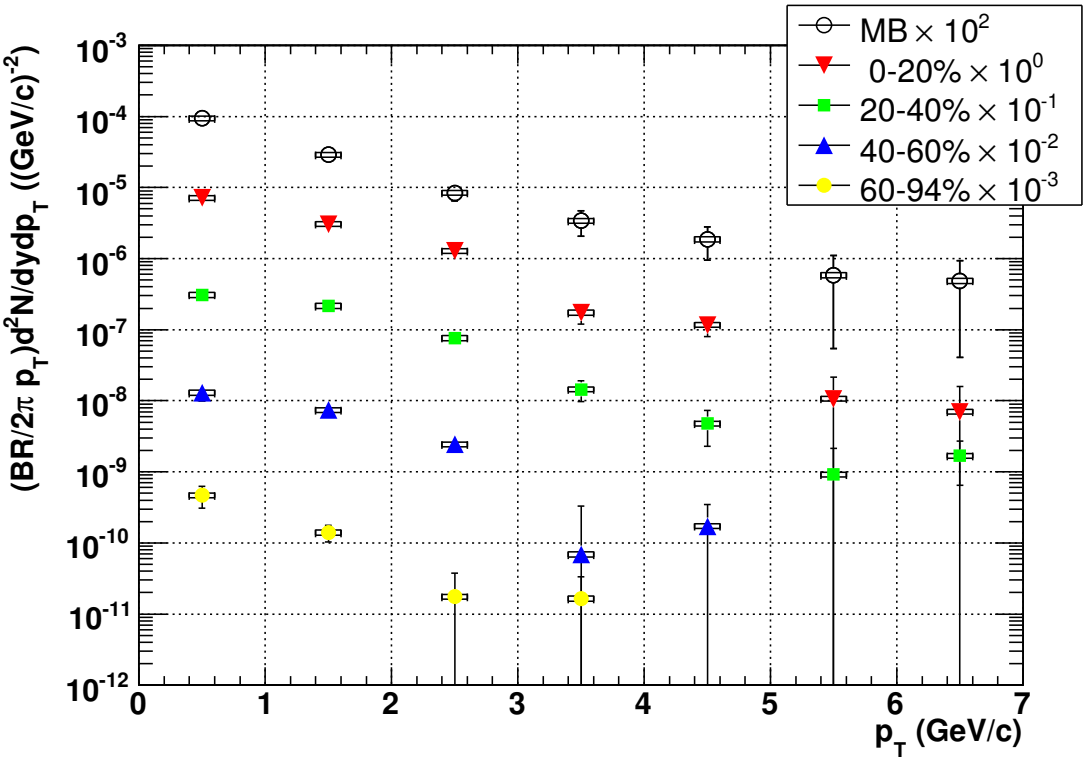

Figure 5.38: Invariant yield of J/ψ as a function of p_T for 0–94%(MB), 0–20%, 20–40%, 40–60% and 60-94%. The bars represent the quadratics sum of the statistical errors and uncorrelated systematic errors. The brackets represent the correlated systematic errors.

5.10.2 Nuclear Modification Factor as a Function of p_T

The nuclear modification factor R_{AA} as a function of p_T was obtained using the results of J/ψ in $p+p$ collisions in Run-5 [7]. Figure 5.39 shows R_{AA} as a function of p_T for 0–94%(MB), 0–20%. 20–40%, 40–60% and 60–94% Centrality bins. The bars correspond to the statistical errors and the brackets correspond to the systematic error. The statistical and systematic errors of the invariant yield in $p+p$ collision are expressed by the shaded boxes. The values of mean value, statistical error and systematic error for each point are summarized in Table E.4 in Appendix E.

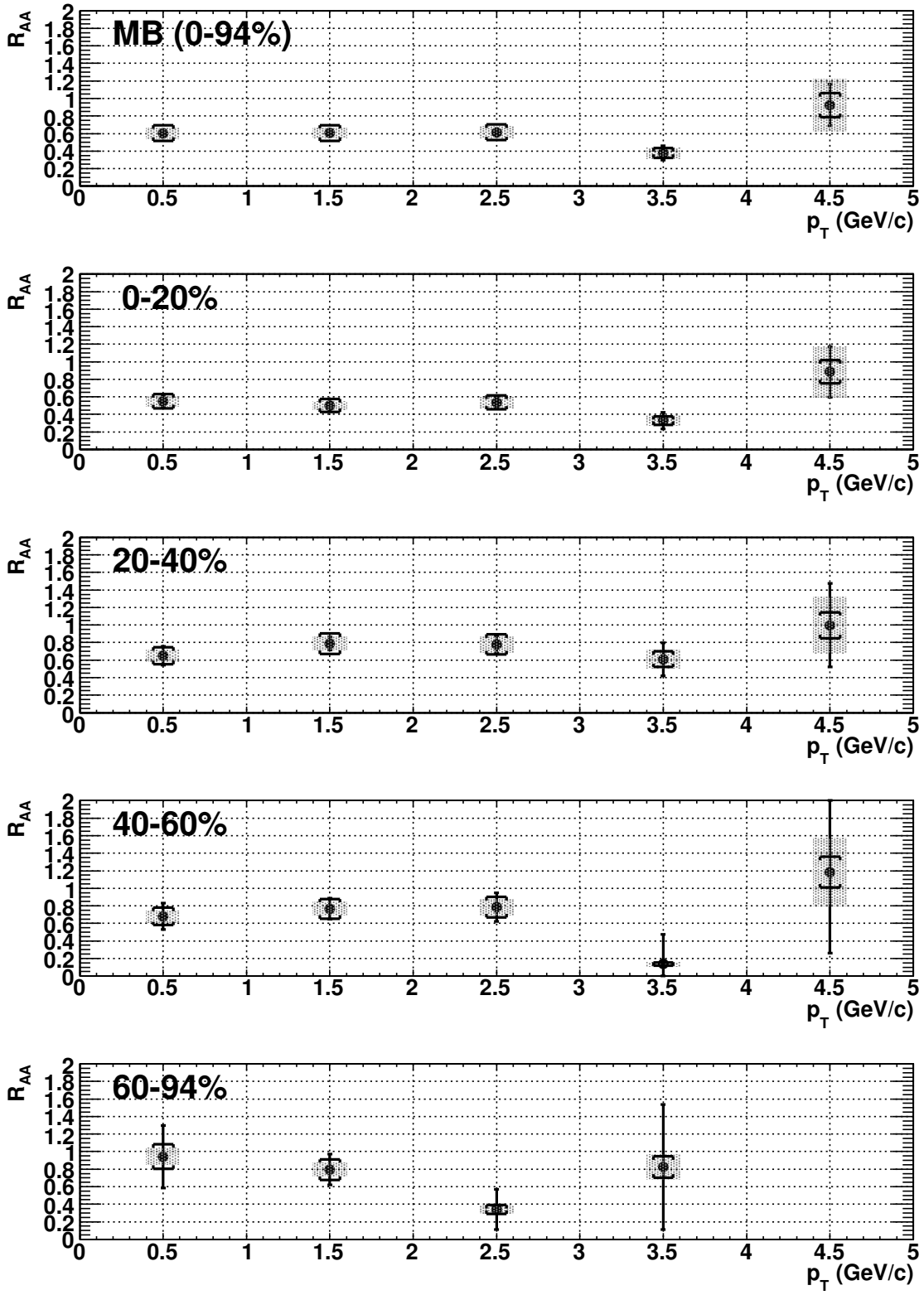

Figure 5.39: The nuclear modification factor R_{AA} of J/ψ as a function of p_T for MB, 0–20%. 20–40%, 40–60% and 60–94%. The bars are the statistical errors and the brackets are the systematic error. The shaded boxes are the quadratic sums of the statistical and systematic errors of the invariant yield in $p + p$ collision.

5.10.3 Integrated Invariant Yield

Integrated invariant yield defined as Eq. (5.7) was obtained by integrating the invariant yield as a function of p_T shown in Fig 5.38. Table 5.10 shows $BRdN/dy$ of J/ψ for each Centrality bin. The statistical and systematic errors are shown.

Centrality(%)	N_{part}	N_{coll}	$BRdN/dy \pm$ stat $\pm$ uncorr. syst $\pm$ corr. syst
0–94 (MB)	35	52	4.9e-06 ± 4.3e-07 ± 2.5e-07 ± 3.9e-07
0–10	98	183	1.0e-04 ± 8.0e-06 ± 5.0e-06 ± 7.9e-06
10–20	74	121	8.0e-05 ± 6.2e-06 ± 4.0e-06 ± 6.3e-06
20–30	53	76	6.1e-05 ± 4.9e-06 ± 3.0e-06 ± 4.8e-06
30–40	37	47	4.6e-05 ± 4.1e-06 ± 2.3e-06 ± 3.6e-06
40–50	25	28	2.7e-05 ± 3.3e-06 ± 1.4e-06 ± 2.1e-06
50–60	17	16	1.3e-05 ± 2.1e-06 ± 6.3e-07 ± 9.9e-07
60–94	6	5	2.5e-06 ± 4.5e-07 ± 1.2e-07 ± 1.9e-07

Table 5.10: Integrated invariant yield, $BRdN/dy$, of J/ψ for MB and 0–10%/10–20%/20–30%/30–40%/40–50%/50–60%/60–94% Centrality bins. The first error in the right column is statistical, second is uncorrelated systematic and third is correlated systematic errors.

5.10.4 Centrality Dependence of R_{AA}

Calculation of the nuclear modification factor (R_{AA}) used the Run-5 $p+p$ J/ψ result [7] as the base line. The production cross section and integrated yield of J/ψ in $p+p$ collisions are as follows:

$$BR\frac{d\sigma}{dy} = 44.3 \pm 1.4(\text{stat}) \pm 5.1(\text{syst}) \pm 4.5(\text{norm}) \text{ nb}, \quad (5.49)$$

$$BR\frac{dN}{dy} = 1.05 \pm 0.03(\text{stat}) \pm 0.16(\text{syst}). \quad (5.50)$$

Figure 5.40 show R_{AA} as a function of the number of participants. Centrality bins are 0–10%, 10–20%, 20–30%, 30–40%, 40–50%, 50–60% and 60–94%. The shaded boxes are the quadratic sums of the statistical and systematic errors of the invariant yield in $p+p$ collision. Table 5.11 shows R_{AA} of J/ψ for each Centrality bin.

5.10.5 Mean p_T Square $\langle p_T^2 \rangle$

The mean p_T square, $\langle p_T^2 \rangle$, for each Centrality was obtained by fitting the invariant yield with the Kaplan function defined as follows:

$$f_{Kaplan}(p_T) = A\left(1 + \frac{p_T^2}{(n-2)B}\right)^n, \quad (5.51)$$

where B is $\langle p_T^2 \rangle$.

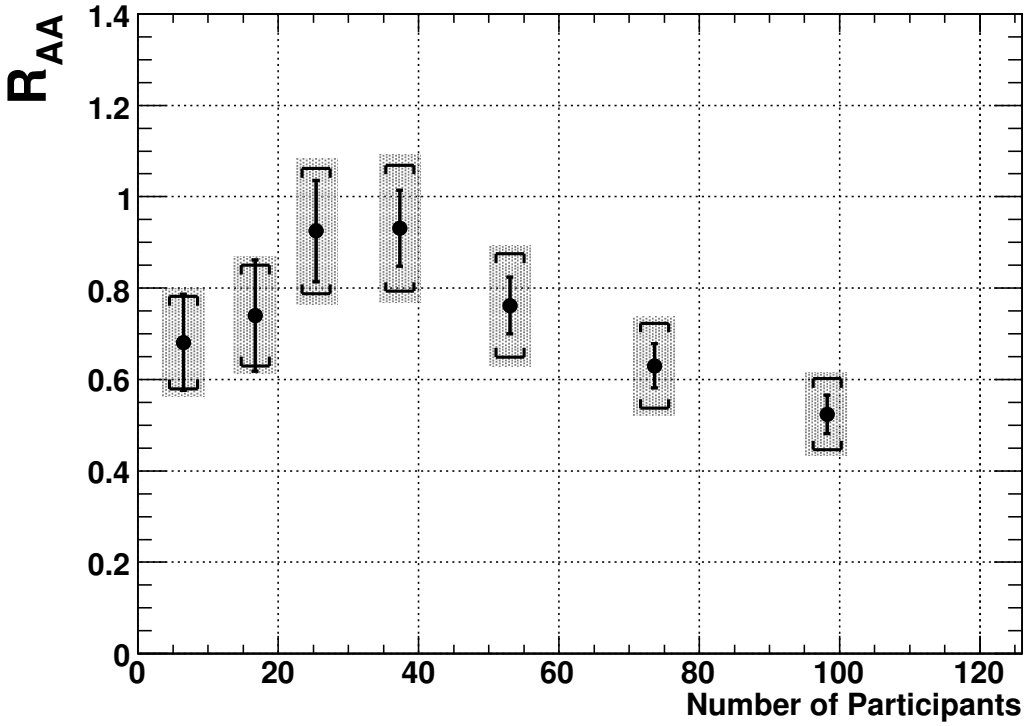

Figure 5.40: The nuclear modification factor, R_{AA}, of J/ψ in Cu+Cu collisions as a function of the number of participants. The bars and brackets represent the statistical errors and systematic errors, respectively. The brackets represent the correlated systematic errors. The shaded boxes are the quadratic sums of the statistical and systematic errors of the invariant yield in $p+p$ collision.

Centrality(%)	N_{part}	N_{coll}	$R_{AA} \pm$ stat $\pm$ total syst $\pm\, p+p$ ref.
0–94 (MB)	35	52	0.66 ± 0.03 ± 0.10 ± 0.12
0–10	98	183	0.52 ± 0.04 ± 0.08 ± 0.09
10–20	74	121	0.63 ± 0.05 ± 0.09 ± 0.11
20–30	53	76	0.76 ± 0.06 ± 0.11 ± 0.13
30–40	37	47	0.93 ± 0.08 ± 0.14 ± 0.16
40–50	25	28	0.93 ± 0.11 ± 0.14 ± 0.16
50–60	17	16	0.74 ± 0.12 ± 0.11 ± 0.13
60–94	6	5	0.68 ± 0.11 ± 0.10 ± 0.12

Table 5.11: Centrality dependence of the nuclear modification factor R_{AA} of J/ψ in Cu+Cu collisions. $p+p$ ref. error is the quadratic sum of the statistical and systematic errors of the integrated invariant yield in $p+p$ collision.

Figure 5.41 shows $\langle p_T^2 \rangle$ as a function of the number of participants N_{part} for 0–20%,20–40%, 40–60% and 60–94% Centrality bins. The bars are the statistical and fitting errors and the brackets are the systematic errors. Table 5.12 shows $\langle p_T^2 \rangle$ for each Centrality bin.

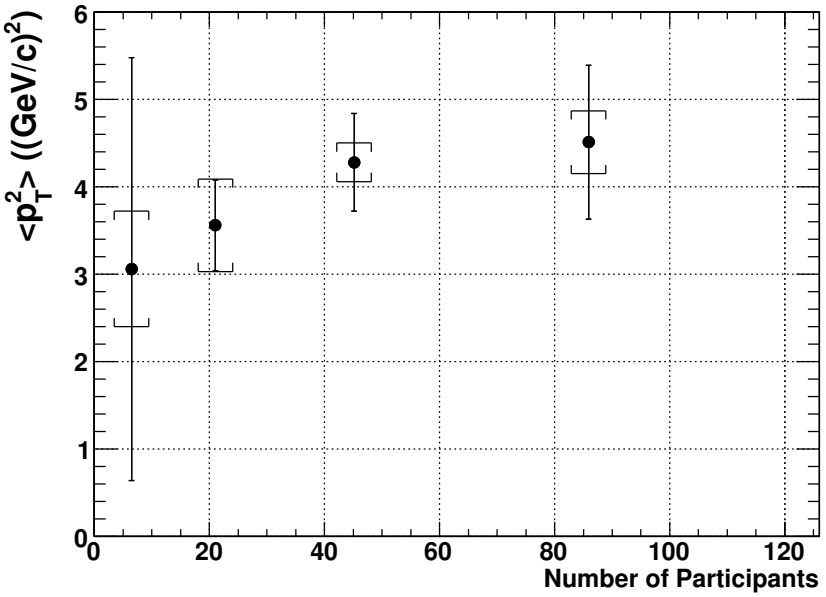

Figure 5.41: The mean p_T square, $\langle p_T^2 \rangle$, as a function of the number of participants N_{part} for 0–20%,20–40%, 40–60% and 60–94% Centrality bins. The bars are the statistical and fitting errors and the brackets are the systematic errors.

Centrality(%)	$\langle p_T^2 \rangle \pm$ stat $\oplus$ fit $\pm$ syst $((\mathrm{GeV}/c)^2)$
0–20	$4.5 \pm 0.9 \pm 0.4$
20–40	$4.3 \pm 0.6 \pm 0.2$
40–60	$3.6 \pm 0.5 \pm 0.5$
60–94	$3.1 \pm 2.4 \pm 0.7$

Table 5.12: The mean p_T square, $\langle p_T^2 \rangle$-N_{part}, for each centrality. The error of stat+fit is the sum of statistical error and fitting error.

5.10.6 Difference from Public Results

Two independent analyses of J/ψ production in Cu+Cu collisions were performed by a graduate student from Florida State University (FSU) in the United States and the author. As shown in Fig. 5.42, results from the two independent analyses are consistent within errors and the results of the graduate student of FSU are used in the submitted paper [9].

The main differences of the two analyses are the fiducial cut and the run selection. The author used tighter cut and selection than the FSU student and the number of J/ψ of the author's analysis is smaller than that of the FSU student's analysis by ~40%. The reason why the author used the tight fiducial cut and run selection is to obtain results with reliable detector parts. The eID cut parameters and the calibrations of EMCal matching parameters are almost the same in the two analyses. The same signal extraction method is used. The correction factors are obtained with the different fiducial cuts and the different run selections with almost identical methods in the two analyses.

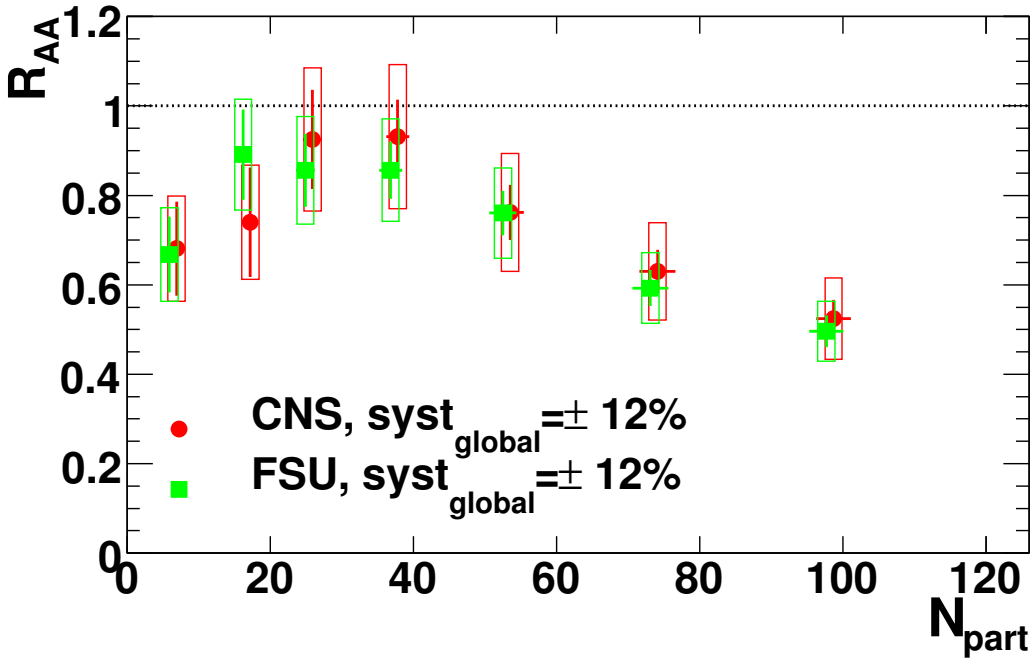

Figure 5.42: The nuclear modification factor, R_{AA}, of J/ψ in Cu+Cu collisions as a function of the number of participants from the two independent analyses. Red points (CNS) represents the author's results and green points (FSU) represents the result of the graduate student from Florida State University (FSU). The offset of N_{part} is to avoid overlapping.

Chapter 6

Data Analysis 2 - χ_c Meson in $p+p$ Collisions

The feed-down fraction of χ_c into J/ψ has been measured in $p+p$ collisions at $\sqrt{s_{NN}} =$ 200 GeV via the decay mode of $\chi_c \to J/\psi\gamma \to e^+e^-\gamma$. The data collected with ERT electron and photon triggers in Run-5 and Run-6 was used for the analysis. In this chapter, the analysis of χ_c will be described.

In section 6.1, the procedure of χ_c measurement is described. The method of the χ_c signal reconstruction is described in section 6.2. One major issue of the χ_c analysis is low-p_T photon detection and it is checked with π^0 mesons as described in section 6.3. The evaluation of χ_c acceptance is described in section 6.4. Section 6.5 describes how to check the signal reconstruction with a realistic event generator. In section 6.6, the χ_c reconstruction with the real data is described. Systematic errors are summarized in section 6.7.

6.1 Introduction

The fraction of J/ψ from the χ_c decays is represented by the ratio R_{χ_c} which is defined as follows.

$$R_{\chi_c} = \frac{1}{\sigma_{J/\psi}} \sum_{J=0}^{2} BR\left(\chi_{cJ} \to J/\psi\gamma\right) \sigma_{\chi_{cJ}}, \tag{6.1}$$

where BR and σ are the branching ratio of the $\chi_{cJ} \to J/\psi\gamma$ decay and cross section of the charmonium, respectively. The branching ratios of χ_c mesons are shown in Table 2.2. The branching ratio of χ_{c0} is small (1.30±0.11%) and its contribution is usually neglected.

6.1.1 How to Measure R_{χ_c}

To measure R_{χ_c}, firstly, the $J/\psi \to e^+e^-$ decay ($BR = (5.94 \pm 0.06)\%$ [19]) is detected with the pair mass range of $2.9 < M_{ee} < 3.3$ GeV/c^2. Secondly, the $e^+e^-\gamma$ mass is reconstructed and the mass difference, $\Delta M \equiv M_{ee\gamma} - M_{ee}$ is calculated. The χ_c mass peak locates at $\Delta M \sim 0.44$ GeV/c^2. Thirdly, we correct the acceptance of the

$\chi_c \to J/\psi$ decay event by event.

$$R_{\chi_c} = \frac{BR\left(\chi_c \to J/\psi\gamma\right) BR\left(J/\psi \to e^+e^-\right) dN_{\chi_c}}{dy} \Big/ \frac{BR\left(J/\psi \to e^+e^-\right) dN_{J/\psi}}{dy} \quad (6.2)$$

$$= \frac{\frac{1}{N_{evt}} \frac{1}{\Delta y_{\chi_c}} \sum_{i=1}^{N_{\chi c}} \frac{1}{\varepsilon_{acc,\chi_c \to J/\psi\gamma \to ee\gamma}\left(p_{T,\chi_c}\right)} \frac{1}{\varepsilon_{LVL1,\chi_c}\left(p_{T,\chi_c}\right)}}{\frac{1}{N_{evt}} \frac{1}{\Delta y_{J/\psi}} \sum_{j=1}^{N_{J/\psi}} \frac{1}{\varepsilon_{acc,J/\psi \to ee}\left(p_{T,J/\psi}\right)} \frac{1}{\varepsilon_{LVL1,J/\psi}\left(p_{T,J/\psi}\right)}}, \quad (6.3)$$

where $\varepsilon_{acc,\chi_c \to J/\psi\gamma \to ee\gamma}\left(p_{T,\chi_c}\right)$ is the χ_c acceptance including efficiency as a function of p_T of χ_c and $\varepsilon_{acc,J/\psi \to ee}(p_{T,J/\psi})$ is the J/ψ acceptance including efficiency as a function of p_T of J/ψ. $\varepsilon_{LVL1,\chi_c}$ and $\varepsilon_{LVL1,J/\psi}$ are ERT LVL1 trigger efficiencies of χ_c and J/ψ, respectively. N_{evt} is the number of analyzed events and Δy is the rapidity gap used in the acceptance (ε_{acc}) calculation. The ERT LVL1 trigger efficiency of χ_c, $\varepsilon_{LVL1,\chi_c}(p_{T,\chi_c})$, can be replaced by $\varepsilon_{LVL1,J/\psi}\left(p_{T,J/\psi}\right)$. The acceptance of χ_c, $\varepsilon_{acc,\chi_c \to J/\psi\gamma \to ee\gamma}(p_{T,\chi_c})$, can be divided into two parts,

$$\varepsilon_{acc,\chi_c \to J/\psi\gamma \to ee\gamma}\left(p_{T,\chi_c}\right) = \varepsilon^{J/\psi \text{ detected}}_{acc,\chi_c \to J/\psi\gamma}\left(p_{T,\chi_c}\right) \varepsilon_{acc,J/\psi \to ee}\left(p_{T,J/\psi}\right), \quad (6.4)$$

where $\varepsilon^{J/\psi \text{ detected}}_{acc,\chi_c \to J/\psi\gamma}\left(p_{T,\chi_c}\right)$ is the χ_c conditional efficiency if J/ψ is detected. Using Eq. (6.4), R_{χ_c} can be represented by

$$R_{\chi_c} = \frac{\frac{1}{\Delta y_{\chi_c}} \sum_{i=1}^{N_{\chi c}} \frac{1}{\varepsilon^{J/\psi \text{ detected}}_{acc,\chi_c \to J/\psi\gamma}\left(p_{T,\chi_c}\right) \varepsilon_{acc,J/\psi \to ee}\left(p_{T,J/\psi}\right)} \frac{1}{\varepsilon_{LVL1,J/\psi}\left(p_{T,J/\psi}\right)}}{\frac{1}{\Delta y_{J/\psi}} \sum_{i=1}^{N_{J/\psi}} \frac{1}{\varepsilon_{acc,J/\psi \to ee}\left(p_{T,J/\psi}\right)} \frac{1}{\varepsilon_{LVL1,J/\psi}\left(p_{T,J/\psi}\right)}},$$

$$= \frac{1}{N_{J/\psi}} \left\langle \frac{1}{\varepsilon_{acc,J/\psi \to ee} \varepsilon_{LVL1,J/\psi}} \right\rangle^{-1} \times$$

$$\frac{\Delta y_{J/\psi}}{\Delta y_{\chi_c}} \sum_{i=1}^{N_{\chi c}} \frac{1}{\varepsilon^{J/\psi \text{ detected}}_{acc,\chi_c \to J/\psi\gamma}\left(p_{T,\chi_c}\right)} \frac{1}{\varepsilon_{acc,J/\psi \to ee}(p_{T,J/\psi}) \varepsilon_{LVL1,J/\psi}(p_{T,J/\psi})}, \quad (6.5)$$

where $\langle \cdots \rangle$ means the average over J/ψ.

The ERT LVL1 trigger efficiency of J/ψ, $\varepsilon_{LVL1,J/\psi}(p_{T,J/\psi})$, is evaluated with the real data. The acceptance of J/ψ, $\varepsilon_{acc,J/\psi \to ee}$, and conditional efficiency of χ_c, $\varepsilon^{J/\psi \text{ detected}}_{acc,\chi_c \to J/\psi\gamma}$, are estimated using the PISA simulation. PISA is the GEANT3 simulator [124] of the PHENIX detector.

There is irreducible large background and it leads a fake χ_c peak when the statistics are low. An event generator, PYTHIA (version 6.403, [129]), and PISA are used to evaluate the fake χ_c effect and the correction is applied to the raw R_{χ_c} value.

6.2 Reconstruction of χ_c Signal

In this section, cut parameters for the χ_c reconstruction and the adopted mass difference method are described.

6.2.1 Cut Parameters for χ_c

The following cuts were applied to both the real data and simulation for the χ_c search in the decay channel of $\chi_c \to J/\psi\gamma \to e^+e^-\gamma$.

- Event cut
  - |BbcZvertex| <30 cm (collision vertex cut)
- Electron cut
  - n1 ≥ 2 (RICH hit phototube cut, the number of hit phototubes is required to be greater than 1)
  - $p_T > 0.2$ GeV (transverse momentum cut)
  - $0.5 <$ ecore/mom < 2 (E/p cut with EMCal energy and DC momentum)
  - |emcsdphi_e| < 5 (5σ EMCal matching cut in the ϕ direction)
  - |emcsdz_e| < 5 (5σ EMCal matching cut in the z direction)
  - quality == 29||30||31||49||50||51||61||62||63 (Hit quality cut for DC and PC1)
- Electron pair cut
  - $2.9 < M_{ee} < 3.3$ GeV/c^2 (J/ψ mass cut)
- Photon cut
  - ecore > 0.3 GeV (EMCal energy cut)
  - emcchi2 < 2.5 (electromagnetic shower profile cut)
  - $|\text{pemcz}_{\text{charged track}} - \text{emcz}_{\gamma}| > 35$ cm ||
    $|\text{pemcphi}_{\text{charged track}} - \text{emcphi}_{\gamma}| > 0.07$ radian
    (square charged particle veto for the closest DC (drift chamber) track projection point from the centroid of the EMCal cluster)
  - Fiducial cut
  - EMCal (electromagnetic calorimeter) clusters associated with e^+ and e^- from J/ψ are removed using emcid (EMCal cluster ID).

The emcchi2 parameter represents how electromagnetic a shower is and a emcchi2 $<$ 2.7 cut has 90% efficiency for 2 GeV/c electrons. The DC charged particle veto is described in section 6.3.2.

Figure. 6.1 shows the energy distribution of photons at midrapidity in χ_{c1} events by PYTHIA simulation. The energy of photons from the $\chi_{c1} \to J/\psi\gamma$ decay is soft and the energy region is occupied by the large background from the $\pi^0 \to 2\gamma$ decay photons. This large background is one of the main difficulty in the χ_c measurement at RHIC.

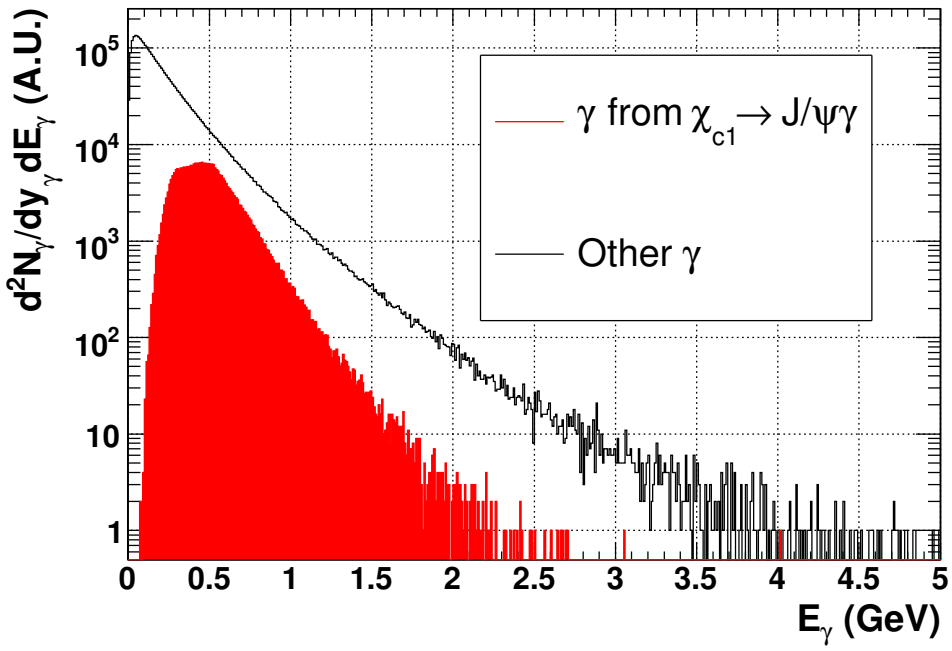

Figure 6.1: The photon energy distribution of photons from the $\chi_{c1} \rightarrow J/\psi\gamma$ decay (red) and background photons, mainly from $\pi^0 \rightarrow 2\gamma$ decay (black), by PYTHIA simulation. The photon rapidity range is $-0.5 < y_\gamma < +0.5$. The input parameters of PYTHIA are described in section 6.5.

Fiducial Cut of EMCal

There exist dead towers, noisy towers and towers with failed energy calibration using π^0 in EMCal and these towers are defined as bad towers. To determine noisy and dead towers, sector by sector distribution of the number of hits per tower were plotted for energy bins 1 GeV wide from 0–10 GeV (for the lowest energy bin, clusters with energy below 0.1 GeV (0.2 GeV) in PbSc (PbGl) were not used). For each energy bin, towers in which the number of hits was greater than the mean plus 10×RMS were declared noisy. Any tower that was declared noisy in any energy bin was declared noisy for the full data sample. The lowest energy bin had a wider distribution, and a 10×RMS cut excludes many towers which were not noisy in higher energy bins. To prevent this, noisy towers in the lowest energy bin were defined as towers with hits greater than the mean plus 30×RMS. Dead towers were defined as towers with hits less than the mean minus 10×RMS. Edge towers are not calibrated and are thus declared bad. A 3×3 block of towers around any bad tower is excluded. Figure 6.2 represents the bad tower definition schematically. In Run-5 (Run-6), 22% (24%) of the EMCal was masked (14% (17%) of non-edge towers).

EMCal tower ID is converted into the position at the EMCal plane (emcz and emcphi). The regions which were good in both Run-5 and Run-6 are used in this analysis. Figure 6.3 shows the fiducial cut used in this analysis.

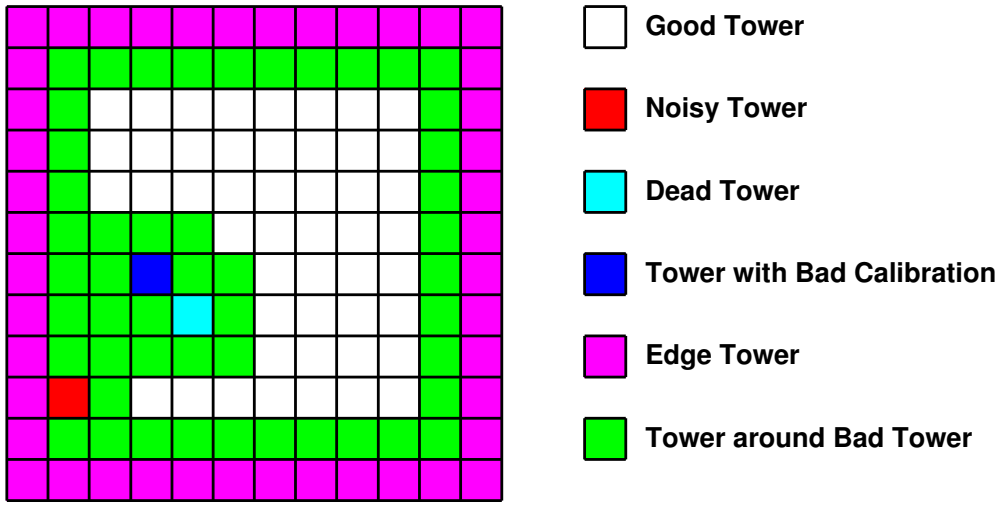

Figure 6.2: A schematic view of the definition of edge towers and towers around bad towers.

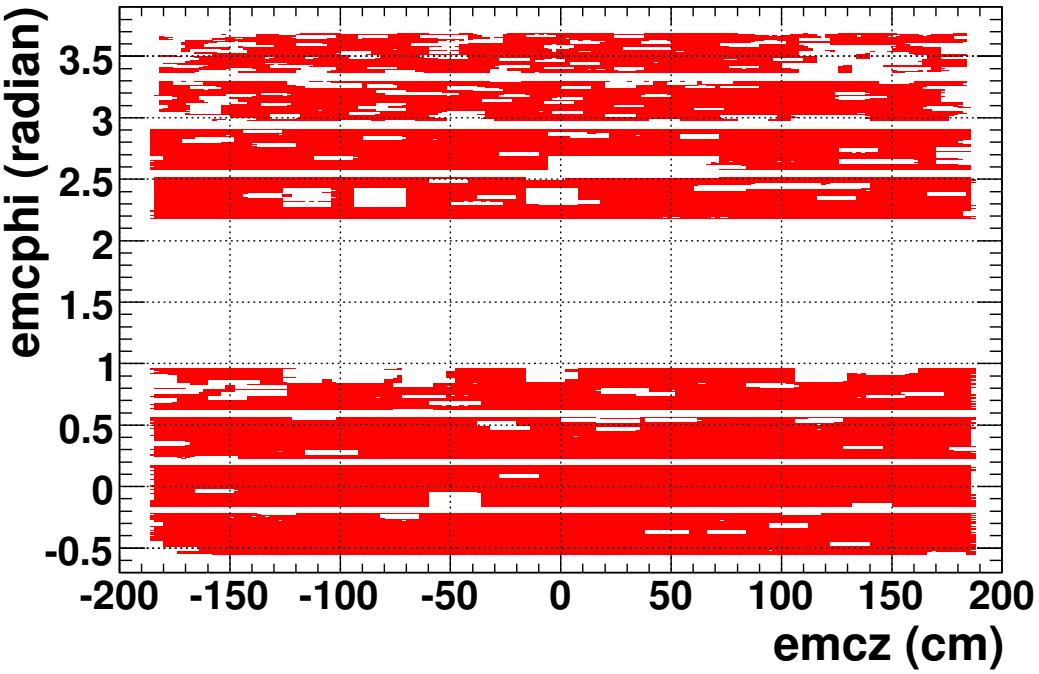

Figure 6.3: The EMCal fiducial cut used in this analysis. X-axis is emcz (cm) and Y-axis is emcphi (radian).

6.2.2 Mass Difference

In order to minimize the reconstructed mass width of the χ_c peak, the mass difference method is adopted. The invariant mass of the electron and positron, M_{ee}, peaks around the J/ψ mass with some width $\sigma \sim 60$ MeV/c^2. The invariant mass of the electron, positron and photon, $M_{ee\gamma}$, peaks around the χ_c mass and the reconstructed χ_c mass width is about 110 MeV/c^2. However, if we calculate the mass difference between the two invariant masses, $\Delta M = M_{ee\gamma} - M_{ee}$, the reconstructed width for ΔM becomes $\sigma \sim 50$ MeV/c^2. Figure 6.4 shows the spectra of M_{ee}, $M_{ee\gamma}$ and ΔM obtained from PYTHIA χ_{c1} and PISA simulation.

The mass resolution of ΔM is mainly determined by photon energy resolution of EMCal. Parameterization of energy resolution of PbSc and PbGl is described in subsection 3.5.4. At the photon energy of 500 MeV, the energy resolution $\sigma(E)$ is 58 MeV (42 MeV) for PbSc (PbGl). This inferior energy resolution is one of the main difficulty in the χ_c measurement at RHIC.

6.2.3 Ratio of Cross Sections $\sigma_{\chi_{c1}}/\sigma_{\chi_{c2}}$

There is only limited knowledge on the ratio of cross sections of χ_{c1} to χ_{c2}, $\sigma_{\chi_{c1}}/\sigma_{\chi_{c2}}$, as shown in Fig. 6.5 [44, 133, 134, 135]. For simplicity, the ratio is assumed to be $\sigma_{\chi_{c1}}/\sigma_{\chi_{c2}} = 0.567$ to satisfy the following relation,

$$\frac{BR\,(\chi_{c1} \to J/\psi\gamma)\,\sigma_{\chi_{c1}}}{BR\,(\chi_{c2} \to J/\psi\gamma)\,\sigma_{\chi_{c2}}} = 1. \tag{6.6}$$

The magenta point at $\sqrt{s}$=200 GeV in Fig. 6.5 represents this assumed value. In the simulation, based on this assumption, the mean mass of 3533.43 MeV/c^2(=$(M_{\chi_{c1}} + M_{\chi_{c2}})/2$) is used. The expected mass resolution of the χ_{c1} and χ_{c2} convoluted peak is $\sigma \sim$52 MeV/c^2 and this value is not much worsened from the single χ_{c1} (χ_{c2}) resolution of $\sigma \sim$46 MeV/c^2. The contribution of χ_{c0} is neglected in this analysis.

6.3 Low-p_T π^0 Spectrum

The J/ψ peak is seen clearly enough as will be shown in subsection 6.6.1. The most important point of this χ_c analysis is the photon detection by EMCal. The photons interested in this analysis are low p_T photons as shown in Fig. 6.1. Neutral pions are the most appropriate tool to check that the low p_T photons are surely detected. In this section, the measurement of the π^0 invariant cross section using the $\pi^0 \to 2\gamma$ decay channel ($BR = (98.798 \pm 0.032)\%$ [19]) will be described.

6.3.1 Data Set and Cut Parameters for π^0 Analysis

For the π^0 measurement, the minimum bias data of Run-5 p+p $\sqrt{s}$ =200 GeV and Run-6 p+p $\sqrt{s}$ =200 GeV is used. The similar cuts used for the χ_c analysis (subsection 6.2.1) is used for the π^0 analysis.

- Event cut

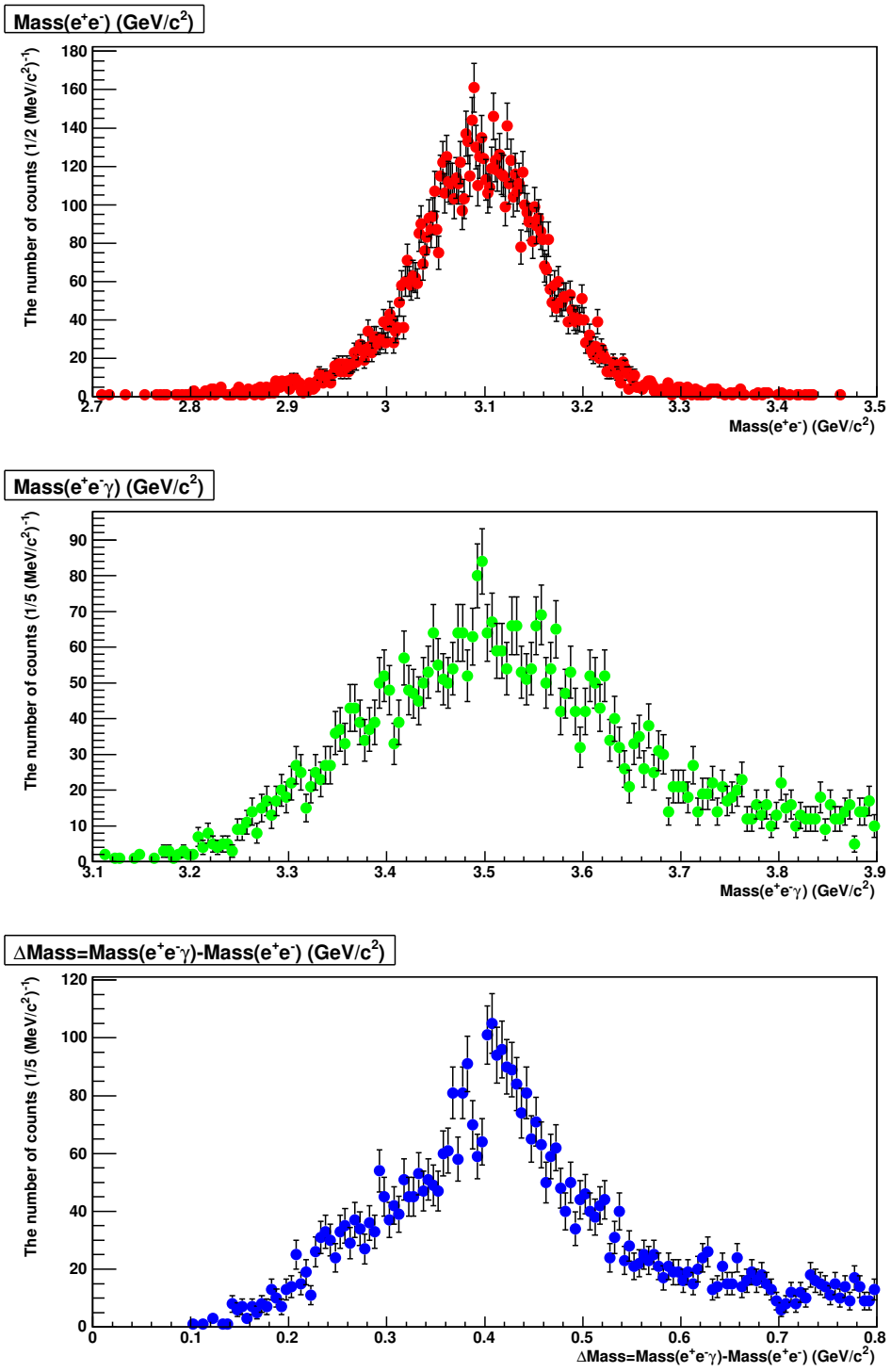

Figure 6.4: The mass spectra of χ_{c1} simulation using PYTHIA and PISA. Top, middle and bottom panels show the mass spectra of $M_{e^+e^-}$, $M_{e^+e^-\gamma}$ and the mass difference $\Delta M = M_{e^+e^-\gamma} - M_{e^+e^-}$, respectively. The mass resolution is about 60, 110 and 50 MeV/c^2 from top to bottom. The mass scales of three panels are the same. The settings of PYTHIA and PISA are described in section 6.5.

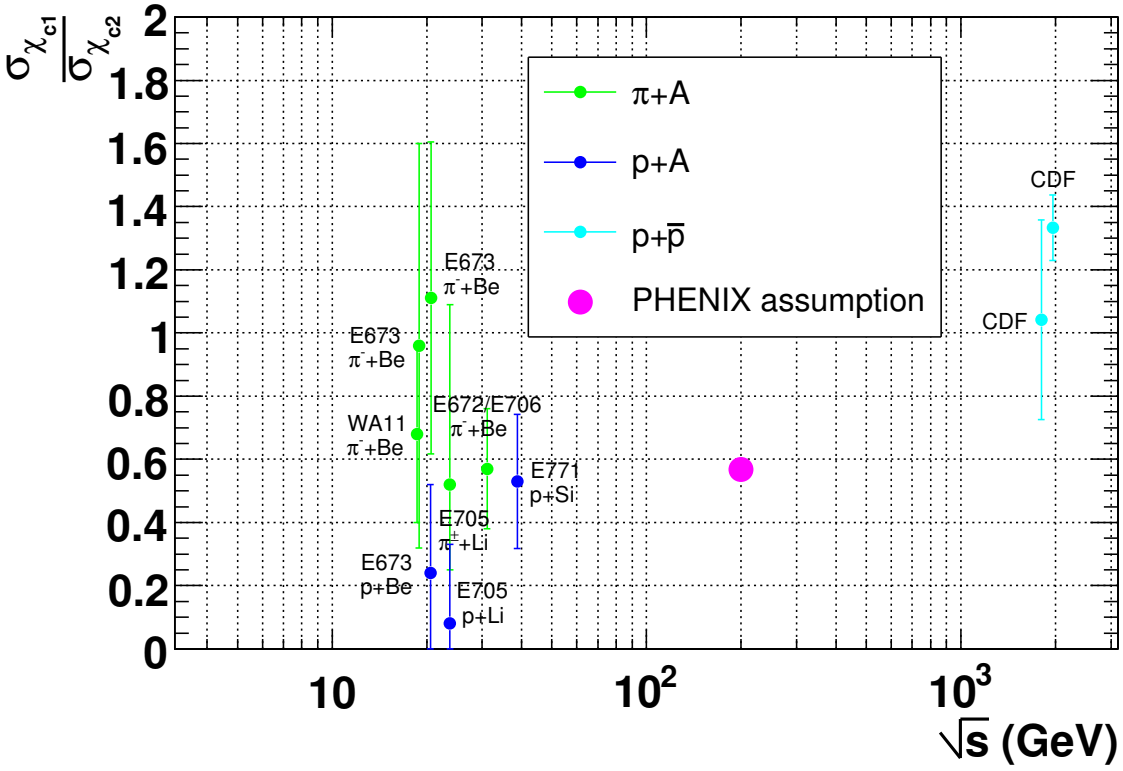

Figure 6.5: The ratios of cross sections $\sigma_{\chi_{c1}}/\sigma_{\chi_{c2}}$ from various experiments are shown as a function of center of mass energy $\sqrt{s}$ [44, 133, 134, 135]. The assumed ratio of the PHENIX experiment is shown as the magenta point at $\sqrt{s} = 200$ GeV.

- |BbcZvertex| <30 cm

- Photon cut
  - ecore > 0.2 GeV (energy cut, lower than that for the χ_c analysis.)
  - emcchi2 < 2.5 (electromagnetic shower profile cut)
  - $|\text{pemcz}_{\text{charged track}} - \text{emcz}_\gamma| > 35$ cm $||$
    $|\text{pemcphi}_{\text{charged track}} - \text{emcphi}_\gamma| > 0.07$ radian
    (square charged particle veto for the closest DC (drift chamber) track projection point from the centroid of the EMCal cluster)
  - Fiducial cut (Fig. 6.3)

Signal Extraction

Since most of the low-p_T π^0 mesons are not identified as π^0 due to those large opening angle between two photons, the S/N ratio in the low-p_T region is low. To extract the signals from the di-photon mass spectrum and to estimate the background, a convoluted function of Gaussian and third order polynomial (seven parameters) are used to fit the spectrum in the range of $0.05 < M_{\gamma\gamma} < 0.25$ GeV/c^2. By this fitting the uncorrected yield (the number of counts), mass and mass width of the π^0 peak are extracted. Figure 6.6 and 6.7 show the di-photon mass spectra of Run-5 and Run-6 $p+p$ data with the DC charged particle veto without di-photon p_T cut, respectively.

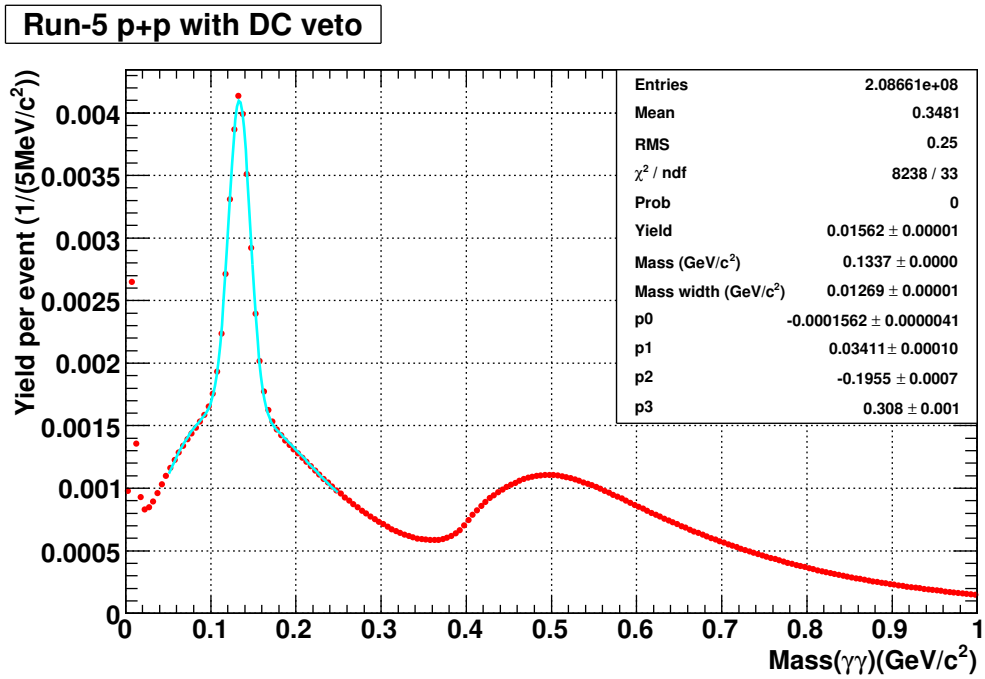

Figure 6.6: The di-photon mass spectrum of Run-5 $p+p$ data with the DC charged particle veto without di-photon p_T cut. The aqua solid line is the fitted convoluted function.

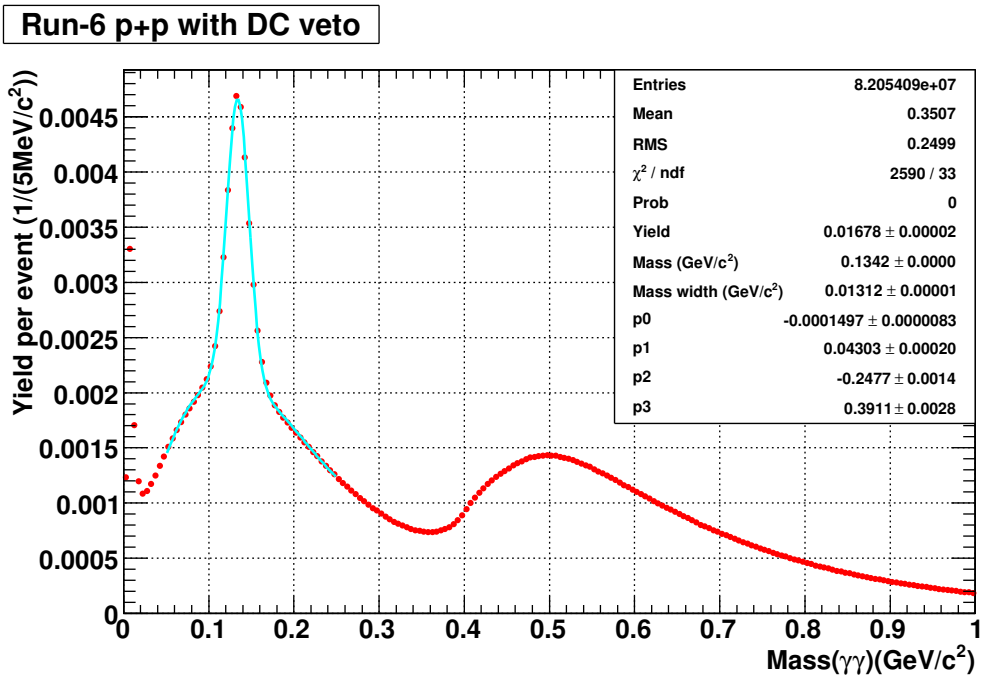

Figure 6.7: The di-photon mass spectrum of Run-6 $p+p$ data with the DC charged particle veto without di-photon p_T cut. The aqua solid line is the fitted convoluted function.

Fitting was also performed with the di-photon p_T binning of 0.05 GeV/c^2 to extract the p_T spectrum.

6.3.2 Acceptance of π^0

To calculate the $\pi^0 \to 2\gamma$ acceptance, PISA simulation was performed with the Run-5 $p+p$ configuration. Since there is an energy smearing effect of EMCal, the input p_T distribution was taken from the Hagedorn function fit of Run-3 $p+p$ $\sqrt{s}$ =200-GeV π^0 data [136, 137]. The fit was performed for $p_T > 1$ GeV/c.

$$\frac{d\sigma}{2\pi p_T dp_T} = \frac{A}{2\pi \left(1 + p_T/p_0\right)^m}, \tag{6.7}$$

with $A = 230 \pm 44$ mb GeV$^{-2}c^3$, $p_0 = 1.47 \pm 0.12$ GeV/c and $m = 10.65 \pm 0.35$. The input distributions of the azimuthal angle, rapidity and Zvertex are flat and those ranges are $0 \sim 2\pi$, $-0.5 \sim +0.5$ and $-35 \sim +35$ cm, respectively. The Zvertex is the z coordinate (beam direction) of the collision vertex. The obtained π^0 acceptance with and without the DC charged particle veto is shown in Fig. 6.8 as a function of p_T of π^0. In this acceptance simulation, charged particles are not included, and the loss of the acceptance by the charged particles are estimated using the real data as described in the following.

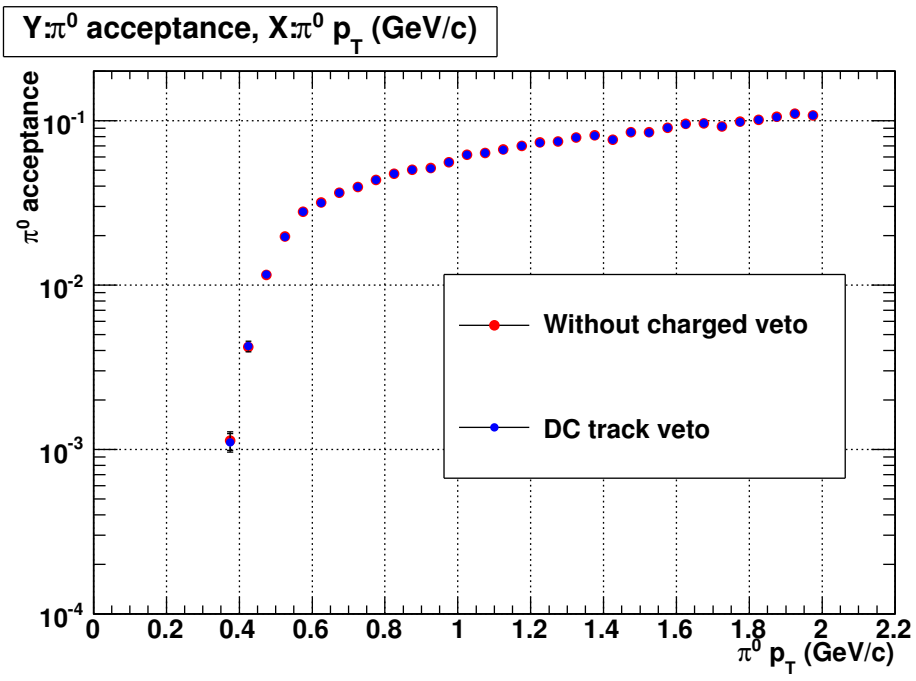

Figure 6.8: π^0 acceptance as a function of π^0 p_T (GeV/c) with and without the DC charged particle veto.

DC Charged Particle Veto

To estimate the loss by the DC charged particle veto, the acceptance corrected π^0 spectra with the DC charged particle veto and without the veto were compared in the p_T region of $0.8 < p_T < 2.0$ GeV/c. Figure 6.9 shows the ratio of measured yields with and without the DC charged particle veto in Run-5 and Run-6. It was found that the loss of π^0 signals by the DC charged particle veto is 3.4% (3.3%) in Run-5 (Run-6). It means that 3.4%/2 = 1.7% (3.3%/2 = 1.65%) of single photons are lost. The average value of 1.7% is used as a correction factor in the χ_c analysis and 100% of the correction factor (1.7%) is regarded as a systematic error. The difference of the two spectra with and without the DC charged particle veto in the low-p_T region is probably due to large combinatorial background. Figure 6.10 and 6.11 show the di-photon spectra in the p_T range of 0.45–0.5 GeV/c without and with the DC charged particle veto, respectively. Large combinatorial background in the π^0 mass region in Fig. 6.10 and 6.11 makes the signal extraction difficult.

It is needed to know how the size of the DC charged particle veto affects the inefficiency of single photons. The number of π^0 signals are counted varying the size of the DC charged particle veto in both the real data and simulation. The square root of the ratio of counts between the real data and simulation is normalized at the nominal 35-cm and 0.07-radian veto to 100% − 1.7% = 98.3%, since this number represents the inefficiency of single photons due to the charged particles which is not taken into account in single particle simulation. The inefficiency of Run-5 $p+p$ and Run-6 $p+p$ is shown in Fig. 6.12. In Fig. 6.12, a fitted curve, $\exp(-0.01633 \cdot X^{1.666})$, where X means the relative size of a DC charged particle veto and the nominal DC charged particle

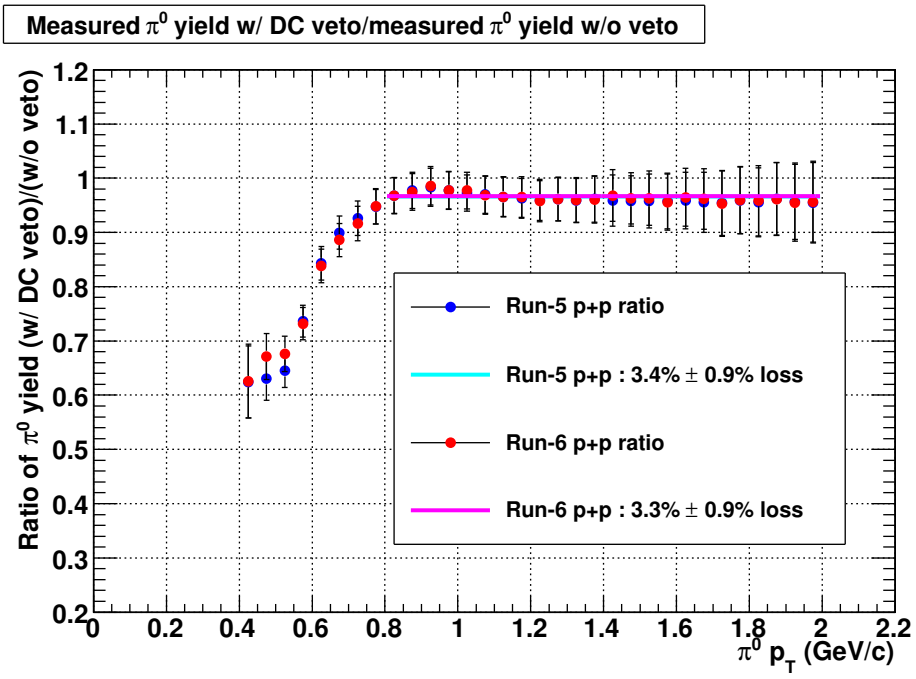

Figure 6.9: The ratios of measured π^0 invariant cross sections with and without the DC charged particle veto in Run-5 and Run-6 as a function of p_T of π^0.

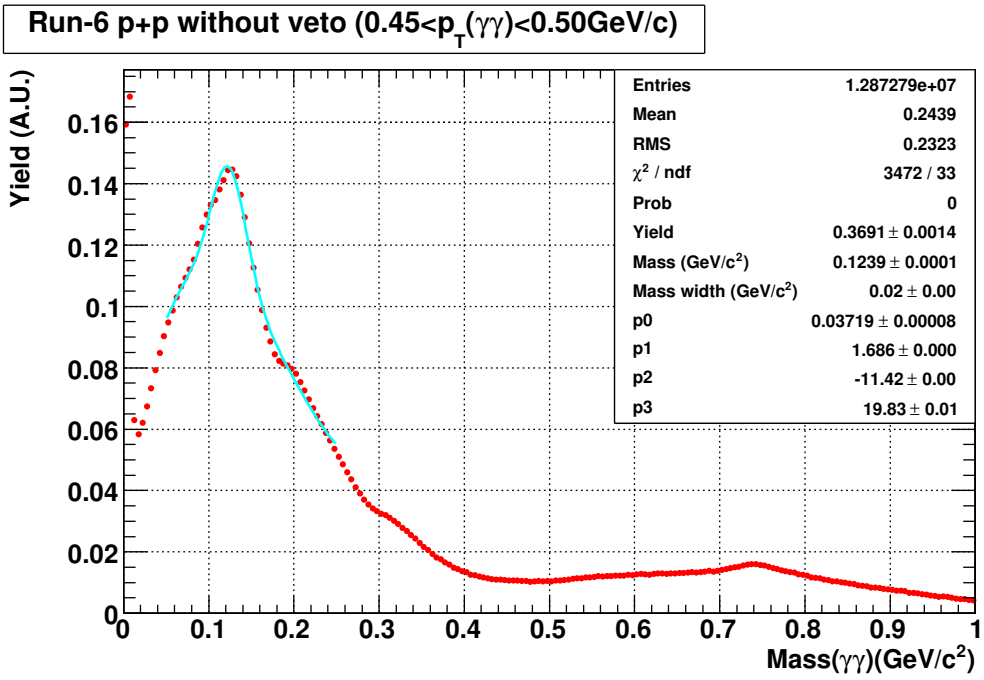

Figure 6.10: The di-photon mass spectrum of Run-6 $p+p$ data without the DC charged particle veto with a di-photon $0.45 < p_T < 0.5$ GeV/c cut. The aqua solid line is the fitted convoluted function.

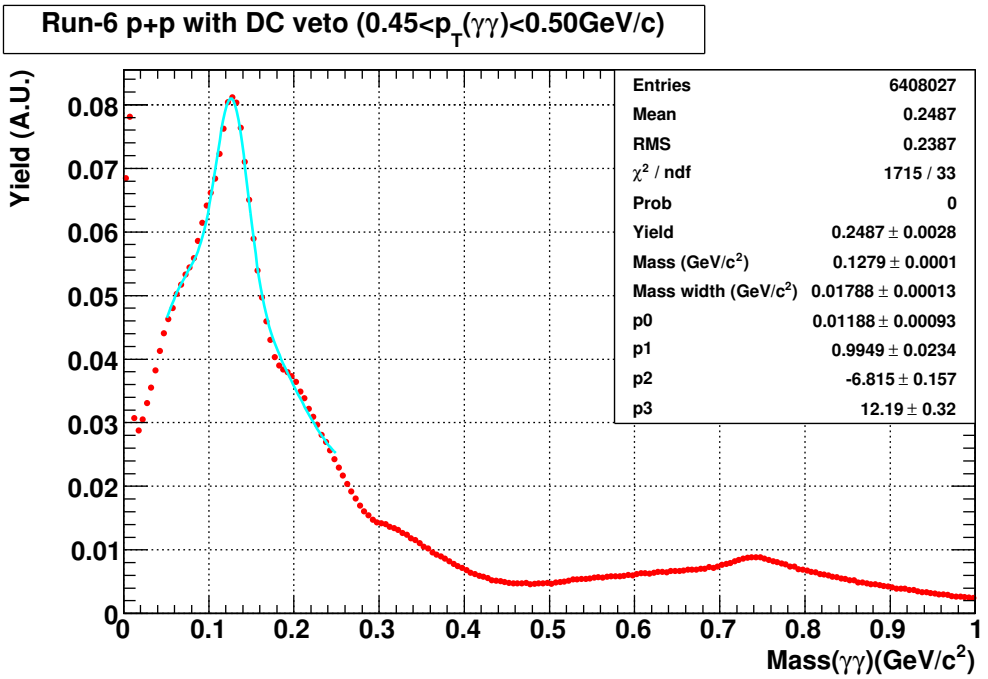

Figure 6.11: The di-photon mass spectrum of Run-6 $p+p$ data with the DC charged particle veto with a di-photon $0.45 < p_T < 0.5$ GeV/c cut. The aqua solid line is the fitted convoluted function.

veto is the one with $X = 1$, is shown.

6.3.3 Cross Section of π^0

To obtain the invariant cross section, the correction of acceptance and DC charged particle veto were applied to the uncorrected π^0 yield. Figure 6.13 shows the invariant cross sections of Run-5 and Run-6 with the DC charged particle veto as a function of p_T of π^0. In Fig. 6.13, the Hagedorn function obtained from Run-3 $p+p$ π^0 data and the invariant cross section of charged pion $((\pi^+ + \pi^-)/2)$ from Run-3 $p+p$ data [138] are also shown.

Figure 6.14 shows the ratios of measured data to the Hagedorn function. In the region of π^0 $p_T > 0.6$ GeV/c, the measured π^0 spectrum agrees with the Hagedorn function well. Roughly speaking, the π^0 p_T of 0.6 GeV/c corresponds to single photon energy of 0.3 GeV, which is the threshold value of the nominal χ_c cut. There is irreducible large background for π^0 in the low p_T region as shown in Fig. 6.11, it probably causes the deviations of the ratios from unity in the low p_T region. Therefore, there is no obvious problem in the low p_T photon detection by EMCal. The systematic error of photon detection is assumed to be half of the maximum deviation of the ratio of measured π^0 invariant cross section. The maximum deviation from unity above π^0 $p_T = 0.6$ GeV/c is 26% and 26%/2=13% is assigned as the systematic error including run-by-run fluctuation for single photon detection.

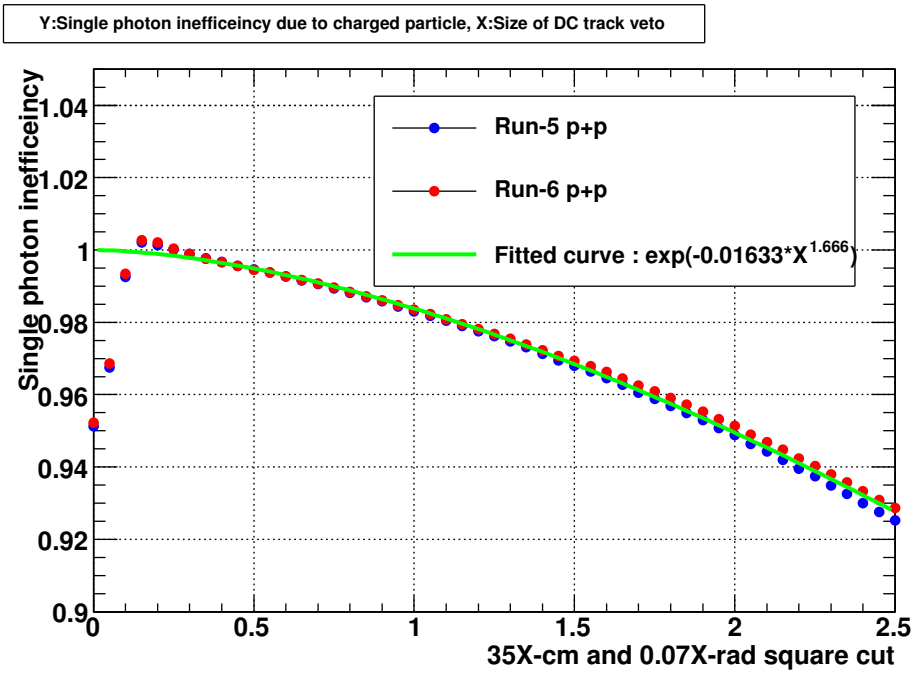

Figure 6.12: The inefficiencies of single photon due to the DC charged particle veto in Run-5 and Run-6 as a function of the size of DC charged particle veto. The nominal veto size is $X = 1$ (35 cm $\times$ 0.07 rad).

6.4 Calculation of χ_c Acceptance

As expressed by Eq. (6.4), the χ_c acceptance can be divided into the χ_c conditional efficiency and the J/ψ acceptance. They are individually calculated in this section.

6.4.1 Conditional Efficiency of χ_c

The main item of the χ_c acceptance calculation is the conditional χ_c efficiency if J/ψ is detected in the acceptance, $\varepsilon^{J/\psi\ detected}_{acc,\chi_c\to J/\psi\gamma}(p_{T,\chi_c})$. To obtain $\varepsilon^{J/\psi\ detected}_{acc,\chi_c\to J/\psi\gamma}(p_{T,\chi_c})$, single χ_c simulation using PISA was performed. The input rapidity distribution is flat between $-0.6 < y_{\chi_c} < +0.6$ and the input azimuthal angle distribution is flat between $0 < \phi_{\chi_c} < 2\pi$. The Zvertex distribution is also flat from -35 cm to $+35$ cm. The p_T distribution of χ_c is monochromatic and simulation was performed from $p_{T,\chi_c} = 0$ GeV/c to $p_{T,\chi_c} = 10$ GeV/c with a 0.01-GeV/c p_{T,χ_c} step. Ten thousand events are generated for each p_{T,χ_c} bin.

The number of reconstructed χ_c signals, N_{χ_c}, with the cut listed in subsection 6.2.1 is the number of counts in the mass range of $0.3 < \Delta M < 0.6$ GeV/c^2. The ratio of the number of reconstructed χ_c to the number of reconstructed J/ψ, is regarded as the χ_c conditional efficiency.

$$\varepsilon^{J/\psi\ detected}_{acc,\chi_c\to J/\psi\gamma}(p_{T,\chi_c}) \;=\; \frac{N_{\chi_c}(p_{T,\chi_c})}{N_{J/\psi}(p_{T,\chi_c})} \tag{6.8}$$

The value of $\varepsilon^{J/\psi\ detected}_{acc,\chi_c\to J/\psi\gamma}$ is shown as a function of p_{T,χ_c} in Fig. 6.15.

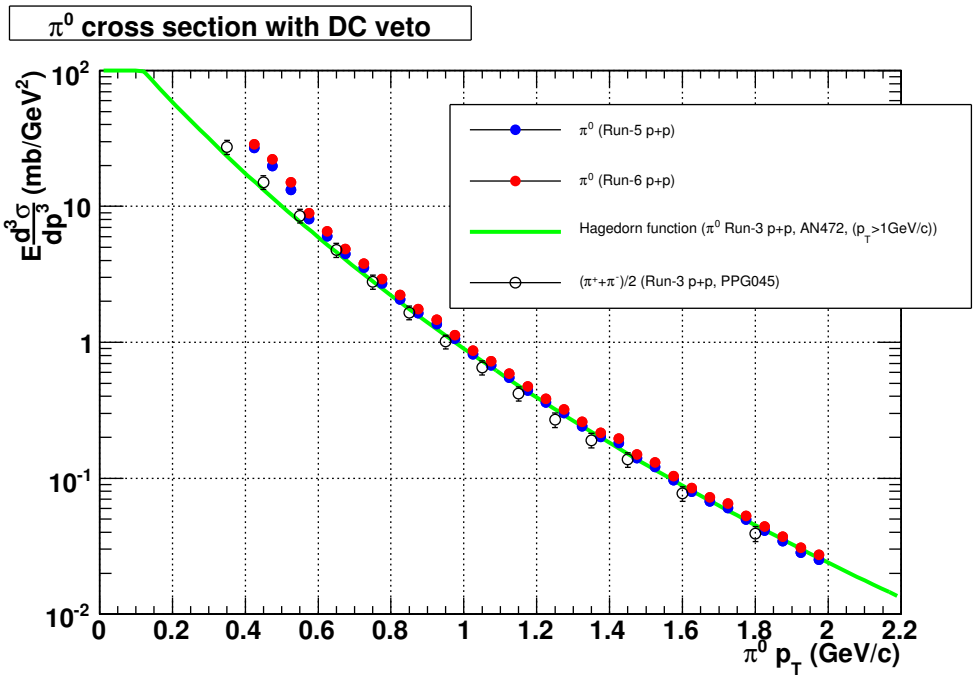

Figure 6.13: The π^0 invariant cross sections with the DC charged particle veto in Run-5 and Run-6 as a function of p_T of π^0. The Hagedorn function obtained from Run-3 π^0 result is shown as the green solid curve. The charged pion invariant cross section obtained from Run-3 $p+p$ data is also shown as black open circles.

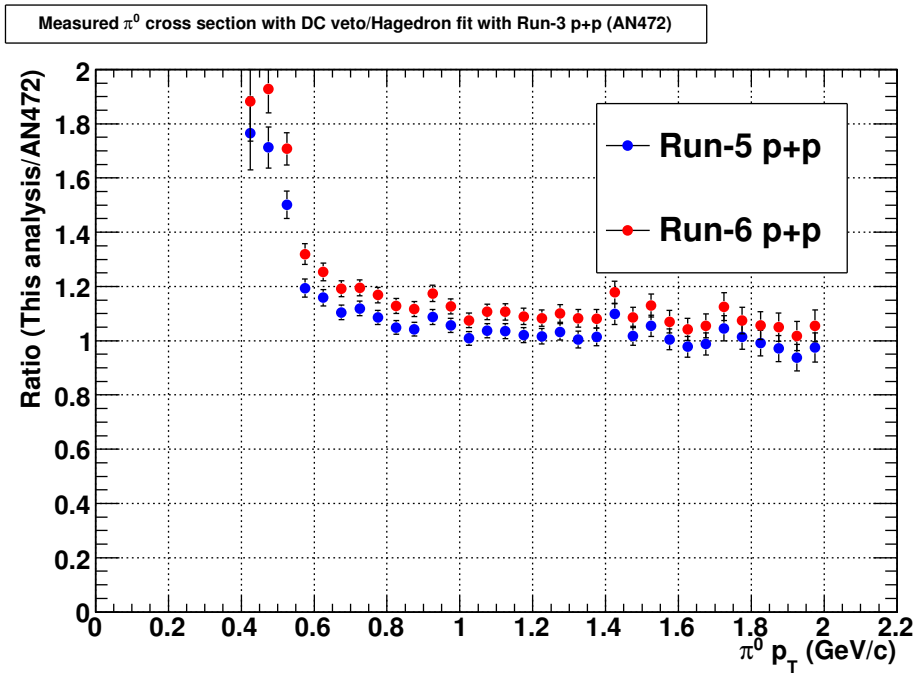

Figure 6.14: The ratios of measured π^0 invariant cross section with the DC particle veto and expected cross section in Run-5 and Run-6 as a function of p_T of π^0.

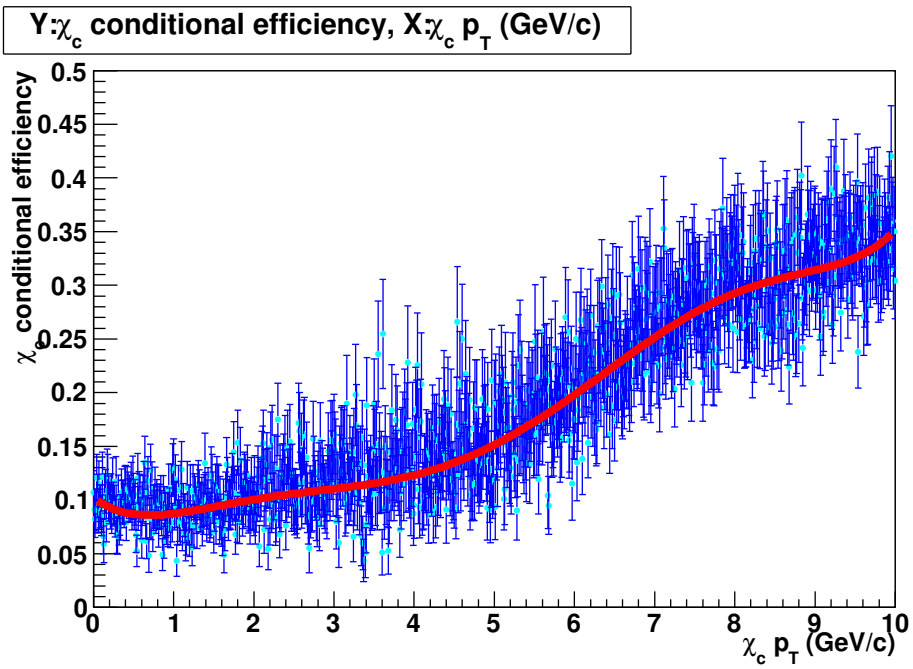

Figure 6.15: The χ_c conditional efficiency if J/ψ detected, $\varepsilon^{J/\psi\ detected}_{acc,\chi_c\to J/\psi\gamma}$, as a function of p_T of χ_c.

While each point has the large error due to small statistics, there are 1001 points in total and the statistical uncertainty of $\varepsilon^{J/\psi\ detected}_{acc,\chi_c\to J/\psi\gamma}$ is small. The sixth order polynomial function of p_T of χ_c is fitted to $\varepsilon^{J/\psi\ detected}_{acc,\chi_c\to J/\psi\gamma}(p_{T,\chi_c})$ and is used as $\varepsilon^{J/\psi\ detected}_{acc,\chi_c\to J/\psi\gamma}(p_{T,\chi_c})$ instead.

Systematic Error of Parameterization of χ_c Conditional Efficiency

To evaluate the systematic error of the parametrization of the χ_c conditional efficiency, the range of p_{T,χ_c} is divided into ten parts and is fitted with the second order polynomials. The difference between the fitted functions of the sixth order and second order polynomials are used as the systematic error of the χ_c conditional efficiency. Figure 6.16 shows the difference between the fitted functions. The systematic error is 1.4%.

Systematic Error from Ratio of $\sigma_{\chi_{c1}}/\sigma_{\chi_{c2}}$

The χ_c conditional efficiency is calculated with the assumption of $\sigma_{\chi_{c1}}/\sigma_{\chi_{c2}} = 0.567$ (Eq. (6.6)). As shown in Fig. 6.5, however, there is the large uncertainty in this ratio. To evaluate the systematic error of this assumption, the χ_c conditional efficiency is calculated for the two extreme cases; $\sigma_{\chi_{c1}}/\sigma_{\chi_{c2}} = +\infty$ and $\sigma_{\chi_{c1}}/\sigma_{\chi_{c2}} = 0$. The difference between the two cases is used as the systematic error and it is 4.3%.

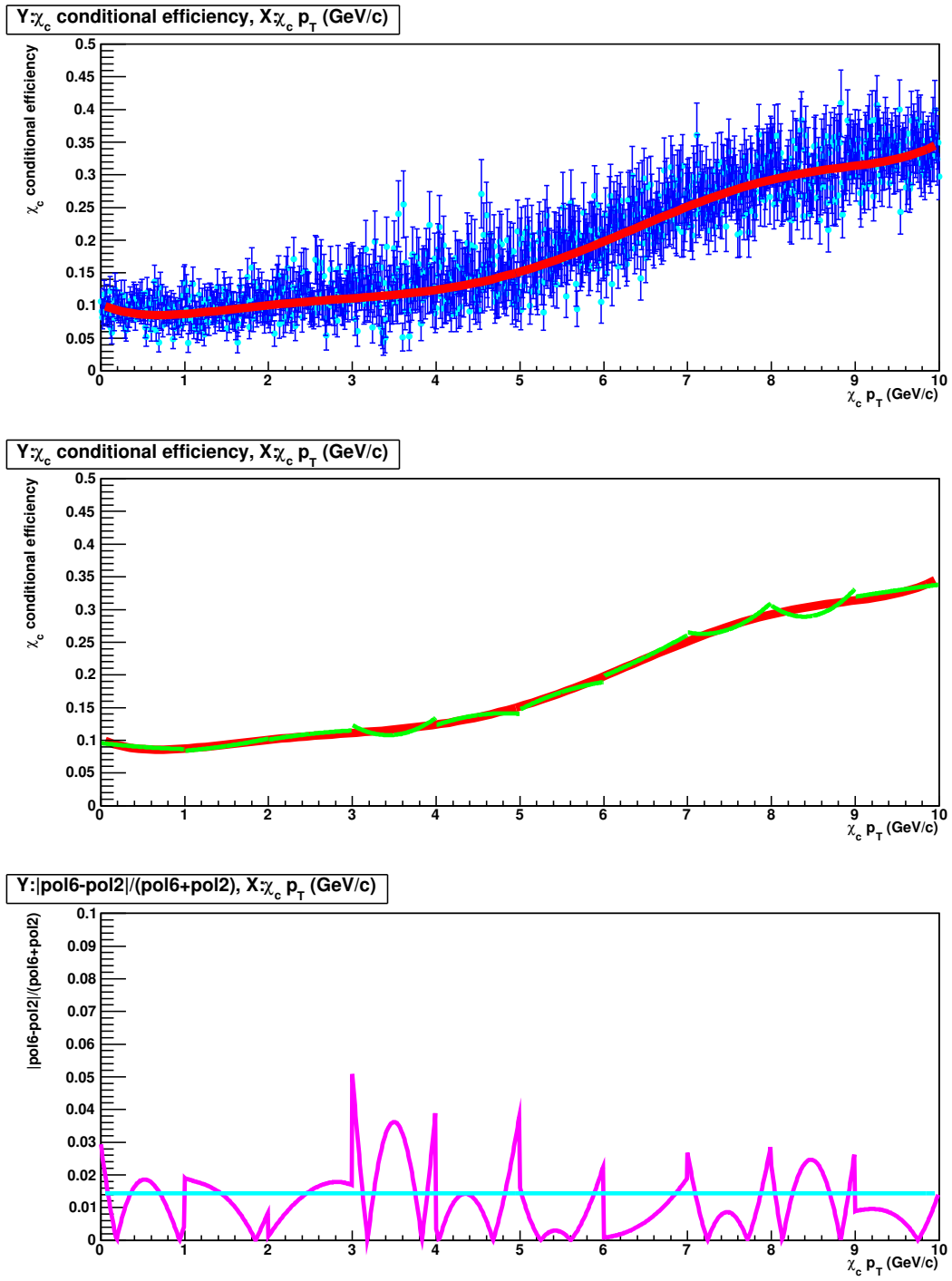

Figure 6.16: The χ_c conditional efficiency. Obtained data points and the fitted six order polynomial (top). The fitted sixth order and second order polynomials (middle). The difference between the fitted sixth and second order polynomials (bottom). The systematic error is estimated to be 1.4%

Systematic Error from BbcZvertex Distribution

In the χ_c conditional efficiency calculation, the Zvertex distribution is assumed to be flat. However, as shown in Fig. 4.5, the BbcZvertex distribution is not flat in the real data with minimum bias triggers. To estimate the systematic error from the difference of BbcZvertex distribution, the χ_c conditional efficiency is also calculated with the weight of the real data BbcZvertex distribution. The difference between the mean efficiency with Run-5 p+p and Run-6 p+p distribution, and the efficiency with the flat distribution is used as the systematic error from BbcZvertex distribution. It is estimated to be 0.3%.

Systematic Error from Azimuthal Distribution of J/ψ

In this analysis, no fiducial cut for electrons and positrons is applied to the DC, PC1, RICH nor EMCal. It means that there is uncertainty in the distributions of J/ψ in ϕ and y directions. Figure 6.17 shows the ϕ distribution of J/ψ in simulation and real data. J/ψ reconstruction of the real data will be described in subsection 6.6.1. The maximum difference between the real data and simulation in the ϕ distribution is about 70%. To estimate the systematic error from the difference of the azimuthal distribution of J/ψ, the χ_c conditional efficiency is also calculated with the ratio of the azimuthal distribution of J/ψ between the real data and simulation as a weight. The difference between the mean efficiency with Run-5 $p+p$ and Run-6 $p+p$ distribution, and the efficiency without weighting is used as the systematic error from the azimuthal distribution of J/ψ. It is estimated to be 0.8%.

Effect of χ_c and J/ψ Polarization

The polarization (spin alignment) of χ_c and J/ψ states can introduce a systematic change of the χ_c acceptance and R_{χ_c}. We have evaluated the effect of one χ_c state decay into $J/\psi\gamma$ with a distribution given by

$$\frac{dN_\gamma}{d\cos\theta_{\chi_c\gamma}} \propto 1 + \alpha_{\chi_c}\cos^2\theta_{\chi_c\gamma}, \tag{6.9}$$

where $\theta_{\chi_c\gamma}$ is the polar angle between χ_c momentum vector in the laboratory frame and γ momentum vector in the χ_c rest frame. Similarly, the distribution of $J/\psi \to e^+e^-$ is given by

$$\frac{dN_{e^+}}{d\cos\theta_{J/\psi e^+}} \propto 1 + \alpha_{J/\psi}\cos^2\theta_{J/\psi e^+}, \tag{6.10}$$

where $\theta_{J/\psi e^+}$ is the polar angle between J/ψ momentum vector in the χ_c rest frame and e^+ momentum vector in the J/ψ rest frame. The permitted ranges of α_{χ_c} are $-\frac{1}{3} < \alpha_{\chi_{c1}} < 1$ and $-\frac{3}{5} < \alpha_{\chi_{c2}} < 1$ for hadronicly produced χ_{c1} and χ_{c2}, respectively [140]. It is expected that the parameters $\alpha_{J/\psi}$ of χ_c decayed J/ψ are $\alpha_{J/\psi}(\chi_{c1} \to J/\psi \to e^+e^-) = -1/3$ and $\alpha_{J/\psi}(\chi_{c2} \to J/\psi \to e^+e^-) = 1/13$ from theories and was experimentally confirmed at less than 10% uncertainty [141, 142]. The χ_c acceptance is calculated with the assumption of $\alpha_{\chi_c} = \alpha_{J/\psi} = 0$. The χ_c acceptance in the case of $\alpha_{\chi_{c1}} = -\frac{1}{3}$ and $\alpha_{J/\psi} = -\frac{1}{3}$ is found to be maximally deviated from that with the assumption of $\alpha_{\chi_c} = \alpha_{J/\psi} = 0$. The maximal deviation of 5.6% is assigned as the systematic error of R_{χ_c} value due to the χ_c polarization.

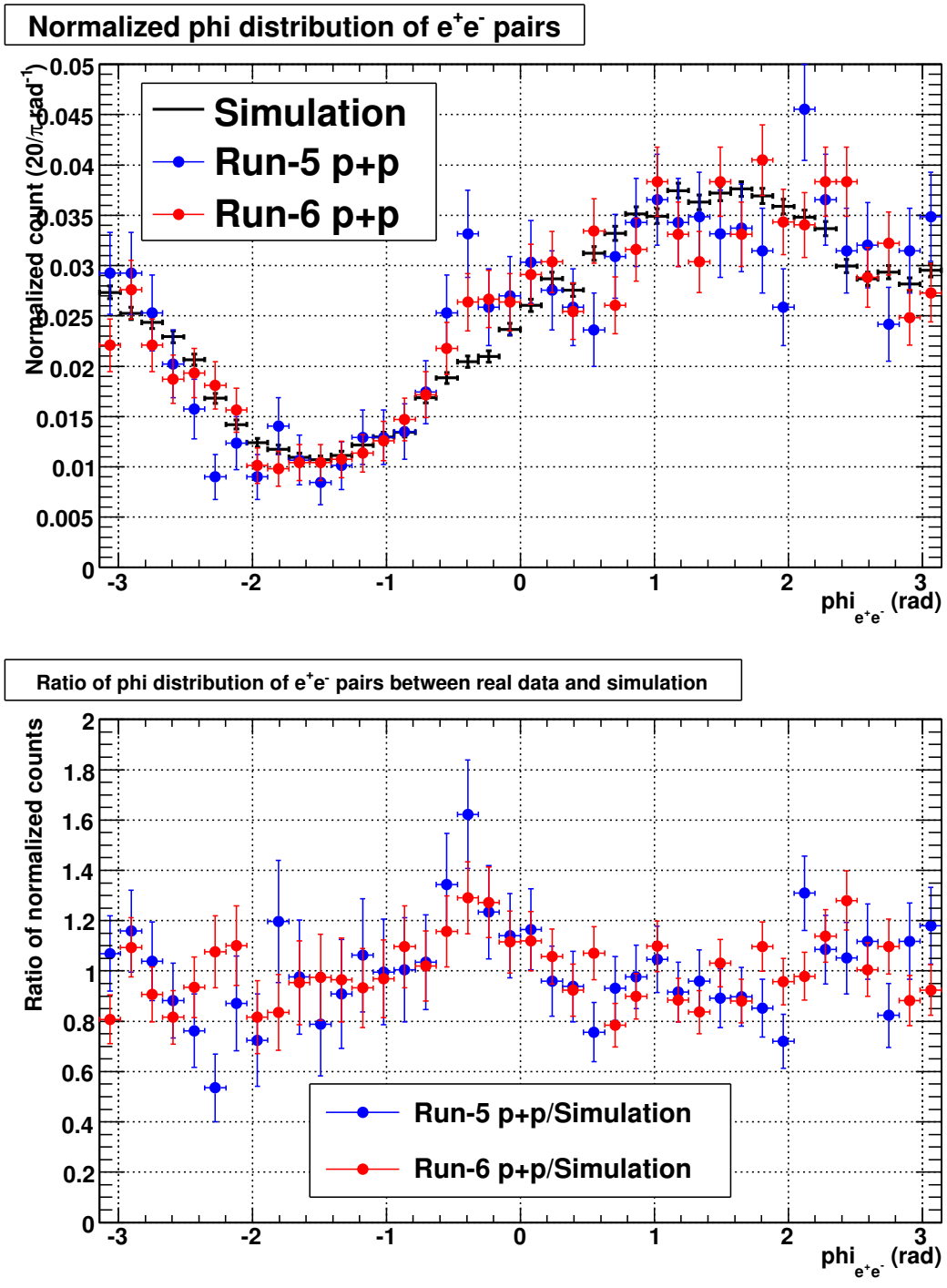

Figure 6.17: The azimuthal angle distribution of J/ψ in the real data and simulation.

6.4.2 Acceptance of J/ψ

The acceptance of J/ψ with the cut written in section 6.2.1 is also calculated using PISA. The input parameters are as follows.

- rapidity : flat $(-0.5 < y_{J/\psi} < +0.5)$
- p_T : flat $(0 < p_{T,J/\psi} < 10$ GeV/$c)$
- azimuthal angle : flat $(0 < \phi_{J/\psi} < 2\pi$ radian$)$
- Zvertex : flat $(-35 < Z_{vertex} < +35$ cm$)$

The number of input events is 3×10^6. Since no fiducial cut is applied to e^+e^- pairs, two simulation settings, Run-5 $p+p$ 200 GeV (run179846) (default in this analysis) and Run-4 Au+Au 200 GeV (run122223) are used to estimate the systematic error of J/ψ acceptance calculation. Figure 6.18 shows the obtained J/ψ acceptance as a function of J/ψ p_T.

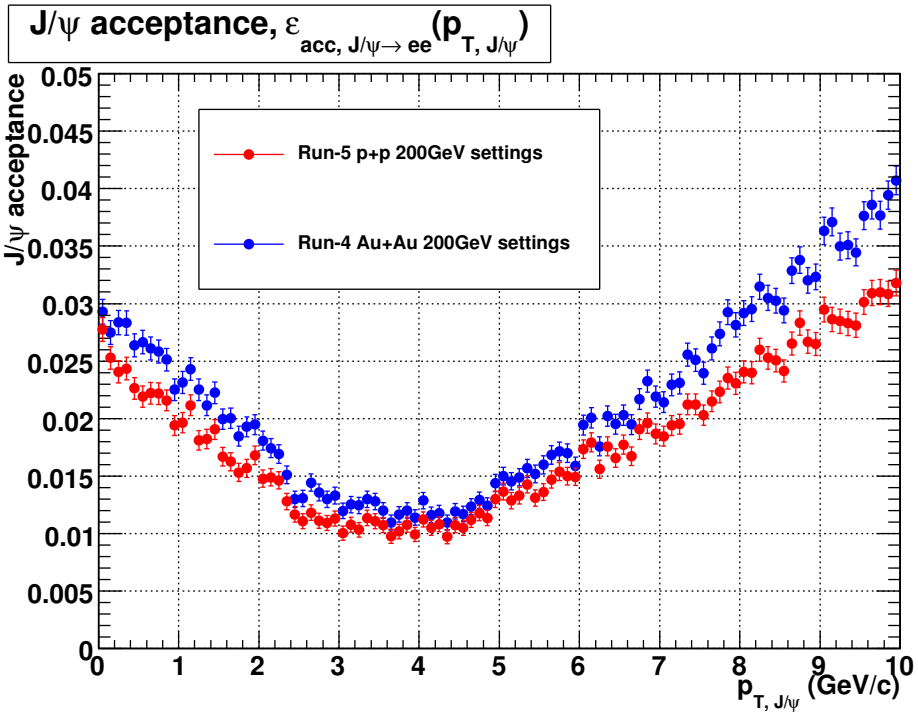

Figure 6.18: J/ψ acceptance as a function of J/ψ p_T (GeV/c) with Run-5 $p+p$ 200 GeV and Run-4 Au+Au 200 GeV settings.

The average acceptance of $J/\psi \to e^+e^-$ is ~2% and the average conditional $\chi_c \to J/\psi\gamma$ efficiency is ~10%. Therefore after including the decay branching ratios, ~1/30,000 of produced χ_c is detected by the PHENIX central arm.

6.5 PYTHIA and PISA Simulation

Single χ_c simulation is not enough for verification of χ_c signal reconstruction, because there is correlation between J/ψ and π^0, and γ from π^0 is the main background. It can be verified that signal reconstruction works with the large background using event generator and simulation. The effect of the large background on the signal reconstruction can also be estimated from the simulation. PYTHIA and PISA are used for these purposes.

6.5.1 PYTHIA Simulation

The PYTHIA event generator was used to study the capability of the signal reconstruction and the effect of the background in the $\chi_c \rightarrow J/\psi\gamma$ channel with PISA. The PYTHIA parameters used are as follows.

- $p + p$ collisions at 200 GeV in the center of mass system
- MSEL=0; Full user control
- MSUB(ISUB)=1; A specific process (ISUB) is selected. [1]
  - ISUB=86; $g + g \rightarrow J/\psi + g$
  - ISUB=88; $g + g \rightarrow \chi_{c1} + g$
  - ISUB=89; $g + g \rightarrow \chi_{c2} + g$
- MSTP(51)=7; Parton distribution function (PDF) is CTEQ 5L.
- PMAS(4,1)=1.25; Charm quark mass (GeV/c^2)
- PMAS(5,1)=4.1; Bottom quark mass (GeV/c^2)
- MSTP(33)=1; A common K factor is used.
- PARP(31); K factor
  - $K = 3.7$ for ISUB=86, J/ψ
  - $K = 2.3$ for ISUB=88, χ_{c1}
  - $K = 2.4$ for ISUB=89, χ_{c2}
- MSTP(91)=1; Primordial Gaussian k_T distribution in hadrons
- PARP(91); σ_{k_T} (GeV/c)
  - $\sigma_{k_T} = 1.48$ for ISUB=86, J/ψ
  - $\sigma_{k_T} = 0.10$ for ISUB=88, χ_{c1}

[1] Processes 104 and 105 are the equivalents of 87 and 89 in the limit of $p_T \rightarrow 0$. As always one should beware of double-counting between 87 and 104, and between 89 and 105, and thus use either the one or the other depending on the kinematic domain to be studied [129].

  - $\sigma_{k_T} = 1.96$ for ISUB=89, χ_{c2}

- PARP(41)=1; All resonance decays are on.

All stable particles are put into PISA simulation. Typical multiplicity is about 100. The K factor was tuned with the EMCal cluster multiplicity (photon multiplicity) per event with a photon energy cut of $0.3 < E_\gamma < 2.0$ GeV so that the real data and simulation have the same EMCal multiplicity. The number of photons in the events with χ_c production might be larger than that with J/ψ due to the existence of χ_c decay photons. However, the possibility is neglected here. The σ_{k_T} value was tuned so that the mean p_T square of J/ψ, $\langle p_{T,J/\psi} \rangle$, in the real data and the subprocesses of simulation have the same value.

With the above parameters, a large number of events are simulated as summarized in Table 6.1.

ISUB	Particle	The number of PYTHIA events	The number of reconstructed events	The number of reconstructed J/ψ
86	J/ψ	0.75×10^8	1127132	19528
88	χ_{c1}	1.50×10^8	564846	10130
89	χ_{c2}	1.42×10^8	515580	9125

Table 6.1: Statistics of PYTHIA and PISA simulation.

6.5.2 PISA simulation

To check the χ_c signal reconstruction capability, a full simulation, a combination of PYTHIA and PISA, was performed.

The efficiency corrected mass spectra of J/ψ, χ_{c1} and χ_{c2} are shown in Fig. 6.19, Fig. 6.20 and Fig. 6.21, respectively. These mass spectra are divided by the number of J/ψ. The χ_c peaks are seen in the χ_{c1} and χ_{c2} simulation and the mass resolution is 46 MeV/c^2. Although the simulation samples do not have χ_c component in the J/ψ simulation, the correlated background of J/ψ and photon makes wide peak structure and the obtained R_{χ_c} is non zero as shown in Fig. 6.19. This background effect on the signal extraction will be estimated in the following.

Combined Samples of J/ψ, χ_{c1} and χ_{c2}

To extract the χ_c signal, the fitting with the convolution function of Gaussian (signal) and third order polynomial (background) is used. The fitting range is 0.3–1.0 GeV/c^2 and the peak width is fixed to be the expected resolution of 52 MeV/c^2 for the χ_{c1} and χ_{c2} convoluted peak. The peak height is required to be positive and the peak position is required to locate between 0.35 and 0.55 GeV/c^2. However, there is a systematical deviation between the input R_{χ_c} fraction and extracted (output) R_{χ_c} fraction. This deviation is due to the irreducible correlated background which makes a fake χ_c peak as shown in Fig. 6.19. The input R_{χ_c} value was varied from 0 to 1 by a step of 1/29 by changing the fractions of PYTHIA J/ψ, χ_{c1} and χ_{c2} simulation events. The number of

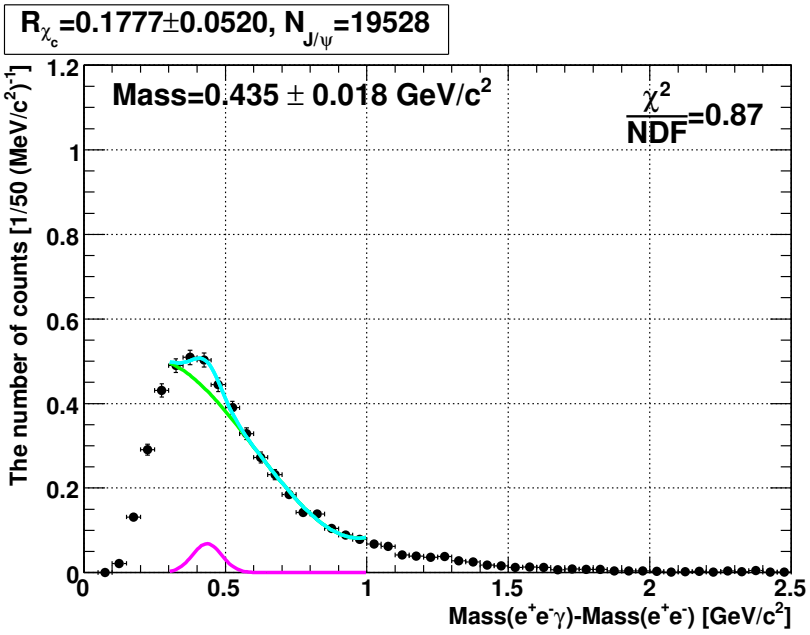

Figure 6.19: The efficiency corrected mass spectrum divided by the number J/ψ of PYTHIA $gg \rightarrow J/\psi g$ events. The curves are the fitted Gaussian and third order polynomial function (aqua), Gaussian (magenta) and third order polynomial (green).

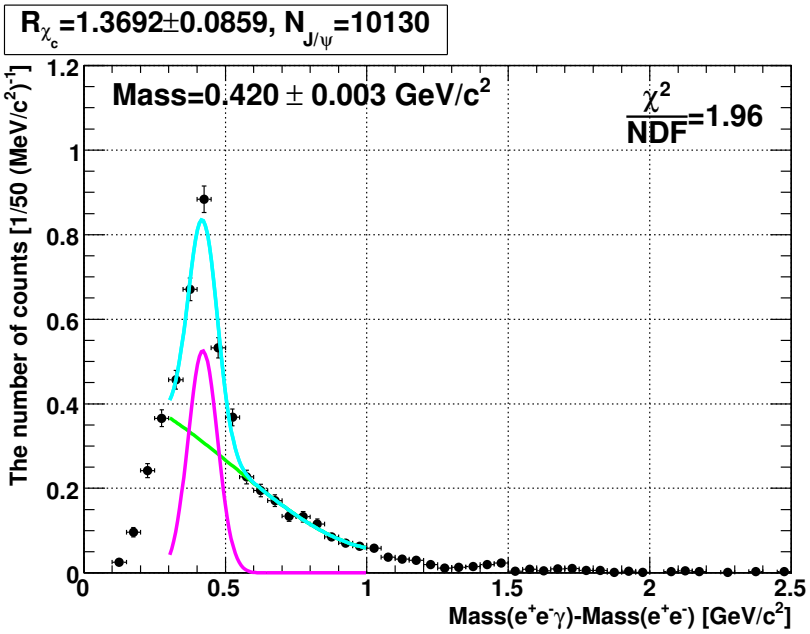

Figure 6.20: The efficiency corrected mass spectrum divided by the number J/ψ of PYTHIA $gg \rightarrow \chi_{c1} g$ events. The curves are the fitted Gaussian and third order polynomial function (aqua), Gaussian (magenta) and third order polynomial (green).

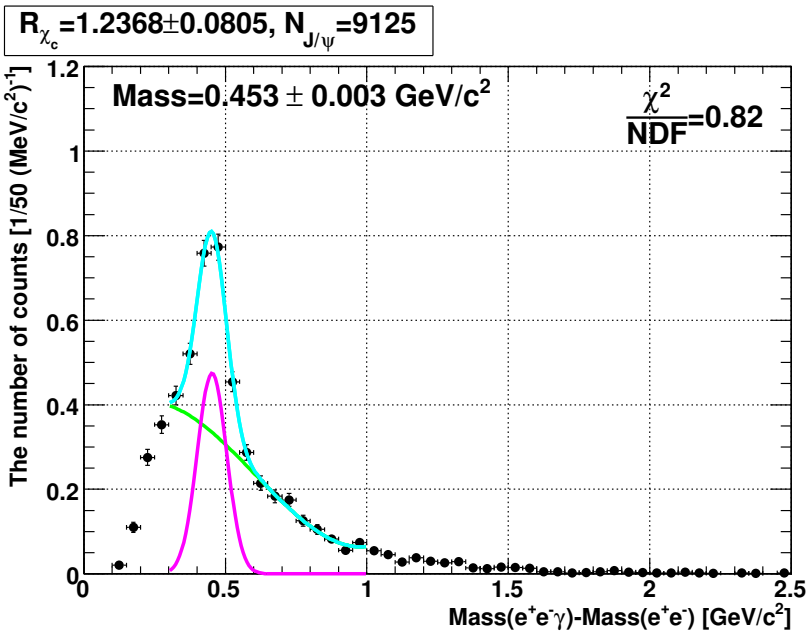

Figure 6.21: The efficiency corrected mass spectrum divided by the number J/ψ of PYTHIA $gg \rightarrow \chi_{c2}g$ events. The curves are the fitted Gaussian and third order polynomial function (aqua), Gaussian (magenta) and third order polynomial (green).

J/ψ was set to ~ 4145, which is the number of J/ψ in the real data (subsection 6.6.1). Figure 6.22 shows the relation between input R_{χ_c} and output R_{χ_c}. The relation can be written as output $R_{\chi_c} \sim 0.2 + \text{input } R_{\chi_c}$. What we want to measure is the input R_{χ_c} and what we measure is the output R_{χ_c}. To transform the output R_{χ_c} value to the input R_{χ_c} value, this relation will be used for the real data analysis in section 6.6.

6.6 Real Data Analysis

The data collected with the ERT electron trigger and ERT photon triggers is used for this analysis.

Since many kinds of ERT LVL1 triggers are used, it is hard to calculate ERT LVL1 trigger efficiency even for single electrons. The ERT LVL1 trigger efficiency is not important in the current analysis with the low statistics. Therefore, the ratio of the measured J/ψ p_T distribution to the expected J/ψ p_T distribution is used as the ERT LVL1 trigger efficiency. The expected J/ψ p_T distribution is obtained from Kaplan function fit of Run-5 $p+p$ data ($\langle p_T^2 \rangle = 4.14 \pm 0.18 \pm^{0.30}_{0.20}$ (GeV/c^2)^2) [7].

The runs where the EMCal calibration (subsection 6.2.1) failed were rejected for the χ_c analysis.

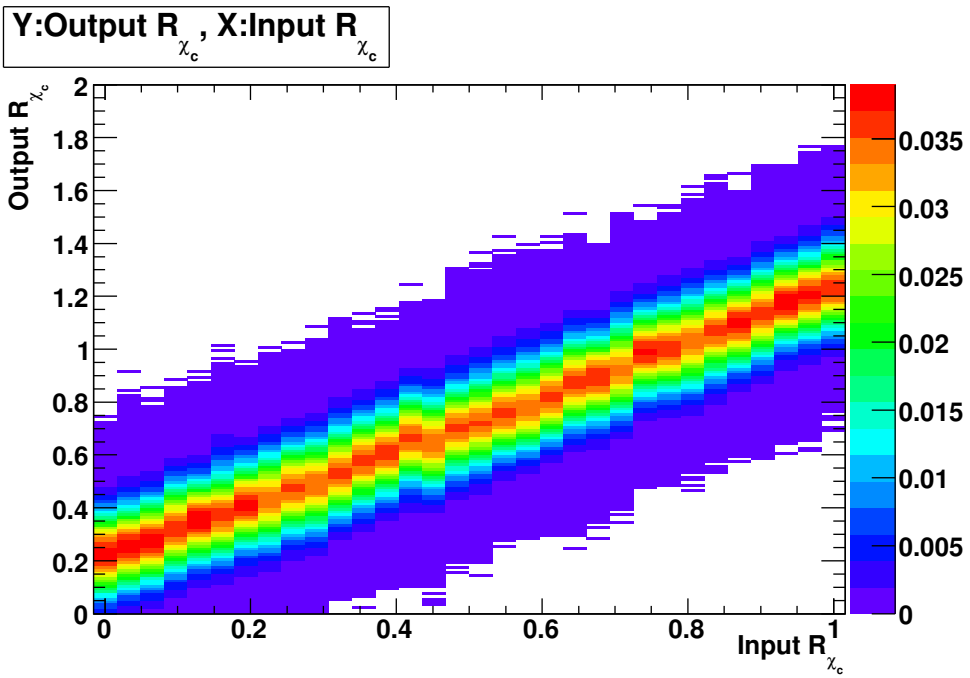

Figure 6.22: The relation between the input R_{χ_c} and output R_{χ_c} obtained with the fit function of third order polynomial+Gaussian.

6.6.1 Reconstruction of J/ψ

The cut parameters listed in section 6.2.1 are used for J/ψ reconstruction. The number of J/ψ, $N_{J/\psi}$, in the mass window of 2.9–3.3 GeV/c^2 can be represented by

$$N_{J/\psi} = (1 - R_{cont}) \{N_{+-} - (N_{++} + N_{--})\} = (1 - R_{cont}) \left(1 - \frac{N_{++} + N_{--}}{N_{+-}}\right) N_{+-} \quad (6.11)$$

where R_{cont} is the fraction of the continuum of e^+e^- from $c\bar{c}$, $b\bar{b}$ and Drell-Yan production, and N_{+-}, N_{++} and N_{--} are the numbers of the counts of e^+e^-, e^+e^+ and e^-e^- in the mass window, respectively.

The value of R_{cont} was estimated by PYTHIA [7, 139] and is 4% and half of which, i.e. 2% is assumued as the systematic error.

The measured number of counts, mass center and mass width of J/ψ are listed in Table 6.2. Figure 6.23 shows the dielectron mass spectra of Run-5 $p + p$, unlike sign pairs (red, top), like sign pairs (blue, top) and net counts (bottom). Figure 6.24 shows the mass spectra of Run-6 $p + p$.

Effect of J/ψ Polarization

The directly produced J/ψ can also have polarization. The J/ψ polarization parameter $\alpha_{J/\psi}$ is measured with the real data. The measured polarization parameter is $\alpha_{J/\psi} = 0.16 \pm 0.07$. Since the $\alpha_{J/\psi}$ parameter is assumed to be zero in the J/ψ acceptance calculation, the deviation of the J/ψ acceptance due to finite $\alpha_{J/\psi}$ should be corrected. The correction for the real data is estimated to be 1% $\pm$ 1% (syst) by fast simulation.

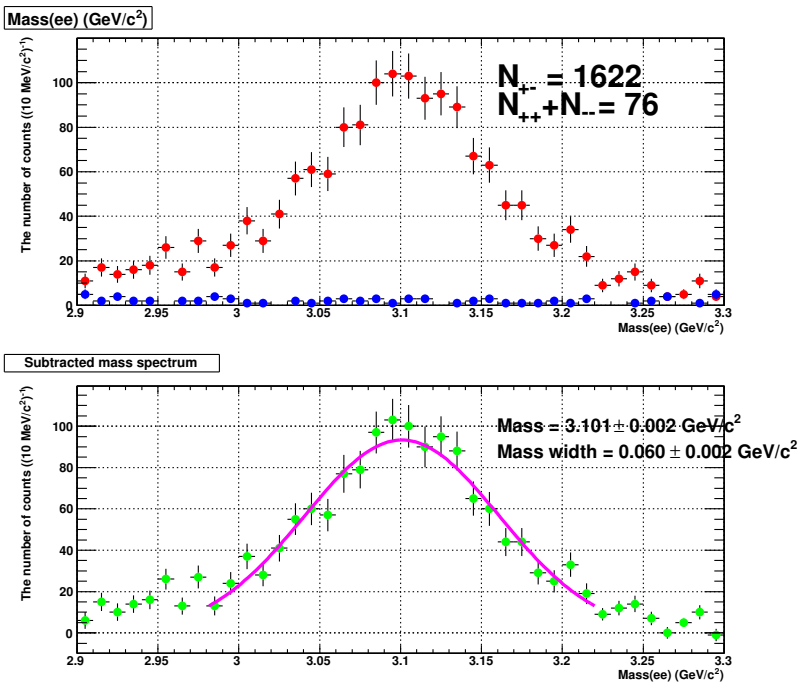

Figure 6.23: The $J/\psi \to e^+e^-$ peak in Run-5 $p+p$. (Top) The mass spectra of unlike sign pairs (red) and like sign pairs are shown. (Bottom) The subtracted spectrum is shown.

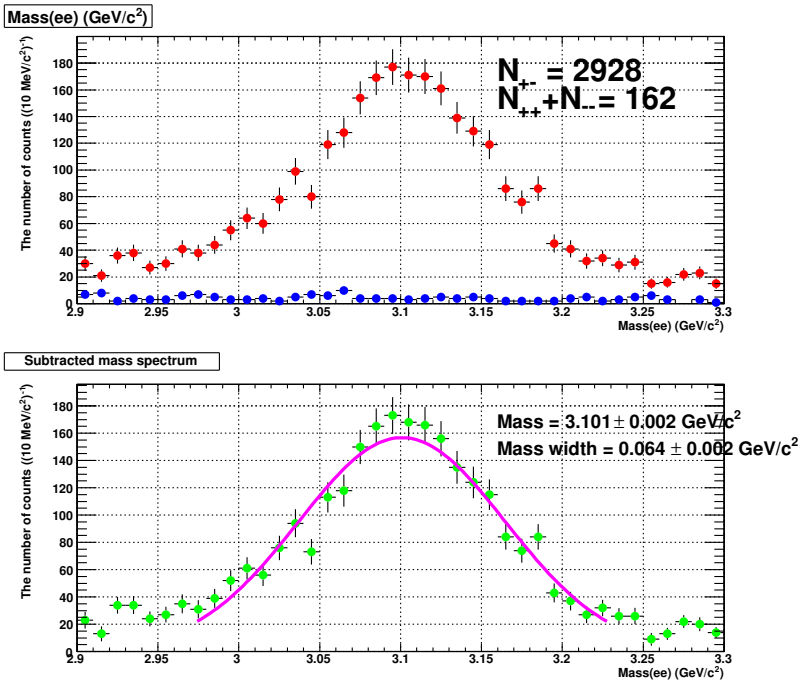

Figure 6.24: The $J/\psi \to e^+e^-$ peak in Run-6 $p+p$. (Top) The mass spectra of unlike sign pairs (red) and like sign pairs are shown. (Bottom) The subtracted spectrum is shown.

Run	$N_{J/\psi}$	Reconstructed mass (GeV/c^2)	Reconstructed mass width (GeV/c^2)
Run-5 $p+p$	1486 ± 40	3.101 ± 0.002	0.060 ± 0.002
Run-6 $p+p$	2659 ± 53	3.101 ± 0.002	0.064 ± 0.002

Table 6.2: The measured number of counts, reconstructed mass and width, which are obtained from $\pm 2\sigma$ fitting, of J/ψ in Run-5 $p+p$ and Run-6 $p+p$.

6.6.2 ERT LVL1 Trigger Efficiency

In this analysis, the ERT LVL1 efficiency is not calculated from single electron spectrum. The ERT LVL1 efficiency is calculated using measured and expected J/ψ spectra. The expected J/ψ spectrum is the Kaplan function with $\langle p^2_{T,J/\psi} \rangle = 4.14 \pm^{0.35}_{0.27}$ GeV/c^2. Figure 6.25 shows the ERT LVL1 trigger efficiency of J/ψ as a function of p_T of J/ψ with the mean and mean plus/minus 1σ of $\langle p^2_{T,J/\psi} \rangle$.

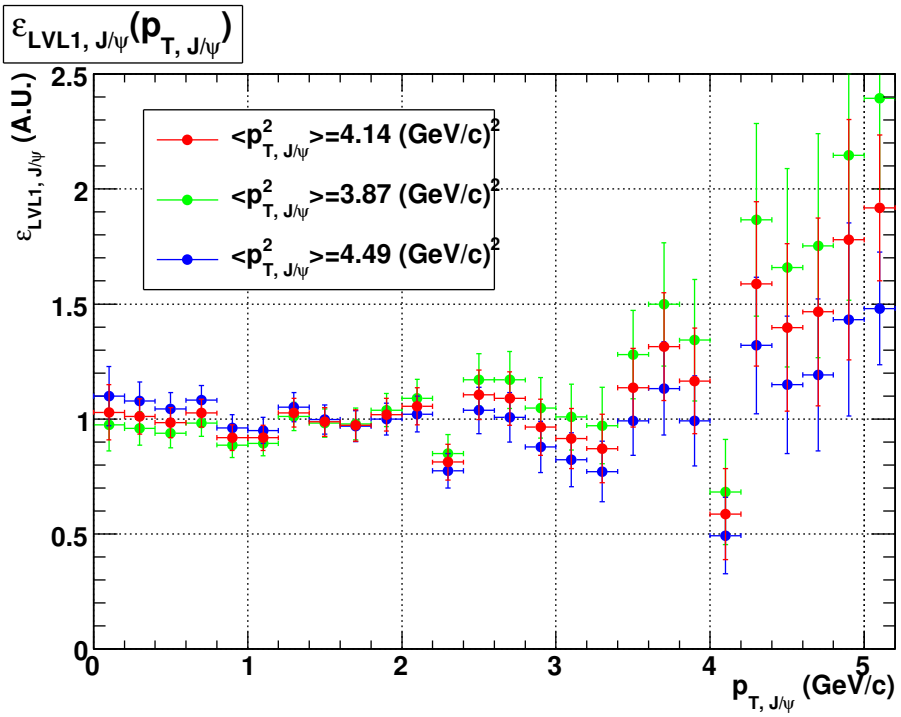

Figure 6.25: ERT LVL1 trigger efficiency of J/ψ, $\varepsilon_{LVL1,J/\psi}\left(p_{T,J/\psi}\right)$.

Figure 6.26 shows the normalized J/ψ acceptance and ERT LVL1 trigger efficiency of $\left\langle \frac{1}{\varepsilon_{acc,J/\psi\to ee}\varepsilon_{LVL1,J/\psi}} \right\rangle \varepsilon_{acc,J/\psi\to ee}(p_{T,J/\psi})\varepsilon_{LVL1,J/\psi}(p_{T,J/\psi})$ with different J/ψ $\langle p^2_T \rangle$ of 3.87, 4.14 (default) and 4.49 (GeV/c)^2. The obtained three kinds of normalized efficiency agree within errors.

Figure 6.27 shows the normalized J/ψ acceptance and ERT LVL1 trigger efficiency of $\left\langle \frac{1}{\varepsilon_{acc,J/\psi\to ee}\varepsilon_{LVL1,J/\psi}} \right\rangle \varepsilon_{acc,J/\psi\to ee}(p_{T,J/\psi})\varepsilon_{LVL1,J/\psi}(p_{T,J/\psi})$ with different simulation set-

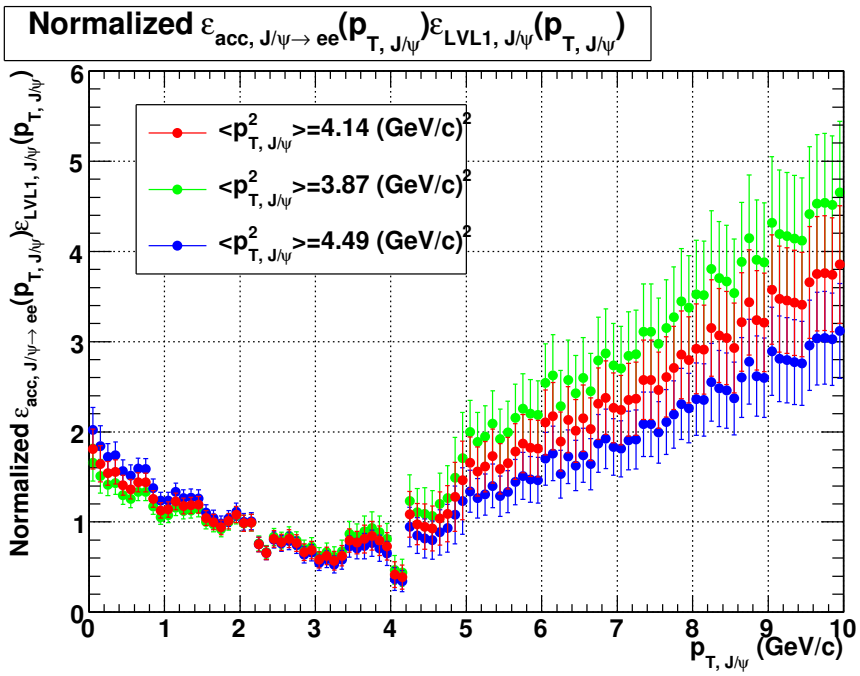

Figure 6.26: Normalized J/ψ acceptance and ERT LVL1 trigger efficiency of J/ψ, $\left\langle \frac{1}{\varepsilon_{acc,J/\psi\to ee}\varepsilon_{LVL1,J/\psi}} \right\rangle \varepsilon_{acc,J/\psi\to ee}(p_{T,J/\psi})\varepsilon_{LVL1,J/\psi}(p_{T,J/\psi})$ with different J/ψ $\langle p_T^2 \rangle$.

tings of Run-5 $p+p$ 200 GeV (default) and Run-4 Au+Au 200 GeV. Difference of the two kinds of normalized efficiency is found to be small.

Figures 6.26 and 6.27 are also used to systematic error estimation.

6.6.3 Reconstruction of χ_c and R_{χ_c} Value

Figure 6.28 shows the raw spectrum of the mass difference $\Delta M = M_{e^+e^-\gamma} - M_{e^+e^-}$ of combined Run-5 and Run-6 $p+p$ 200 GeV data.

Figure 6.29 shows the efficiency corrected spectrum of the mass difference ΔM of combined Run-5 and Run-6 $p+p$ 200 GeV data. The curves in the panel are the fitted convoluted Gaussian and third order polynomial function (aqua), Gaussian (magenta) and third order polynomial (green). The output R_{χ_c} is found to be 0.39 ± 0.10 (stat). The efficiency corrected spectrum with a finer binning of the mass difference ΔM of combined Run-5 and Run-6 $p+p$ 200 GeV data is shown in Fig. F.22 of Appendix F.

As described in subsection 6.5.2, it is needed to transform the output R_{χ_c} to the input R_{χ_c}. With Fig. 6.22, the probability density function of the input R_{χ_c} for the output $R_{\chi_c} = 0.39$ was obtained and is shown in Fig. 6.30. The input R_{χ_c} is estimated to be R_{χ_c} =$0.19 \pm {}^{0.11}_{0.10}$ (stat).

6.7 Systematic Error

Systematic errors are evaluated and summarized in this section.

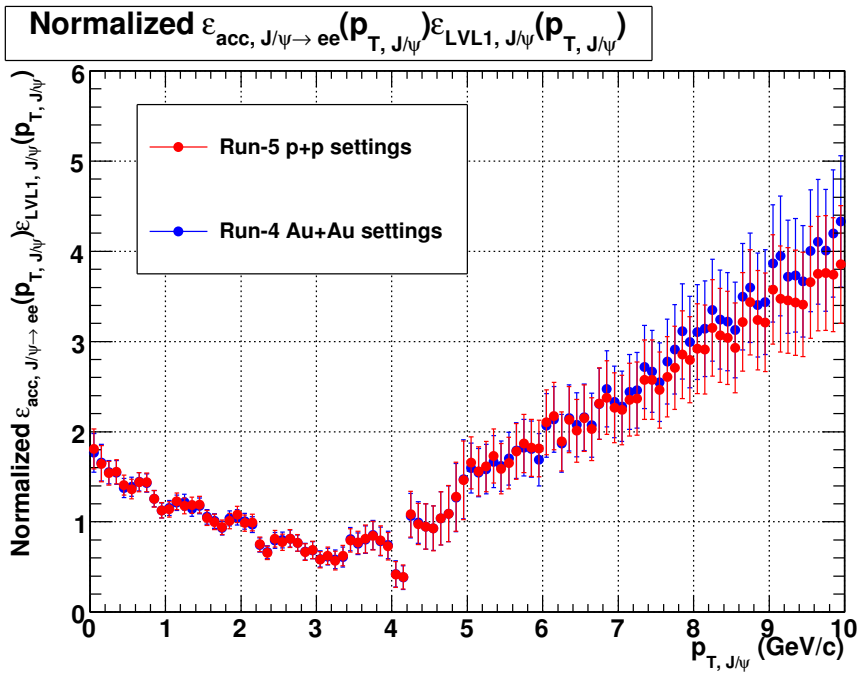

Figure 6.27: Normalized J/ψ acceptance and ERT LVL1 trigger efficiency of J/ψ, $\varepsilon_{LVL1,J/\psi}\left(p_{T,J/\psi}\right)$ with different simulation settings of Run-5 $p+p$ 200 GeV (default) and Run-4 Au+Au 200 GeV.

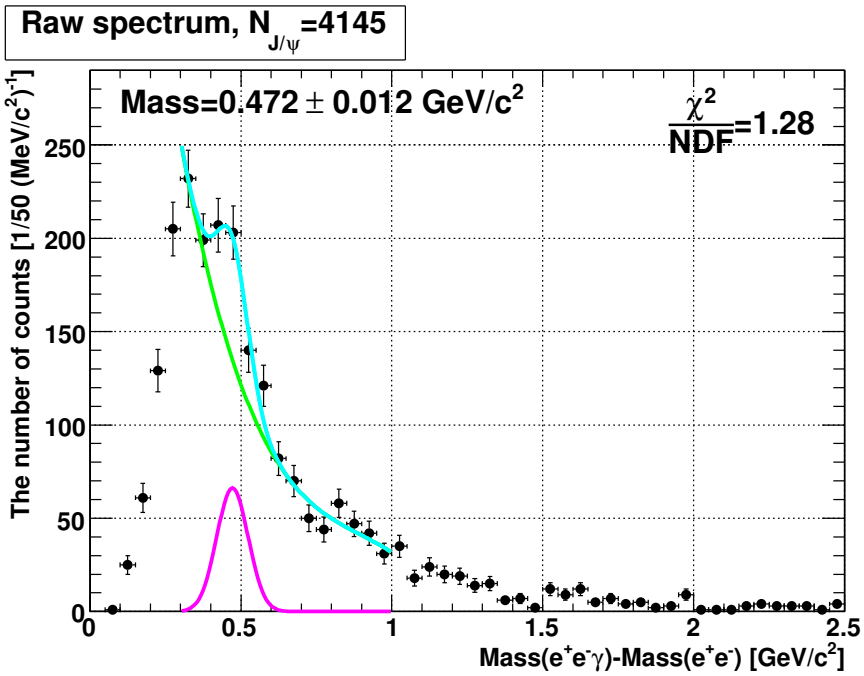

Figure 6.28: The raw mass difference spectra of combined data of Run-5 and Run-6 $p+p$ 200 GeV.

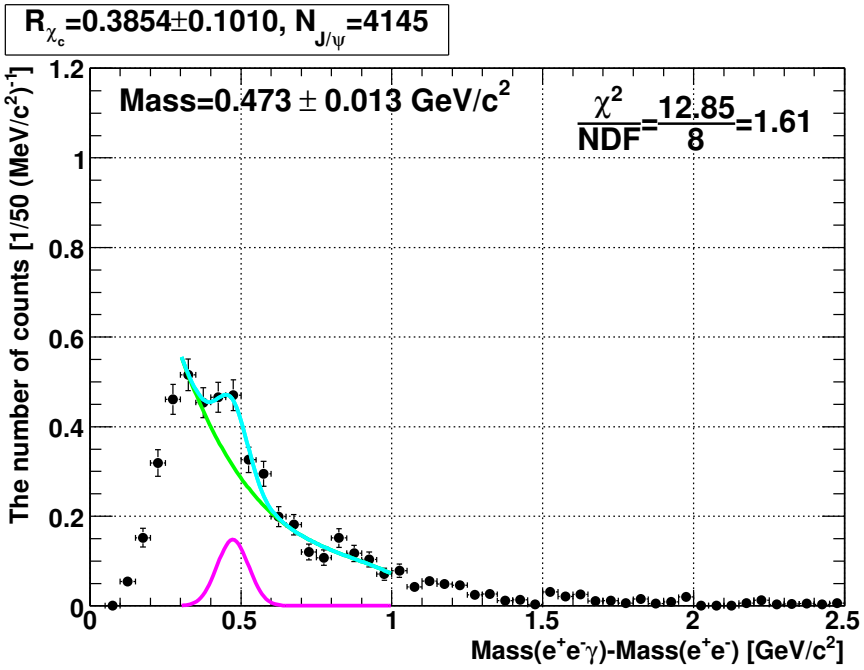

Figure 6.29: The efficiency corrected mass spectrum divided by the number J/ψ of combined data of Run-5 and Run-6 $p+p$ 200 GeV. The curves are the fitted Gaussian and third order polynomial function (aqua), Gaussian (magenta) and third order polynomial (green). The output R_{χ_c} is 0.39 ± 0.10 (stat).

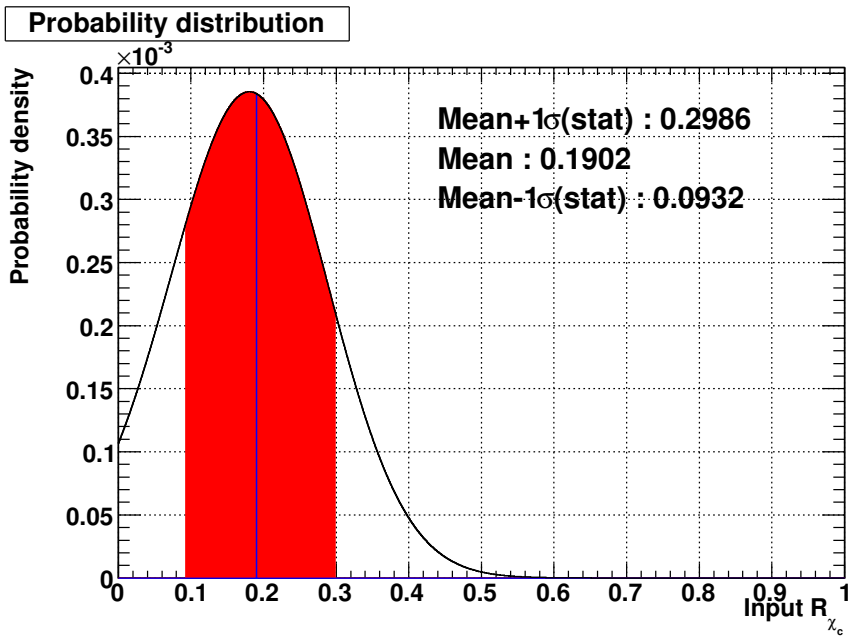

Figure 6.30: Probability density function of R_{χ_c} with third order polynomial and Gaussian fitting with the spectrum. The input R_{χ_c} is estimated to be R_{χ_c} =0.19 ± $^{0.11}_{0.10}$ (stat) for the output R_{χ_c} =0.39 ± 0.10 (stat).

6.7.1 Photon Cut Dependence of R_{χ_c}

To study the systematics of the photon cut, the photon cut parameters were varied.

Dependence of ecore Cut Threshold

The threshold of the ecore cut was varied from 0.20 to 0.45 GeV. Dependence of R_{χ_c} on the ecore cut threshold is tabulated in Table 6.3 and shown in Fig. 6.31. In Table 6.3, the corresponding figures in Appendix F are written. The RMS of input R_{χ_c} of 0.108 is assigned as the systematic error of the ecore cut. The input R_{χ_c} increases with the ecore threshold. This increment is partially due to the artificial peak produced by the ecore cut. With a low ecore threshold, the artificial peak locates at the lower side. With a high ecore threshold, the artificial peak locates the same place of the χ_c peak.

ecore threshold (GeV)	Output R_{χ_c}	Input R_{χ_c}	
0.20	0.25 ± 0.11	$0.12 \pm {}^{0.17}_{0.08}$	Fig. F.1
0.25	0.37 ± 0.10	0.20 ± 0.11	Fig. F.2
0.30	0.39 ± 0.10	$0.19 \pm {}^{0.11}_{0.10}$	Fig. 6.29, nominal
0.35	0.46 ± 0.10	0.29 ± 0.10	Fig. F.3
0.40	0.42 ± 0.11	$0.31 \pm {}^{0.10}_{0.11}$	Fig. F.4
0.45	0.47 ± 0.13	$0.42 \pm {}^{0.14}_{0.18}$	Fig. F.5

Table 6.3: The ecore cut threshold dependence of R_{χ_c}.

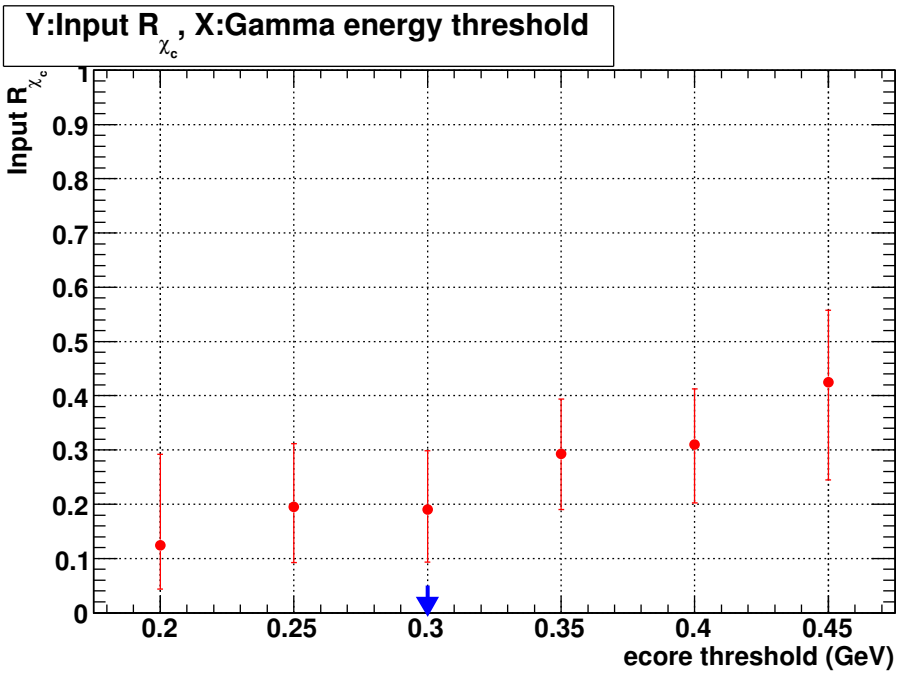

Figure 6.31: The ecore cut threshold dependence of input R_{χ_c}.

Dependence of emcchi2 Cut Threshold

The threshold of the emcchi2 cut was varied from 1.5 to 3.5. Dependence of R_{χ_c} on the emcchi2 cut threshold is tabulated in Table 6.4. The RMS of input R_{χ_c} of 0.007 is assigned as the systematic error of the emcchi2 cut.

emcchi2 threshold	Output R_{χ_c}	Input R_{χ_c}	
1.5	0.37 ± 0.10	$0.18 \pm {}^{0.11}_{0.10}$	Fig. F.6
2.5	0.39 ± 0.10	$0.19 \pm {}^{0.11}_{0.10}$	Fig. 6.29, nominal
3.5	0.40 ± 0.10	$0.19 \pm {}^{0.11}_{0.13}$	Fig. F.7

Table 6.4: The emcchi2 cut threshold dependence of R_{χ_c}.

Dependence of Size of DC Charged Particle Veto

The size of of the DC charged particle veto was varied from 17.5 cm $\times$ 0.035 radian to 70 cm $\times$ 0.14 radian. The dependence of R_{χ_c} on the size of the DC charged particle veto is tabulated in Table 6.5. The RMS of input R_{χ_c} of 0.010 is assigned as the systematic error of the DC charged particle veto.

Size of DC charged particle veto	Output R_{χ_c}	Input R_{χ_c}	
17.5 cm $\times$ 0.035 radian	0.41 ± 0.10	$0.20 \pm {}^{0.12}_{0.10}$	Fig. F.8
35 cm $\times$ 0.07 radian	0.39 ± 0.10	$0.19 \pm {}^{0.11}_{0.10}$	Fig. 6.29, nominal
70 cm $\times$ 0.14 radian	0.45 ± 0.10	$0.18 \pm {}^{0.05}_{0.08}$	Fig. F.9

Table 6.5: The dependence of R_{χ_c} on the size of DC charged particle veto.

Dependence of Fiducial Cut

It is necessary to know that the fiducial cut surely removes noisy and dead area. However, varying of the fiducial cut, especially loosening of fiducial cut, can lead to large background for photon detection. Instead of loosening and tightening of the fiducial cut, PbGl sectors are dropped and the ecore dependence of R_{χ_c} is checked without PbGl. The ecore cut threshold dependence of R_{χ_c} without PbGl is tabulated in Table 6.6. The difference of average input R_{χ_c} with and without PbGl of 0.029 is assigned as the systematic error of the fiducial cut.

ecore threshold (GeV)	Output R_{χ_c}	Input R_{χ_c}	
0.25	0.34 ± 0.12	$0.18 \pm {}^{0.13}_{0.10}$	Fig. F.10
0.30	0.40 ± 0.11	$0.19 \pm {}^{0.12}_{0.10}$	Fig. F.11
0.35	0.44 ± 0.11	$0.22 \pm {}^{0.08}_{0.10}$	Fig. F.12

Table 6.6: The ecore cut threshold dependence of R_{χ_c} without PbGl.

6.7.2 Counting Method Dependence of R_{χ_c}

To understand the systematics of the counting method, the counting method was varied.

Dependence of Fitting Range

The fitting range was varied from 0.35–0.95 GeV/c^2 to 0.25–1.05 GeV/c^2. The fitting range dependence of R_{χ_c} is tabulated in Table 6.7. The RMS of input R_{χ_c} of 0.020 is assigned as the systematic error of the fitting range.

Fitting range (GeV/c^2)	Output R_{χ_c}	Input R_{χ_c}	
0.35–0.95	0.33 ± 0.09	$0.19 \pm {}^{0.12}_{0.11}$	Fig. F.13
0.30–1.00	0.39 ± 0.10	$0.19 \pm {}^{0.11}_{0.10}$	Fig. 6.29, nominal
0.25–1.05	0.40 ± 0.09	$0.15 \pm {}^{0.10}_{0.08}$	Fig. F.14

Table 6.7: The fitting range dependence of R_{χ_c}.

Dependence of Fixed Peak Width

The fixed peak width for the fitting was varied from 0.042 to 0.062 GeV/c^2. and its dependence of R_{χ_c} is tabulated in Table 6.8. The RMS of input R_{χ_c} of 0.003 is assigned as the systematic error of the peak width.

Width (GeV/c^2)	Output R_{χ_c}	Input R_{χ_c}	
0.042	0.31 ± 0.08	0.20 ± 0.10	Fig. F.15
0.052	0.39 ± 0.10	$0.19 \pm {}^{0.11}_{0.10}$	Fig. 6.29, nominal
0.062	0.49 ± 0.12	$0.19 \pm {}^{0.11}_{0.10}$	Fig. F.16

Table 6.8: The peak width dependence of R_{χ_c}.

Dependence of Fitting Function

Three types of the fitting function were tested. The fitting function dependence of R_{χ_c} is tabulated in Table 6.9. The RMS of input R_{χ_c} of 0.044 is assigned as the systematic error of the fitting function.

Fitting function	Output R_{χ_c}	Input R_{χ_c}	
Second order polynomial+Gaussian	0.32 ± 0.09	$0.12 \pm {}^{0.10}_{0.07}$	Fig. F.17
Third order polynomial+Gaussian	0.39 ± 0.10	$0.19 \pm {}^{0.11}_{0.10}$	Fig. 6.29, nominal
Fourth order polynomial+Gaussian	0.19 ± 0.08	$0.11 \pm {}^{0.12}_{0.07}$	Fig. F.18

Table 6.9: The fitting function dependence of R_{χ_c}.

6.7.3 ERT LVL1 Trigger Efficiency for J/ψ

In this analysis, the ERT LVL1 trigger efficiency is not calculated from single electron spectrum. The level-1 efficiency is calculated using measured and expected J/ψ spectra. The expected J/ψ spectrum is the Kaplan function with $\langle p^2_{T,J/\psi}\rangle = 4.14\pm^{0.35}_{0.27}$ GeV/c^2. The Kaplan function is varied by these errors (Fig. 6.26) and R_{χ_c} values are obtained and tabulated in Table 6.10. The RMS between the three R_{χ_c} values, 0.017, is assigned as the systematic error of the J/ψ level-1 efficiency.

$\langle p^2_{T,J/\psi}\rangle$ (GeV/c)^2	Output R_{χ_c}	
3.87	0.40 ± 0.10	Fig. F.19
4.14	0.39 ± 0.10	Fig. 6.29, nominal
4.49	0.37 ± 0.10	Fig. F.20

Table 6.10: The J/ψ level-1 efficiency dependence of R_{χ_c}.

6.7.4 Dependence of J/ψ Acceptance

While the nominal setting for the J/ψ acceptance calculation is Run-5 $p+p$ 200 GeV, the setting with Run-4 Au+Au 200 GeV was also tested (Fig. 6.27). The result is tabulated in Table 6.11. The difference between the two R_{χ_c} values, 0.01, is used as the systematic error of the J/ψ acceptance.

Settings	Output R_{χ_c}	
Run-4 Au+Au 200 GeV	0.38 ± 0.10	Fig. F.21
Run-5 $p+p$ 200 GeV	0.39 ± 0.10	Fig. 6.29, nominal

Table 6.11: The J/ψ acceptance dependence of R_{χ_c}.

6.7.5 Systematic Error Summary

The systematic errors are summarized in Table 6.12. The relative part of the total systematic error is 15% for the output R_{χ_c}. The constant term of the total systematic error is 0.12 for the input R_{χ_c}. The constant term which is needed here is one for the output R_{χ_c}. As shown in Fig.6.22, the differential coefficient between the input and output R_{χ_c} is ∼1 and the systematic error of 0.12 is used for the output R_{χ_c}. The total systematic error for the output $R_{\chi_c} = 0.39$ is 0.14.

The probability density function of the input R_{χ_c} with the output R_{χ_c} of 0.39±0.14 (syst) is obtained and shown in Fig. 6.32. The 90% confidence level upper limit of R_{χ_c} is determined to be 0.40. The most probable value of R_{χ_c} is close to zero.

Source	Systematic error	Description
The number of χ_c		
Fitting function	0.044	6.7.2
Fitting range	0.020	6.7.2
Peak width	0.003	6.7.2
The conditional efficiency of χ_c		
ecore threshold	0.108	6.7.1
emcchi2 threshold	0.007	6.7.1
Size of charged particle veto	0.010	6.7.1
Fiducial cut	0.029	6.7.1
Photon identification including		
run-by-run fluctuation	13% (relative)	6.3.3
Polarization of χ_c	5.6% (relative)	6.4.1
Assumption of $\sigma_{\chi c1}/\sigma_{\chi c2}$	4.3% (relative)	6.4.1
DC charged particle veto	1.7% (relative)	6.3.2
Parameterization	1.4% (relative)	6.4.1
The azimuthal distribution of J/ψ	0.8% (relative)	6.4.1
BbcZvertex distribution	0.3% (relative)	6.4.1
J/ψ acceptance		
Simulation settings	0.01	6.7.4
Polarization of J/ψ	1% (relative)	6.6.1
J/ψ efficiency of ERT LVL1 trigger	0.017	6.7.3
Background in J/ψ candidate	2% (relative)	6.6.1

Table 6.12: Summary of systematic errors of R_{χ_c}.

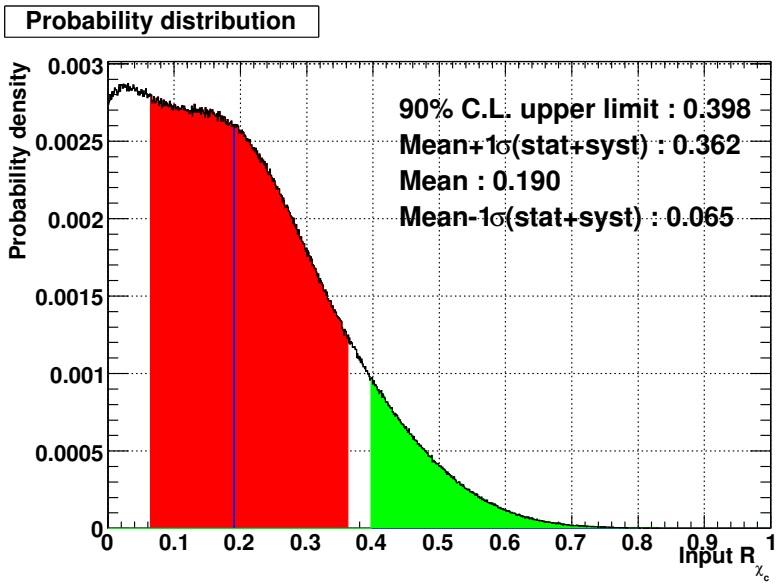

Figure 6.32: Probability density function of the input R_{χ_c} with third order polynomial and Gaussian fitting with the output R_{χ_c} of 0.39±0.14 (syst). The 90% confidence level upper limit of the input R_{χ_c} is 0.40.

6.8 Result

The fraction of J/ψ from the χ_c decay, R_{χ_c}, in $p+p$ collisions is shown in Fig. 6.33. The 90% confidence level upper limit of the R_{χ_c} is 0.40. The R_{χ_c} values obtained from other experiments are also shown in Fig. 6.33.

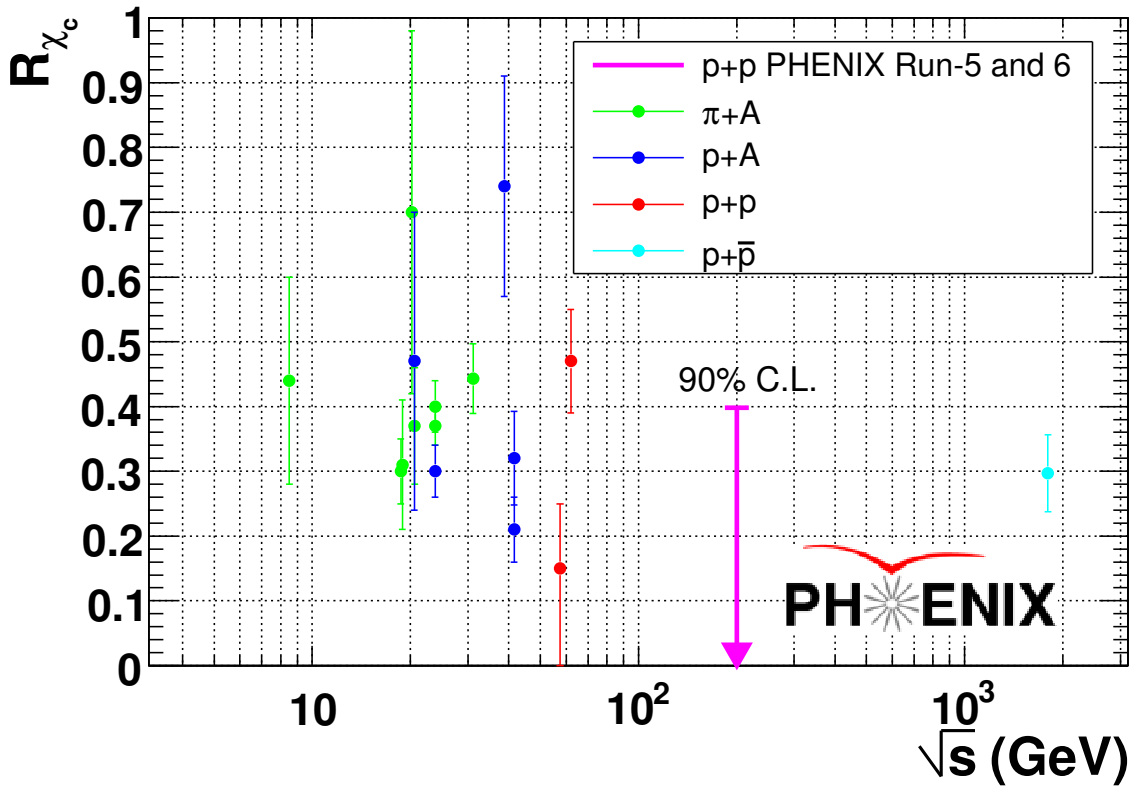

Figure 6.33: The upper limit of the fraction of J/ψ from the χ_c decay, R_{χ_c}, in $p+p$ collisions at $\sqrt{s_{NN}} = 200$ GeV is represented by the magenta arrow. The 90% confidence level upper limit of the R_{χ_c} is 0.40. The R_{χ_c} values obtained from other experiments are also shown as a function of center of mass energy $\sqrt{s}$.

Chapter 7

Discussion

Discussions are made on the obtained results of J/ψ production in Cu+Cu collisions and χ_c production in $p+p$ collisions in this chapter. In section 7.1, the χ_c result is discussed to understand the charmonium production mechanism. In section 7.2, the measured yields of J/ψ in Cu+Cu collisions at mid and forward rapidity are compared. Cold nuclear matter effects of J/ψ in d+Au and Cu+Cu collisions are discussed in section 7.3. In section 7.4, the measured yields of J/ψ in Cu+Cu and Au+Au collisions are compared. Section 7.5 describes the comparison between the measured data of J/ψ at RHIC and that at the SPS. The measured yields of J/ψ at RHIC are compared to theoretical models to understand the behavior of charmonia in the hot and dense medium produced at RHIC in section 7.6. Future measurements needed to understand the behavior of quarkonia in high-energy heavy-ion collisions will be written in section 7.7.

7.1 Feed-down Fraction of χ_c and Production Mechanism of Charmonia

The fraction of J/ψ from χ_c decay feed-down (R_{χ_c}) in $p+p$ collisions at $\sqrt{s} = 200$ GeV is found to be less than 0.40 at the 90% confidence level. This feed-down information is important to understand the suppression of inclusive J/ψ by the cold nuclear matter effect and dissociation in the hot and dense matter. The R_{χ_c} values obtained from low energy ($\sqrt{s} < 42$ GeV) experiments with high statistics distribute from 0.2 to 0.5 as shown in Fig. 6.33. The R_{χ_c} value is found to be $0.297 \pm 0.017(\text{stat}) \pm 0.057(\text{syst})$ in $p+\bar{p}$ collisions at $\sqrt{s} = 1800$ GeV [42]. Thus, the obtained upper bound at $\sqrt{s}$ =200 GeV and the data from other experiments strongly suggest that the energy dependence of R_{χ_c} is small and the average value of R_{χ_c} is 0.34.

Figure 7.1 shows the fitted polynomial functions of $\log_{10}(\sqrt{s}/\text{GeV})$ with the data points and the collision system dependence is neglected here. Table 7.1 shows the reduced χ^2 value for each fitted polynomial, and the zeroth and first order polynomial functions are the best fitted functions. However, the probability is not large (1.4×10^{-2}) and this is due to the limited and fluctuated data of the χ_c measurement in hadronic collisions.

The obtained upper bound of R_{χ_c} at $\sqrt{s}$ =200 GeV and data of other experiments

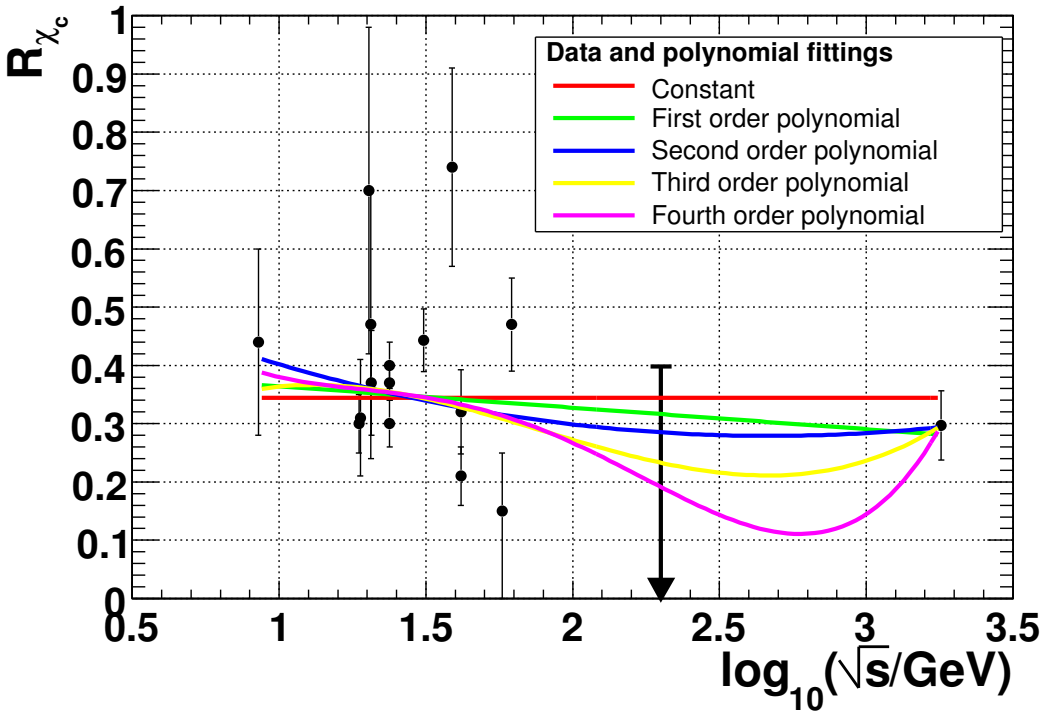

Figure 7.1: Experimental data points of R_{χ_c} and fitted polynomial functions of $\log_{10}(\sqrt{s}/\mathrm{GeV})$.

Order of polynomial function	χ^2/NDF	Probability
Zeroth (constant)	30.9/16=1.93	1.4×10^{-2}
First	29.6/15=1.97	1.4×10^{-2}
Second	29.1/14=2.08	1.0×10^{-2}
Third	28.9/13=2.22	6.9×10^{-3}
Fourth	28.7/12=2.39	4.3×10^{-3}

Table 7.1: Summary of reduced χ^2 with fitted polynomial functions of $\log_{10}(\sqrt{s}/\mathrm{GeV})$.

are compared with theoretical model predictions in this section.

7.1.1 Color Evaporation Model

The predictions of the R_{χ_c} value by two color evaporation models represented by a dashed line [145] and a solid line [146] are shown in Fig. 7.2. The color evaporation models essentially have no energy dependence of R_{χ_c}. The values of R_{χ_c} by the two model calculations are 0.24 [145] and 0.3 [146] and these values are consistent with the obtained upper bound of 0.40 at $\sqrt{s}$=200 GeV. While the values of χ^2/NDF for all data points are large, 4.75 for R_{χ_c}=0.24 and 2.35 for R_{χ_c}=0.30, the no energy dependence of R_{χ_c} of this model agrees with the observed constant tendency of R_{χ_c}.

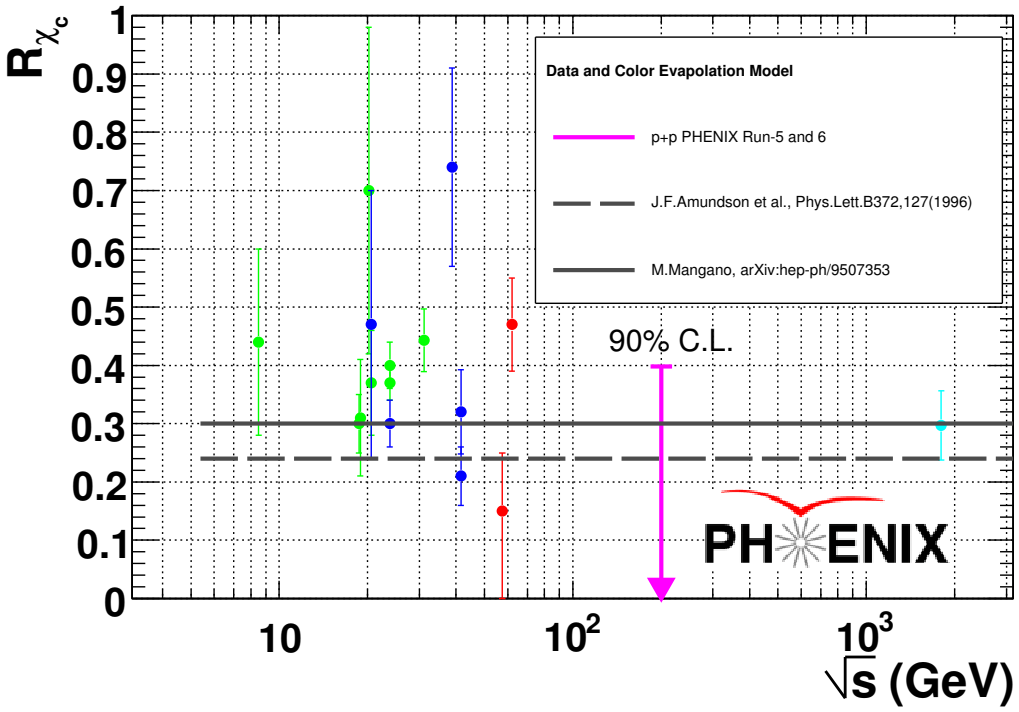

Figure 7.2: The predictions of the R_{χ_c} value by two color evaporation models (a dashed line [145] and a solid line [146]) and the experiment data.

7.1.2 NRQCD

The predictions of the R_{χ_c} value by the two NRQCD (Non-Relativistic QCD) model calculations represented by dashed lines ([143] $\pi + N$ collisions (green) and $p + N$ collisions (blue) [1]) and solid lines ([38] $\pi^- + N$ collisions (green) and $p + N$ collisions (blue) at $\sqrt{s} = 23.7$ GeV) at $R_{\chi_c} \sim 0.27$ are shown in Fig. 7.3. No NRQCD predictions are available at $\sqrt{s}$=200 GeV from literature. One model ([143], dashed lines) predicts strong energy dependence of R_{χ_c} in the energy range of $\sqrt{s} < 60$ GeV and a small value

[1]The curves are obtained from Fig. 5 in Ref. [45].

of $R_{\chi_c} < 0.2$ at $\sqrt{s} = 20$ GeV. Experimental results at $\sqrt{s} \sim 20$ GeV contradict with the prediction of the small R_{χ_c}. Another prediction at $\sqrt{s} = 23.7$ GeV agrees with experimental results within errors.

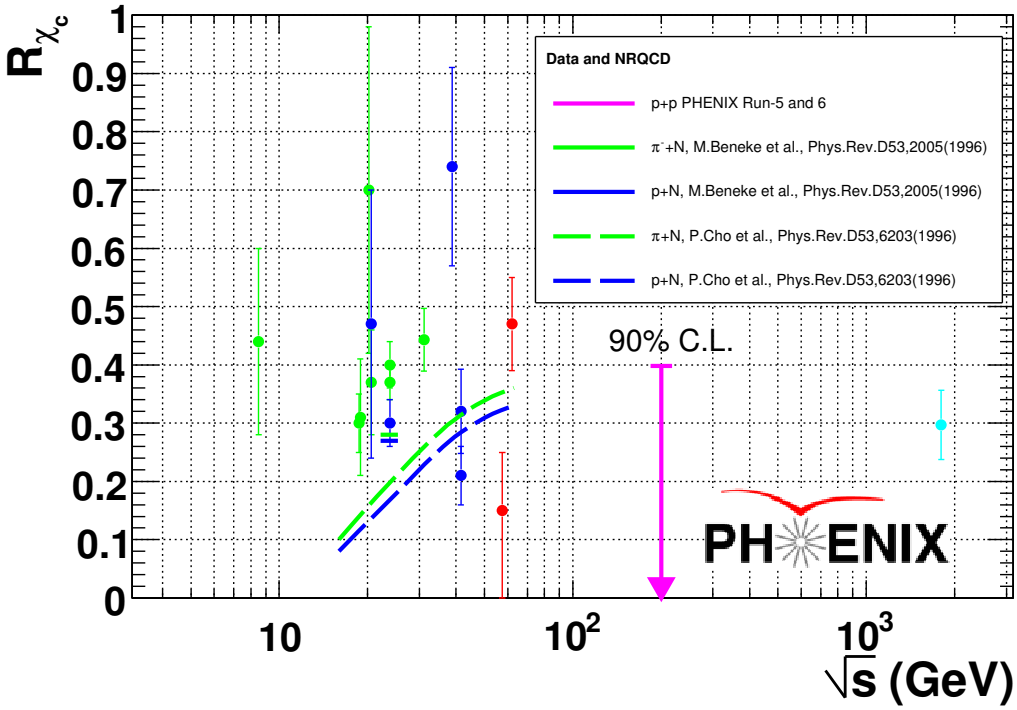

Figure 7.3: The predictions of the R_{χ_c} value by two NRQCD models (dashed lines [143] and solid lines [38]) and experiment data.

7.1.3 Color Singlet Model

The predictions of the R_{χ_c} value by three types of the color singlet model represented by dashed lines ([147] $\pi + N$ collisions (green) and $p + N$ collisions (blue) [2]), a dotted line ([148] $\pi^- + p$ collisions [3]) and solid lines ([38] $\pi^- + N$ collisions (green) and $p + N$ collisions (blue) at $\sqrt{s} = 23.7$ GeV) are shown in Fig. 7.4. No predictions of the color singlet model are available at $\sqrt{s}$=200 GeV from literature. The absolute values of R_{χ_c} of the five predictions are greater than 0.45 and contradict with results of high statistics experiments at $\sqrt{s}$ ~18–42 GeV. Two models which predict the energy dependence of R_{χ_c} have the opposite energy dependence; One model [148] predicts R_{χ_c} decreases as energy increases and the other model [147] predicts R_{χ_c} increases as energy increases.

7.1.4 Comover Model

The prediction of the R_{χ_c} value by a comover model represented by solid lines ([150] $\pi + A$ collisions (green) and $p + A$ collisions (blue)) is shown in Fig. 7.5. This model has

[2]The curves are obtained from Fig. 5 in Ref. [45].
[3]The curve is obtained from Fig. 4 in Ref. [149].

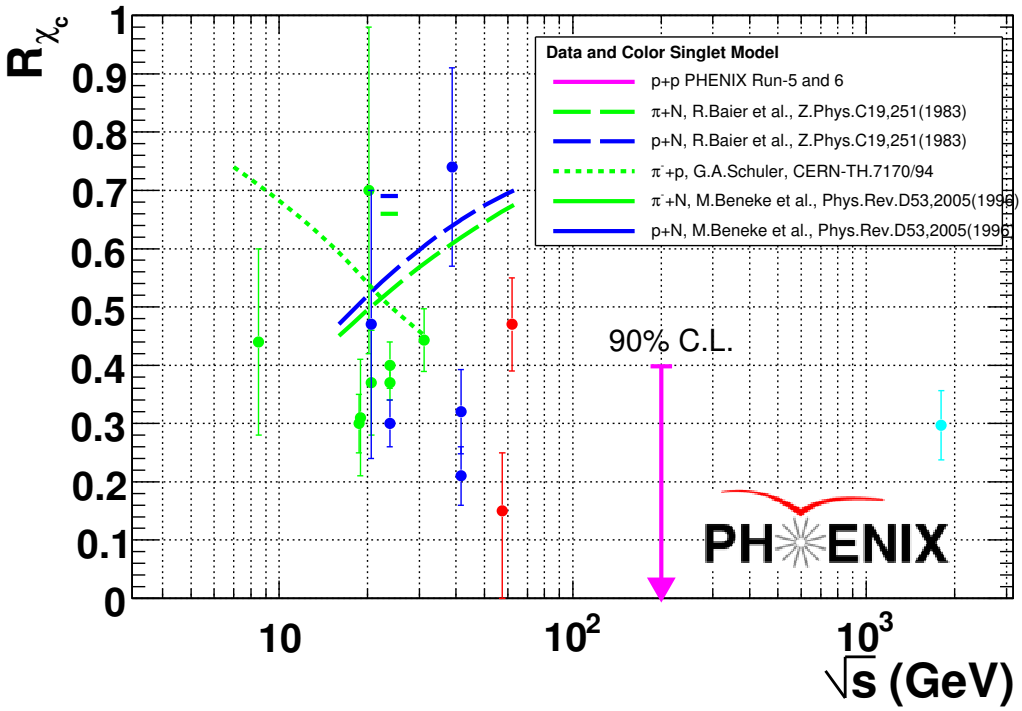

Figure 7.4: The predictions of the R_{χ_c} value by three color singlet models (dashed lines [147], a dotted line [148] and solid lines [38]) and experiment data.

small positive energy dependence of R_{χ_c} and the predicted value at the RHIC energy is almost equal to the obtained upper bound of R_{χ_c}.

7.1.5 Predictions by PYTHIA

Since no prediction values of R_{χ_c} from the color singlet model and NRQCD are available at $\sqrt{s} = 200$ GeV from literature, the event generator PYTHIA [129], is used to obtain predictions at the energy. The color singlet model from Ref. [147] and NRQCD from Ref. [144] are implemented in PYTHIA.

PYTHIA provides only the highest order processes of the color singlet model:

- $gg \to \chi_{c0}$ (ISUB=104, α_s^2),
- $gg \to \chi_{c2}$ (ISUB=105, α_s^2),
- $gg \to J/\psi g$ (ISUB=86, α_s^3).

While the following processes producing χ_{cJ} $(J = 0, 1, 2)$ at the α_s^3 order can contribute to inclusive J/ψ production, the processes are not available in PYTHIA.

- $gq \to \chi_{cJ} q$
- $g\bar{q} \to \chi_{cJ} \bar{q}$
- $q\bar{q} \to \chi_{cJ} g$

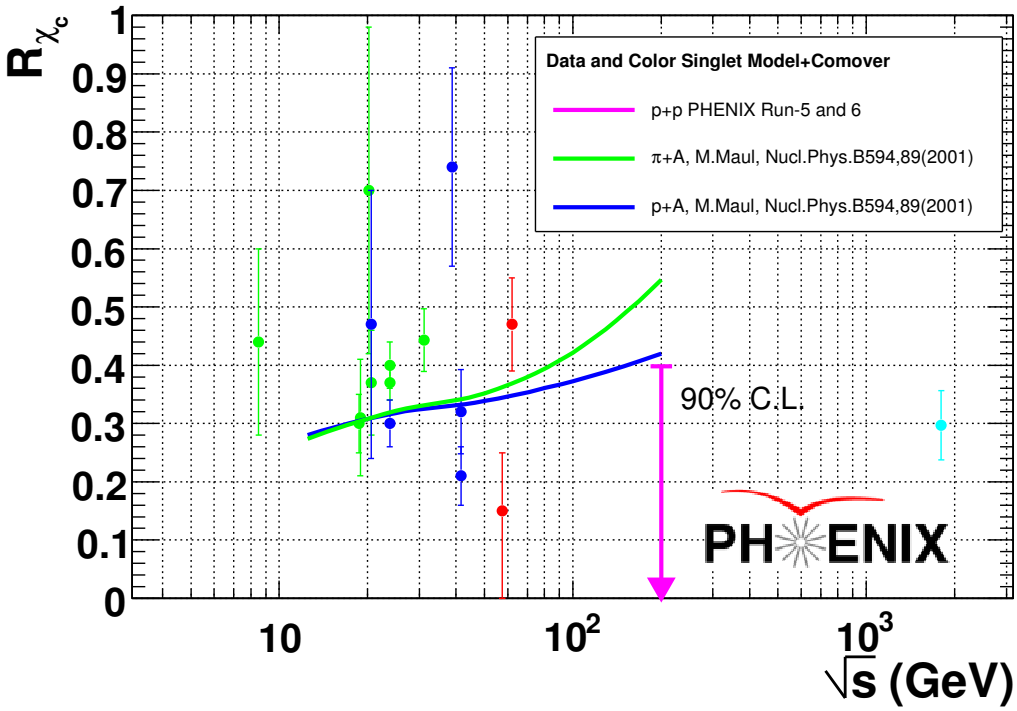

Figure 7.5: The predictions of the R_{χ_c} value by a comover model (solid lines) and experiment data [150].

- $gg \rightarrow \chi_{cJ} g$

The processes listed in Table 7.2 of NRQCD are included in PYTHIA.

The predictions of R_{χ_c} values for $p+p$ collisions with the color singlet model and NRQCD obtained with PYTHIA are shown in Fig. 7.6 with the experimental data. The parameters of PYTHIA were the default of version 6.403 except the following parameters: charm quark mass (PMAS(4,1)=1.25 (GeV/c^2)), primordial Gaussian k_T distribution in hadrons (PARP(91)=1.5 (GeV/c)). The difference of R_{χ_c} between $p+p$ and $\pi+p$ collisions at $\sqrt{s}$ = 10–50 GeV is less than 3% and the difference of R_{χ_c} between $p+p$ and $p+\bar{p}$ collisions at $\sqrt{s}$ = 1.8 TeV is also less than 3% for both cases of the color singlet model and NRQCD. The prediction from the color singlet model is larger than the experimental data and decreases with the increase of $\sqrt{s}$. The prediction from NRQCD is smaller than the experimental data and increases with the increase of $\sqrt{s}$. The measured upper bound of $R_{\chi_c} < 0.40$ at $\sqrt{s}$ = 200 GeV is consistent with the NRQCD prediction.

7.1.6 Conclusion of Model Comparison with Respect to R_{χ_c}

The reduced χ^2 and probability of the model predictions for the data points are shown in Table 7.3. These values are calculated for the whole available range of $\sqrt{s}$ including the RHIC energy of $\sqrt{s}$ = 200 GeV.

Since there are large variations even in the same theoretical framework, definitive conclusion cannot be drawn from the current experimental data. However, the experi-

Subprocess	Subprocess number in PYTHIA
$gg \to c\bar{c}[^3S_1^{(1)}]g$	421
$gg \to c\bar{c}[^3S_1^{(8)}]g$	422
$gg \to c\bar{c}[^1S_0^{(8)}]g$	423
$gg \to c\bar{c}[^3P_J^{(8)}]g$	424
$gq \to c\bar{c}[^3S_1^{(8)}]q$	425
$gq \to c\bar{c}[^1S_0^{(8)}]q$	426
$gq \to c\bar{c}[^3P_J^{(8)}]q$	427
$q\bar{q} \to c\bar{c}[^3S_1^{(8)}]g$	428
$q\bar{q} \to c\bar{c}[^1S_0^{(8)}]g$	429
$q\bar{q} \to c\bar{c}[^3P_J^{(8)}]g$	430
$gg \to c\bar{c}[^3P_0^{(1)}]g$	431
$gg \to c\bar{c}[^3P_1^{(1)}]g$	432
$gg \to c\bar{c}[^3P_2^{(1)}]g$	433
$gq \to c\bar{c}[^3P_0^{(1)}]q$	434
$gq \to c\bar{c}[^3P_1^{(1)}]q$	435
$gq \to c\bar{c}[^3P_2^{(1)}]q$	436
$q\bar{q} \to c\bar{c}[^3P_0^{(1)}]g$	437
$q\bar{q} \to c\bar{c}[^3P_1^{(1)}]g$	438
$q\bar{q} \to c\bar{c}[^3P_2^{(1)}]g$	439

Table 7.2: NRQCD subprocesses included in PYTHIA.

Model	Reference	χ^2/NDF	Probability
Color evaporation model (1)	[145]	81/17=4.75	2.8×10^{-10}
Color evaporation model (2)	[146]	40/17=2.35	1.3×10^{-3}
NRQCD	[144, 129]	205/15=13.7	$< 10^{-10}$
Color singlet model	[147, 129]	1133/15=75.6	$< 10^{-10}$
Comover model	[150]	37/15=2.45	1.4×10^{-3}
Average	$R_{\chi_c} = 0.344$	31/16=1.93	1.4×10^{-2}

Table 7.3: Summary of reduced χ^2 of the predictions including the RHIC energy and data points.

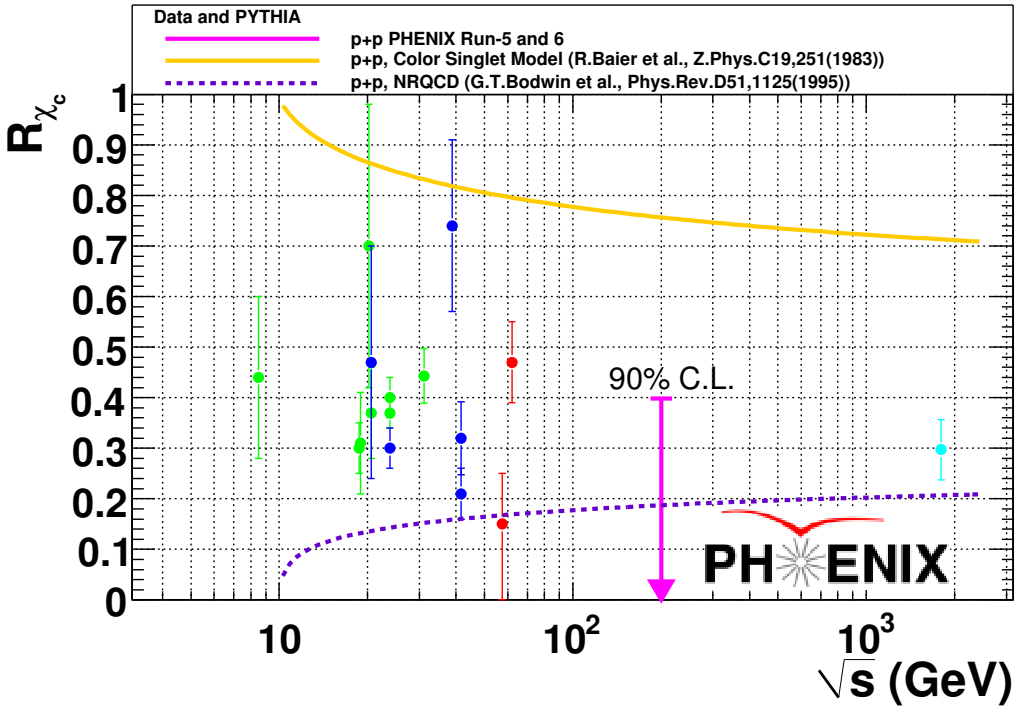

Figure 7.6: The predictions of the R_{χ_c} value obtained with PYTHIA and R_{χ_c} obtained by experiments. Orange solid line is the prediction of the color singlet model and violet dotted line is that of NRQCD.

mental data seems to favor the color evaporation model prediction with the experimental results with respect to the magnitude and energy dependence of R_{χ_c}. The comover model also seems to be favored by the data. The color singlet model prediction disagrees with the experimental result with respect to the magnitude of R_{χ_c}. The NRQCD predicts smaller R_{χ_c} values than the data points at $\sqrt{s} \sim 20$ GeV. However, the NRQCD prediction is not excluded by the obtained upper bound at $\sqrt{s} = 200$ GeV. The failure of the color singlet model in R_{χ_c} probably means that the color octet state has sizable contribution to the charmonium production. This fact agrees with the NRQCD result (Fig. 2.14) where the singlet contribution to the J/ψ production is about a half at $\sqrt{s} = 200$ GeV.

As described in section 2.5.2, the cold nuclear matter model used for the comparison to the RHIC data includes the color octet contribution which is estimated by the NRQCD calculation.

Since both uncertainties of experimental data and theoretical predictions of R_{χ_c} are large, we cannot give any quantitative conclusion on the color octet contribution in the charmonium production. As shown in Fig. 2.19, the crossing time is smaller than the charmonium formation times in the rapidity range of the PHENIX detector ($-2.2 < y < 2.2$). Therefore, as shown in Fig. 2.29, most of the nuclear absorption is due to the color octets and the uncertainty of the color octet contribution almost directly contributes the uncertainty of the absorption cross section.

At the RHIC energy, absorption cross sections of charmonia have the following order, $\sigma_{abs}^{\chi_c} < \sigma_{abs}^{J/\psi} < \sigma_{abs}^{\psi'}$, during crossing as shown in Fig. 2.25. Therefore, R_{χ_c} will increase as N_{part} increases by nuclear absorption if dissociation of charmonia in the QGP does not occur.

7.1.7 Ratio of $\sigma_{\chi_{c1}}/\sigma_{\chi_{c2}}$

Figure 7.7 shows data points and theoretical predictions of the ratio of $\sigma_{\chi_{c1}}/\sigma_{\chi_{c2}}$. There seems to be small energy dependence of $\sigma_{\chi_{c1}}/\sigma_{\chi_{c2}}$ in the data.

Since the χ_{c1} production is strongly suppressed in the color singlet model, the color singlet model predicts small $\sigma_{\chi_{c1}}/\sigma_{\chi_{c2}}$ values and fails to explain the data.

The NRQCD needs experimental data to obtain the nonperturbative coefficients by fitting (Eq. (2.42)). Although the NRQCD succeeds to explain the data at the fitting points ($\sqrt{s} = 23.7$ GeV and 1.8 TeV), it does not explain the energy dependence of $\sigma_{\chi_{c1}}/\sigma_{\chi_{c2}}$ (orange line in Fig. 7.7 is obtained by NRQCD implemented in PYTHIA).

The color evaporation model predicts that $\sigma_{\chi_{cJ}}$ is proportional to the spin multiplicity $2J + 1$. Therefore, $\sigma_{\chi_{c1}}/\sigma_{\chi_{c2}}$ will be $(2 \times 1 + 1)/(2 \times 2 + 1) = 3/5 = 0.6$ in the color evaporation model. This value contradicts the Tevatron data at $\sqrt{s} = 1.8$ and 1.96 TeV.

The comover model predicts the opposite energy dependence to the experimental results.

Although the experimental data of R_{χ_c} and $\sigma_{\chi_{c1}}/\sigma_{\chi_{c2}}$ cannot be explained by no models at the same time, it is strongly suggested that the contribution of the color octet is sizable at the RHIC energy ($\sqrt{s}$=200 GeV).

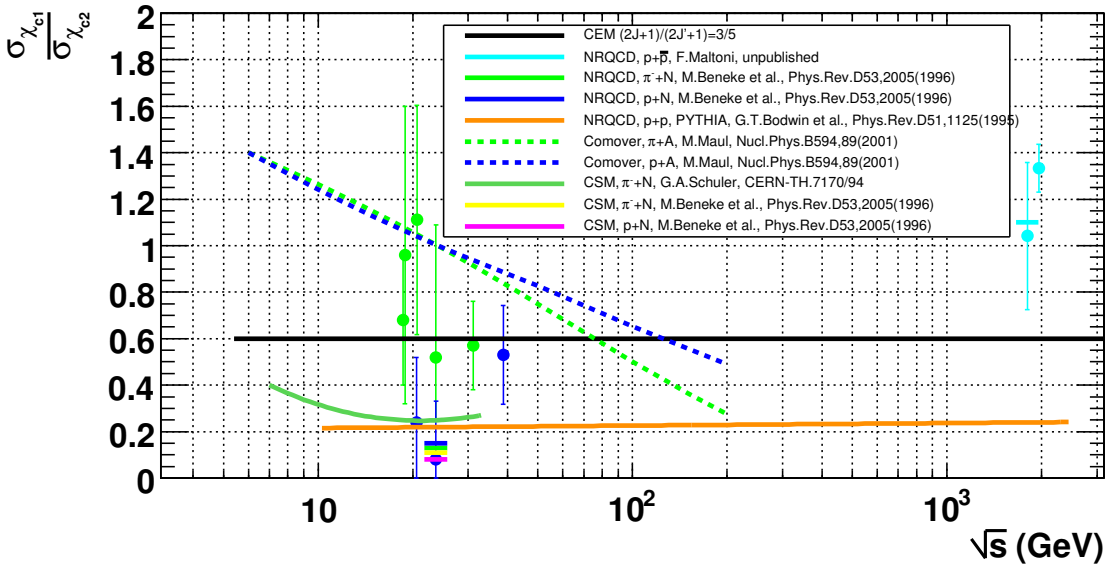

Figure 7.7: The ratio of cross sections of χ_{c1} and χ_{c2}, $\sigma_{\chi_{c1}}/\sigma_{\chi_{c2}}$. The names of experiments are shown in Fig. 6.5.

7.2 Comparison with J/ψ Data at Forward Rapidity in Cu+Cu Collisions

The yield of J/ψ in Cu+Cu collisions was also measured at forward and backward rapidity ($1.2 < y < 2.2$ and $-2.2 < y < -1.2$) via the $\mu^+\mu^-$ decay mode ($BR = 5.93 \pm 0.06\%$ [19]) using the PHENIX muon arms and the analysis short summary is written in Appendix G and Ref. [9]. Since a Cu+Cu collision is symmetric with respect to rapidity, backward rapidity is treated together with forward rapidity. The results of J/ψ production in Cu+Cu collisions at mid and forward rapidity are compared in this section.

7.2.1 Centrality Dependence of R_{AA}

Figure 7.8 shows nuclear modification factors R_{AA} for J/ψ production in Cu+Cu collisions at midrapidity and forward rapidity as a function of the number of participants N_{part}. The global systematic error is factorized and is 12% for midrapidity and 8% for forward rapidity. In the most central collisions ($N_{part} = 98$, Centrality = 0–10%), suppression of J/ψ production by a factor of ~ 2 is observed at both mid and forward rapidity. The significance of deviation from unity is 3.7σ for midrapidity and 5.7σ for forward rapidity where the statistical and systematic errors are added in quadrature. However, suppression patterns are different at the smaller N_{part} region at mid and forward rapidity. R_{AA} increases with the decrease of N_{part} at forward rapidity, while R_{AA} has the maximum of about 0.9 around $N_{part} \sim 30$ at midrapidity.

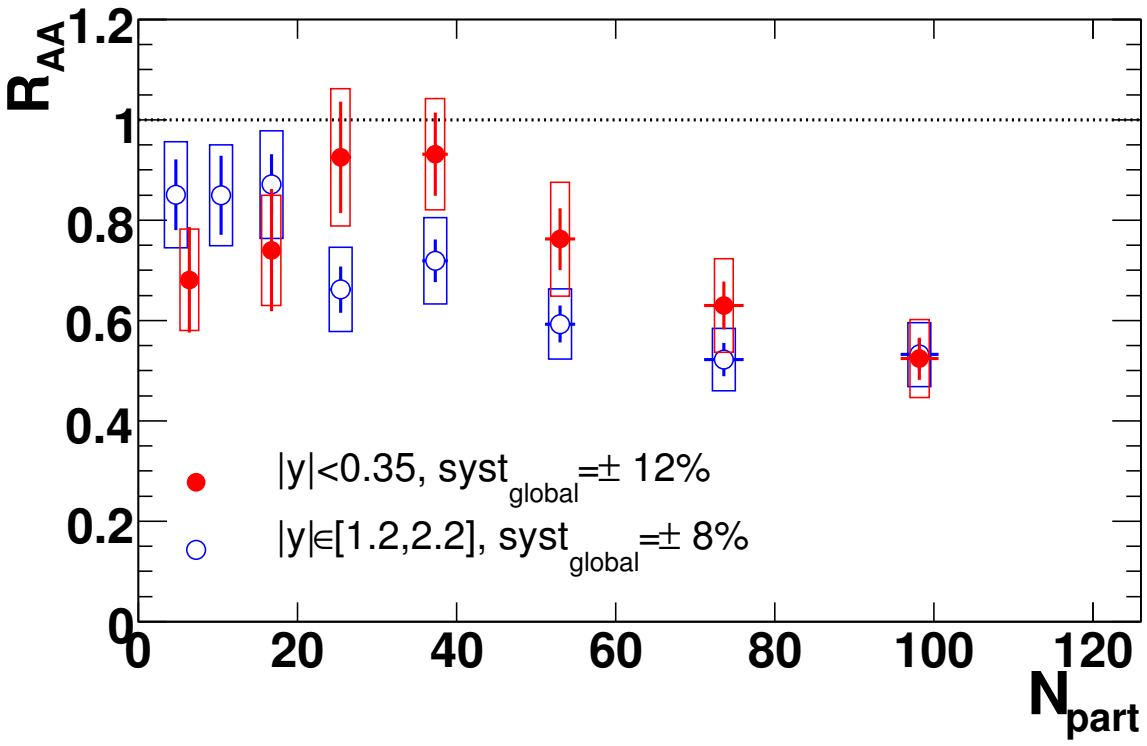

Figure 7.8: R_{AA} vs N_{part} for J/ψ production in Cu+Cu collisions at midrapidity (blue open circle, measured by e^+e^- pairs) and forward rapidity (red closed circle, measured by $\mu^+\mu^-$ pairs). Centrality bins are 0–10%, 10–20%, 20–30%, 30–40%, 40–50%, 60–94% (midrapidity), 60–70% and 70–94% (forward rapidity).

7.2.2 Data Points in Peripheral Cu+Cu Collisions at Midrapidity

In Table 7.4, the results of the χ^2 test for the data points in peripheral Cu+Cu collisions ($N_{part} < 45$) at midrapidity are shown. The significance of the positive slope p_1 of the linear function of N_{part} in the table is not very significant, $8.9/6.8 = 1.3\sigma$.

Fitting function	χ^2/NDF	Probability	parameters
1	7.66/4=1.92	0.10	
0.88 ($p+p$ error is 12%)	2.76/4=0.69	0.60	
p_0	1.95/3=0.65	0.58	$p_0 = 0.81 \pm 0.08$
$p_0 + p_1 \cdot N_{part}$	0.24/2=0.12	0.89	$p_0 = 0.62 \pm 0.16$
			$p_1 = (8.9 \pm 6.8) \times 10^{-3}$

Table 7.4: The χ^2 test with the quadrature sum of statistical and systematic errors for R_{AA} data points in peripheral Cu+Cu collisions (Centrality = 30–94%, $N_{part} < 45$) at midrapidity.

As will be discussed in the following sections, most of the theoretical models predict a monotonic decrease of R_{AA} with the increase of N_{part}. The observed suppression at midrapidity contradicts to these predictions and can recall us to a doubt whether the measurement is reliable. Possible sources of small R_{AA} values are as follows:

- Analysis artifact (failure)
  - Signal counting
  - Embedding efficiency, ε_{embed}(Centrality)
  - ERT electron trigger efficiency for J/ψ, $\varepsilon_{LVL1,J/\psi}(p_{T,J/\psi}$, Centrality)
- The number of collisions N_{coll} estimated by the Glauber model
- Impact parameter dependence of nuclear shadowing
- Beam-gas collisions and ultra peripheral collisions
- Statistical fluctuation

Signal counting is based on the subtraction of like sign pairs (Eq. (5.31)). If there is large background, signal counting can fail. The number of raw counts N_{+-}, N_{++} and N_{--}, the number of net counts N_{net} and the background fraction for each Centrality bin are shown in Table 7.5. While the background fraction is large in central collisions, it is less than 20% and statistical fluctuation is small enough in mid-central and peripheral collisions (Centrality $\geq$ 30%). Large loss (under extraction) of signals can happen in central collisions but is unlikely in peripheral collisions.

The Centrality dependent correction factors (section 5.8) are embedding efficiency and ERT electron trigger efficiency.

The embedding efficiency is shown in Fig. 5.26 and is only 3% correction in the most central collisions and is less than 1% in peripheral collisions (Centrality $\geq$ 50%).

Centrality	N_{+-}	$N_{++}+N_{--}$	N_{net} $= N_{+-}-(N_{++}+N_{--})$	Background fraction $(N_{++}+N_{--})/N_{+-}$
0–10%	778	353	425 ± 34	0.45±0.03
10–20%	475	144	331 ± 25	0.30±0.03
20–30%	290	58	232 ± 19	0.20±0.03
30–40%	215	37	178 ± 16	0.17±0.03
40–50%	119	15	104 ± 12	0.13±0.03
50–60%	69	7	62 ± 9	0.10±0.04
60–94%	59	5	54 ± 8	0.08±0.04

Table 7.5: The number of raw counts of electron pairs and background fraction in Cu+Cu collisions.

A large amount of underestimation of the embedding efficiency for peripheral collisions is unlikely because it means much larger underestimation of the embedding efficiency for central and mid-central collisions.

The ERT electron trigger efficiency including random benefit for J/ψ is shown in Fig. 5.28. Due to the limited statistics, 40–94% Centrality classes are treated as one bin. This treatment can lead to overestimation of the ERT electron trigger efficiency including random benefit for peripheral collisions (Centrality $\geq$ 50%). However, the random benefit is less than 4% for Centrality $\geq$ 40%. Since the ERT electron trigger efficiency including random benefit is about 70%, it will be only overestimation of 6%$\sim$ 4%/70%.

The nuclear modification factor R_{AA} is obtained by the yield and the number of collisions N_{coll} (Eq. (5.8)). The larger the number of collisions, the smaller the nuclear modification factor. The Glauber model is used to estimate the number of collisions.

The nucleon density function of ^{63}Cu in the Glauber model is assumed to be identical with the nuclear charge distribution in ^{63}Cu. The Woods-Saxon (Fermi) type function is used to parameterized the distribution (Eq. (2.18)). Although different types of parameterizations are possible, the uncertainty of the density function due to parameterization is small as shown in Fig. 7.9.

The uncertainty of other input parameters for the Glauber model (the nucleon-nucleon inelastic cross section σ_{NN} and the nucleon-nucleon overlapping function $t(\mathbf{b})$) are well taken into account as the systematic errors of N_{coll} and N_{part}.

In the most peripheral Cu+Cu collisions, the average values obtained from the Glauber calculation are $N_{part} = 6.5 \pm 0.6$ and $N_{coll} = 5.1 \pm 0.6$ (Table 5.1). These numbers are small and statistical event-by-event fluctuation of the collision geometry is large. However, if large statistics of events are accumulated, the fluctuation of the yield should vanish.

One of verifications of the N_{coll} calculation using the Glauber model is the measurement of direct photons produced by hard processes of the quark-gluon Compton scattering, quark-antiquark annihilation and fragmentation from Bremsstrahlung. Since photons do not interact strongly, the production cross section of photons would be proportional to N_{coll}. Figure 7.10 shows R_{AA} of direct photons and π^0 mesons with $p_T > 6$ GeV/c in Au+Au collisions at $\sqrt{s_{NN}} = 200$ GeV at PHENIX in Run-2 [151].

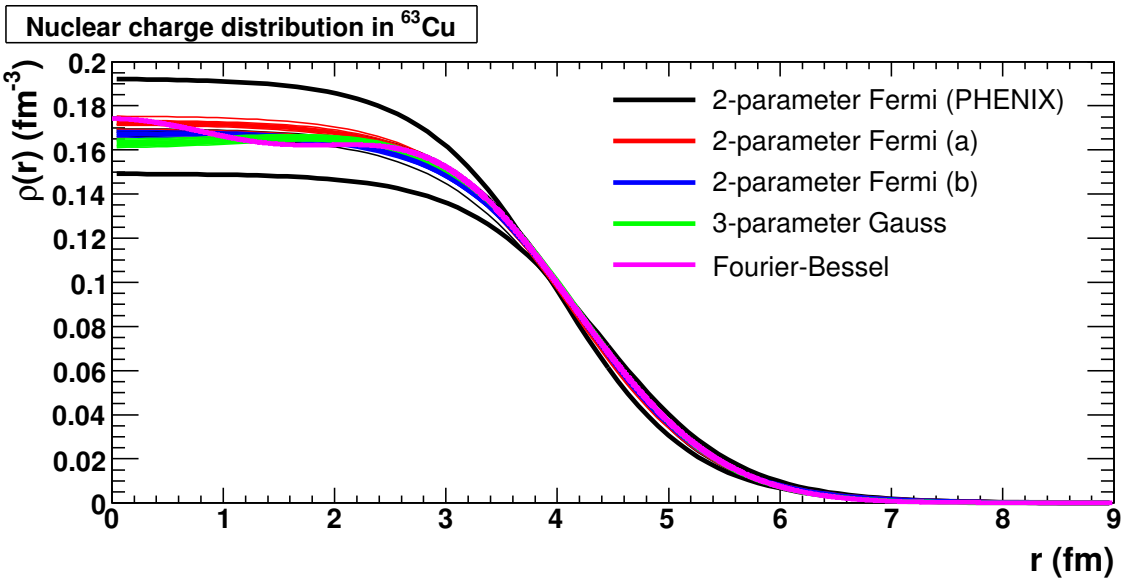

Figure 7.9: Nuclear charge distribution in a ^{63}Cu nucleus with different parameterization including uncertainty of parameters. Three types of two-parameter Fermi models including the PHENIX assumption (section 5.2.3), a three-parameter Gaussian model and a 17-parameter Fourier-Bessel model are shown. Those models except the PHENIX assumption are found in Ref. [127].

The direct photon yield is shown to scale with N_{coll} with errors of $> 10\%$ for all Centrality classes. The dominant error is the systematic error for central collisions and is the statistical error for peripheral collisions. For $N_{part} < 50$, there are very large statistical errors of direct photon R_{AA}. While the statistics of data at PHENIX in Run-4 are larger than those in Run-2 by a factor of 25, the statistical and systematic errors of direct photon R_{AA} are not small in the small N_{part} region.

Since π^0 mesons strongly interacts with the created medium, those yields are suppressed in central collisions. In peripheral collisions, the medium effects are expected to be small and R_{AA} is expected to be almost unity. The single electrons produced by semi-leptonic decay of heavy quarks with high transverse momenta are regarded as a hard probe. Figure 7.11 shows R_{AA} of single electrons with $p_T > 0.3$ and 3 GeV/c and π^0 with $p_T > 4$ GeV/c in Au+Au collisions at $\sqrt{s_{NN}} = 200$ GeV at PHENIX [152]. The values of R_{AA} of single electrons and π^0 in the most peripheral Au+Au collisions ($N_{part} \leq 20$) are less than 1 likewise.

Therefore, it is not verified that the yields of the particles which are regarded as hard probes scale with N_{coll} in the most peripheral collisions ($N_{part} \leq 20$). The application of the Glauber model to peripheral collisions can be wrong. The systematic uncertainty of the use of the Glauber model is not included in the systematic errors of N_{coll} and N_{part}.

If beam-gas collision events and/or ultra peripheral collision events account for a large fraction of collected events, N_{coll} is overestimated by the Glauber model. However, the minimum bias trigger of Cu+Cu collisions requires the coincidence of BBC hits at forward and backward rapidity ($3.0 < |\eta| < 3.9$) and the vertex location within 30 cm.

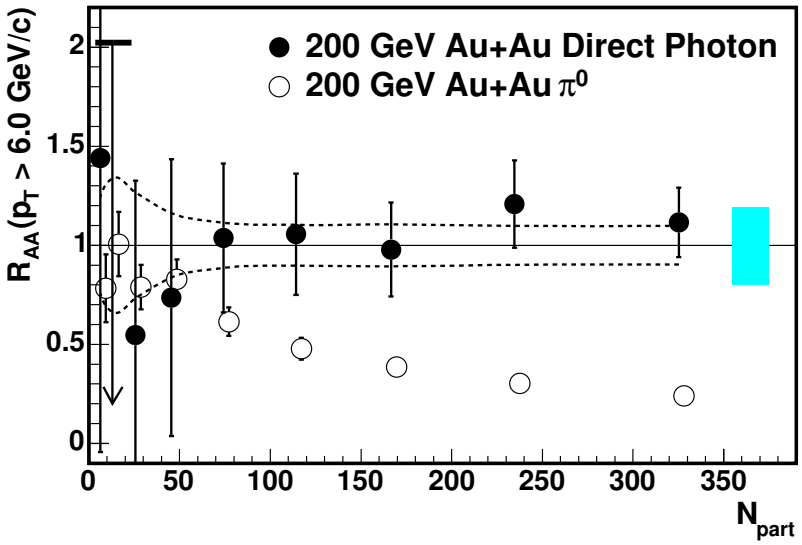

Figure 7.10: R_{AA} of direct photons and π^0 mesons in Au+Au collisions at $\sqrt{s_{NN}} = 200$ GeV at PHENIX in Run-2 as a function of Centrality given by N_{part} [151]. The error bars indicate the total error excluding the error on $\langle N_{coll} \rangle$ shown by the dashed lines and the scale uncertainty of the $p+p$ yields shown by the shaded region at the right.

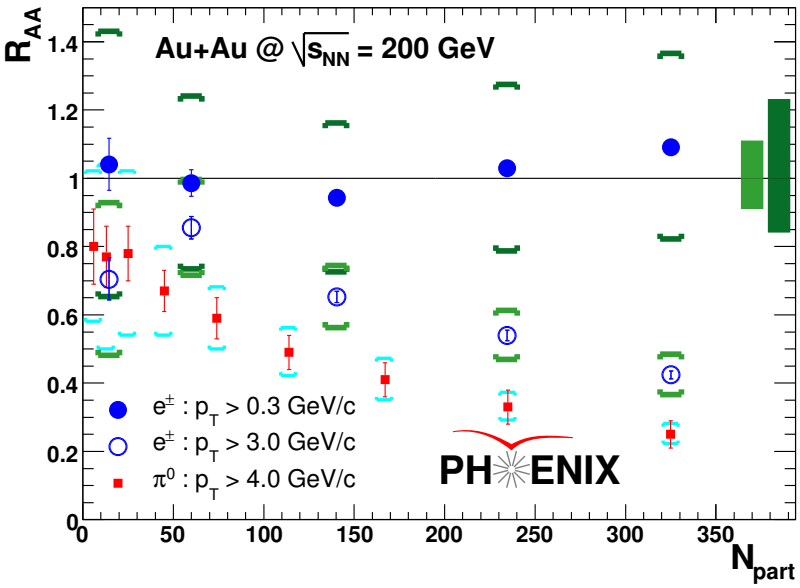

Figure 7.11: R_{AA} of single electrons with p_T above 0.3 and 3 GeV/c and neutral pions with $p_T > 4$ GeV/c in Au+Au collisions at $\sqrt{s_{NN}} = 200$ GeV [152]. Error bars (boxes) depict statistical (point-by-point systematic) uncertainties. The right (left) box at $R_{AA} = 1$ shows the relative uncertainty from the $p+p$ reference common to all points for $p_T > 0.3(3)$ GeV/c.

This tight requirement removes most of the beam-gas/ultra peripheral collision events. Only the coincidence of two energetic beam-gas/ultra peripheral collision events in the nominal vertex region can fire the minimum bias trigger but such coincidence is expected to be extremely rare.

In peripheral collisions, J/ψ is created by collisions of gluons in halos of nuclei. Some nuclear shadowing models explicitly predict the impact parameter dependence as shown in Fig. 7.12. However, these predicted dependencies will lead to less shadowing in peripheral collisions and do not explain the suppression of J/ψ in peripheral Cu+Cu collisions at midrapidity.

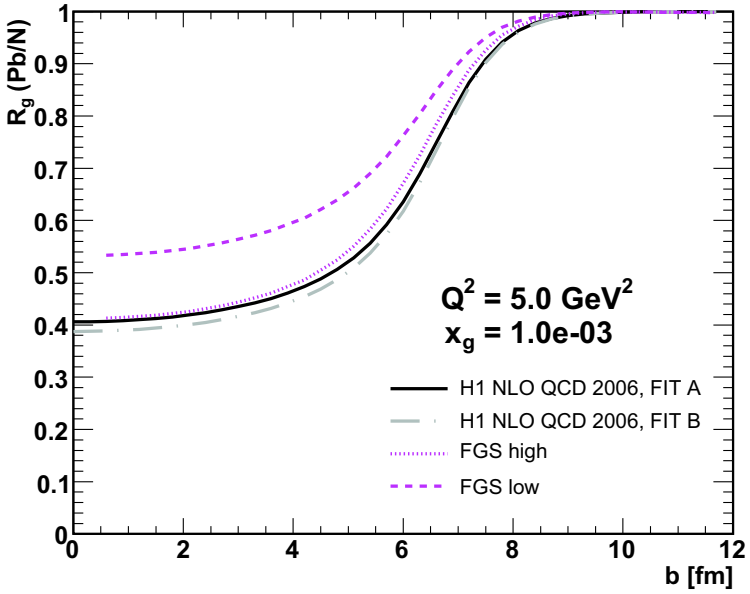

Figure 7.12: Impact parameter dependence of gluon shadowing in the Glauber-Gribov model [153] in a Pb nucleus, compared to the predictions of the FGS model [154].

Since the statistics of peripheral collisions are limited as shown in Table 7.5, more statistics are needed to obtain conclusive results.

7.2.3 Rapidity Dependence of R_{AA}

Figure 7.13 shows the rapidity distribution of J/ψ for 0–20%, 20–40%, 40–60% and 60–94% Centrality bins. Although data points at forward rapidity for 60–94% show some rapidity dependence within errors, the rapidity distribution in Cu+Cu collisions does not show any significant change from that in $p+p$ collisions.

7.2.4 Transverse Momentum Dependence of R_{AA}

Figure 7.14 shows the p_T distribution of J/ψ for 0–20%, 20–40%, 40–60% and 60–94% Centrality bins. The p_T distribution at midrapidity and that at forward rapidity almost

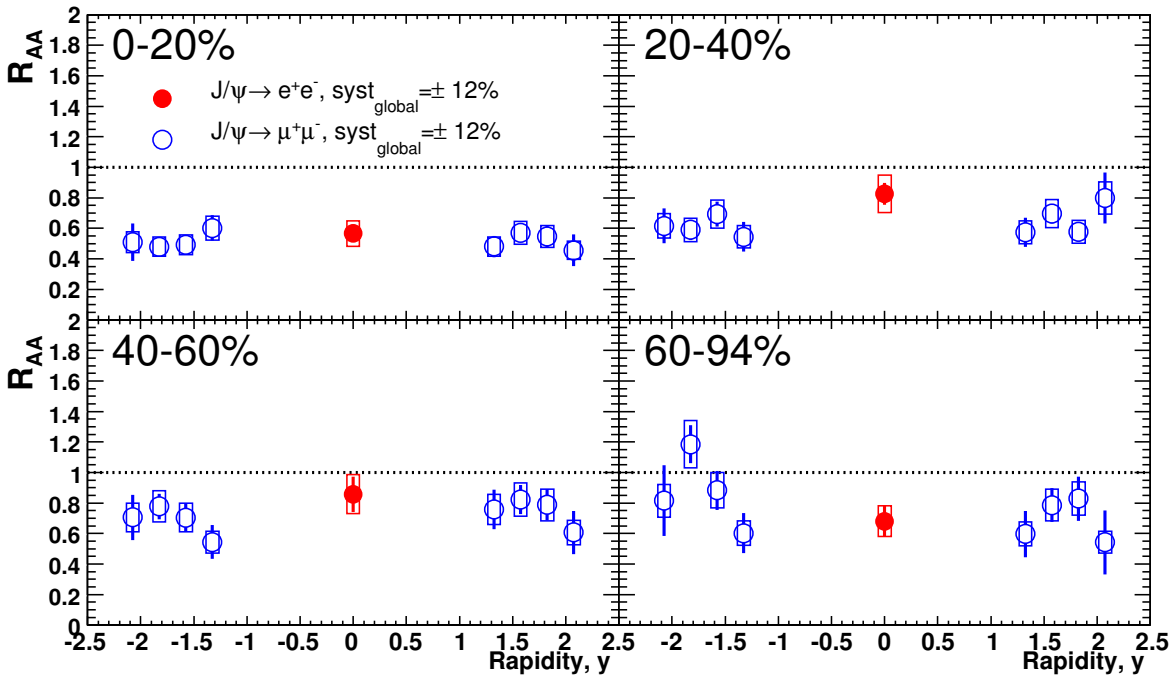

Figure 7.13: R_{AA} vs rapidity y for J/ψ production in Cu+Cu collisions via e^+e^- pairs (blue open circle) and $\mu^+\mu^-$ pairs (red closed circle) for 0–20% (top left), 20–40% (top right), 40–60% (bottom left) and 60–94% (bottom right) Centrality bins.

agree within errors and there appears to be no strong p_T dependence in all Centrality classes.

7.3 Cold Nuclear Matter Effect in d+Au and Cu+Cu Collisions

7.3.1 Comparison with Cold Nuclear Matter Effect with Rapidity Independent Breakup Cross Section

The breakup (absorption) cross sections $\sigma_{breakup}$=(σ_{abs}) obtained from the d+Au data in Run-3 with the two shadowing models, EKS and NDSG, are used to estimate the cold nuclear matter (CNM) effect in Cu+Cu collisions [8]. With the simultaneous fitting for all rapidity range of $[-2.2, 2.2]$, $\sigma_{breakup}$ is determined to be $2.8^{+1.7}_{-1.4}$ mb with the EKS shadowing model (Fig. 2.35) and $2.2^{+1.6}_{-1.5}$ mb with the NDSG shadowing model (Fig. 2.36). Figure 7.15 shows R_{AA} as a function of N_{part} in Cu+Cu collisions with predictions with the two shadowing models. The color octet contribution was found to be important in the charmonium production from the R_{χ_c} values (section 7.1) and the predictions of the CNM effect include the color octet contribution as described in subsection 2.5.2.

In the most central Cu+Cu collisions, the R_{AA} values expected from the two CNM models are about 0.7 and data show larger suppression of $R_{AA} \simeq 0.5$ at both mid and

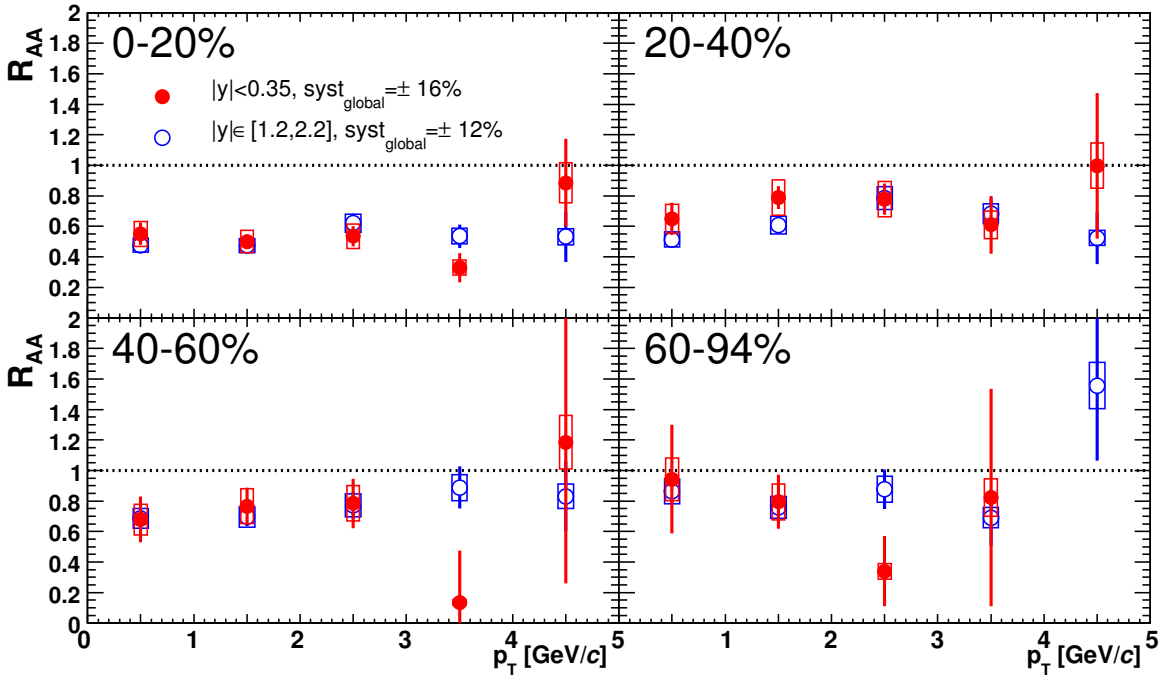

Figure 7.14: R_{AA} vs transverse momentum p_T for J/ψ production in Cu+Cu collisions via e^+e^- pairs (blue open circle) and $\mu^+\mu^-$ pairs (red closed circle) for 0–20% (top left), 20–40% (top right), 40–60% (bottom left) and 60–94% (bottom right) Centrality bins.

forward rapidity, however, the expected and measured R_{AA} are consistent within errors.

Although the suppression pattern of the forward rapidity data has a similar shape (monotonic decrease) to that of the shadowing models, the data shows larger magnitude of suppression than the models.

While the suppression patterns of the midrapidity data and models look different, those magnitudes of the suppression are consistent within errors except the most peripheral bin (60–94%).

7.3.2 Comparison with Cold Nuclear Matter Effect with Rapidity Dependent Breakup Cross Section

The breakup cross section $\sigma_{breakup}$ can depend on the rapidity of J/ψ. Figure 7.16 shows the center of mass energy of a collision of J/ψ and a nucleon, N, in the Au nucleus in d+Au collisions at $\sqrt{s_{NN}}$=200 GeV as a function of longitudinal and transverse momenta of J/ψ. The center of mass energy $\sqrt{s}$ of J/ψ and N is distributed from 10 to 100 GeV in the PHENIX acceptance ($-2.2 < y < 2.2$ and $p_T < 5$ GeV/c). For example, the values of $\sqrt{s}$ for J/ψ with $p_T = 2$ GeV/c are 12.2 GeV at $y = -1.7$, 27.4 GeV at $y = 0$ and 63.6 GeV at $y = 1.7$. As shown in Figure 7.17, the inelastic cross section of $\pi^{\pm} + p$ collisions has small but finite energy dependence of ~20% in the energy range. While the collision of J/ψ and N would be largely different from the collision of π and N, the rapidity dependence of the breakup cross section of J/ψ can be expected.

Using the N_{coll} dependence of $R_{d\mathrm{Au}}$ in d+Au collisions, $\sigma_{breakup}$ was obtained inde-

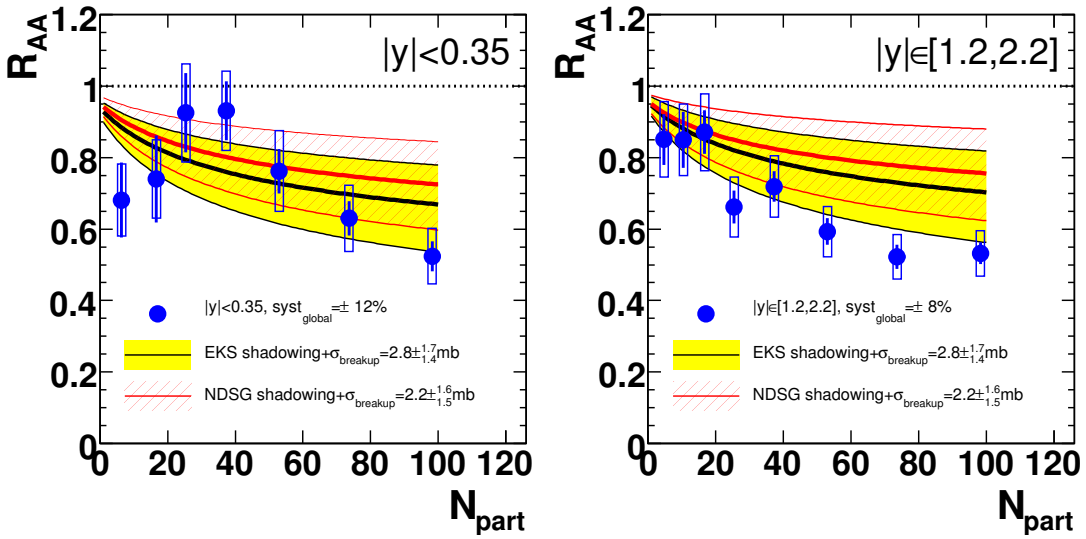

Figure 7.15: R_{AA} vs N_{part} in Cu+Cu collision compared to a band of theoretical curves for the breakup cross section $\sigma_{breakup}$ values obtained from the d+Au data with the simultaneous fitting for all rapidity range. The midrapidity data and forward rapidity data in Cu+Cu collisions are shown in left and right panels, respectively. The yellow-black bands and red bands correspond to EKS and NDSG shadowing models, respectively.

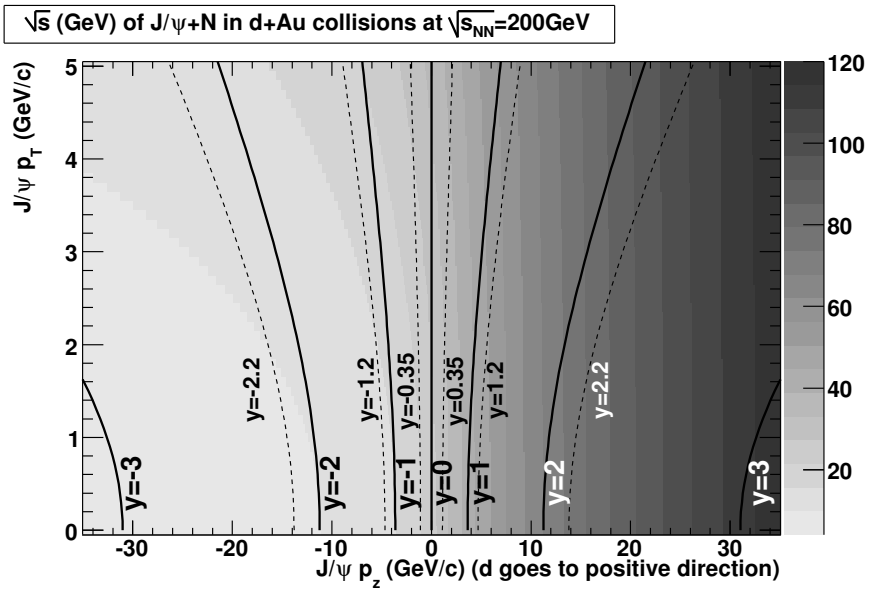

Figure 7.16: The center of mass energy $\sqrt{s}$ (GeV) of $J/\psi+N$ (nucleon in Au) collisions in d+Au collisions at $\sqrt{s_{NN}} = 200$ GeV.

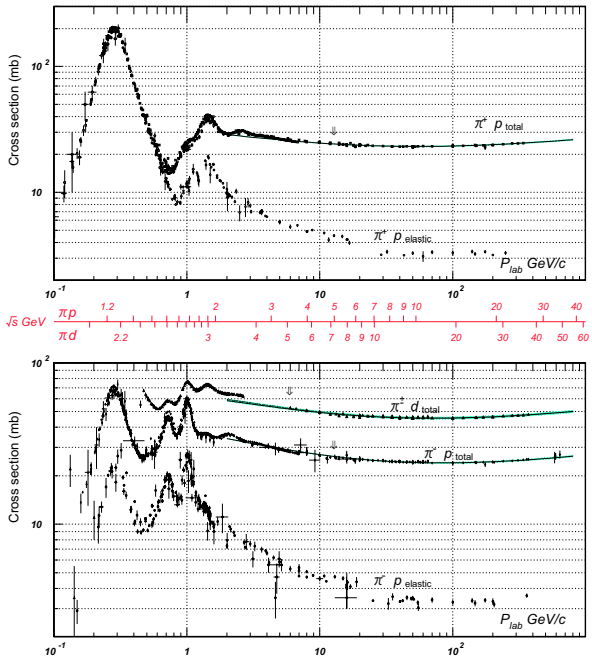

Figure 7.17: Total and elastic cross sections for $\pi^{\pm}+p$ and $\pi^{\pm}+d$ (total only) collisions as a function of laboratory beam momentum and total center of mass energy [19].

pendently in three rapidity ranges [8]. The average $\sigma_{breakup}$ at forward and backward rapidity in d+Au collision is used as $\sigma_{breakup}$ at forward rapidity in Cu+Cu collisions. The values of $\sigma_{breakup}$ are $2.4^{+1.9}_{-1.6}$ mb ($1.0^{+1.8}_{-1.7}$ mb) at midrapidity and $4.2^{+1.1}_{-1.2}$ mb ($3.3^{+1.2}_{-1.1}$ mb) at forward rapidity with the EKS (NDSG) shadowing model. The cross section $\sigma_{breakup}$ at forward rapidity is larger than that at midrapidity with both the models. Figure 7.18 shows expected R_{AA} curves with the rapidity dependent $\sigma_{breakup}$ and data. Except the NDSG shadowing model at midrapidity, agreement between data and model becomes better with introduction of the rapidity dependent $\sigma_{breakup}$. The value of $\sigma_{breakup}$ with the NDSG shadowing model at midrapidity is $1.0^{+1.8}_{-1.7}$ mb, and is smaller than the values in other cases.

7.3.3 Calculation of Breakup Cross Section from Cu+Cu Data

Since the cold nuclear matter effect can be dominant in the J/ψ suppression in the small N_{part} region of Cu+Cu collisions, breakup cross sections might also be extracted from the J/ψ data in Cu+Cu collisions.

Figure 7.19 shows the theoretical CNM curves for $\sigma_{breakup}$=0–6 mb. All data points except the most peripheral collision data at midrapidity locate within $\sigma_{breakup}$=0–6 mb.

Figure 7.20 (7.21) shows the probability of breakup cross section calculated from Cu+Cu data where $N_{part} < 63$ (Centrality $\geq 20\%$) with EKS (NDSG) shadowing model.

The obtained breakup cross sections with different N_{part} range are shown in Fig. 7.22 and Table 7.6. The breakup cross sections obtained from Cu+Cu data are consistent with those from d+Au data within errors. Errors of the cross sections from Cu+Cu

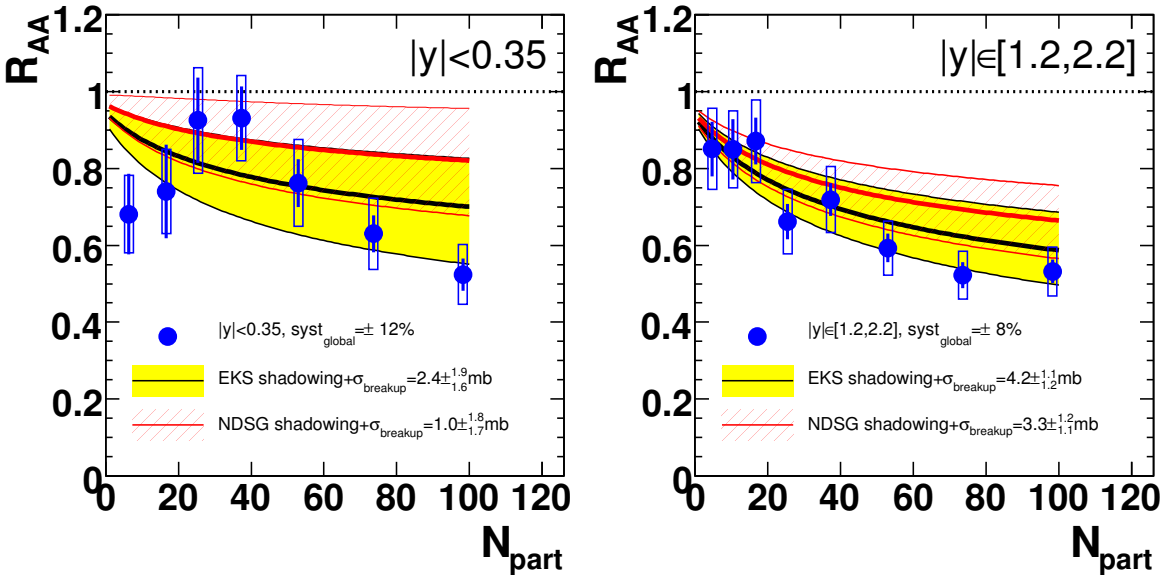

Figure 7.18: R_{AA} vs N_{part} in Cu+Cu collision compared to a band of theoretical curves for the rapidity dependent breakup cross section $\sigma_{breakup}$ values obtained from the d+Au data with three independent fittings. The midrapidity data and forward rapidity data in Cu+Cu collisions are shown in left and right panels, respectively. The yellow-black bands and red bands correspond to EKS and NDSG shadowing models, respectively.

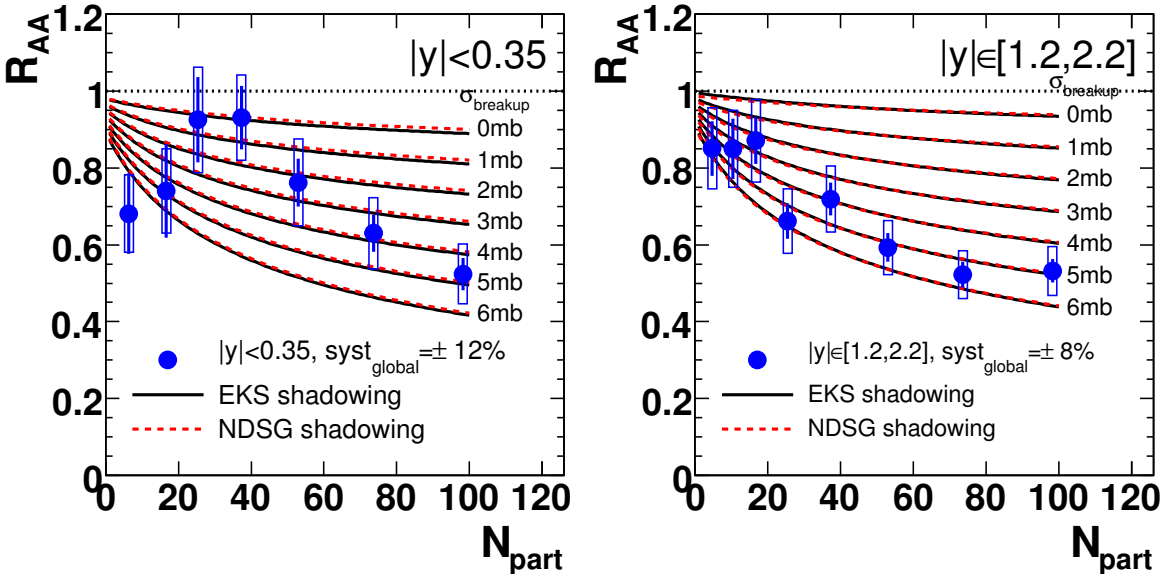

Figure 7.19: R_{AA} vs N_{part} in Cu+Cu collisions compared to theoretical curves for breakup cross sections $\sigma_{breakup}$ from 0 mb to 6 mb. The black solid lines and red dashed lines correspond to EKS and NDSG shadowing models, respectively. The midrapidity data and forward rapidity data are shown in left and right panels, respectively.

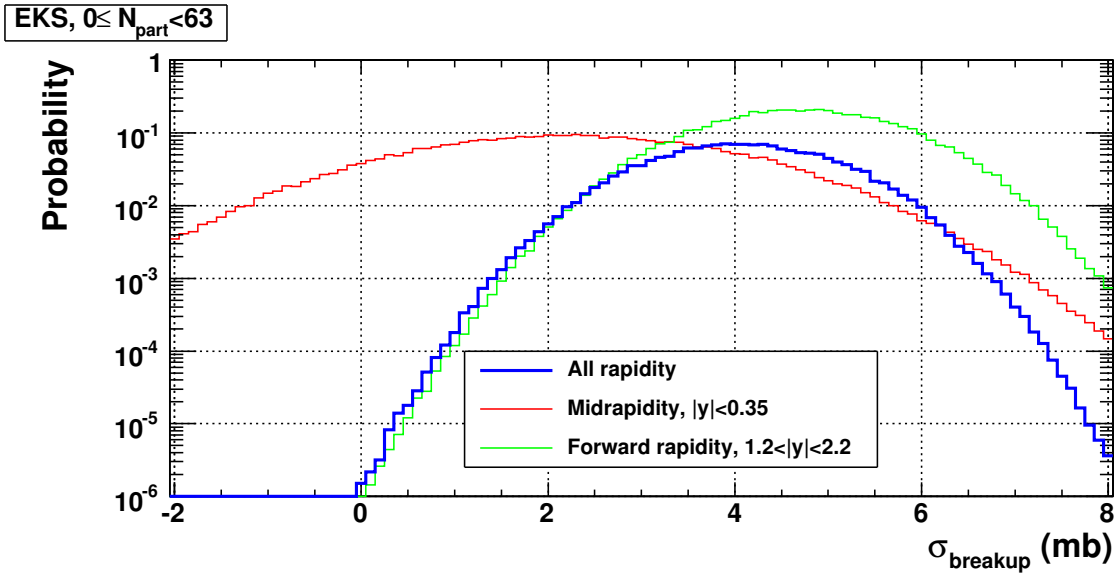

Figure 7.20: The probability distribution of breakup cross sections calculated from Cu+Cu data where $N_{part} < 63$ with EKS shadowing model.

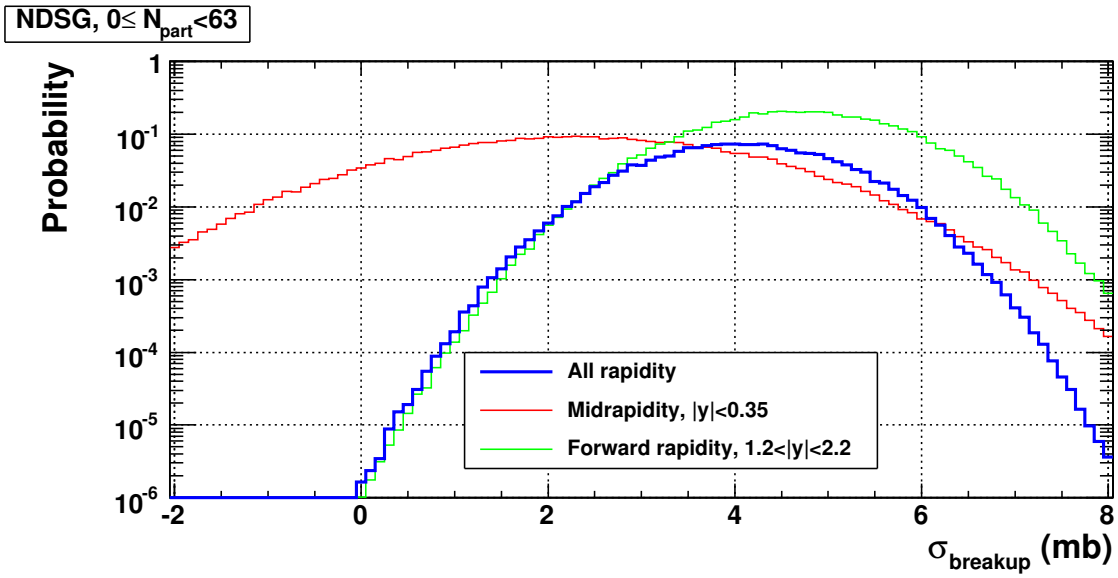

Figure 7.21: The probability distribution of breakup cross sections calculated from Cu+Cu data where $N_{part} < 63$ with NDSG shadowing model.

data are comparable to or smaller than those from d+Au data. The cross sections from combined data of d+Au and Cu+Cu collisions can reduce the errors by a factor of about two from the errors obtained from the d+Au data.

Although the cross sections are consistent within errors, the cross sections from Cu+Cu data seem to be larger than those from d+Au data at forward rapidity. This might be an indication of non-linear effects of nuclear shadowing, such as color glass condensate (CGC) [71].

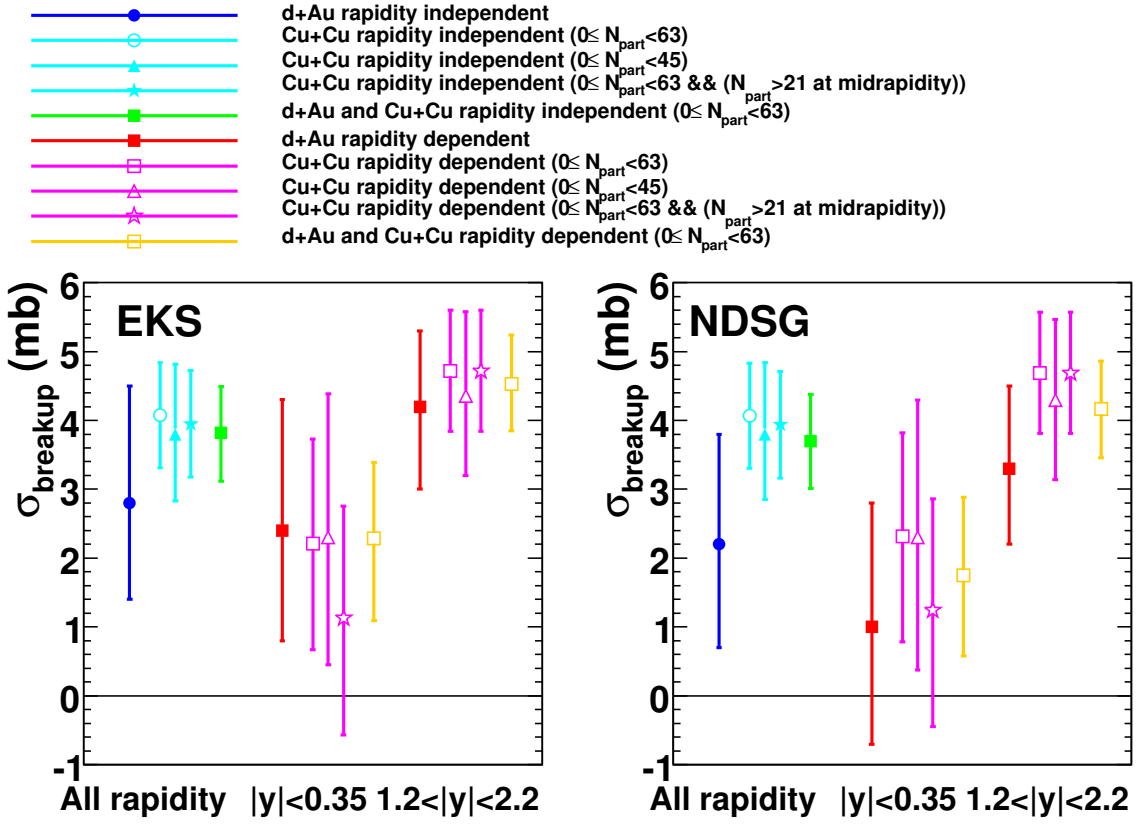

Figure 7.22: Breakup cross sections calculated from Cu+Cu data and d+Au data with EKS shadowing model (left) and NDSG shadowing model (right). Breakup cross sections were calculated for all rapidity, midrapidity ($|y| < 0.35$) and forward rapidity ($1.2 < |y| < 2.2$). Used N_{part} range is shown with the marker.

7.4 Comparison with J/ψ Data in Au+Au collisions

Figure 7.23 shows R_{AA} in Cu+Cu and Au+Au collisions at $\sqrt{s_{NN}} = 200$ GeV as a function of N_{part} with the CNM predictions using the EKS shadowing model (left panels) and the NDSG shadowing model (right panels). The data in Au+Au collisions agrees with that in the Cu+Cu collisions within errors across the entire N_{part} range of Cu+Cu collisions at both mid and forward rapidity.

The rapidity dependent CNM model predicts larger suppression at forward rapidity than at midrapidity due to the larger breakup cross section, $\sigma_{breakup}$. The ratios of R_{AA}

Shadowing model	Used data	$\sigma_{breakup}$ (mb) All rapidity	$\lvert y\rvert < 0.35$	$1.2 < \lvert y\rvert < 2.2$
EKS				
	d+Au	$2.8^{+1.7}_{-1.4}$	$2.4^{+1.9}_{-1.6}$	$4.2^{+1.1}_{-1.2}$
	Cu+Cu ($0 \le N_{part} < 63$)	$4.1^{+0.7}_{-0.8}$	$2.2^{+1.6}_{-1.5}$	$4.7^{+0.9}_{-0.9}$
	Cu+Cu ($0 \le N_{part} < 45$)	$3.8^{+1.0}_{-1.0}$	$2.3^{+1.8}_{-2.1}$	$4.4^{+1.1}_{-1.2}$
	Cu+Cu ($0 \le N_{part} < 63$ && ($N_{part} > 21$ at $\lvert y\rvert < 0.35$))	$3.9^{+0.8}_{-0.7}$	$1.1^{+1.7}_{-1.6}$	$4.7^{+0.9}_{-0.9}$
	d+Au and Cu+Cu ($0 \le N_{part} < 63$)	$3.8^{+0.7}_{-0.6}$	$2.3^{+1.2}_{-1.1}$	$4.5^{+0.7}_{-0.7}$
NDSG				
	d+Au	$2.2^{+1.6}_{-1.5}$	$1.0^{+1.8}_{-1.7}$	$3.3^{+1.2}_{-1.1}$
	Cu+Cu ($0 \le N_{part} < 63$)	$4.1^{+0.7}_{-0.8}$	$2.3^{+1.5}_{-1.5}$	$4.7^{+0.9}_{-0.9}$
	Cu+Cu ($0 \le N_{part} < 45$)	$3.8^{+0.9}_{-1.0}$	$2.3^{+1.9}_{-2.0}$	$4.3^{+1.2}_{-1.2}$
	Cu+Cu ($0 \le N_{part} < 63$ && ($N_{part} > 21$ at $\lvert y\rvert < 0.35$))	$3.9^{+0.8}_{-0.7}$	$1.2^{+1.7}_{-1.6}$	$4.7^{+0.9}_{-0.9}$
	d+Au and Cu+Cu ($0 \le N_{part} < 63$)	$3.7^{+0.7}_{-0.7}$	$1.7^{+1.2}_{-1.1}$	$4.2^{+0.7}_{-0.7}$

Table 7.6: The obtained breakup cross sections with different N_{part} range of Cu+Cu and d+Au data.

at forward rapidity to that at midrapidity are shown in bottom panels of Fig. 7.23. The data points which show rapidity narrowing in the bottom panels agree with the CNM model prediction within errors across the entire N_{part} range of Au+Au collisions. However, the data points seem to indicate stronger dependence on N_{part}.

In the most central Au+Au collisions, suppression beyond the CNM predictions is clearly seen at both mid and forward rapidity. The values of R_{AA} of experimental results and the CNM predictions are tabulated in Table 7.7. The significance of the observed suppression beyond the CNM effect in the most central Au+Au collisions is about 2σ.

Rapidity y	Centrality	N_{part}	N_{coll}	R_{AA}^{exp}	$R_{AA}^{\rm EKS}$	$R_{AA}^{\rm NDSG}$	$\Delta_{\rm EKS}^{exp}$	$\Delta_{\rm NDSG}^{exp}$
$\lvert y\rvert < 0.35$	0–5%	351±3	1065±105	0.26±0.07	$0.57^{+0.18}_{-0.20}$	$0.57^{+0.14}_{-0.15}$	-1.5σ	-1.9σ
$1.2 < \lvert y\rvert < 2.2$	0–10%	325±3	955±94	0.16±0.07	0.42±0.13	0.45±0.12	-1.7σ	-2.1σ

Table 7.7: The nuclear modification factors R_{AA} of J/ψ in the most central Au+Au collisions at mid and forward rapidity. The measured values R_{AA}^{exp} and the values of CNM predictions with the EKS shadowing $R_{AA}^{\rm EKS}$ and with the NDSG shadowing $R_{AA}^{\rm NDSG}$ are shown. The $\Delta_{\rm S}^{exp}$ (S=EKS, NDSG) is the difference between R_{AA}^{exp} and $R_{AA}^{\rm S}$ divided by the error, $\Delta_{\rm S}^{exp} = (R_{AA}^{exp} - R_{AA}^{\rm S})/\sqrt{(\delta R_{AA}^{exp})^2 + (\delta R_{AA}^{\rm S})^2}$, and means the significance of the observed J/ψ suppression beyond the CNM effects.

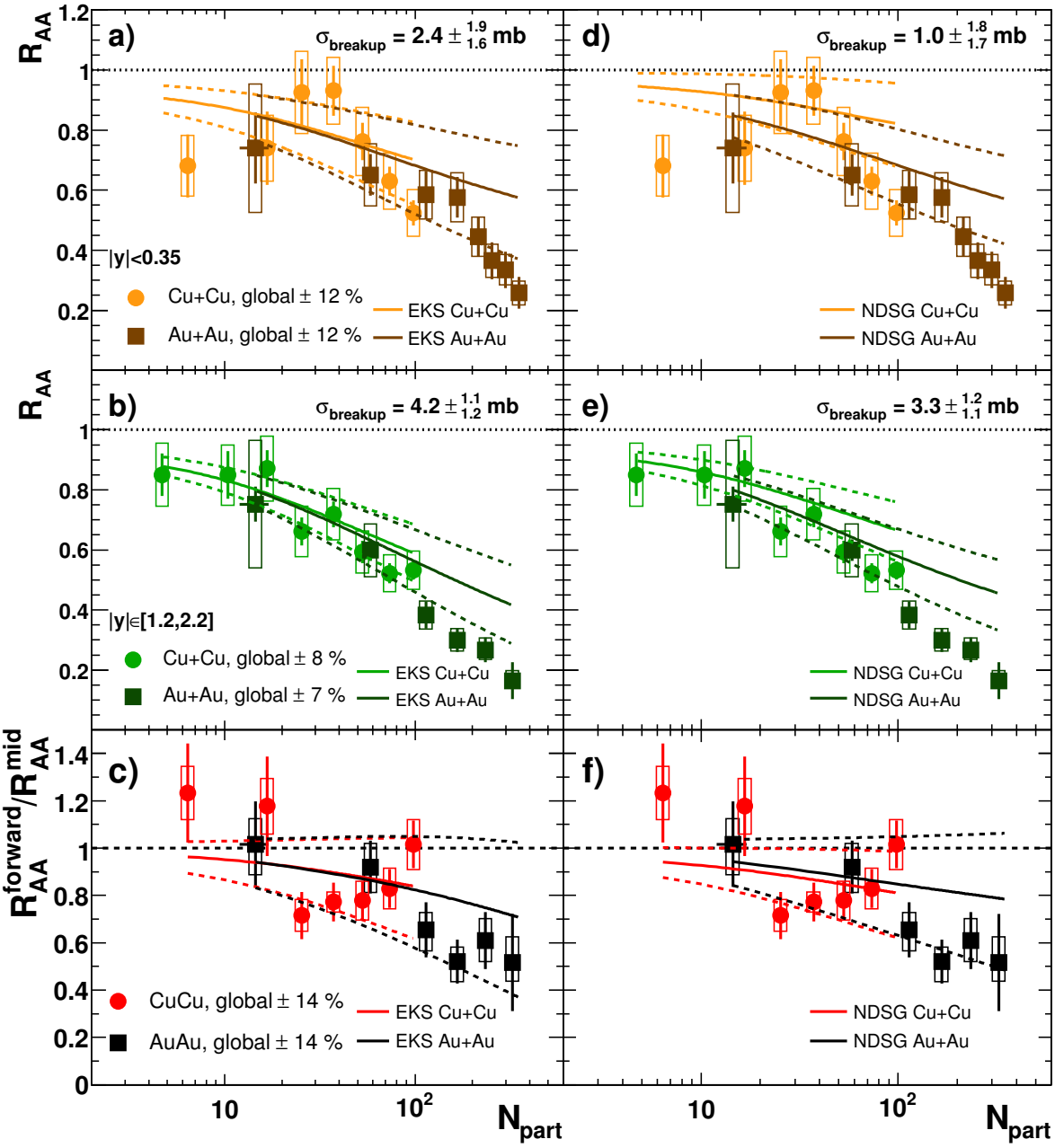

Figure 7.23: a) R_{AA} vs N_{part} for J/ψ production in Cu+Cu and Au+Au collisions at midrapidity with the prediction curves of the EKS shadowing model. b) The same figure at forward rapidity. c) Forward/mid rapidity R_{AA} ratio. d, e, f) The same figures with the prediction curves of the NDSG shadowing model. The breakup cross sections for the prediction curves are obtained from fits to the d+Au data.

7.5 Comparison with J/ψ Data at SPS

In this section, J/ψ results at the SPS and RHIC are compared as survival probability, $S_{J/\psi}$, as a function of the Bjorken energy density, ε_0, which is introduced in subsection 2.2.3.

Survival probability of J/ψ at RHIC is defined as the ratio of measured R_{AA}^{exp} to expected $R_{AA}^{\rm CNM}$ from the CNM effects,

$$S_{J/\psi} \;=\; \frac{R_{AA}^{exp}}{R_{AA}^{\rm CNM}}, \tag{7.1}$$

where the EKS shadowing model is used.

The obtained Bjorken energy density ε_0 in Au+Au collisions at $\sqrt{s_{NN}} = 200$ GeV for $N_{part} \geq 22$ in Fig. 2.5 ([18]) with $\tau_0 = 1$ fm/c is used for the RHIC results with the following parameterization,

$$\varepsilon_0 \;=\; p_0 + p_1 \cdot N_{part}^{p_2}, \tag{7.2}$$

where the coefficients p_0, p_1 and p_2 were obtained by the fitting to Fig. 2.5. This parameterization is used for $N_{part} > 14$.

At the SPS, the J/ψ cross section including the branching ratio is divided by the Drell-Yan cross section in the mass range of 2.9–4.5 GeV/c^2 for normalization. Survival probability of J/ψ at the SPS is the ratio of the measured ratio to the expected ratio,

$$S_{J/\psi} \;=\; \frac{\text{Measured } B_{\mu\mu}\sigma(J/\psi)/\sigma(DY)_{2.9-4.5}}{\text{Expected } B_{\mu\mu}\sigma(J/\psi)/\sigma(DY)_{2.9-4.5}}. \tag{7.3}$$

For the NA38 and NA50 results, the ε_0 dependence of $S_{J/\psi}$ is taken from Ref. [93]. For the NA60 results, N_{part} dependence of $S_{J/\psi}$ is given in Ref. [97] and is converted to the ε_0 dependence using the ε_0-N_{part} relation in Pb+Pb collisions at the same energy obtained by NA50 [93] with similar parameterization to Eq. (7.2).

Figure 7.24 shows the survival probability of J/ψ as a function of the Bjorken energy density. The results of S+U collisions at $\sqrt{s_{NN}} = 19.4$ GeV at NA38, Pb+Pb collisions at $\sqrt{s_{NN}} = 17.3$ GeV at NA50, In+In collisions at $\sqrt{s_{NN}} = 17.3$ GeV at NA60, Cu+Cu and Au+Au collisions at $\sqrt{s_{NN}} = 200$ GeV at PHENIX are shown.

Although the errors of RHIC results are large due to the limited constraint on the CNM effects, all the SPS and RHIC results are consistent within errors. The J/ψ suppression seems to start at $\varepsilon_0 \sim 2.5$ GeV/fm^3. This energy density corresponds to those in the most central S+U collisions at $\sqrt{s_{NN}} = 19.4$ GeV and the most central Cu+Cu collisions at $\sqrt{s_{NN}} = 200$ GeV. If the QGP consists of gluons, up, down and strange quarks, $\varepsilon_0 \sim 2.5$ GeV/fm^3 corresponds to the temperature of ~ 180 MeV according to Eq. (2.9).

In the most central Au+Au collisions at $\sqrt{s_{NN}} = 200$ GeV, the J/ψ yield is suppressed to about 0.4 by other effects than the CNM effects. In $p + p$ collisions at $\sqrt{s} = 200$ GeV, the fraction of J/ψ from χ_c decay feed-down is less than 0.40 (90% C.L.) and the fraction of J/ψ from ψ' decay feed-down is expected to be ~ 0.1. More precise experimental data and theoretical progress are necessary to reduce uncertainties and to test the picture of sequential dissociation.

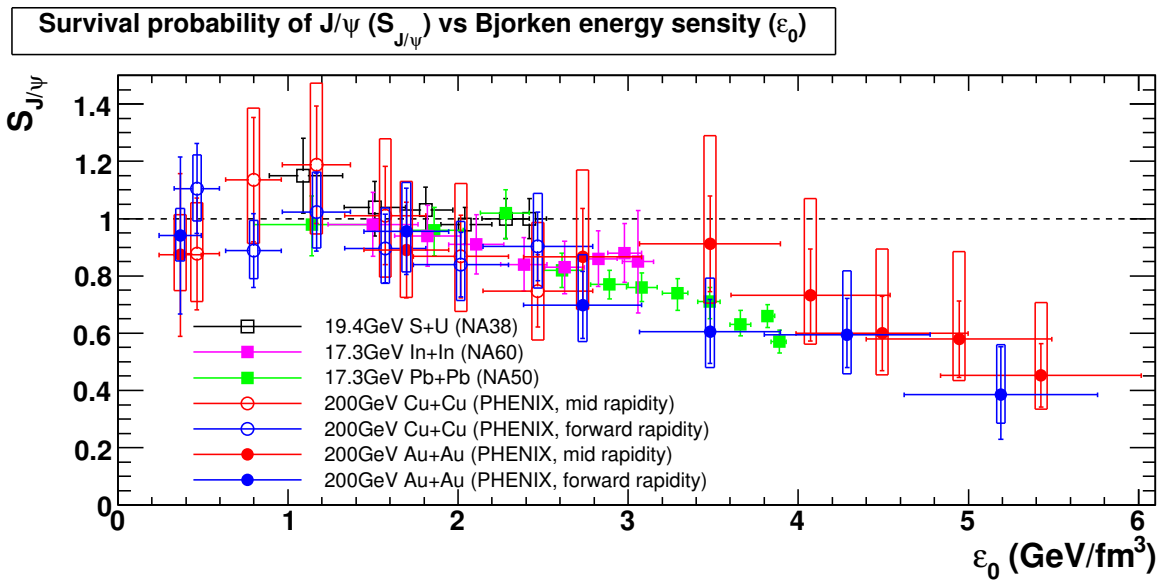

Figure 7.24: Survival probability of J/ψ ($S_{J/\psi}$) is shown as a function of the Bjorken energy density (ε_0). The SPS and RHIC results are shown. For the SPS result, all errors are added in quadrature. For the RHIC result, the quadrature sum of statistical, uncorrelated and correlated systematic errors is represented by a bar, and the global systematic errors including the error of the breakup cross section is represented by a box.

7.6 Comparison with Theoretical Models of J/ψ in Heavy-Ion Collision

Figure 7.25 shows predictions of theoretical models for the J/ψ suppression at midrapidity for collisions at $\sqrt{s_{NN}}$=200 GeV. Predictions of the Hadron-string-dynamics (HSD) model [61, 156], comover model [63, 155], statistical coalescence model (SCM) [60, 157] and kinetic formation model [57] are shown in Fig. 7.25. Figure 7.26 shows predictions of the same theoretical models (comover, HSD and SCM) for the J/ψ suppression for Pb+Pb collisions at $\sqrt{s_{NN}}$=17.3 GeV at the SPS [61]. While the models succeed to describe the SPS data as shown in Fig. 7.26, no model succeeds to describe the RHIC data at both mid and forward rapidity. The result of the χ^2 test of the models for the mid rapidity data is shown in Table 7.8. Although HSD and comover model succeed to reproduce the mid rapidity, they fail at forward rapidity as will be described.

The comover and HSD models do not assume the QGP, and the SCM and kinetic formation models assume the QGP. While the comover model does not include the recombination of charmonia from uncorrelated $c\bar{c}$ pairs, other models take into account the recombination.

The comover model with $\sigma_{co} = 0.65$ mb (the same comovers interaction cross section obtained from the SPS data) predicts stronger suppression than the data at midrapidity and opposite rapidity dependence as shown in Fig. 7.27.

The HSD model describes the J/ψ suppression by the breakup interaction with

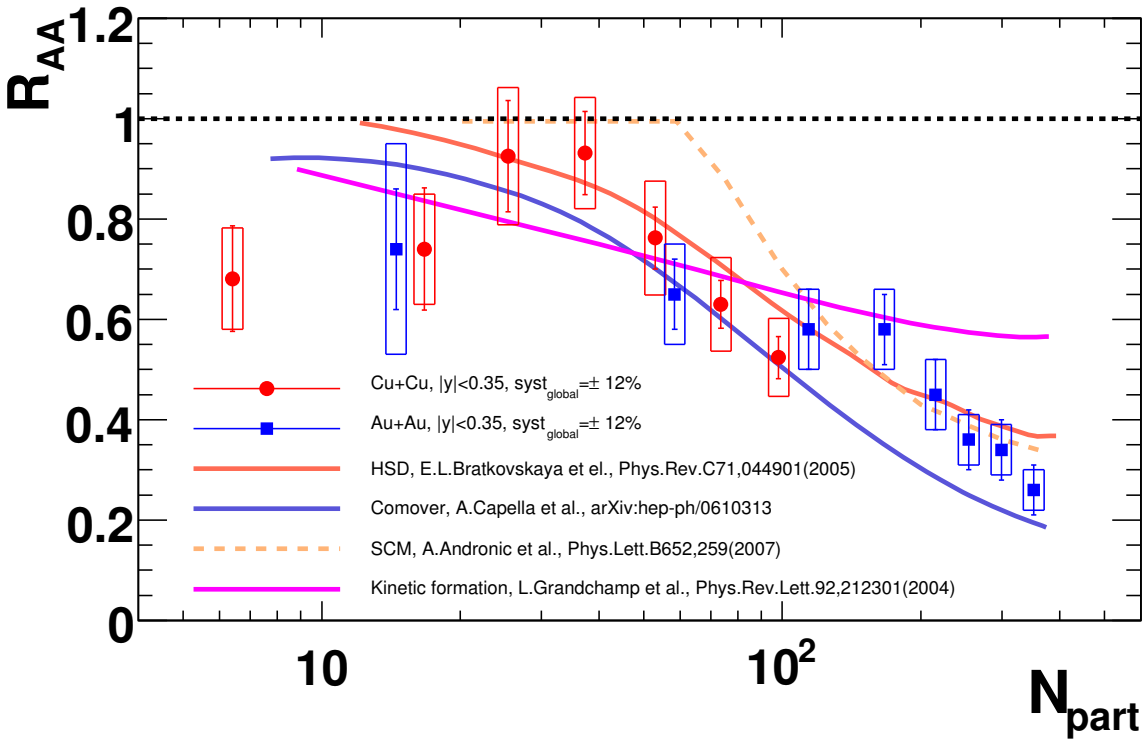

Figure 7.25: R_{AA} vs N_{part} for J/ψ in Cu+Cu and Au+Au collisions at $\sqrt{s_{NN}}$=200 GeV at midrapidity with predictions of theoretical models for the J/ψ suppression.

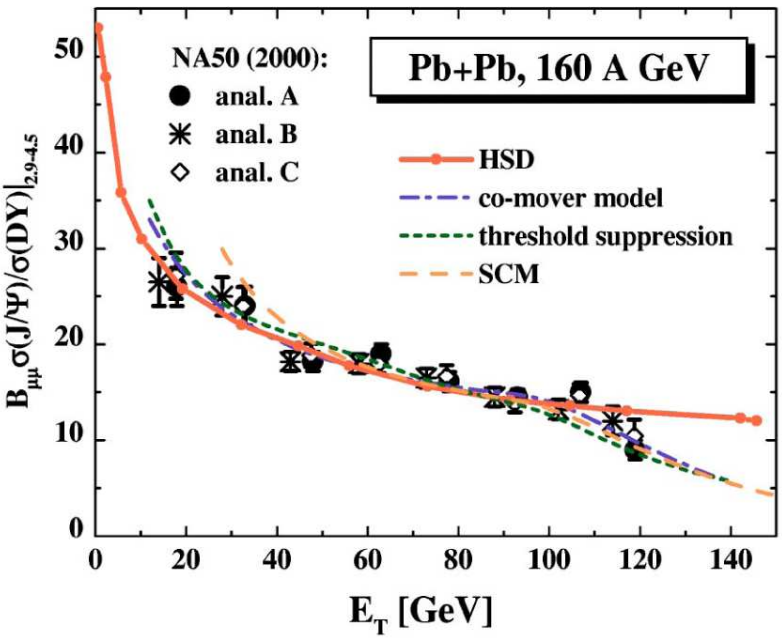

Figure 7.26: R_{AA} vs N_{part} for J/ψ in Pb+Pb collisions at $\sqrt{s_{NN}}$=17.3 GeV with predictions of theoretical models for the J/ψ suppression [61].

Model	χ^2/NDF	Probability
Hadron-string-dynamics (HSD) model	15.7/14	0.33
Comover model	21.8/14	0.083
Statistical coalescence model (SCM)	39.3/14	3.3×10^{-4}
Kinetic formation model	51.5/14	3.4×10^{-6}

Table 7.8: The χ^2 test for theoretical models with R_{AA} in Cu+Cu and Au+Au collisions at $\sqrt{s_{NN}} = 200$ GeV at midrapidity.

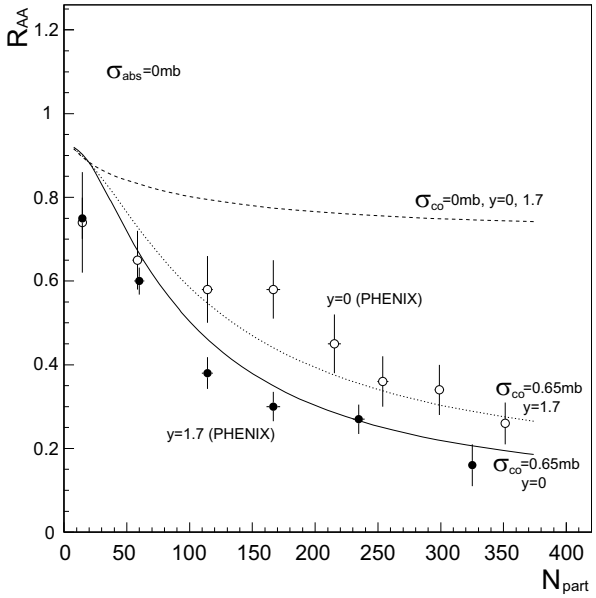

Figure 7.27: R_{AA} of the comover model prediction and of the PHENIX data in Au+Au collisions at $\sqrt{s_{NN}} = 200$ GeV at mid (open circle) and forward (closed circle) rapidity [155].

comover hadrons and includes reformation of charmonia by the backward reactions of $D\bar{D}$ channels. The HSD model agrees with data at midrapidity but fails to describe the suppression at forward rapidity as shown in Fig. 7.28.

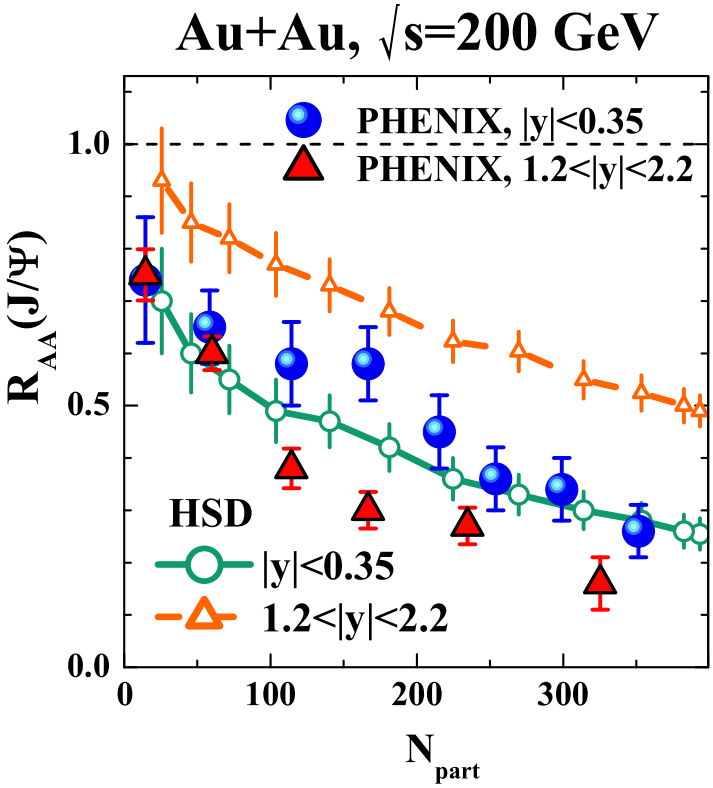

Figure 7.28: R_{AA} of the HSD model prediction including charmonium reformation channels and of the PHENIX data in Au+Au collisions at $\sqrt{s_{NN}}$ = 200 GeV at mid and forward rapidity [156].

In the SCM model, primordial J/ψ is completely suppressed in the QGP and J/ψ is statistically created at the hadronization stage from uncorrelated $c\bar{c}$ pairs. The SCM model agrees with data in central Au+Au collisions at both mid and forward rapidity (Fig. 7.29) but fails to describe the suppression at small N_{part}.

In the recombination model with kinetic formation, the number of J/ψ is related to the dissociation process of J/ψ by thermal gluons and the inverse process in which charm quarks and gluons form J/ψ with the balance equation,

$$\frac{dN_{J/\psi}}{dt} = -\Gamma_{J/\psi}(N_{J/\psi} - N^{eq}_{J/\psi}), \tag{7.4}$$

where $\Gamma_{J/\psi}$ is the dissociation rate, $N^{eq}_{J/\psi}$ is the number of J/ψ at thermal equilibrium [57]. This model predicts smaller suppression than the data due to large recombination.

There is no model which explains the J/ψ suppression across the whole N_{part} range at both mid and forward rapidity simultaneously.

Figure 7.30 shows the $\langle p_T^2 \rangle$ of J/ψ in $p+p$, d+Au, Cu+Cu and Au+Au collisions as a function of the number of collisions N_{coll}. No significant N_{coll} dependence of $\langle p_T^2 \rangle$ is

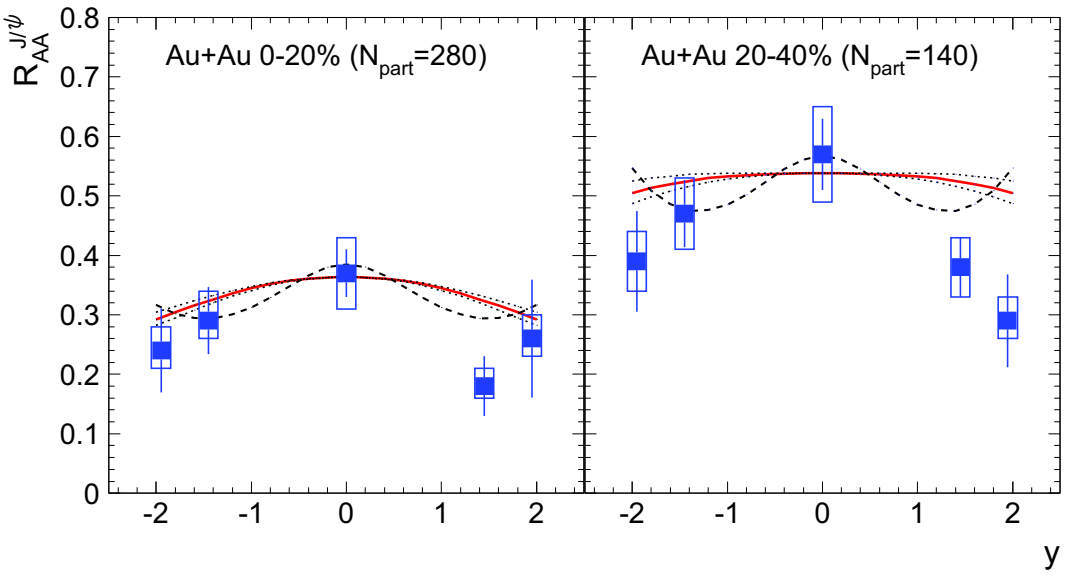

Figure 7.29: Rapidity dependence of J/ψ R_{AA} in Au+Au collisions at $\sqrt{s_{NN}} = 200$ GeV for two Centrality classes. The data points from the PHENIX experiment (symbols with errors) are compared to the SCM calculations (lines) [157].

seen. Since the observed $\langle p_T^2 \rangle$ change in the SPS (Fig. 2.33) is $\Delta\langle p_T^2 \rangle \sim 1$ ((GeV/c)^2), more statistics are needed to study the N_{coll} dependence of $\langle p_T^2 \rangle$.

Two bands in Fig. 7.30 are predictions of two other recombination models [58, 59]. While these two models have opposite N_{part} dependence, neither of the models is excluded by the data.

A data driven threshold suppression model is shown in Fig. 7.31 [158]. In the model, hot quark-gluon matter is described by the full (3+1)-dimensional relativistic hydrodynamics and J/ψ is treated as an impurity traversing through the matter.

The components of J/ψ production are divided into two parts, direct J/ψ and feed-down from χ_c and ψ'. The obtained fraction of J/ψ from χ_c and ψ' decay feed-down of 0.30 in the model is consistent with the obtained upper limit of $R_{\chi_c} < 0.40$. The dissociation temperature of direct J/ψ is constrained to be about $2T_c$ by the N_{part} dependence.

The critical temperature is assumed to be $T_c = 170$ MeV in the model. As shown in Fig. 7.32, temperature largely depends on the position in the collision system in the hydrodynamical picture. Therefore, it is difficult to compare Bjorken's picture and the hydrodynamical picture. However, the suppression of direct J/ψ starts from $N_{part} \sim 170$ and this corresponds to the Bjorken energy density of $\varepsilon_0 \sim 3.5$ GeV/fm^{-3} and $2.02T_c = 343$ MeV in the hydrodynamical model. From Fig. 7.33, it is known that the temperature of 343 MeV corresponds to the energy density of $\varepsilon > 20$ GeV/fm^3. The energy density in the hydrodynamical model is much larger than the Bjorken energy density with the thermalization time of $\tau_0 = 1$ fm/c. The hydrodynamical model succeeded at the RHIC energy but might not be applicable to the SPS energy due to shorter duration of produced hot and dense matter. The behavior of charmonia can be largely different at the SPS and RHIC energy, and the scaling of J/ψ survival

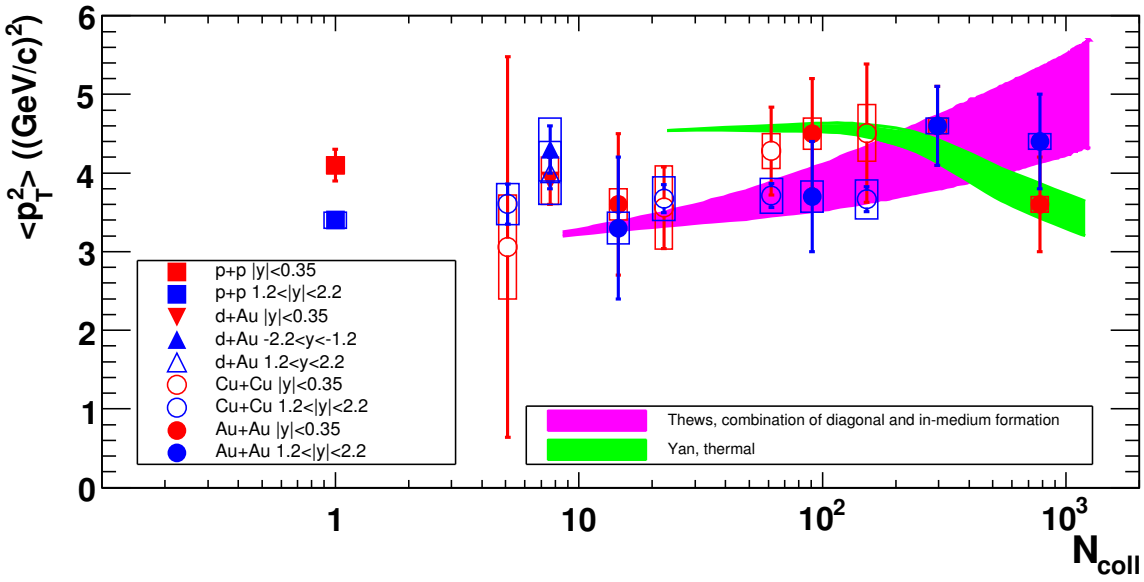

Figure 7.30: The $\langle p_T^2 \rangle$ vs N_{coll} for J/ψ production in $p+p$, d+Au, Cu+Cu and Au+Au collisions.

probability with the Bjorken energy density can be an accidental coincidence.

It can be concluded that there is additional effect other than the CNM effects in central Au+Au collisions. However, no definite conclusion about the additional effect is deduced with the current data.

7.7 Toward Future Measurements

The following measurements can help to understand the behavior of quarkonia in high-energy heavy-ion collisions.

7.7.1 Ongoing Measurements at RHIC

Elliptic Flow of J/ψ in Au+Au Collisions at $\sqrt{s_{NN}} = 200$ GeV

In RHIC Run-7, Au+Au collision data was collected by PHENIX with three times larger statistics than those in Run-4 and improved resolution of reaction plane determination. The azimuthal anisotropy in the configuration space with respect to the reaction plane in the initial state leads to the azimuthal anisotropy in the momentum space in the final state. Some recombination models predict that J/ψ has finite elliptic azimuthal anisotropy in the momentum space (elliptic flow) [160, 59, 161]. The J/ψ elliptic flow is originated from the partial thermalization process and the flow of open charm hadrons. The measurement of the elliptic flow of J/ψ will give information about the existence and magnitude of the recombination.

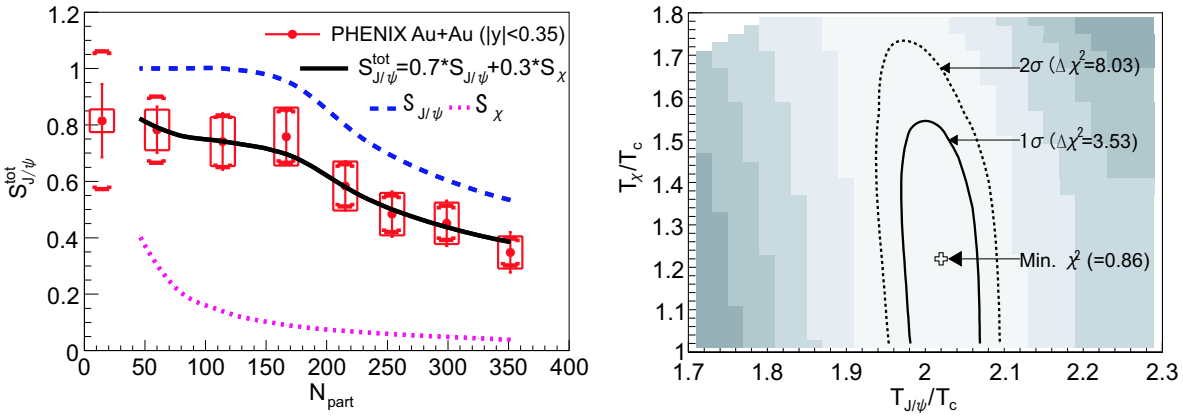

Figure 7.31: (Left) Survival probabilities $S^{tot}_{J/\psi}$ (solid line), $S_{J/\psi}$ (dashed line) and S_{χ_c} (dotted line) in the hydro+J/ψ model as a function of the number of participants N_{part} with $(T_{J/\psi}, T_{\chi_c}, f_{\rm FD})$=(2.02$T_c$, 1.22$T_c$, 0.30), where $T_{J/\psi}$, T_{χ_c} are the dissociation temperature of J/ψ and the mixture of χ_c and ψ', and $f_{\rm FD}$ is the fraction of J/ψ from feed-down from χ_c and ψ' [158]. Filled symbols are the experimental survival probability in the midrapidity of J/ψ in Au+Au collisions at RHIC. (Right) χ^2 contour plot in the $T_{J/\psi}/T_c$-T_χ/T_c plane with $f_{\rm FD}$ being fixed to 0.30.

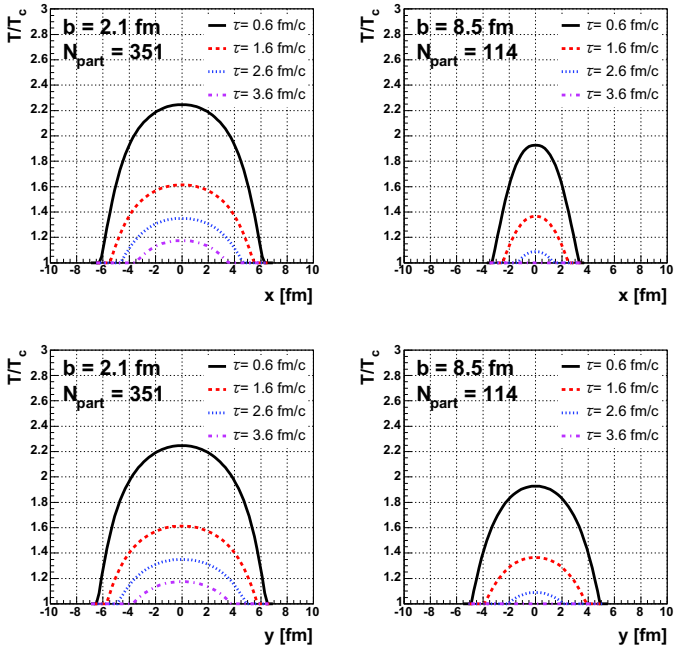

Figure 7.32: Local temperature in the unit of T_c as functions of the transverse coordinate x (upper) and y (lower), for various proper time τ at midrapidity ($y = 0$) in Au+Au collisions at $\sqrt{s_{NN}}$ = 200 GeV [158]. The impact parameter b = 2.1 fm (left panels) corresponds to $\langle N_{part}\rangle$=351, while b = 8.5 fm (right panels) corresponds to $\langle N_{part}\rangle$=114. The critical temperature is assumed to be T_c = 170 MeV in this model.

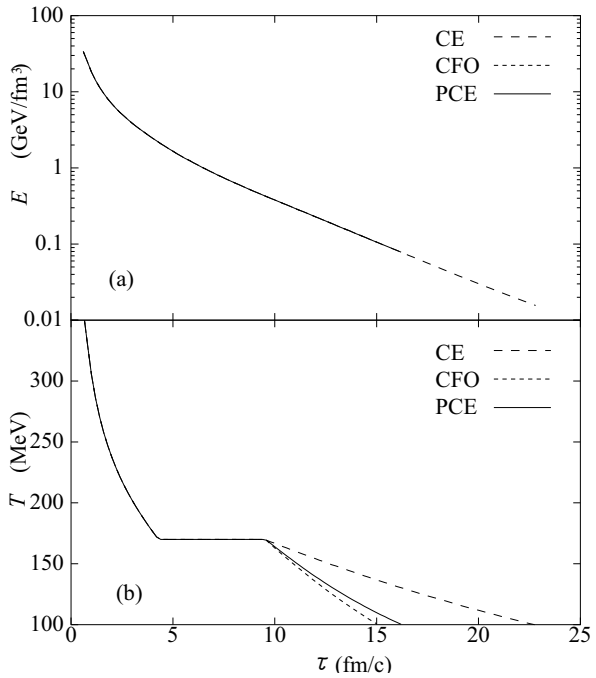

Figure 7.33: Time evolution of energy density (a) and temperature (b) at the center of the fluid [159].

Production of J/ψ in d+Au Collisions at $\sqrt{s_{NN}} = 200$ GeV with Higher Statistics

In RHIC Run-8, d+Au collision data was collected. The statistics are 81 nb^{-1} and 30 times higher than those in Run-3. It will surely help to constrain the nuclear absorption cross section of J/ψ, and will make better understanding of nuclear shadowing.

Production of J/ψ in Cu+Cu Collisions at $\sqrt{s_{NN}} = 62.4$ GeV at Midrapidity

Data of Cu+Cu collisions at $\sqrt{s_{NN}} = 62.4$ GeV was obtained in RHIC Run-5 and contains about 50 J/ψ mesons at midrapidity. As shown in Fig. 2.29, J/ψ at midrapidity in $\sqrt{s_{NN}} = 62.4$ GeV corresponds to the anti-shadowing region ($x \sim 0.05$) of the EKS nuclear shadowing model. Since the enhancement of J/ψ yield is very significant and may be detectable with the current statistics, the measurement will help an understanding of nuclear shadowing.

7.7.2 Future Measurements at RHIC

Production of ψ' and Υ in Heavy-Ion Collisions

Measurement of χ_c and η_c will be very difficult in heavy-ion collisions due to irreducible large background and absence of non-hadronic two-body decay channel with large branching ratio. If high statistics are accumulated, the measurements of ψ' and Υ states having di-lepton decay channels become possible. The measurements will be a good test of the picture of sequential quarkonium dissociation.

Direct Photon Production in Heavy-Ion Collisions with Higher Statistics

Verification of N_{coll} estimated from the Glauber model by transparent probes in the entire rapidity range is desirable. In the PHENIX experiment, electromagnetic and hadron calorimeters will be installed at forward rapidity of $1 < |\eta| < 3$. These calorimeters will also help the measurement of χ_c in $p + p$ collisions at forward rapidity.

7.7.3 Future Measurements at LHC

In 2008, the Large Hadron Collider (LHC) at CERN will start its operation. The maximum center of mass energy per nucleon pair at the LHC is 14 TeV in $p + p$ collisions, 8.8 TeV in p+Pb collisions and 5.56 TeV in Pb+Pb collisions and leads to large production cross section of quarkonia. Since the LHC will achieve very high luminosity, it will open a new era of the QGP study. The nuclear crossing time will become smaller (< 0.01 fm/c) than the $Q\bar{Q}$ production time scale and smaller nuclear absorption cross sections are naively expected. However, quarkonia will be produced from gluons with very small x ($\sim 10^{-4}$–10^{-2}) and the nuclear shadowing will be more important.

Simultaneous Measurement of Three Υ States in Heavy-Ion Collisions

Since large production cross sections are expected for Υ states, a test of the sequential dissociation picture will be much easier than RHIC. Even if there is large contribution of recombination, properties of the recombination will be revealed by the large statistics. Absence of heavier resonance which decays into the Υ states except relatively rare W and Z bosons is advantage.

Simultaneous Measurement of J/ψ and ψ' in Heavy-Ion Collisions

Since the production cross sections of B mesons will be large at LHC, the feed-down from B into J/ψ and ψ' will be large and should be statistically identified using off-vertex measurement. If the isolation of J/ψ originated from B mesons is possible, simultaneous measurement of J/ψ and ψ' is interesting.

Measurement of Nuclear Dependence of Production of Quarkonia in $p + p$ and $p + A$ Collisions

The cold nuclear matter effect at the LHC can be largely different from that at the SPS and RHIC. Measurements of quarkonium production in $p + p$ and $p + A$ collisions are necessary and should help understanding of quarkonium production mechanism.

7.7.4 Future Measurements at eRHIC

To know the gluon distribution in nuclei at small x with good accuracy, a deep inelastic scattering experiment of electron-nucleus (e+A) collisions is demanded. Modification of RHIC to an e+A collider, eRHIC, is being proposed to achieve unique opportunity [162]. Electron beam energy will be 10 GeV and the center of mass energy of $e + p$ collisions

will be $\sqrt{s} = 63$ GeV. The gluon distribution at $x > 10^{-3}$ is directly measured via di-jets and high p_T hadrons produced by photon-gluon fusion.

Chapter 8

Conclusion

The measurements of J/ψ in Cu+Cu collisions at $\sqrt{s_{NN}}$=200 GeV and χ_c in $p+p$ collisions at $\sqrt{s}$=200 GeV have been carried out with the PHENIX detector in the RHIC Run-5 (2005) and Run-6 (2006) to study the hot and dense matter produced by heavy ion collisions using J/ψ as a probe.

Pairs of electrons and positrons were used to reconstruct J/ψ, and pairs of J/ψ and photons were used to reconstruct χ_c. Electrons and photons were measured at midrapidity ($-0.35 < y < 0.35$).

The fraction of J/ψ from $\chi_c \to J/\psi\gamma$ decay R_{χ_c} has been measured with about 4000 reconstructed J/ψ in $p+p$ collisions. The obtained upper limit of R_{χ_c} is 0.40 at the 90% confidence level. Since there are large uncertainties on both experimental and theoretical sides, any quantitative conclusion on the charmonium production mechanism cannot be drawn. However, the obtained upper limit disfavors the color singlet model. The color evaporation model, which contain the color octet contribution, agrees with the obtained upper limit and the small energy dependence. This result indicates that there seems to be a significant fraction of the color octet contribution to the charmonium production.

The input R_{χ_c} value of the cold nuclear matter model is consistent with the obtained upper limit. Since the color octet state has the effectively larger breakup cross section in the nuclear environment than the color singlet state, the fraction of the color octet contribution is important to understand the cold nuclear matter effect as well as nuclear shadowing. In the cold nuclear matter model, the Non-relativistic QCD which is not excluded by the obtained upper limit is used to estimate the color octet contribution and nuclear shadowing is included.

About 1400 J/ψ were observed in Cu+Cu collisions. From the comparison with the yield in $p+p$ collisions at the same energy scaled by the number of underlying nucleon-nucleon collisions in Cu+Cu collisions, the nuclear modifications on J/ψ production in Cu+Cu collisions were studied as functions of centrality and p_T. In the most central collisions, the suppression of J/ψ by a factor of $\sim$2 has been observed. No significant p_T dependence of suppression was observed. The data at midrapidity was compared to the data at forward rapidity ($1.2 < |y| < 2.2$) measured by $\mu^+\mu^-$ pairs and there is no significant rapidity dependence.

From the J/ψ data in Cu+Cu collisions with the number of participants nucleon range of $N_{part} < 63$ and d+Au collisions, the breakup cross sections were independently

extracted. The breakup cross section at midrapidity is $\sigma_{breakup} = 2.2^{+1.6}_{-1.5}$ (2.3 ± 1.5) mb from Cu+Cu data and $\sigma_{breakup} = 2.4^{+1.9}_{-1.6}$ $(1.0^{+1.8}_{-1.7})$ mb from d+Au data with EKS (NDSG) shadowing model and these values are consistent within errors.

The same model calculation of the cold nuclear matter was applied to the J/ψ data of heavier Au+Au collisions and Cu+Cu collisions, and the large J/ψ suppression in central Au+Au collisions was not explained by the model calculation. Therefore, the J/ψ suppression in Au+Au collisions strongly indicates additional contributions besides the cold nuclear matter effect in the intermediate stages of collisions. The suppression of inclusive J/ψ seems to start from $N_{part} \sim 100$, which corresponds to the most central Cu+Cu collisions.

The survival probability of J/ψ defined by the ratio of the measured yield to the expected yield including the cold nuclear matter effect of RHIC data and SPS data, where the collision energy is 10 times different, seems to scale with the Bjorken energy density with the thermalization time of $\tau_0 = 1$ fm/c. However, the Bjorken energy density is 6 times smaller than the energy density expected from the hydrodynamical model, which succeeds to reproduce the hadron spectra and anisotropy.

While the J/ψ data at RHIC was compared with the theoretical models which succeeds to reproduce the J/ψ data at the SPS, there is no model which can reproduce the data at both mid and forward rapidity at RHIC. To test the picture of sequential dissociation, more precise experimental data is needed to give tighter constraint on theoretical models.

Acknowledgments

I am very pleased to express my gratitude to everyone who helped this study.

First of all, I would like to thank Prof. H. Hamagaki for his appropriate advice and profound discussion about the experiment, analysis and physics. His entire support and rich knowledge guided me to the completion of this thesis.

I am grateful to Dr. K. Ozawa for his kind support for the analysis and my life at BNL and in Japan. I wish to thank Dr. T. Gunji for his thoroughly excellent precedent work on J/ψ production at the PHENIX experiment and his sincere encouragement for the completion of this thesis. I am obliged to Dr. F. Kajihara for his abundant experience of the electron analysis and friendly association at BNL. I would like to express my thanks to Dr. T. Isobe and Prof. T. Sakaguchi for their thoughtful advice on my scientific activities and daily life.

I express my acknowledgments to all the collaborators of the PHENIX experiment. I would like to give many thanks to the previous and present spokespersons Prof. W.A. Zajc and Prof. B.V. Jacak for their excellent leadership and continuous support. I thank Prof. A.D. Frawley, Mr. K. Das, Prof. Y. Akiba and Prof. W. Xie for their productive cooperation in the analysis of J/ψ production in Cu+Cu collisions in the e^+e^- channel. I would like to thank the other members of Paper Preparation Group 071, Dr. D. Sivermyr, Dr. A.A. Bickley, Dr. V. Cianciolo, Dr. F. Fleuret, Dr. A. Glenn, Dr. A. Rakotozafindrabe for their quick and certain activities. I would like to express my thanks to the conveners of the Heavy Flavor/Light Vector Meson Physics Working Group, Dr. A. Lebedev, Dr. R. Granier de Cassagnac, Prof. T.K. Hemmick and Dr. A. Toia for improving discussions on the analysis of χ_c production in $p+p$ collisions. I wish to thank Prof. R. Seto and Dr. M.J. Leitch for their legitimate questions on the analysis of χ_c production in $p+p$ collisions. I give my thanks to Mr. K. Boyle for his kind and important helps with the EMCal analysis in $p+p$ collisions. I am obliged to Dr. C. Pinkenburg, Dr. R. Averbeck, Dr. D.P. Morrison and Dr. J.T. Mitchel for their marvelous assistance on the analysis environment at BNL. I appreciate Prof. J.S. Haggerty's wonderful insight into the experiments. I would like to acknowledge Ms. D. Earley, Ms. J. Nasta, Ms. R. Inguanta and Ms. Y. Suenaga for their sincere administrative and secretarial support at BNL.

I wish to express my obligation to Dr. S. Yokkaichi, Dr. T. Ichihara, Dr. Y. Watanabe and Mr. T. Nakamura for their steady operation of CC-J at RIKEN. Especially, I wish to express my gratitude to Dr. S. Kametani for encouraging to write this thesis and discussion about the cold nuclear matter effects of charmonia. I am grateful to all the members of the PHENIX-J group, Prof. T. Sugitate, Prof. K. Shigaki, Dr. K. Homma, Mr. Y. Tsuchimoto, Mr. Y. Nakamiya, Ms. M. Ouchida, Mr. K. Yamaura, Mr. K. Kijima, Mr. D. Watanabe, Mr. K. Mizoguchi, Mr. Y. Iwanaga, Prof. Y. Miake,

Prof. S. Esumi, Dr. T. Chujo, Dr. H. Masui, Dr. S. Sakai, Dr. M. Konno, Ms. M. Shimomura, Mr. M. Oka, Mr. K. Miki, Prof. K. Imai, Prof. N. Saito, Dr. K. Tanida, Dr. Y. Fukao, Mr. M. Togawa, Mr. K. Aoki, Mr. K. Shoji, Mr. N. Kamihara, Mr. K. Nakano, Prof. H. En'yo, Dr. K. Okada, Dr. M. Kaneta for their gentle support and perpetual cooperation.

I express my obligation to Dr. T. Hirano and Dr. M. Isse for invitation to the workshop at the RCNP, Osaka University. The activities related to the workshop really helps me in completion of this thesis.

I wish to express my thanks to all the present and past members of Hamagaki's group, Dr. M. Inuzuka, Dr. K. Kino, Mr. N. Kurihara, Mr. Y. Morino, Mr. S. Saito, Mr. Y. Aramaki, Mr. Y.L. Yamaguchi, Mr. S. Sano, Mr. S. Sugawara, Mr. A. Takahara for their fruitful discussions, tender helps and continuous friendships.

I express my appreciation to all the present and past members of Center for Nuclear Study, University of Tokyo, Prof. H. Sakai, Prof. T. Otsuka, Prof. S. Kubono, Prof. T. Uesaka, Dr. E. Ideguchi, Dr. T. Kawabata, Dr. H. Yamaguchi, Dr. S. Michimasa, Dr. S. Fujii, Dr. K. Suda, Dr. Y. Shimizu, Dr. Y. Maeda, Dr. A. Saito, Dr. K. Nakanishi, Dr. Y. Wakabayashi, Mr. S. Ota, Mr. K. Itoh, Mr. M. Niikura, Mr. S. Sakaguchi, Ms. Y. Sasamoto, Mr. H. Fujikawa, Mr. S. Hayakawa, Mr. A. Yoshida, Ms. T. Kawahara, Mr. Y. Kurihara, Mr. H. Miya, Ms. M. Hirano, Ms. T. Endo, Ms. I. Yamamoto, Ms. T. Itagaki, Ms. M. Yamaguchi, Ms. Y. Kishi and Ms. Y. Fujiwara for their ceaseless support and usual kindness.

I am sincerely thankful to Ms. S. Maki and her family for their good wishes.

I am obliged to Prof. S. Asai, Prof. T. Matsui, Prof. H. Sakurai and Prof. S. Shimoura for their valuable comments and important advice. I would like to express my appreciation to Prof. T. Kobayashi for his truly relevant advice.

Final of all, I wish to express my gratitude to my parents, Nobuteru and Sumi, and my sisters, Yumi and Kimi, for their continuous and kind support.

Appendix A

Kinematic Variables

A.1 Transverse Momentum

In this thesis, the z axis is chosen as the beam going direction. The transverse momentum, p_T, and transverse mass, m_T, are defined in terms of the energy momentum components of a particle.

$$p_T \equiv \sqrt{p_x^2 + p_y^2}, \tag{A.1}$$

$$m_T \equiv \sqrt{m^2 + p_T^2} = \sqrt{E^2 - p_z^2}, \tag{A.2}$$

where E, p_x, p_y, p_z and m are the energy, x, y and z components of the momentum and the mass of the particle, respectively.

A.2 Rapidity and Pseudo Rapidity

The rapidity, y, of the particle is defined as

$$y \equiv \frac{1}{2} \ln \left(\frac{E + p_z}{E - p_z} \right). \tag{A.3}$$

The rapidity is transformed under the Lorentz boost in the z direction with the velocity of β as follows.

$$y \rightarrow y + \tanh^{-1} \beta. \tag{A.4}$$

The particle energy and z component of the momentum (p_z) can be written in terms of the rapidity (y) and transverse mass (m_T) as follows.

$$E = m_T \cosh y, \tag{A.5}$$

$$p_z = m_T \sinh y. \tag{A.6}$$

The pseudo rapidity, η, can be expressed in terms of the angle, θ, between the particle momentum, $\vec{p}$, and z axis as follows.

$$\eta \equiv \frac{1}{2} \ln \left(\frac{|\vec{p}| + p_z}{|\vec{p}| - p_z} \right) = -\ln \left(\tan \frac{\theta}{2} \right). \tag{A.7}$$

Appendix B

Run Selection

Figure B.1 and Figure B.2 show the number of electrons and positrons per event with the standard eID cut and $p_T > 0.2$ GeV/c cut in MB data as a function of runnumber for each EMCal sector, respectively.

Figure B.3 and Figure B.4 show the number of electrons and positrons per event with the standard eID cut and $p_T > 0.7$ GeV/c cut in MB data as a function of runnumber for each EMCal sector, respectively.

Figure B.5 and Figure B.6 show the number of electrons and positrons per event with the standard eID cut and $p_T > 0.2$ GeV/c cut in ERT electron data as a function of runnumber for each EMCal sector, respectively.

Figure B.7 and Figure B.8 show the number of electrons and positrons per event with the standard eID cut and $p_T > 0.7$ GeV/c cut in ERT electron data as a function of runnumber for each EMCal sector, respectively.

As described in section 5.6, these figures were used to select good runs for the J/ψ analysis.

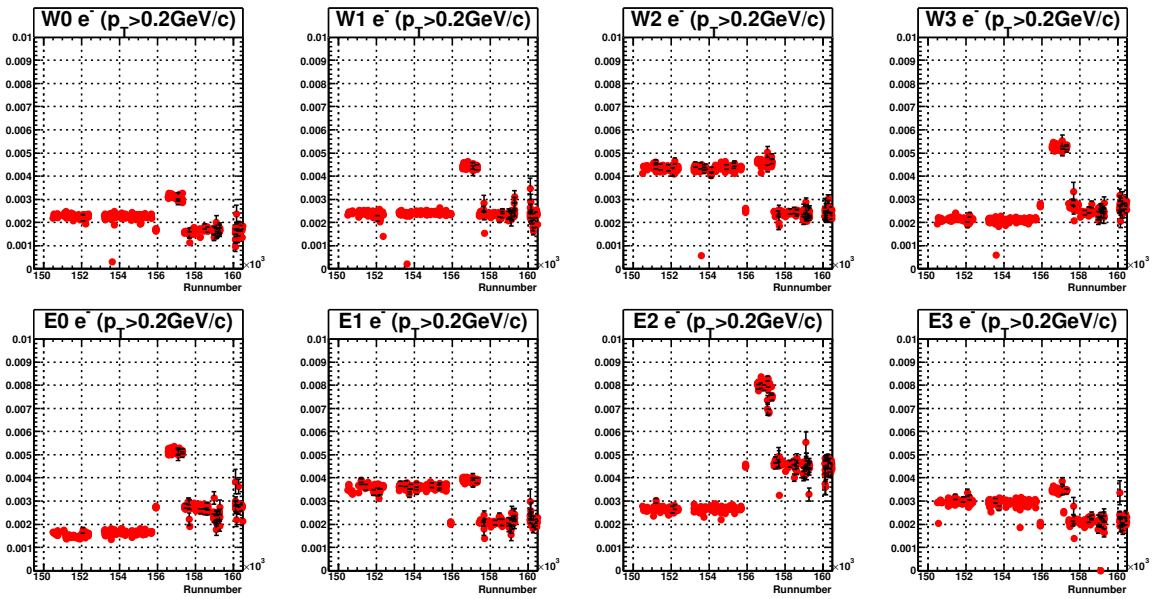

Figure B.1: The number of electrons per event with the standard eID cut and $p_T > 0.2$ GeV/c cut in MB data as a function of runnumber for each EMCal sector.

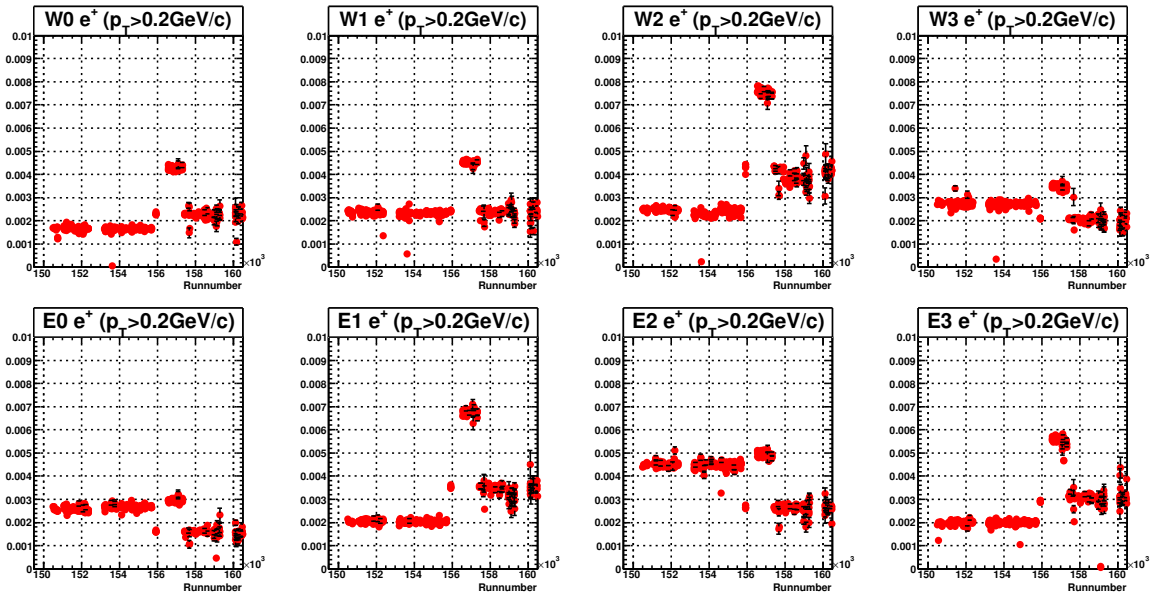

Figure B.2: The number of positrons per event with the standard eID cut and $p_T > 0.2$ GeV/c cut in MB data as a function of runnumber for each EMCal sector.

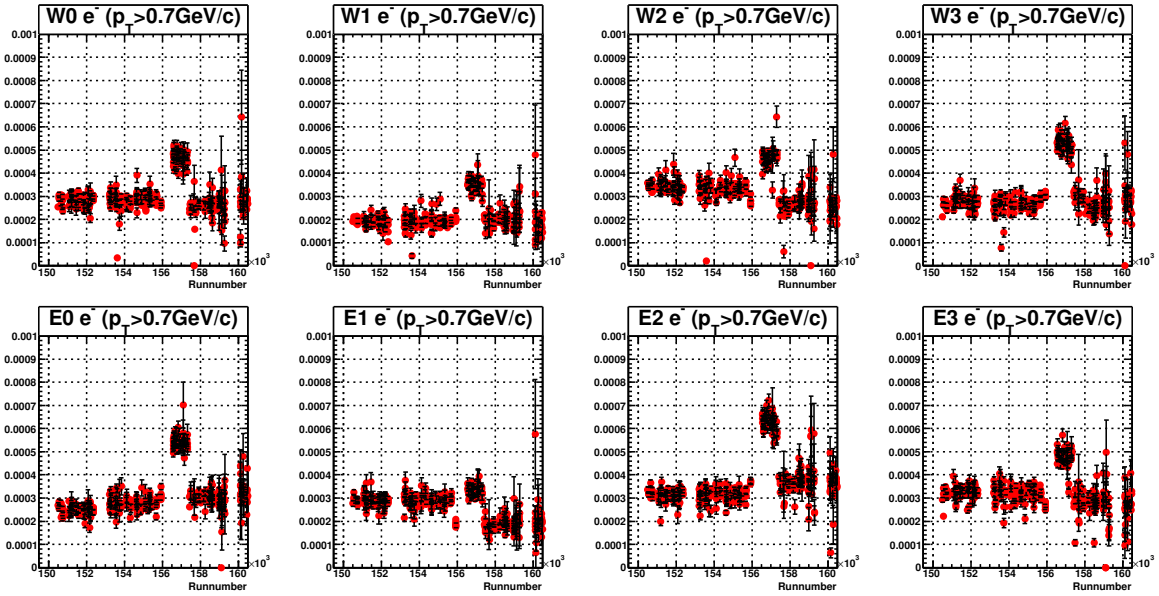

Figure B.3: The number of electrons per event with the standard eID cut and $p_T > 0.7$ GeV/c cut in MB data as a function of runnumber for each EMCal sector.

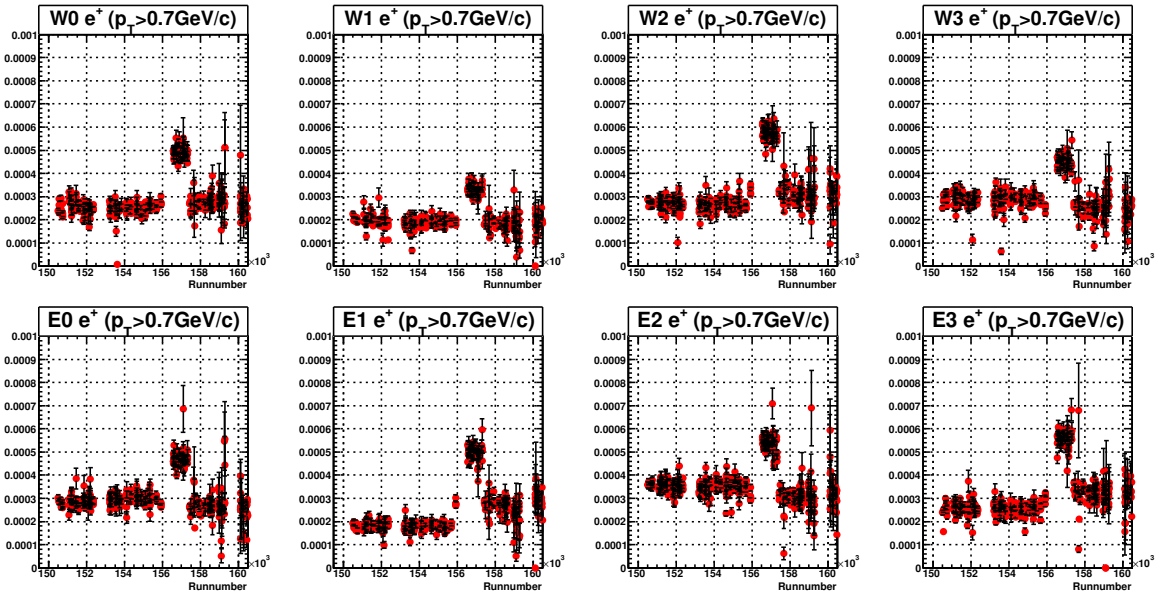

Figure B.4: The number of positrons per event with the standard eID cut and $p_T > 0.7$ GeV/c cut in MB data as a function of runnumber for each EMCal sector.

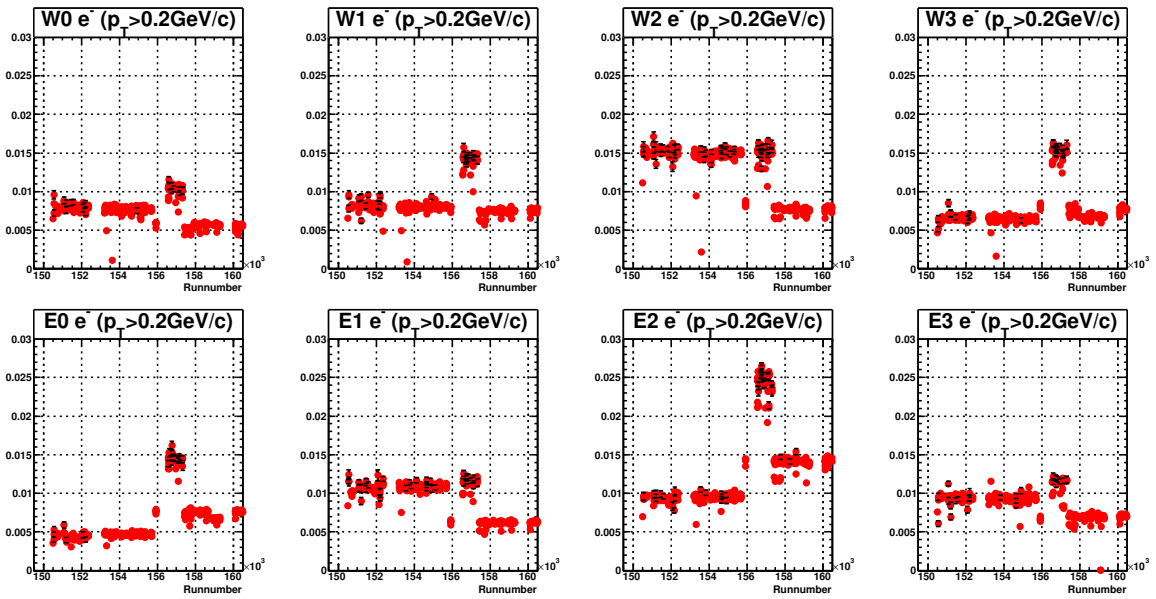

Figure B.5: The number of electrons per event with the standard eID cut and $p_T > 0.2$ GeV/c cut in ERT electron data as a function of runnumber for each EMCal sector.

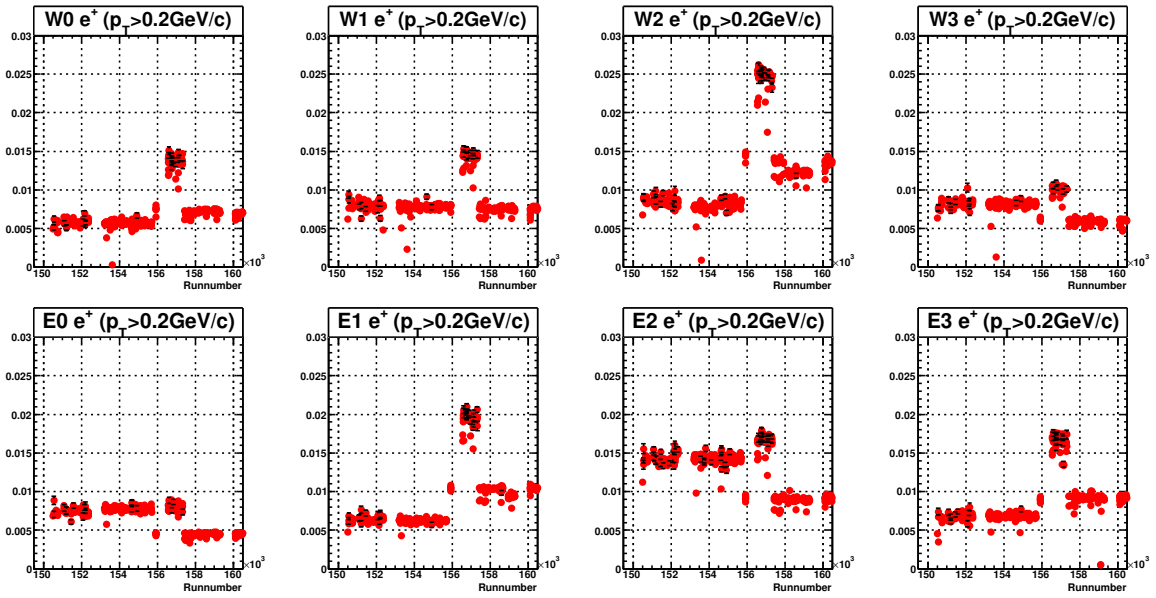

Figure B.6: The number of positron per event with the standard eID cut and $p_T > 0.2$ GeV/c cut in ERT electron data as a function of runnumber for each EMCal sector.

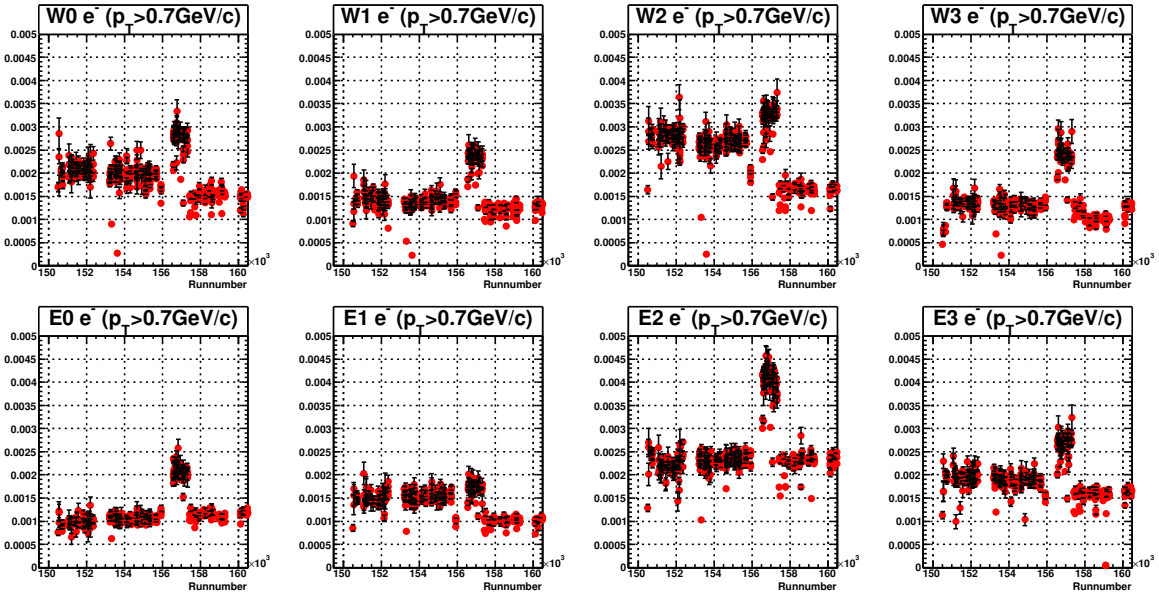

Figure B.7: The number of electron per event with the standard eID cut and $p_T > 0.7$ GeV/c cut in ERT electron data as a function of runnumber for each EMCal sector.

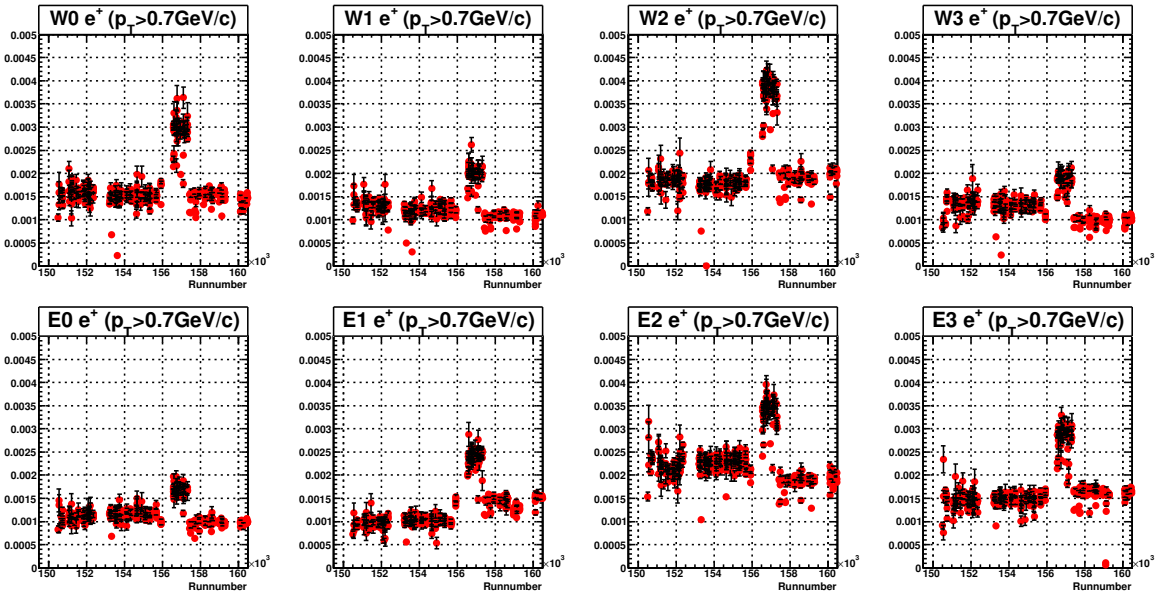

Figure B.8: The number of positron per event with the standard eID cut and $p_T > 0.7$ GeV/c cut in ERT electron data as a function of runnumber for each EMCal sector.

Appendix C

Invariant Mass Spectrum and Raw p_T Spectrum

Figure C.1, Figure C.2, Figure C.3, Figure C.4, Figure C.5, Figure C.6 and Figure C.7 show the invariant mass spectra and raw p_T spectra for 0–10%, 10–20%, 20–30%, 30–40%, 40–50%, 50–60% and 60–94% Centrality in all run groups (G0–G3).

Figure C.8, Figure C.9, Figure C.10 and Figure C.11 show the invariant mass spectra and raw p_T spectra for MB (0–94%) in run group G0, G1, G2 and G3, respectively.

The signal extraction of J/ψ is described in section 5.7.

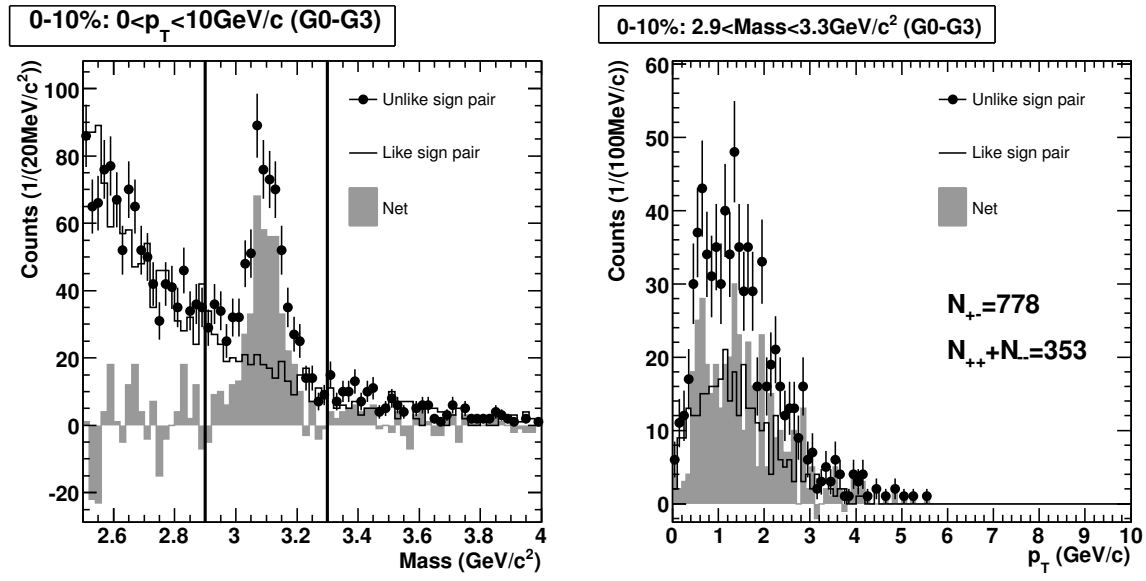

Figure C.1: The invariant mass distribution (left) and the raw p_T distribution in the J/ψ mass region (right) in 0–10% data in all run groups.

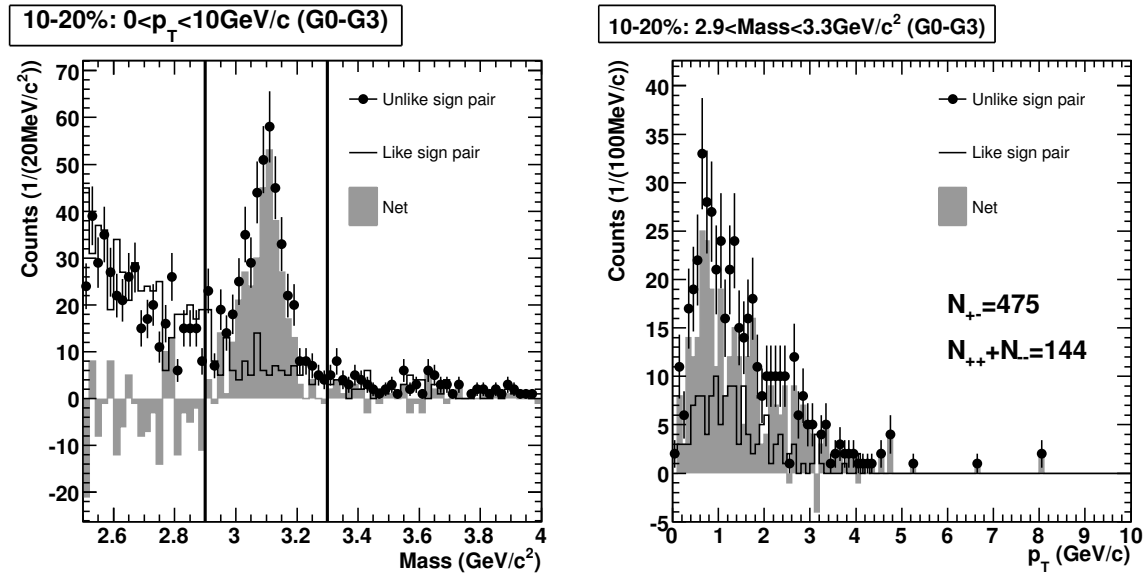

Figure C.2: The invariant mass distribution (left) and the raw p_T distribution in the J/ψ mass region (right) in 10–20% data in all run groups.

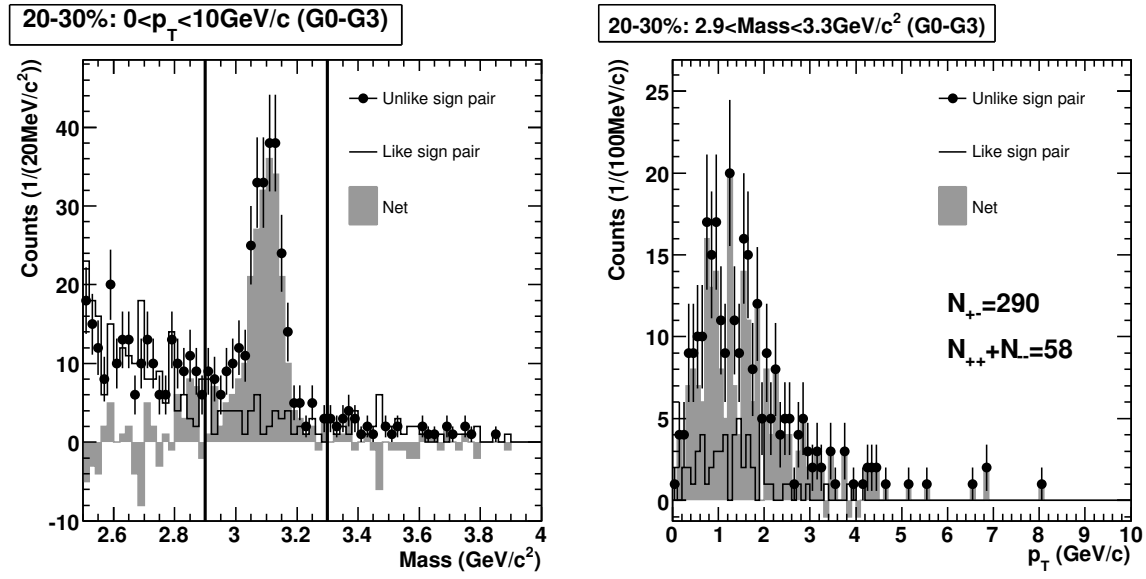

Figure C.3: The invariant mass distribution (left) and the raw p_T distribution in the J/ψ mass region (right) in 20–30% data in all run groups.

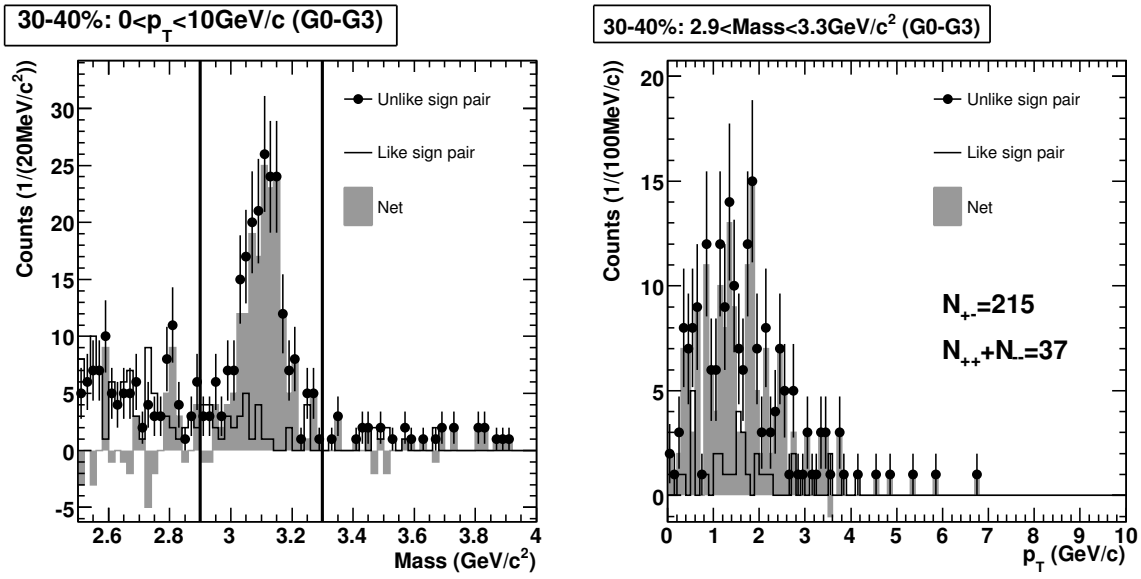

Figure C.4: The invariant mass distribution (left) and the raw p_T distribution in the J/ψ mass region (right) in 30–40% data in all run groups.

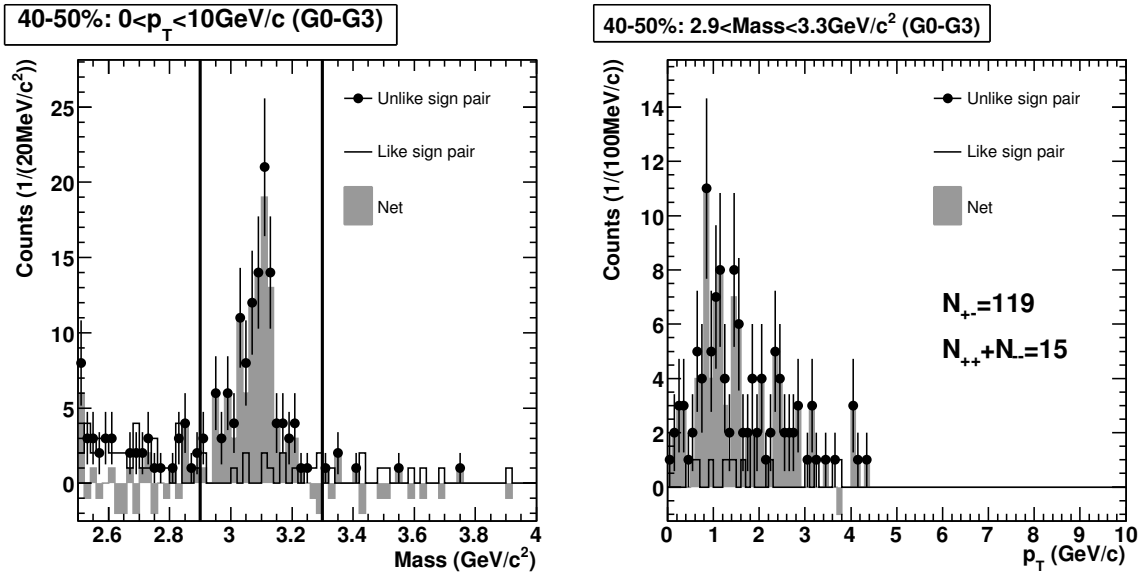

Figure C.5: The invariant mass distribution (left) and the raw p_T distribution in the J/ψ mass region (right) in 40–50% data in all run groups.

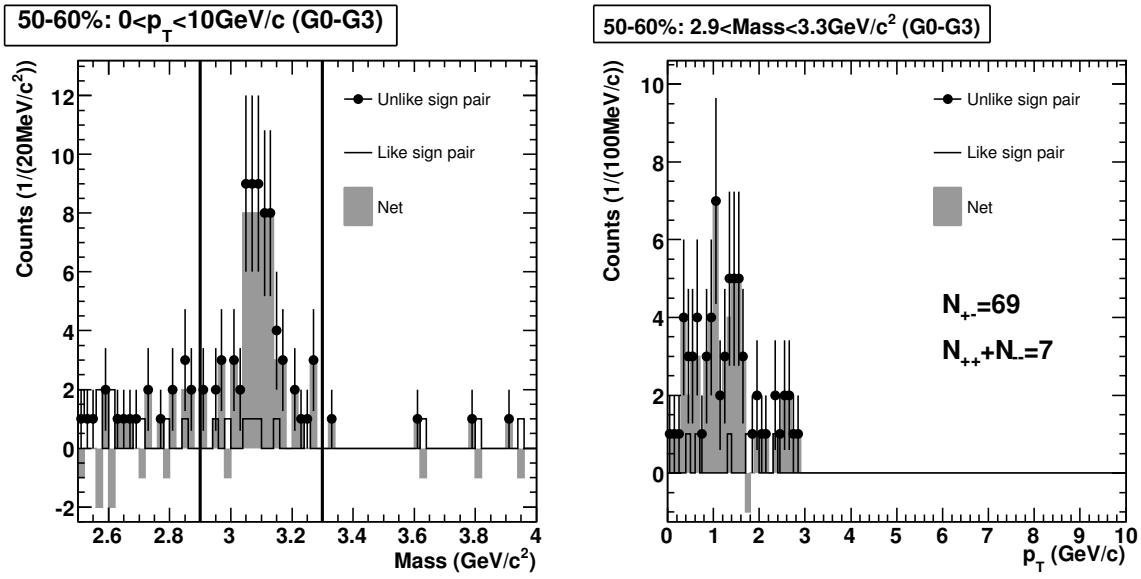

Figure C.6: The invariant mass distribution (left) and the raw p_T distribution in the J/ψ mass region (right) in 50–60% data in all run groups.

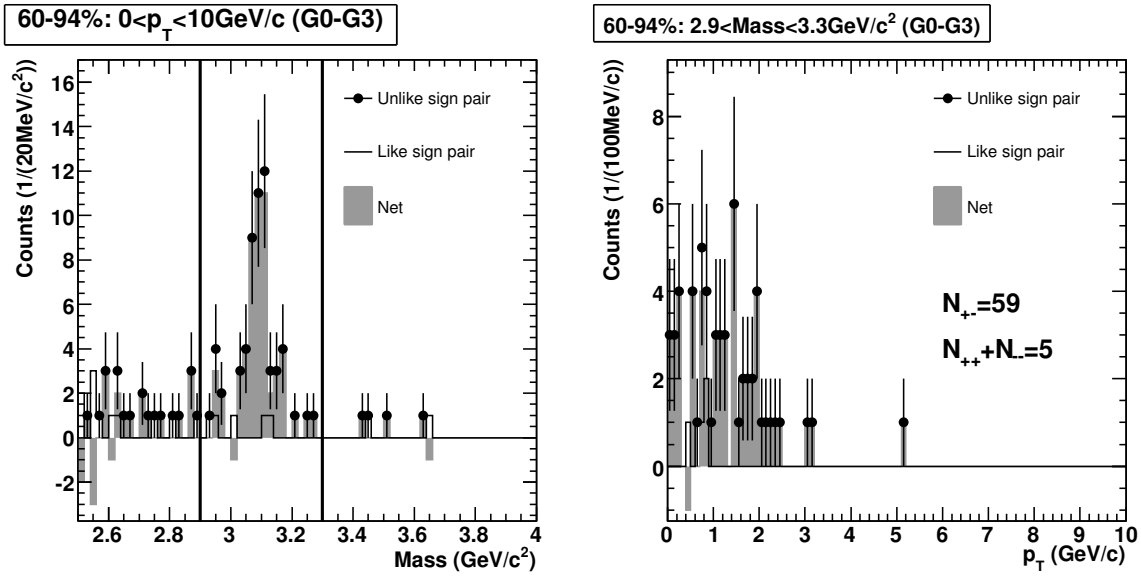

Figure C.7: The invariant mass distribution (left) and the raw p_T distribution in the J/ψ mass region (right) in 60–94% data in all run groups.

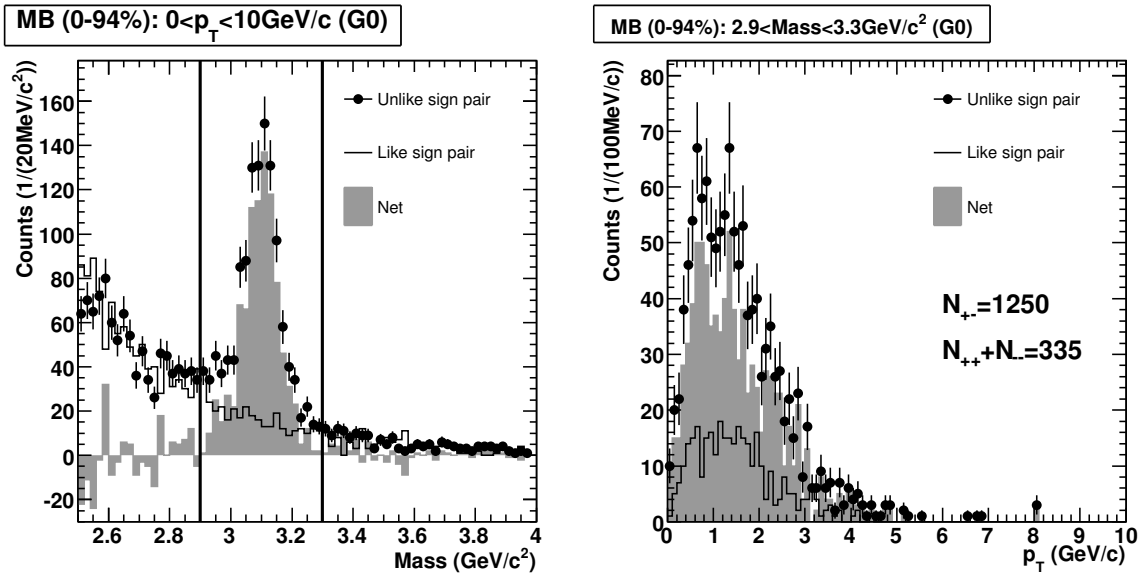

Figure C.8: The invariant mass distribution (left) and the raw p_T distribution in the J/ψ mass region (right) in MB (0–94%) data in the run group G0.

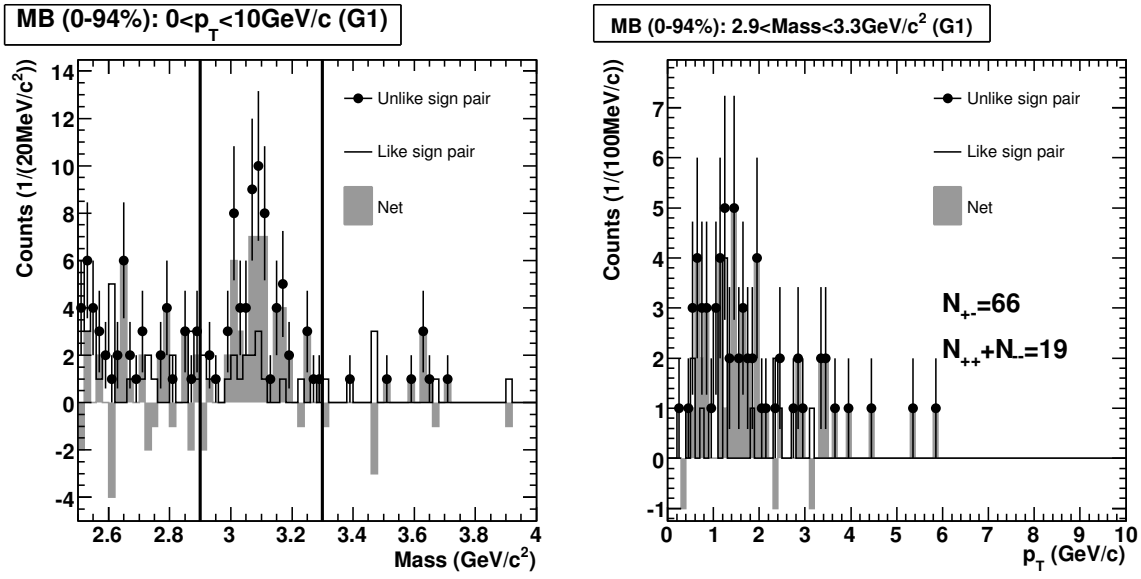

Figure C.9: The invariant mass distribution (left) and the raw p_T distribution in the J/ψ mass region (right) in MB (0–94%) data in the run group G1.

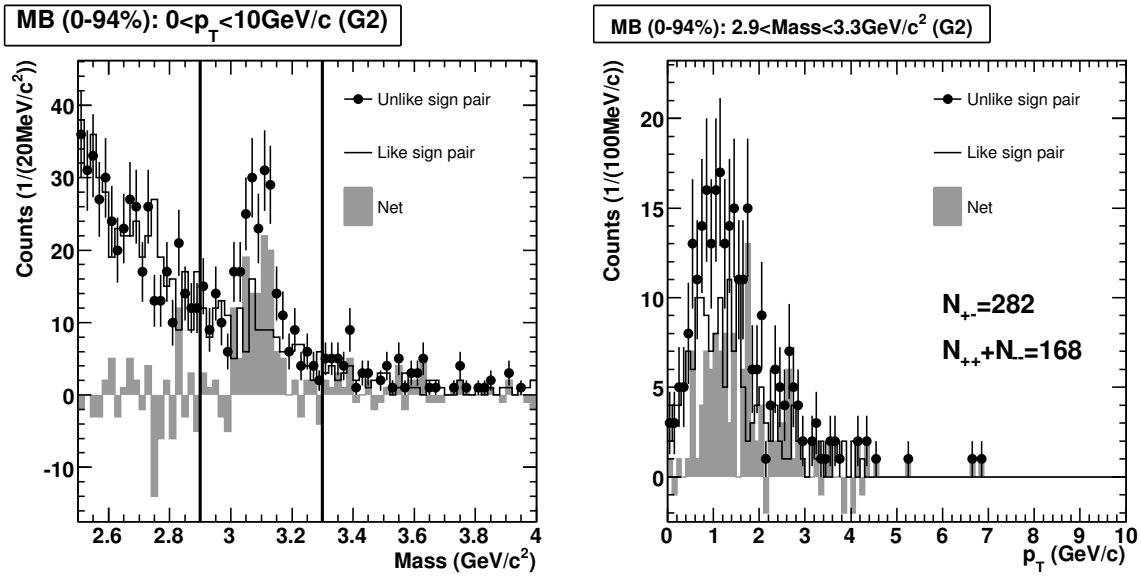

Figure C.10: The invariant mass distribution (left) and the raw p_T distribution in the J/ψ mass region (right) in MB (0–94%) data in the run group G2.

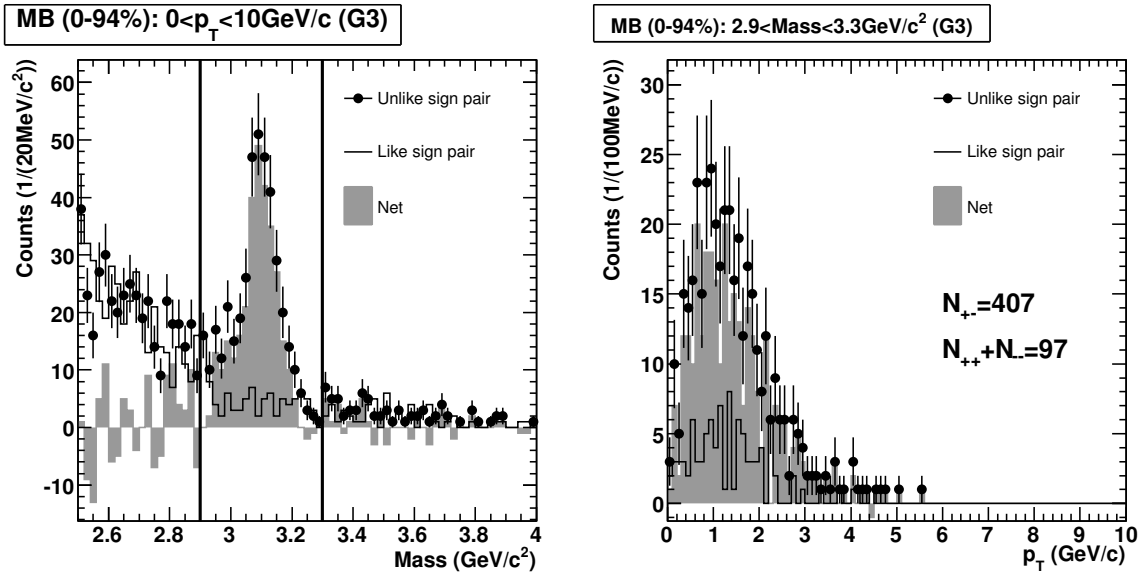

Figure C.11: The invariant mass distribution (left) and the raw p_T distribution in the J/ψ mass region (right) in MB (0–94%) data in the run group G3.

Appendix D

ERT Electron Trigger Efficiency of Single Electron

Figure D.1 and Figure D.2 show the ERT electron trigger efficiency for single electrons in run groups G0 and G1 with and without random benefit, respectively. There are 4 EMCal sectors in the west arm (W0, W1, W2 and W3) and 4 EMCal sectors in the east arm (E0, E1, E2 and E3). Centrality is divided into 5 bins (0–10%, 10–20%, 20–30%, 30–40% and 40–94%). The determination of the ERT electron trigger efficiency for single electrons is described in subsection 5.8.3.

Figure D.3 and Figure D.4 are the same figures in the run group G2.

Figure D.5 and Figure D.6 are the same figures in the run group G3.

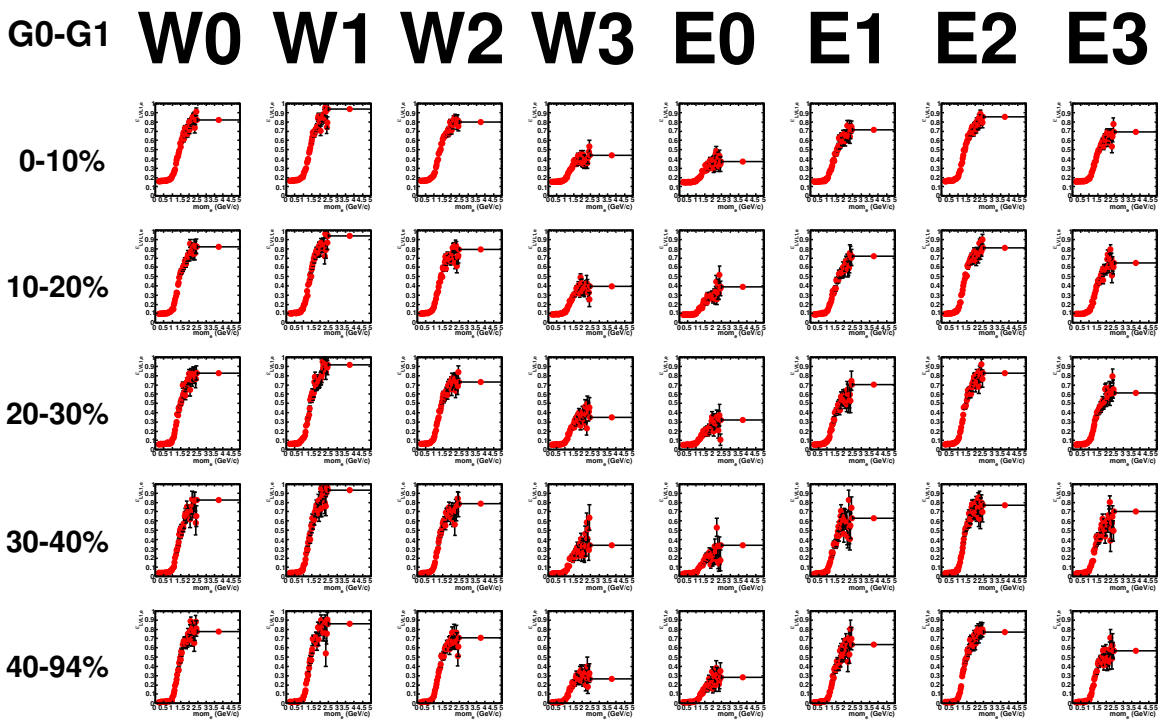

Figure D.1: Single electron trigger efficiency including random benefit in G0 and G1.

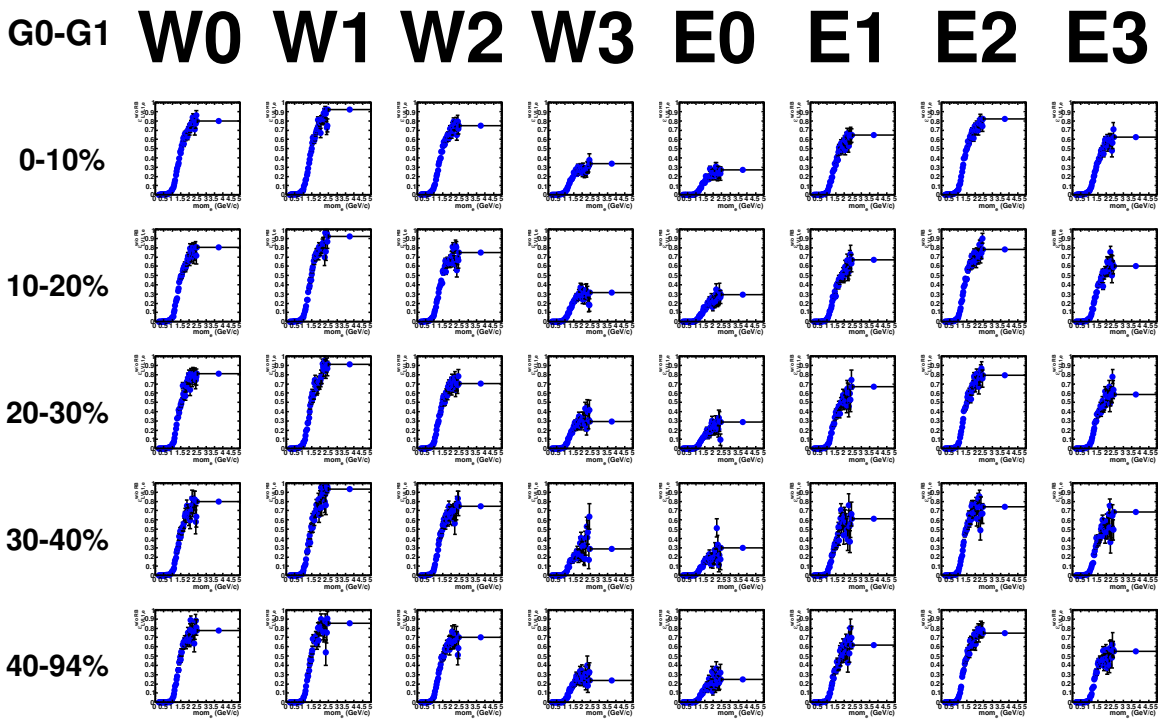

Figure D.2: Single electron trigger efficiency in G0 and G1.

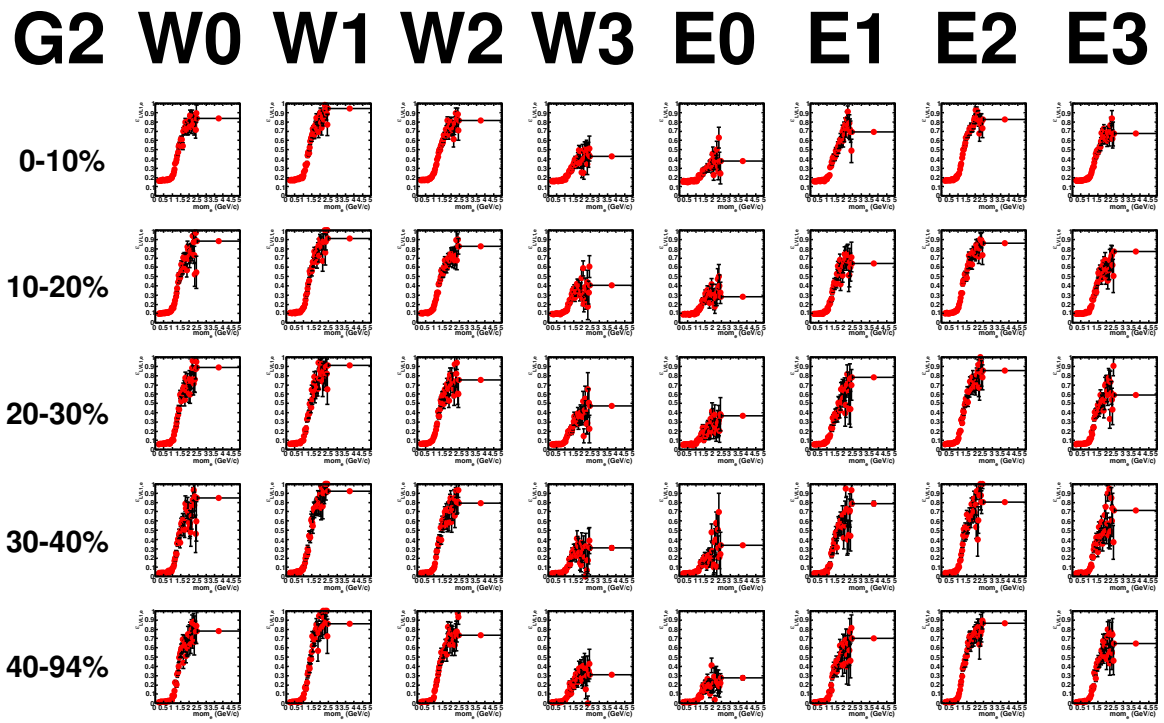

Figure D.3: Single electron trigger efficiency including random benefit in G2.

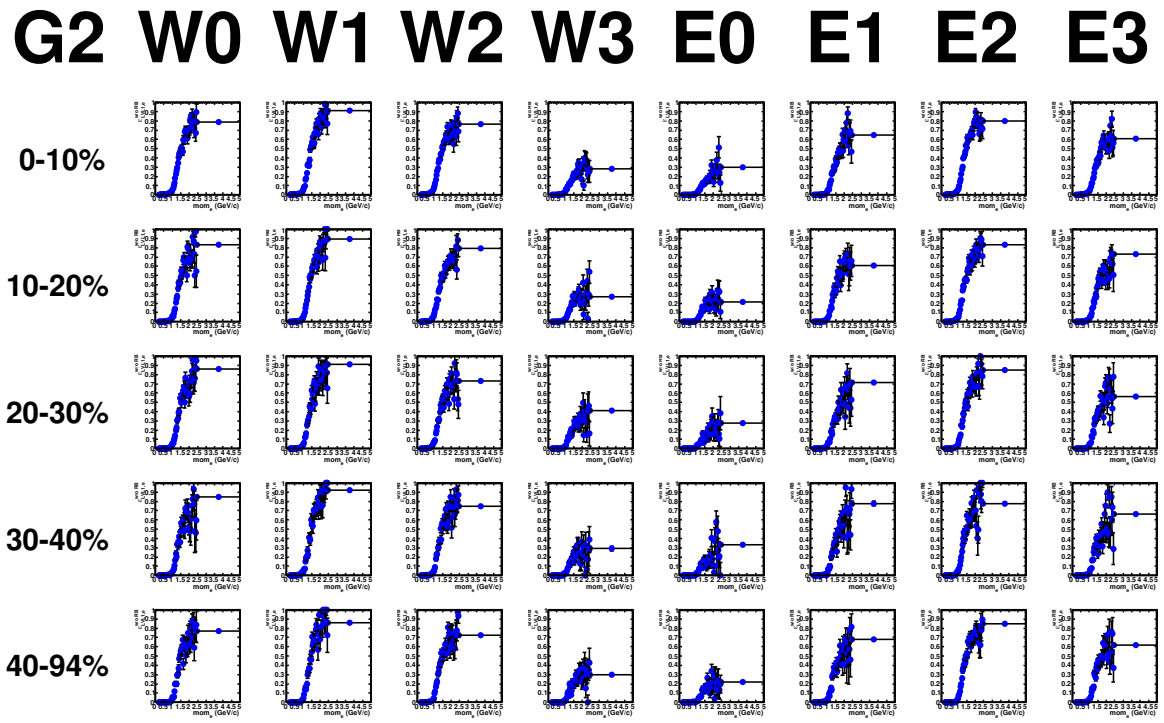

Figure D.4: Single electron trigger efficiency in G2.

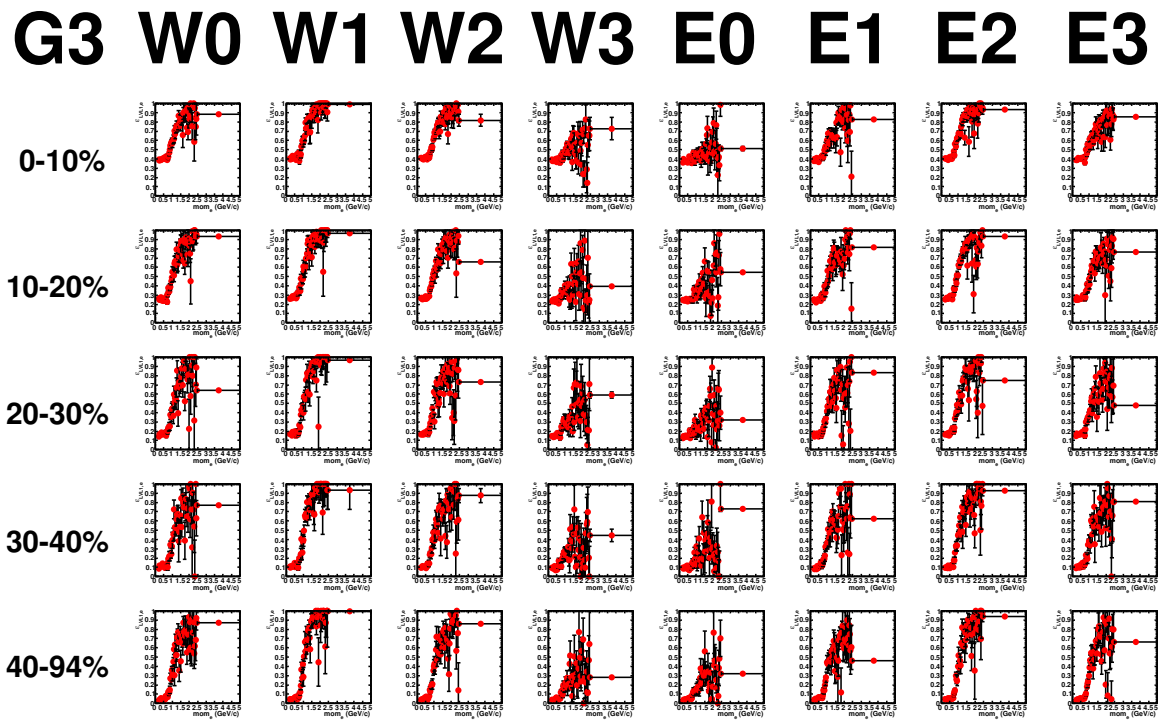

Figure D.5: Single electron trigger efficiency including random benefit in G3.

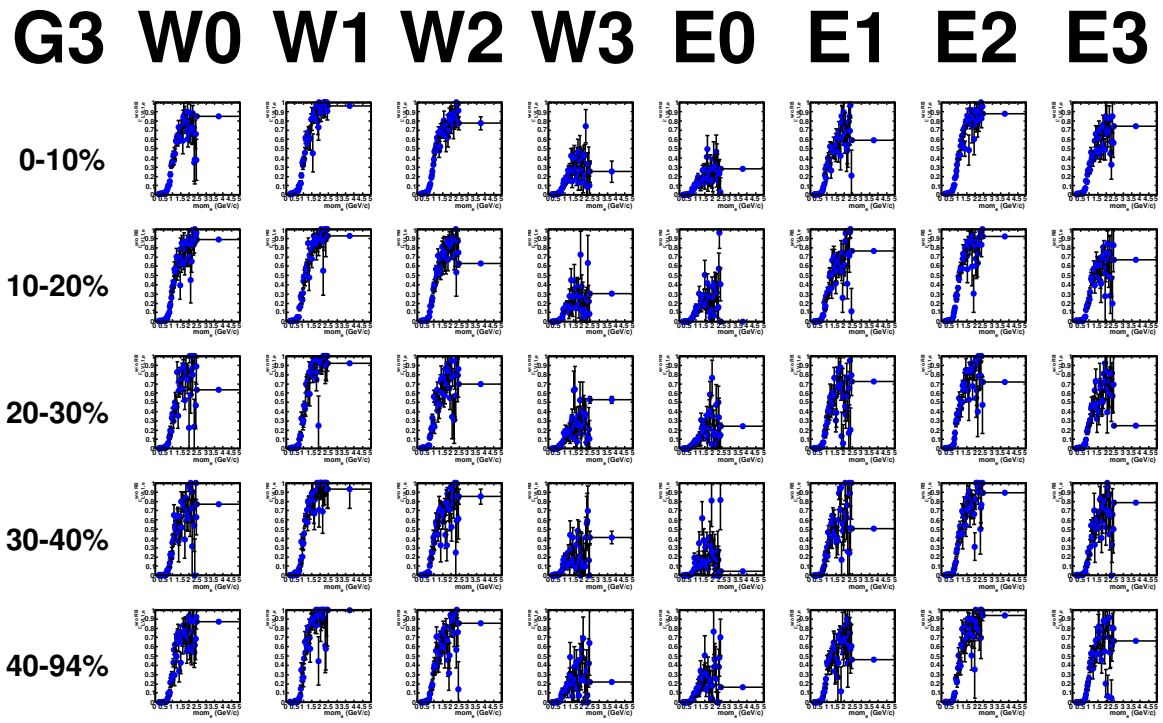

Figure D.6: Single electron trigger efficiency in G3.

Appendix E

Data Table of Results of J/ψ Production in Cu+Cu Collisions

Table E.1 is the summary of the invariant yield of J/ψ for 0–20%, 20–40%, 40–60% and 60–94%.

Table E.2 is the summary of the invariant yield of J/ψ divided by the number of binary nucleon-nucleon collisions for 0–20%, 20–40%, 40–60% and 60–94%.

Table E.3 is the summary of the integrated invariant yield of J/ψ divided by the number of binary nucleon-nucleon collisions for 0–20%, 20–40%, 40–60% and 60–94%.

Figure E.1 shows the invariant yield of J/ψ divided by the number of binary nucleon-nucleon collisions, $\frac{BR}{2\pi p_T N_{coll}} \frac{d^2N}{dydp_T}$ as a function of N_{part}.

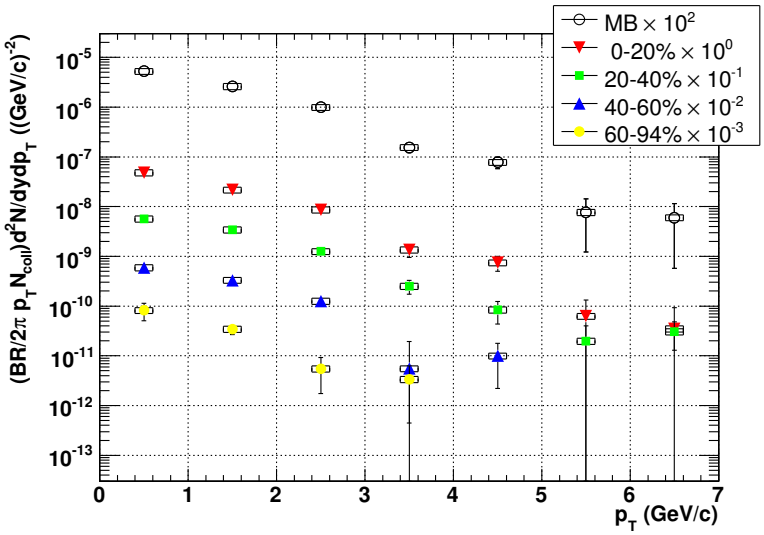

Figure E.1: Invariant yield of J/ψ divided by the number of binary nucleon-nucleon collisions, $\frac{BR}{2\pi p_T N_{coll}} \frac{d^2N}{dydp_T}$, as a function of N_{part}.

Table E.4 is the summary of the nuclear modification factor of J/ψ for each Centrality and each p_T bin.

Centrality (%)	p_T (GeV/c)	$BR/2\pi p_T d^2N/dp_T dy \pm$ stat $\pm$ uncorr. syst $\pm$ corr. syst ((GeV/c)$^{-2}$)
0–94	0–1	9.4e−07 ± 1.4e−07 ± 4.7e−08 ± 7.8e−08
(MB)	1–2	2.9e−07 ± 3.4e−08 ± 1.5e−08 ± 2.3e−08
	2–3	8.4e−08 ± 1.8e−08 ± 4.2e−09 ± 6.6e−09
	3–4	3.4e−08 ± 1.3e−08 ± 1.7e−09 ± 2.7e−09
	4–5	1.9e−08 ± 9.1e−09 ± 9.3e−10 ± 1.5e−09
	5–6	5.8e−09 ± 5.3e−09 ± 2.9e−10 ± 4.6e−10
	6–7	4.9e−09 ± 4.5e−09 ± 2.4e−10 ± 3.8e−10
0–20	0–1	7.1e−06 ± 9.4e−07 ± 3.6e−07 ± 5.6e−07
	1–2	3.1e−06 ± 2.9e−07 ± 1.5e−07 ± 2.4e−07
	2–3	1.3e−06 ± 1.6e−07 ± 6.4e−08 ± 1.0e−07
	3–4	1.7e−07 ± 5.3e−08 ± 8.7e−09 ± 1.4e−08
	4–5	1.2e−07 ± 3.6e−08 ± 5.8e−09 ± 9.2e−09
	5–6	1.1e−08 ± 1.1e−08 ± 5.3e−10 ± 8.4e−10
	6–7	7.0e−09 ± 8.9e−09 ± 3.5e−10 ± 5.5e−10
20–40	0–1	3.1e−06 ± 5.3e−07 ± 1.5e−07 ± 2.4e−07
	1–2	2.2e−06 ± 2.0e−07 ± 1.1e−07 ± 1.7e−07
	2–3	7.6e−07 ± 1.0e−07 ± 3.8e−08 ± 6.0e−08
	3–4	1.5e−07 ± 4.7e−08 ± 7.2e−09 ± 1.1e−08
	4–5	4.8e−08 ± 2.5e−08 ± 2.4e−09 ± 3.8e−09
	5–6	9.2e−09 ± 1.2e−08 ± 4.6e−10 ± 7.2e−10
	6–7	1.7e−08 ± 1.0e−08 ± 8.4e−10 ± 1.3e−09
40–60	0–1	1.3e−06 ± 3.1e−07 ± 6.5e−08 ± 1.0e−07
	1–2	7.4e−07 ± 1.2e−07 ± 3.7e−08 ± 5.8e−08
	2–3	2.4e−07 ± 5.4e−08 ± 1.2e−08 ± 1.9e−08
	3–4	6.9e−09 ± 2.6e−08 ± 3.5e−10 ± 5.4e−10
	4–5	1.7e−08 ± 1.7e−08 ± 8.6e−10 ± 1.4e−09
60–94	0–1	4.7e−07 ± 1.6e−07 ± 2.3e−08 ± 3.7e−08
	1–2	1.4e−07 ± 3.7e−08 ± 7.0e−09 ± 1.1e−08
	2–3	1.8e−08 ± 2.0e−08 ± 8.8e−10 ± 1.4e−09
	3–4	1.6e−08 ± 1.7e−08 ± 8.2e−10 ± 1.3e−09

Table E.1: Invariant yield of J/ψ for 0–20%, 20–40%, 40–60% and 60–94%.

Centrality (%)	p_T (GeV/c)	$BR/2\pi p_T N_{coll} d^2N/dp_T dy \pm$ stat $\pm$ uncorr. syst $\pm$ corr. syst ((GeV/c)$^{-2}$)
0–94	0–1	5.3e−08 ± 4.8e−09 ± 2.6e−09 ± 7.3e−09
(MB)	1–2	2.6e−08 ± 1.6e−09 ± 1.3e−09 ± 3.7e−09
	2–3	9.9e−09 ± 8.4e−10 ± 5.0e−10 ± 1.4e−09
	3–4	1.6e−09 ± 3.3e−10 ± 7.7e−11 ± 2.2e−10
	4–5	7.8e−10 ± 2.0e−10 ± 3.9e−11 ± 1.1e−10
	5–6	7.7e−11 ± 6.5e−11 ± 3.8e−12 ± 1.1e−11
	6–7	6.0e−11 ± 5.4e−11 ± 3.0e−12 ± 8.4e−12
0–20	0–1	4.8e−08 ± 6.3e−09 ± 2.4e−09 ± 6.7e−09
	1–2	2.2e−08 ± 2.0e−09 ± 1.1e−09 ± 3.0e−09
	2–3	8.6e−09 ± 1.1e−09 ± 4.3e−10 ± 1.2e−09
	3–4	1.4e−09 ± 3.9e−10 ± 6.8e−11 ± 1.9e−10
	4–5	7.5e−10 ± 2.4e−10 ± 3.7e−11 ± 1.0e−10
	5–6	6.3e−11 ± 6.9e−11 ± 3.1e−12 ± 8.7e−12
	6–7	3.5e−11 ± 5.7e−11 ± 1.8e−12 ± 4.9e−12
20–40	0–1	5.7e−08 ± 9.1e−09 ± 2.8e−09 ± 7.9e−09
	1–2	3.4e−08 ± 3.3e−09 ± 1.7e−09 ± 4.7e−09
	2–3	1.3e−08 ± 1.6e−09 ± 6.3e−10 ± 1.8e−09
	3–4	2.5e−09 ± 7.7e−10 ± 1.3e−10 ± 3.4e−10
	4–5	8.4e−10 ± 4.0e−10 ± 4.2e−11 ± 1.2e−10
	5–6	2.0e−10 ± 2.1e−10 ± 9.9e−12 ± 2.8e−11
	6–7	3.1e−10 ± 1.8e−10 ± 1.5e−11 ± 4.3e−11
40–60	0–1	5.9e−08 ± 1.3e−08 ± 3.0e−09 ± 8.2e−09
	1–2	3.3e−08 ± 5.2e−09 ± 1.7e−09 ± 4.6e−09
	2–3	1.3e−08 ± 2.6e−09 ± 6.3e−10 ± 1.8e−09
	3–4	5.6e−10 ± 1.4e−09 ± 2.8e−11 ± 7.7e−11
	4–5	1.0e−09 ± 7.8e−10 ± 5.0e−11 ± 1.4e−10
60–94	0–1	8.2e−08 ± 3.1e−08 ± 4.1e−09 ± 1.1e−08
	1–2	3.4e−08 ± 7.6e−09 ± 1.7e−09 ± 4.8e−09
	2–3	5.5e−09 ± 3.7e−09 ± 2.7e−10 ± 7.6e−10
	3–4	3.4e−09 ± 2.9e−09 ± 1.7e−10 ± 4.7e−10

Table E.2: Invariant yield of J/ψ divided by the number of binary nucleon-nucleon collisions for 0–20%, 20–40%, 40–60% and 60–94%.

Centrality(%)	$BR/N_{coll}dN/dy \pm$ stat $\pm$ uncorr. syst $\pm$ corr. syst
0–94 (MB)	7.0e-07 ± 2.6e-08 ± 3.5e-08 ± 9.7e-08
0–10	5.5e-07 ± 4.4e-08 ± 2.8e-08 ± 7.7e-08
10–20	6.6e-07 ± 5.1e-08 ± 3.3e-08 ± 9.2e-08
20–30	8.0e-07 ± 6.5e-08 ± 4.0e-08 ± 1.1e-07
30–40	9.8e-07 ± 8.7e-08 ± 4.9e-08 ± 1.4e-07
40–50	9.7e-07 ± 1.2e-07 ± 4.9e-08 ± 1.4e-07
50–60	7.8e-07 ± 1.3e-07 ± 3.9e-08 ± 1.1e-07
60–94	7.1e-07 ± 1.1e-07 ± 3.6e-08 ± 1.0e-07

Table E.3: Integrated invariant yield of J/ψ divided by the number of binary nucleon-nucleon collisions for each Centrality.

Centrality(%)	p_T (GeV/c)	$R_{AA}(p_T) \pm$ stat $\pm$ total syst $\pm p +$ pref.
0–94	0–1	0.60 ± 0.06 ± 0.09 ± 0.06
(MB)	1–2	0.61 ± 0.04 ± 0.09 ± 0.06
	2–3	0.62 ± 0.05 ± 0.09 ± 0.07
	3–4	0.38 ± 0.08 ± 0.06 ± 0.06
	4–5	0.93 ± 0.24 ± 0.14 ± 0.30
0–20	0–1	0.55 ± 0.07 ± 0.08 ± 0.06
	1–2	0.50 ± 0.05 ± 0.07 ± 0.05
	2–3	0.54 ± 0.07 ± 0.08 ± 0.06
	3–4	0.33 ± 0.10 ± 0.05 ± 0.06
	4–5	0.89 ± 0.29 ± 0.13 ± 0.29
20–40	0–1	0.65 ± 0.11 ± 0.10 ± 0.06
	1–2	0.79 ± 0.08 ± 0.12 ± 0.08
	2–3	0.78 ± 0.10 ± 0.12 ± 0.09
	3–4	0.61 ± 0.19 ± 0.09 ± 0.10
	4–5	1.00 ± 0.48 ± 0.15 ± 0.32
40–60	0–1	0.68 ± 0.15 ± 0.10 ± 0.06
	1–2	0.77 ± 0.12 ± 0.11 ± 0.07
	2–3	0.78 ± 0.16 ± 0.12 ± 0.09
	3–4	0.14 ± 0.34 ± 0.02 ± 0.02
	4–5	1.19 ± 0.92 ± 0.18 ± 0.38
60–94	0–1	0.94 ± 0.36 ± 0.14 ± 0.09
	1–2	0.80 ± 0.18 ± 0.12 ± 0.08
	2–3	0.34 ± 0.23 ± 0.05 ± 0.04
	3–4	0.82 ± 0.71 ± 0.12 ± 0.14

Table E.4: The nuclear modification factor of J/ψ for each Centrality and each p_T bin.

Appendix F

Mass Spectra of $e^+e^-\gamma$

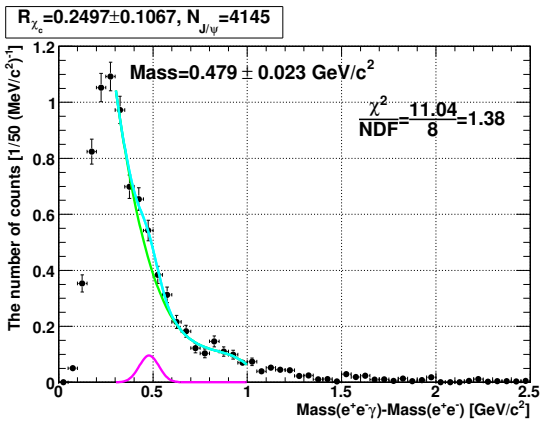

Figure F.1: The mass spectrum of data of Run-5 and Run-6 $p+p$ 200 GeV with ecore > 0.20 GeV. Other cuts are same as the nominal cut.

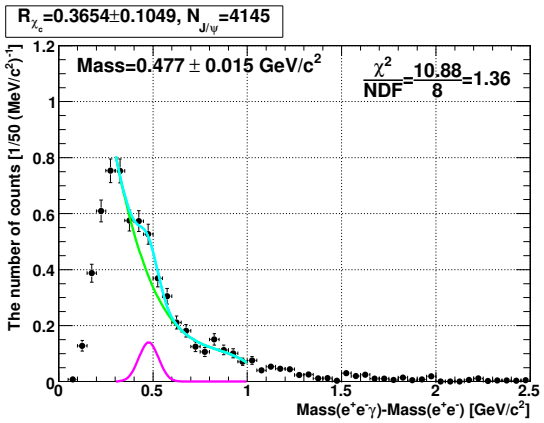

Figure F.2: The mass spectrum of data of Run-5 and Run-6 $p+p$ 200 GeV with ecore > 0.25 GeV. Other cuts are same as the nominal cut.

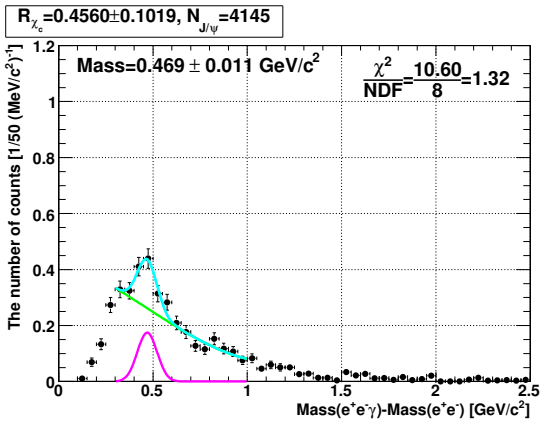

Figure F.3: The mass spectrum of data of Run-5 and Run-6 $p+p$ 200 GeV with ecore > 0.35 GeV. Other cuts are same as the nominal cut.

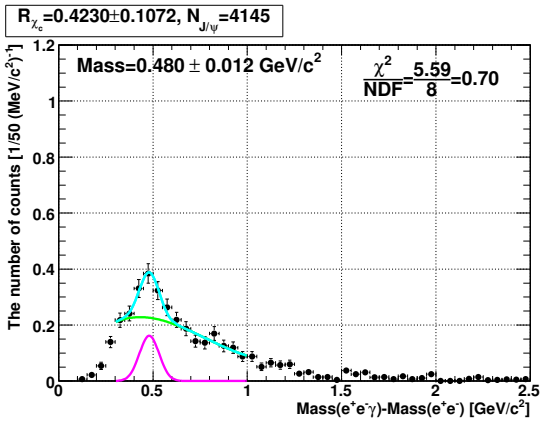

Figure F.4: The mass spectrum of data of Run-5 and Run-6 $p+p$ 200 GeV with ecore > 0.40 GeV. Other cuts are same as the nominal cut.

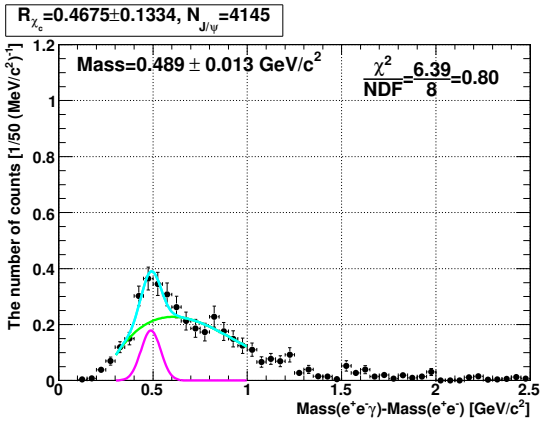

Figure F.5: The mass spectrum of data of Run-5 and Run-6 $p+p$ 200 GeV with ecore > 0.45 GeV. Other cuts are same as the nominal cut.

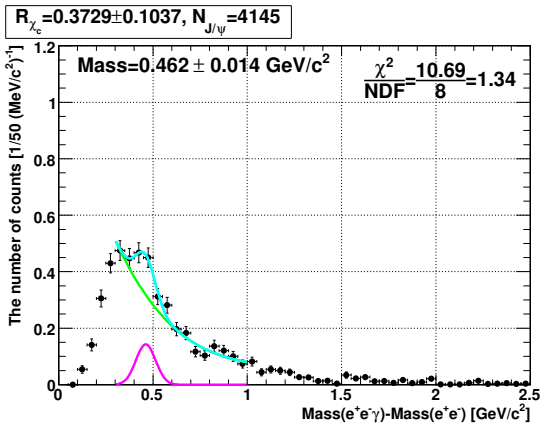

Figure F.6: The mass spectrum of data of Run-5 and Run-6 $p+p$ 200 GeV with a emcchi2 < 1.5 cut. Other cuts are same as the nominal cut.

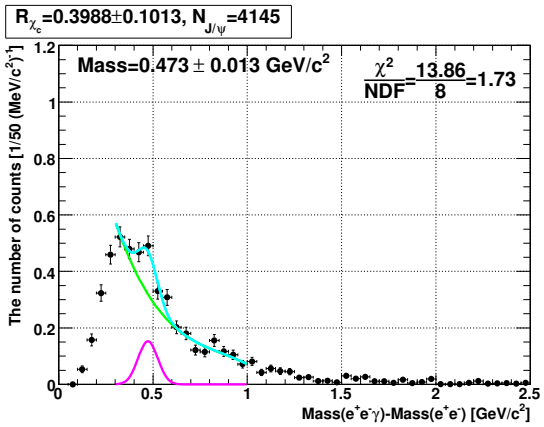

Figure F.7: The mass spectrum of data of Run-5 and Run-6 $p+p$ 200 GeV with a emcchi2 < 3.5 cut. Other cuts are same as the nominal cut.

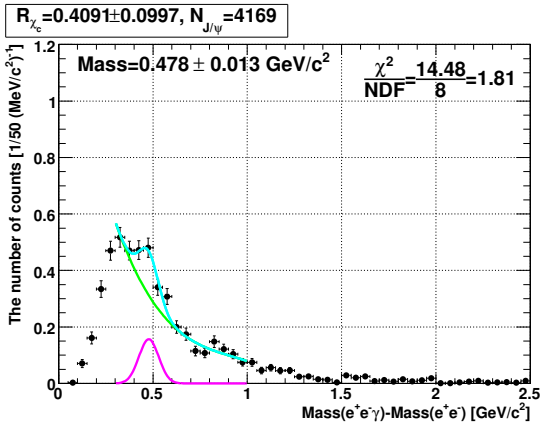

Figure F.8: The mass spectrum of data of Run-5 and Run-6 $p+p$ 200 GeV with a smaller DC charged particle veto of 17.5 cm$\times$0.035 radian. Other cuts are same as the nominal cut.

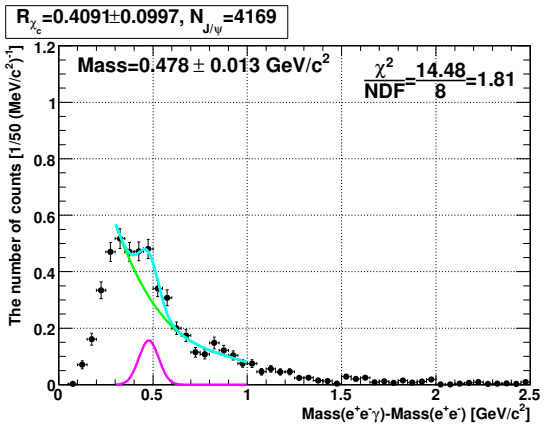

Figure F.9: The mass spectrum of data of Run-5 and Run-6 $p+p$ 200 GeV with a larger DC charged particle veto of 70 cm×0.14 radian. Other cuts are same as the nominal cut.

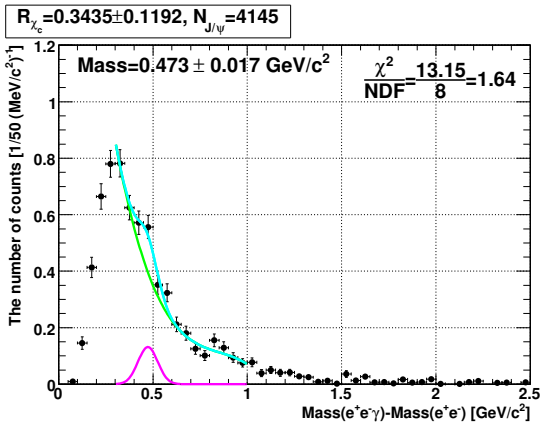

Figure F.10: The mass spectrum of data of Run-5 and Run-6 $p+p$ 200 GeV without PbGl with a ecore > 0.25 GeV cut. Other cuts are same as the nominal cut.

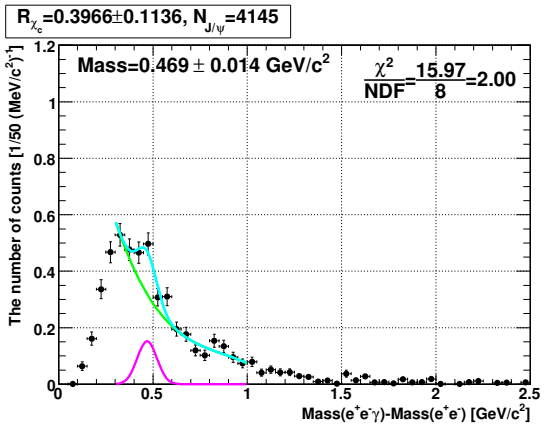

Figure F.11: The mass spectrum of data of Run-5 and Run-6 $p+p$ 200 GeV without PbGl with a ecore > 0.30 GeV cut. Other cuts are same as the nominal cut.

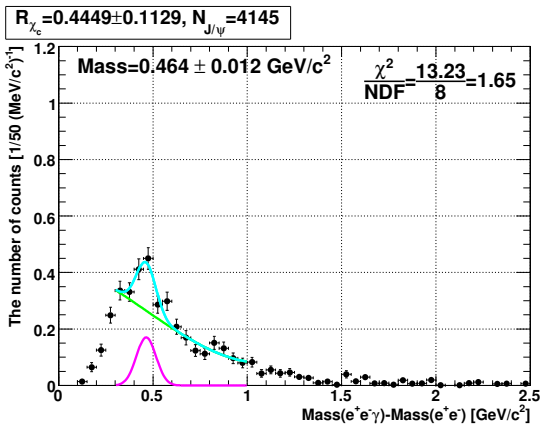

Figure F.12: The mass spectrum of data of Run-5 and Run-6 $p+p$ 200 GeV without PbGl with a ecore > 0.35 GeV cut. Other cuts are same as the nominal cut.

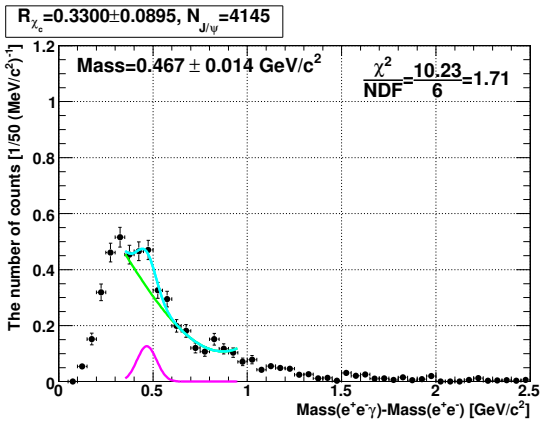

Figure F.13: The mass spectrum of data of Run-5 and Run-6 $p+p$ 200 GeV fitted with a narrower range of 0.35–0.95 GeV/c^2.

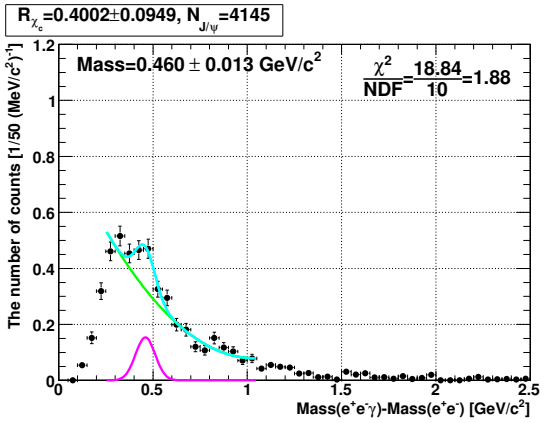

Figure F.14: The mass spectrum of data of Run-5 and Run-6 $p+p$ 200 GeV fitted with a wider range of 0.25–1.05 GeV/c^2.

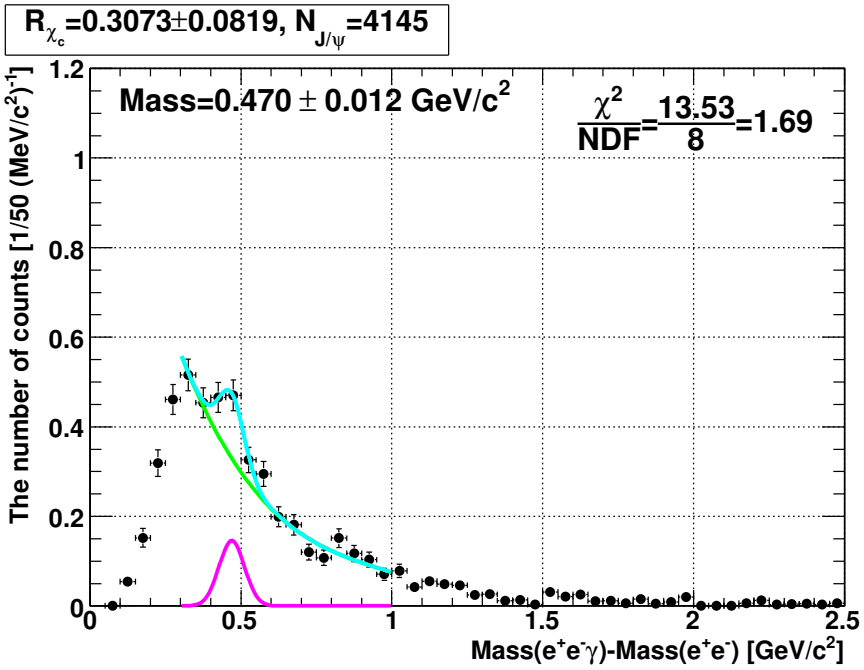

Figure F.15: The mass spectrum of data of Run-5 and Run-6 $p+p$ 200 GeV with the fixed peak width of 42 MeV/c^2.

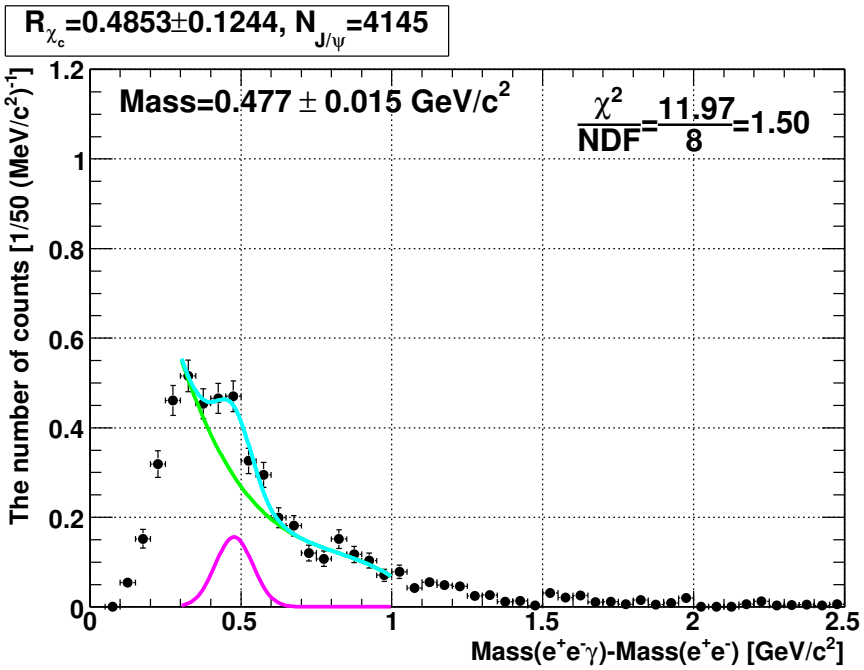

Figure F.16: The mass spectrum of data of Run-5 and Run-6 $p+p$ 200 GeV with the fixed peak width of 62 MeV/c^2.

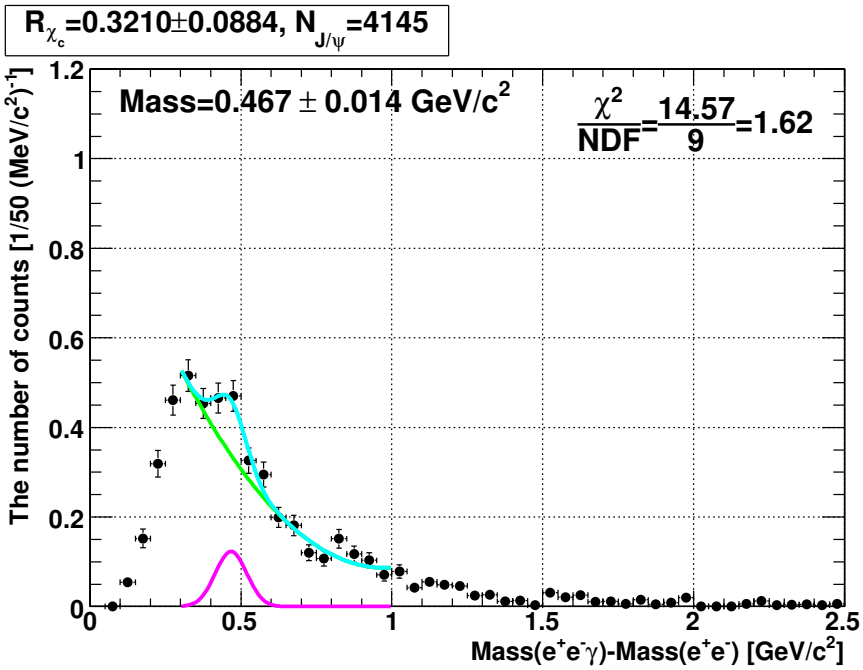

Figure F.17: The mass spectrum of data of Run-5 and Run-6 $p+p$ 200 GeV fitted with the second order polynomial function.

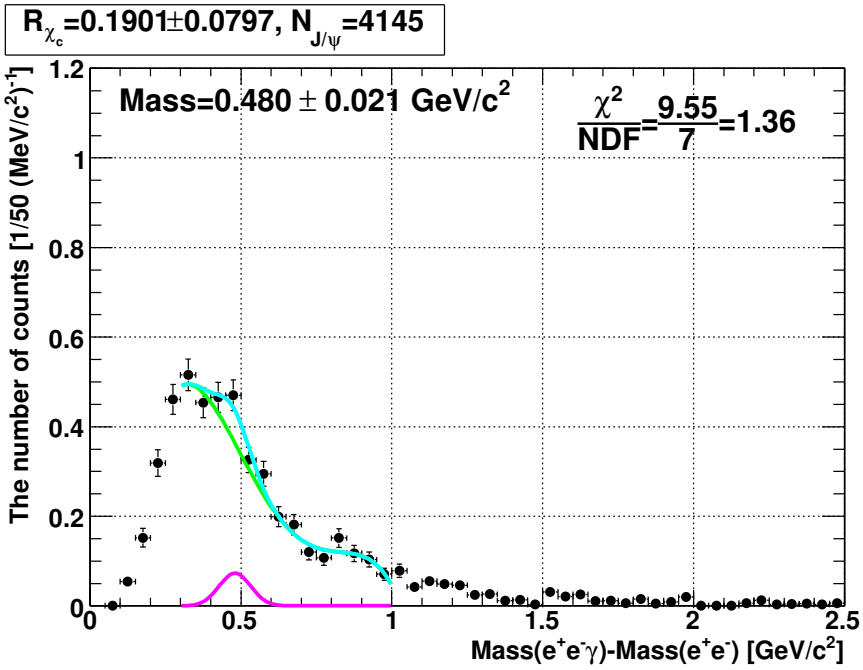

Figure F.18: The mass spectrum of data of Run-5 and Run-6 $p+p$ 200 GeV fitted with the fourth order polynomial function.

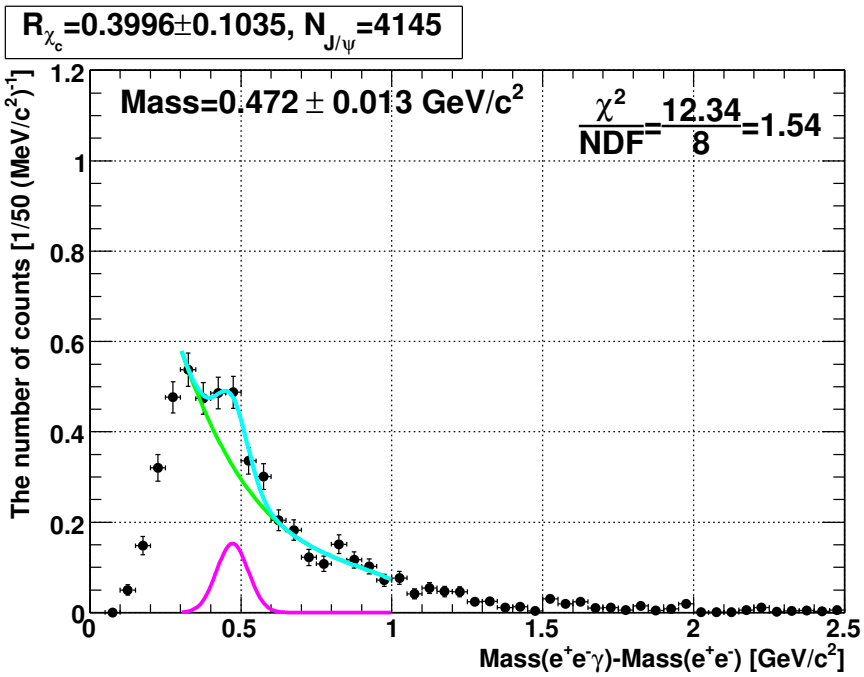

Figure F.19: The mass spectrum of data of Run-5 and Run-6 $p+p$ 200 GeV with the ERT LVL1 trigger efficiency for J/ψ obtained with $\langle p_T^2 \rangle = 3.87$ (GeV/c)^2.

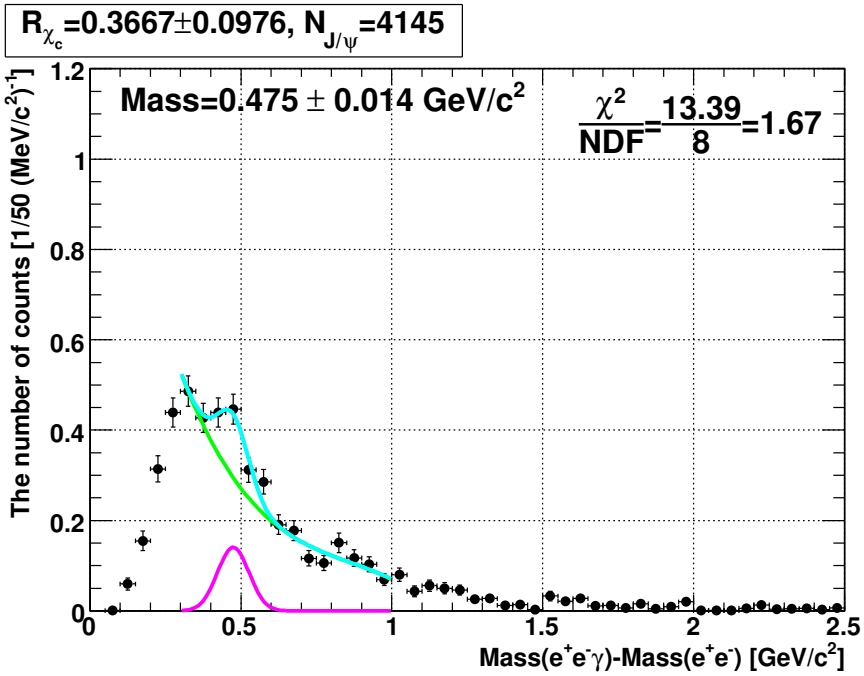

Figure F.20: The mass spectrum of data of Run-5 and Run-6 $p+p$ 200 GeV with the ERT LVL1 trigger efficiency for J/ψ obtained with $\langle p_T^2 \rangle = 4.49$ (GeV/c)^2.

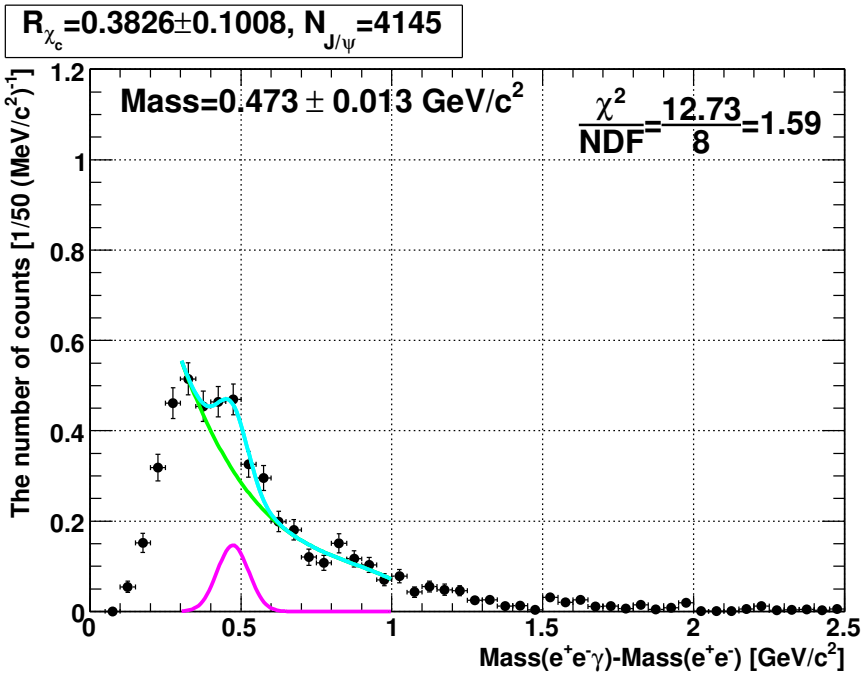

Figure F.21: The mass spectrum of data of Run-5 and Run-6 $p+p$ 200 GeV obtained with the Run-4 Au+Au 200 GeV simulation setting.

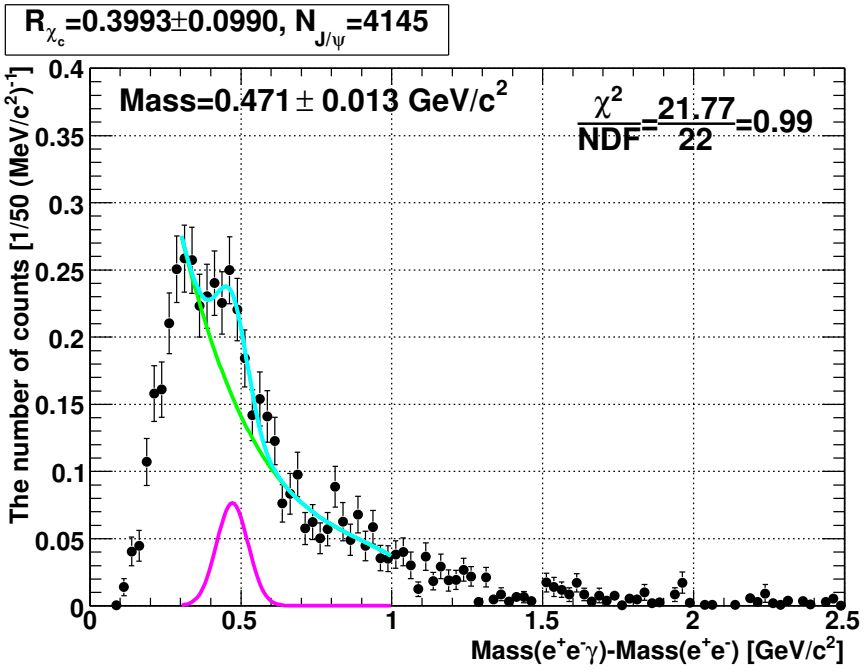

Figure F.22: The mass spectrum of data of Run-5 and Run-6 $p+p$ 200 GeV with a finer binning of 25 MeV/c^2.

Appendix G

Data Analysis of J/ψ Meson in Cu+Cu Collisions in Muon Arms

G.1 Trigger

The analysis of $J/\psi \to \mu^+\mu^-$ in Cu+Cu collisions at $\sqrt{s_{NN}}$ =200 GeV in Run-5 [9] was performed with events triggered by the coincidence of the minimum bias trigger and a MuID (Muon Identifier) level-1 trigger (MUIDLL1). The Muon Arms have two kinds of local triggers. One trigger is fired by tracks which reached to the second gap of MuID and called "Shallow". The other trigger is fired by tracks which reached to the fourth gap of MuID and called "Deep".

The MUIDLL1_N2D and MUIDLL1_S2D are di-muon triggers required two candidate tracks to penetrate the MuID (Deep+Deep) of the North and South arms, roughly point back to the event vertex, and pass an opening angle cut of $> 19°$.

Level-1 triggered events were further required to satisfy an offline filter (a level-2 trigger) which performed a fast reconstruction of particle trajectories in the MuTr (Muon Tracker) and MuID. Accepted events were required to have two tracks penetrating the entire MuID with the invariant mass of $M_{\mu\mu} > 2.0$ GeV/c^2. The MuID road slope is required to be $\theta > 12°$ (corresponding to a p_T cut).

G.2 Reconstruction

The events whose BbcZvertex is within $\pm$30 cm was selected for the analysis. A sampled integrated luminosity of 1.3 nb^{-1} was used.

Muon tracks were reconstructed with the road finding by MuID and tracking by MuTr. First, one-dimensional roads of MuID hits between gaps were searched. Only the roads reaching at least the second gap were used to reconstruct a track. Then, MuTr hits around the road were associated to the road. Finally, the track was reconstructed from BbcZvertex and the positions of MuTr hits associated by the Kalman fit.

In addition, the track selection was performed with the following cuts.

- The difference between the projected position of the MuTr track to the zeroth layer of the MuID and the MuID hit position in the layer is called the DG0 variable. DG0 is required to be less than 15 cm for the North arm and 25 cm for

the South arm. This difference is due to the difference of the gaps between MuTr and MuID in the two arms.

- The angle difference between the MuTr track and the MuID road at the zeroth layer of the MuID is called the DDG0 variable and is required to be less than 10° (9°) for the North (South) arm.

- The tracking quality, TR_chi2, is required to be less than 35 (25) for the North (South) arm.

For di-muon reconstruction, the following cuts were applied for pairs.

- The difference between BbcZvertex and the vertex computed from the two tracks of the pair is required to be less than 5 cm.

- The rapidity of the pair is required to be $1.2 < |y| < 2.2$.

- The invariant mass of the pair is required to be $2.6 < M_{\mu\mu} < 3.6$ GeV/c^2.

G.3 Signal Extraction

The $J/\psi \to \mu^+\mu^-$ signals were subtracted by the like sign method,

$$N_{net} \;=\; N_{+-} - 2\sqrt{N_{++}N_{--}}, \tag{G.1}$$

where N_{+-}, N_{++} and N_{--} are the numbers of pairs of e^+e^-, e^+e^+ and e^-e^-, respectively. The signal count is given by the average of the following three methods used to determine the number of counts in the J/ψ peak ($2.6 < M_{\mu\mu} < 3.6$ GeV/c^2).

1. A fit to the distribution using an exponential to account for the residual background and a Gaussian to account for the J/ψ signal (the Gaussian mean is fixed to 3.1 GeV/c^2 and the Gaussian width is constrained to be between 150 and 300 MeV/c^2.).

2. A fit to the distribution using an exponential to account for the residual background and two Gaussians for which both the mean and the width are fixed based on the results obtained $p + p$ data [7]. The narrow Gaussian corresponds to the main J/ψ signal whereas the wide Gaussian corresponds to tails due to internal and external radiation and tracks passing through faulty regions of the detector. The ratio between the two Gaussian amplitudes is also fixed using the $p+p$ results and only one parameter (the amplitude) is left free for the double Gaussian part of the fit.

3. A fit to the distribution using an exponential to account for the residual background. The fit is performed for muon pair masses falling outside of the J/ψ mass window of 2.6–3.6 GeV/c^2 and interpolated to the J/ψ region. The J/ψ signal is obtained from the number of entries in the distribution sitting on top of the exponential in this mass window.

The variation among these methods gives the systematic error on the signal count. The resulting total J/ψ count in the $\mu^+\mu^-$ channel was about 9000. Figure G.1 shows the di-muon mass spectra of the North and South arms.

The acceptance and trigger efficiency were calculated with PISA simulation.

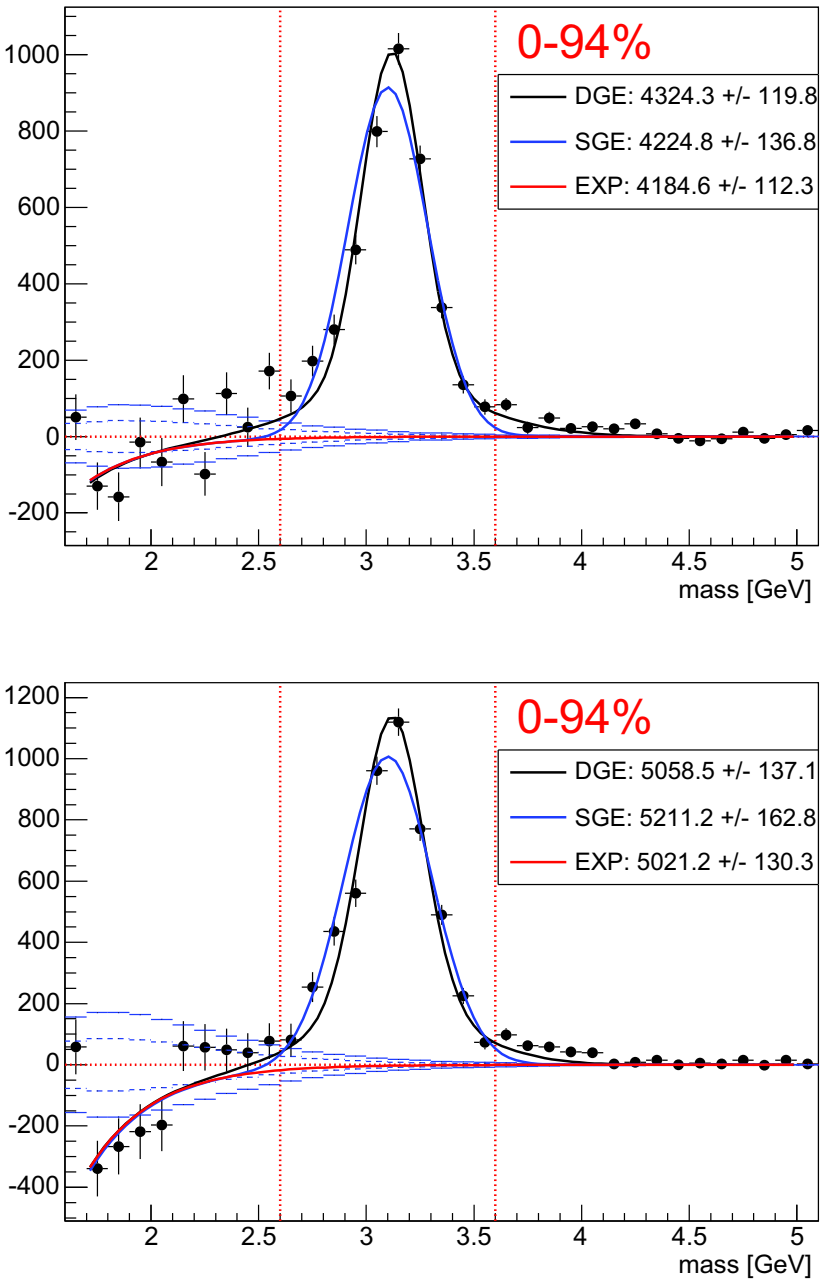

Figure G.1: Mass spectra of $\mu^+\mu^-$ pairs integrated over Centrality and p_T for North (top, $1.2 < y < 2.2$) and South (bottom, $-2.2 < y < -1.2$) arms.

Bibliography

[1] D.J. Gross *et al.*, Phys. Rev. Lett. 30, 1343 (1973).

[2] H.D. Polizer, Phys. Rev. Lett. 30, 1346 (1973).

[3] F. Karsch, arXiv:0711.0656 [hep-lat] (2007).

[4] T. Matsui and H. Satz, Phys. Lett. B 178, 416 (1986).

[5] M.C. Abreu *et al.*, Phys. Lett. B 477, 28 (2000).

[6] A. Adare *et al.*, Phys. Rev. Lett. 98, 232301 (2007).

[7] A. Adare *et al.*, Phys. Rev. Lett. 98, 232002 (2007).

[8] A. Adare *et al.*, arXiv:0711.3917 [nucl-ex] (2007).

[9] A. Adare *et al.*, arXiv:0801.0220 [nucl-ex] (2008).

[10] Cheuk-Yin Wong, Introduction to High-Energy Heavy-Ion Collisions, (World Scientific, 1994).

[11] K. Yagi *et al.*, Quark-Gluon Plasma, (Cambridge University Press, 2005).

[12] R. Vogt, Ultrarelativistic Heavy-Ion Collisions, (Elsevier, 2007).

[13] A. Chods *et al.*, Phys. Rev. D 9, 3471 (1974).

[14] R.J. Glauber, in: Lectures in theoretical physics, ed. W.E. Brittin *et al.*, (Interscience Publishers, New York, 1959) vol. I, p. 315.

[15] J.D. Bjorken, Phys. Rev. D 27, 140 (1983).

[16] P.F. Kolb, arXiv:nucl-th/0304036 (2003).

[17] T. Alber *et al.*, Phys. Rev. Lett. 75, 3814 (1995).

[18] S.S. Adler *et al.*, Phys. Rev. C 71, 034908 (2005).

[19] W.-M. Yao *et al.*, Journal of Physics G 33, 1 (2006).

[20] J.J. Aubert *et al.*, Phys. Rev. Lett. 33, 1404 (1974).

[21] J.-E. Augustin *et al.*, Phys. Rev. Lett. 33, 1406 (1974).

[22] G.S. Abrams *et al.*, Phys. Rev. Lett. 33, 1453 (1974).

[23] W. Braunschweig *et al.*, Phys. Lett. B 57, 407 (1975).

[24] F. Karsch *et al.*, Z. Phys. C 37, 617 (1988).

[25] E. Norrbin *et al.*, Eur. Phys. J. C 17, 137 (2000).

[26] B.L. Combridge, Nucl. Phys. B 151, 429 (1979).

[27] W. Beenakeer *et al.*, Nucl. Phys. B 351, 507 (1991).

[28] C.H. Chang, Nucl. Phys. B 172, 425 (1980).

[29] R. Baier *et al.*, Phys. Lett. B 102, 364 (1981).

[30] E.L. Berger *et al.*, Phys. Rev. D 23, 1521 (1981).

[31] F. Abe *et al.*, Phys. Rev. Lett. 79, 572 (1997).

[32] H. Fritzsch, Phys. Lett. B 67, 217 (1977).

[33] M. Glück *et al.*, Phys. Rev. D 17, 2324 (1978).

[34] A. Abulencia *et al.*, Phys. Rev. Lett. 99, 132001 (2007).

[35] R.V. Gavai *et al.*, Int J. Mod. Phys. A 10, 3043 (1995).

[36] V. Berger *et al.*, Phys. Lett. B 91, 253 (1980).

[37] G.A. Schuler *et al.*, Phys. Lett. B 387, 181 (1996).

[38] M. Beneke *et al.*, Phys. Rev. D 54, 2005 (1996).

[39] M. Bedjidian *et al.*, arXiv:hep-ph/0311048 (2003).

[40] M. Cacciari *et al.*, Phys. Rev. Lett. 95, 122001 (2005).

[41] F. Maltoni *et al.*, Phys. Lett. B 638, 202 (2006).

[42] F. Abe *et al.*, Phys. Rev. Lett. 79, 578 (1997).

[43] M.Krämer, Prog. Part. Nucl. Phys. 47, 141 (2001).

[44] N. Brambilla *et al.*, CERN Yellow Report 2005-005, arXiv:hep-ph/0412158 (2005).

[45] I. Abt *et al.*, Phys. Lett B 561, 61 (2003).

[46] P. Faccioli *et al.*, Nucl. Phys. A 783, e1 (2007).

[47] A. Adare *et al.*, Phys. Rev. Lett. 97, 252002 (2006).

[48] D. Kharzeev *et al.*, Phys. Lett. B 366, 316 (1996).

[49] R. Vogt, Nucl. Phys. A 700, 539 (2002).

[50] O. Kaczmarek *et al.*, Phys. Rev. D 71, 114510 (2005).

[51] D.J. Gross *et al.*, Rev. Mod. Phys. 53, 43 (1981).

[52] M. Asakawa *et al.*, Phys. Rev. Lett. 92, 012001 (2004).

[53] H. Satz, J. Phys. G 32, R25 (2006).

[54] S. Datta *et al.*, Phys. Rev. D 69, 094507 (2004).

[55] T. Umeda *et al.*, Eur. Phys. J. C 39, s9 (2005).

[56] C.-Y. Wong *et al.*, Phys. Rev. C 72, 034906 (2005).

[57] L. Grandchamp *et al.*, Phys. Rev. Lett. 92, 212301 (2004).

[58] R.L. Thews *et al.*, Phys. Rev. C 73, 014904 (2006).

[59] L. Yan *et al.*, Phys. Rev. Lett. 97, 232301 (2006).

[60] P. Braun-Munzinger *et al.*, Phys. Lett. B 465, 15 (1999).

[61] E.L. Bratkovskaya *et al.*, Phys. Rev. C 69, 054903 (2004).

[62] T. Barnes, arXiv:nucl-th/0306031 (2003).

[63] A. Capella *et al.*, Phys. Rev. Lett. 85, 2080 (2000).

[64] J.J. Aubert *et al.*, Phys. Lett. B 31, 275 (1983).

[65] D. de Florian *et al.*, Phys. Rev. D 69, 074028 (2004).

[66] K.J. Eskola *et al.*, Eur. Phys. J. C 9, 61 (1999).

[67] M. Hirai *et al.*, Phys. Rev. D 64, 034003 (2001).

[68] F. Arleo *et al.*, arXiv:hep-ph/0612043 (2006).

[69] B. Povh *et al.*, Phys. Rev. Lett. 58, 1612 (1987).

[70] A.M. Glenn *et al.*, Phys. Lett. B 644, 119 (2007).

[71] E. Iancu *et al.*, arXiv:hep-ph/0303204 (2003).

[72] Y. Maezawa *et al.*, PoS LAT2006, 141 (2006).

[73] M.J. Leitch *et al.*, Phys. Rev. Lett. 84, 3256 (2000).

[74] R. Vogt, Acta. Phys. Hung. A 25, 97 (2006).

[75] J.W. Cronin *et al.*, Phys. Rev. D 11, 3105 (1975).

[76] C.Baglin, *et al.*, Phys. Lett. B 220, 471 (1989).

[77] C.Baglin, *et al.*, Phys. Lett. B 251, 465 (1990).

[78] C.Baglin, *et al.*, Phys. Lett. B 255, 459 (1991).

[79] C.Baglin, *et al.*, Phys. Lett. B 262, 362 (1991).

[80] C.Baglin, *et al.*, Phys. Lett. B 268, 453 (1991).

[81] C.Baglin, *et al.*, Phys. Lett. B 270, 105 (1991).

[82] C.Baglin, *et al.*, Phys. Lett. B 345, 617 (1995).

[83] M.C. Abreu *et al.*, Phys. Lett. B 423, 207 (1998).

[84] M.C. Abreu *et al.*, Phys. Lett. B 444, 516 (1998).

[85] M.C. Abreu *et al.*, Phys. Lett. B 449, 128 (1999).

[86] M.C. Abreu *et al.*, Phys. Lett. B 466, 408 (1999).

[87] M.C. Abreu *et al.*, Phys. Lett. B 410, 327 (1997).

[88] M.C. Abreu *et al.*, Phys. Lett. B 410, 337 (1997).

[89] M.C. Abreu *et al.*, Phys. Lett. B 450, 456 (1999).

[90] M.C. Abreu *et al.*, Phys. Lett. B 499, 85 (2001).

[91] M.C. Abreu *et al.*, Phys. Lett. B 521, 195 (2001).

[92] B. Alessandro *et al.*, Eur. Phys. J. C 33, 31 (2004).

[93] B. Alessandro *et al.*, Eur. Phys. J. C 39, 335 (2005).

[94] B. Alessandro *et al.*, Eur. Phys. J. C 48, 329 (2006).

[95] B. Alessandro *et al.*, Eur. Phys. J. C 49, 559 (2007).

[96] M.C. Abreu *et al.*, Phys. Lett. B 438, 35 (1998).

[97] R. Arnaldi *et al.*, Phys. Rev. Lett. 99, 132302 (2007).

[98] S.S. Adler *et al.*, Phys. Rev. C 69, 014901 (2004).

[99] S.S. Adler *et al.*, Phys. Rev. Lett. 92, 051802 (2004).

[100] S.S. Adler *et al.*, Phys. Rev. Lett. 96, 012304 (2006).

[101] R. Vogt, Phys. Rev. C 71, 054902 (2005).

[102] F. Cooper *et al.*, Phys. Rev. Lett. 93, 171801 (2004).

[103] V.A. Khoze *et al.*, Eur. Phys. J. C 39, 163 (2005).

[104] H. Hahn *et al.*, Nucl. Instr. and Meth. A 499, 245 (2003).

[105] M. Adamczyk *et al.*, Nucl. Instr. and Meth. A 499, 437 (2003).

[106] K. Adcox *et al.*, Nucl. Instr. and Meth. A 499, 469 (2003).

[107] B.B. Back *et al.*, Nucl. Instr. and Meth. A 499, 603 (2003).

[108] K.H. Ackermann *et al.*, Nucl. Instr. and Meth. A 499, 624 (2003).

[109] M. Allen *et al.*, Nucl. Instr. and Meth. A 499, 549 (2003).

[110] T. Ludlam, Nucl. Instr. and Meth. A 499, 428 (2003).

[111] C. Adler *et al.*, Nucl. Instr. and Meth. A 470, 488 (2001).

[112] C. Adler *et al.*, Nucl. Instr. and Meth. A 499, 433 (2003).

[113] S.H. Aronson *et al.*, Nucl. Instr. and Meth. A 499, 480 (2003).

[114] K. Adcox *et al.*, Nucl. Instr. and Meth. A 499, 489 (2003).

[115] M. Aizawa *et al.*, Nucl. Instr. and Meth. A 499, 508 (2003).

[116] Y. Akiba *et al.*, Nucl. Instr. and Meth. A 433, 143 (1999).

[117] T. Sakaguchi *et al.*, Nucl. Instr. and Meth. A 453, 382 (2000).

[118] L. Aphecetche *et al.*, Nucl. Instr. and Meth. A 499, 521 (2003).

[119] H. Akikawa *et al.*, Nucl. Instr. and Meth. A 499, 537 (2003).

[120] S.S. Adler *et al.*, Nucl. Instr. and Meth. A 499, 560 (2003).

[121] S.S. Adler *et al.*, Phys. Rev. C 75, 024909 (2007).

[122] K. Homma, PHENIX Analysis Note 383 (2005).

[123] J. Nagle *et al.*, PHENIX Analysis Note 387 (2005).

[124] GEANT Detector description and simulation tool, CERN Program Library Long Write-up W5013, CERN Geneva.

[125] X.-N. Wang *et al.*, Phys. Rev. D 44, 3501 (1991).

[126] Y. Nara *et al.*, Phys. Rev. C 61, 024901 (1999).

[127] H. de Vries *et al.*, Atomic Data and Nuclear Data Tables 36, 495 (1987).

[128] J.T. Mitchell *et al.*, Nucl. Instr. and Meth. A 482, 491 (2002).

[129] T. Sjostrand *et al.*, arXiv:hep-ph/0603175 (2006), `http://www.thep.lu.se/ torbjorn/Pythia.html`.

[130] T.A. Armstrong *et al.*, Phys. ReV. D 54, 7067 (1996).

[131] A. Spiridonov, arXiv:hep-ex/0510076 (2005).

[132] T. Gunji *et al.*, PHENIX Analysis Note 589 (2006).

[133] S.R. Hahn *et al.*, Phys. Rev. D 30, 671 (1984).

[134] T. Affolder *et al.*, Phys. Rev. Lett. 86, 3963 (2001).

[135] A. Abulencia *et al.*, Phys. Rev. Lett. 98, 232001 (2007).

[136] S. Bathe *et al.*, PHENIX Analysis Note 472 (2005).

[137] S.S. Adler *et al.*, Phys. Rev. Lett. 91, 241803 (2003).

[138] T. Chujo *et al.*, PHENIX Analysis Note PPG045 (2007).

[139] Y. Akiba *et al.*, PHENIX Analysis Note 581 (2007).

[140] F. Yuan *et al.*, Phys. Lett. B 500, 99 (2001).

[141] G. Karl *et al.*, Phys. Rev. Lett. 45, 215 (1980).

[142] M. Ambrogiani *et al.*, Phys. Rev. D 65, 052002 (2002).

[143] P. Cho *et al.*, Phys. Rev. D 53, 6203 (1996).

[144] G.T. Bodwin *et al.*, Phys. Rev. D 51, 1125 (1995).

[145] J.F. Amundson *et al.*, Phys. Lett. B 372, 127 (1996).

[146] M.L. Mangano, AIP Conf. Proc. 357, 120 (1996).

[147] R. Baier *et al.*, Z. Phys. C 19, 251 (1983).

[148] G. Schuler, arXiv:hep-ph/9403387 (1994).

[149] V. Koreshev *et al.*, Phys. Rev. Lett. 77, 4294 (1996).

[150] M. Maul, Nucl. Phys. B 594, 89 (2001).

[151] S.S. Adler *et al.*, Phys. Rev. Lett. 94, 232301 (2005).

[152] A. Adare *et al.*, Phys. Rev. Lett. 98, 172301 (2007).

[153] K. Tywoniuk *et al.*, Phys. Lett. B 657, 170 (2007).

[154] L. Frankfurt *et al.*, Phys. Rev. D 71, 054001 (2005).

[155] A. Capella *et al.*, arXiv:hep-ph/0610313 (2006).

[156] O. Linnyk *et al.*, Phys. Rev. C 76, 041901 (2007).

[157] A. Andronic *et al.*, Phys. Lett. B 652, 259 (2007).

[158] T. Gunji *et al.*, Phys. Rev. C 76, 051901 (2007).

[159] T. Hirano *et al.*, Nucl. Phys. A 715, 821 (2003).

[160] V. Greco *et al.*, Phys. Lett. B 595, 202 (2004).

[161] L. Ravagli *et al.*, Phys. Lett. B 655, 126 (2007).

[162] A. Deshpande *et al.*, Ann. Rev. Nucl. Part. Sci. 55, 165 (2005).